Search for Earth-like planets in the habitable zone of M-dwarfs

Nicola Astudillo-Defru

UNIVERSITÉ DE GRENOBLE

THÈSE

Pour obtenir le grade de

DOCTEUR DE L'UNIVERSITÉ DE GRENOBLE

Spécialité : **Astrophysique et Milieux Dilués**

Arrêté ministériel : 7 Août 2006

Présentée par

Nicola Astudillo-Defru

Thèse dirigée par
Xavier Delfosse
et codirigée par
Xavier Bonfils

préparée au sein de
l'Institut de Planétologie et d'Astrophysique de Grenoble (IPAG)
et de
l'École Doctorale de Physique

Recherche de planètes habitables autour de naines M

Thèse soutenue publiquement le **27 Mars 2015**,
devant le jury composé de :

Mme. Nadège Meunier
Astronome – IPAG, Présidente
Mr. René Doyon
Professeur – Université de Montréal, Rapporteur
Mr. François Bouchy
Astronome – Laboratoire d'Astrophysique de Marseille, Rapporteur
Mr. Christophe Lovis
Maître d'Enseignement et de Recherche – Obs. de Genève, Examinateur
Mr. Xavier Delfosse
Astronome – IPAG, Directeur de thèse
Mr. Xavier Bonfils
Chercheur-CNRS – IPAG, Co-Directeur de thèse

Dédié à toutes les personnes qui ont marqué et soutenue mon chemin

Remerciements

En tant que doctorant a l'IPAG, un fois passé la soutenance, je peux dire que la thèse ce deroulé d'une manière trés agreable et satisfaisante. C'est maintenant le moment de remercier à toutes les personnes (je m'excuse pour les oublis possibles), que d'une manière ou d'un autre, ont fait partie de ces trois années de thèse.

Tout d'abord j'adresse mes plus grands remerciements a Xavier Delfosse et Xavier Bonfils, mes directeurs de thèse. Je sens que j'ai eu un grand privilège des faire ma thèse avec eux, non seulement parce qu'ils sont de scientifiques et encadrants exceptionnels, mais aussi par leur amabilité et toujours grande disposition. Avec eux j'ai appris énormément (et continuera de le faire), ils mon donné l'independance necessaire dans la manière de faire les choses, en même temps d'avoir toujours eu les bons conseils et l'approche constructive pendant nos réunions.

En suite, un grand merci aux membres de mon jury de thèse. Aux rapporteurs, François Bouchy et René Doyon, qui ont bien acceptée d'évaluer ma thèse en seulement deux semaines. À Christophe Lovis, examinateur, qui a montré beacoup d'intérêt sur mon travail (et avec qui je travaille actuellement en tant que Post-doc à l'Observatoire de Genève). Nadège Meunier, prèsidente du jury, qui a fait des précieuses remarques sur le manuscrit de thèse.

Je souhaite aussi remercier à tous les membres de l'IPAG, très specialement à Thierry Forveille. Thierry à eu une importante présence pendant ma thèse, en plus, il a transformé mes papiers pour que l'anglais soit plus agréable à lire. Bien sûr, merci aux doctorants et post-docs du laboratoire (Ana, Jorge, Susana, Alexis, Amy, Linda, Nicole, Ali, Antoine, Florien... la liste est longue) avec qui j'ai passé des très bons moments. En dehors de l'IPAG, spécifiquement de Montréal, je remercie a Etienne Artigau, avec qui j'ai collaboré sur une partie de mon travail.

Je passe maintenant à la famille. Je suis très chanceux d'être accompagné par Daphnea, qui a accepté de faire une nouvelle vie loin de sa famille (au Chili) et avec qui je me suis mariée pendant ma thèse (merci Fabien Malbet, de l'IPAG et Mairie de Grenoble). Peut-être qu'elle a souffert plus que moi pendant les derniers mois de thèse, où j'ai été assez absent du quotidien de la maison mais elle a toujours eu les bonnes activités pour les enfants. Un enorme merci a mes parents, Carole et Felipe, toujours aussi présents dans mes aventures astronomiques, ainsi comme ma bapcha (grand-mère).

Grand merci aux amis, Renzo et Pao, avec qui Daphnea et moi (et les enfants) nous avons fait des très beaux liens. Patricia et Ian, Stefan...les amis du quartier. Merci aussi aux joueurs du club d'ultimate frisbee de Grenoble (les Monkeys).

Enfin, je remercie à Becas-Chile/CONICYT, qui a fait cette thèse possible grâce aux financement d'études en dehors du Chili.

Résumé

Depuis la première détection d'une planète extrasolaire autour d'une étoile de type solaire par Mayor et Queloz (1995), plus de 1500 planètes ont été découverts. Actuellement il existe un énorme intérêt à découvrir et caractériser des planètes semblables à la Terre, en particulier celles situées dans la zone habitable de leur étoile hôte (définie comme la distance à l'étoile hôte où la température de la planète permet l'existence d'eau liquide à la surface). La détection de planètes de type terrestre, et la recherche de biomarqueurs dans leurs atmosphères sont parmi les principaux objectifs de l'astronomie du vingt et unième siècle. La méthode des vitesses radiales (VR), consistant à mesurer le mouvement réflexe de l'étoile induit par des planètes en orbite, est une remarquable technique pour atteindre cet objectif.

Pour atteindre les précisions nécessaire à la detection de telles planètes il est absolument nécessaire de concevoir des spectrographes extrêmement stables, d'avoir une très bonne compréhension de l'activité stellaire (qui peut mimer l'effet d'une planète), d'effectuer un traitement soigneux de l'atmosphère terrestre (laquelle inévitablement laisse des empreintes dans les spectres acquis depuis le sol), et de disposer d'une puissante technique pour extraire, à partir des spectres, autant d'information Doppler que possible. La recherche de planètes orbitant autour des étoiles de très faible masse, plutôt qu'autour des étoiles de type solaire, permet d'aborder dès maintenant la détection de planètes de faible masse dans la zone habitable. En effet, en gardant tout les autres paramètres égaux, le mouvement réflexe (et donc l'amplitude de la variation VR) sera plus grande si l'étoile centrale est de très faible masse. De plus les naines M ont une plus faible luminosité que les étoiles de type solaire, il en resulte des périodes orbitales courtes des planètes dans la zone habitable ($\sim$ 50 jours pour les naines M contre $\sim$ 360 jours pour des étoiles de type solaire), entraînant à nouveau en une plus grande amplitude des VR. Une précision de $\sim 1\ m\,s^{-1}$ en VR permet la détection d'une planète dans la zone habitable d'une naine M, alors que $\sim 0.1\ m\,s^{-1}$ sont nécessaire dans le cas d'une étoile de type solaire.

Cette thèse vise à optimiser l'extraction de VR des spectres des naines M à haute résolution acquis avec le spectrographe HARPS (avec une possibilité d'applications futures sur d'autres instruments comme SOPHIE, HARPS-N et le prochain spectrographe infrarouge SPIRou - prochainement mis en service au CFHT). Les effets de l'activité stellaire des naines M seront également analysées, dans le contexte de la technique des VR. Divers traceurs d'activité stellaire sont utilisés pour rejeter des fausses détections ou pour étudier les relations entre l'activité magnétique et la rotation. Dans cette thèse (chap. 3) je calibre pour la première fois le flux dans les raies H et K du Calcium en fonction de la luminosité bolométrique et je détermine la relation entre cet estimateur R'_{HK} et la période de rotation des naines M. Dans le chapitre 4 je décris l'implémentation d'une méthode d'extraction de VR par une minimisation du χ^2 entre un template spectral et les spectres observés. Je démontre que cette méthode est plus précise que celle classiquement utilisée. Les raies telluriques qui affectent les mesures VR sont prises en compte dans les procédures d'analyse. Ces méthodes sont testées sur des systèmes avec des candidats planétaires, je discuterais l'analyse de certains de ces systèmes.

Abstract

Since the first detection of an extrasolar planet orbiting a Sun-like star by Mayor and Queloz (1995), more than 1500 have been discovered. Enormous interest is currently focused on finding and characterising Earth-like planets, in particular those located in the habitable zone of their host star (defined as the distance from the host star where the planet temperature allows liquid water to flow on its surface). Both the detection of Earth-like planets, and the search for biomarkers in their atmospheres are among the main objectives of the twenty-first century's astronomy. The method known as radial velocities (RV), that consists in the measure of the star's reflex motion induced by orbiting planets, is a promising technique to achieve that quest.

The main difficulties with the RV technique are the needs of an extremely stable spectrograph, a correct understanding of stellar activity (which can mimic the effect of a planet), a careful treatment of our Earth's atmosphere (which inevitable imprints spectra taken from the ground), and the need to dispose of a powerful algorithm to extract as much Doppler information as possible from the recorded spectra. Search for planets orbiting very low-mass stars (M dwarfs) can more easily reach the goal of detecting low-mass planets in the habitable zone of their parent star, compared to solar-type stars. Indeed, everything else being equal, a lower mass of the host star implies a larger reflex motion, and thus a larger RV amplitude. Moreover, the lower luminosity of M dwarfs compared to Sun-like stars, implies shorter orbital periods from planets in the habitable zone ($\sim$ 50 days against $\sim$ 360 days, for M dwarfs compared to solar-type stars, respectively), resulting again in a larger RV amplitude. A RV precision of $\sim 1\ m\,s^{-1}$ allows a planet detection in the habitable zone of an M dwarf, whereas $\sim 0.1\ m\,s^{-1}$ is required in the case of a solar-type stars.

This thesis aims to optimise the RV extraction from HARPS high-resolution spectra (and to open similar analysis on other instruments like SOPHIE, HARPS-N and the upcoming infrared spectrograph SPIRou – to be commissioned to the 3.6-m CFH-Telescope). The effects of stellar activity will also be analysed, and contextualised in the RV technique. Stellar activity tracers are used to reject false detections or to study the relationships between the stellar magnetic activity and rotation. In this thesis (Chap.3) I calibrate for the first time the ratio between the Ca II H&K chromospheric lines and the bolometric luminosity for M dwarfs. I determine a relationship between the R'_{HK}-index and the rotation period of M dwarfs. In chapter 4 I describe my algorithm to extract RVs through a χ^2-minimisation between a stellar template and the observed spectra. I demonstrate the improved accuracy of this method. Telluric spectral lines also affect the measurements of RV and are taken into account in the analysis procedures. I tested these methods on systems with planetary candidates, and for some systems, I took in charge the Keplerian analysis.

My thesis in 100 words

List of Figures

1.1 Diagram of the stars in the (20 light-years) Solar neighbourhood. Credits: http://holtz.org/Library/Natural%20Science/Astronomy/Cosmology/Cosmic%20Atlas%20by%20Richard%20Powell/ . . . 3

1.2 Artist's conception of the Milky Way with the Sun's position. During the last decade it was clearly established that the Milky Way is a barred spiral galaxy (Burton, 1988; Dame et al., 2001; Benjamin et al., 2005). Credits: http://en.wikipedia.org . . . 4

1.3 Diagram of the galaxies in the Local Group relative to the Milky Way. Andrew Z. Colvin, Credits: http://en.wikipedia.org . . . 5

1.4 The position of the Local Group within the Virgo Supercluster. Andrew Z. Colvin, Credits: http://en.wikipedia.org . . . 6

1.5 Diagram of transits and occultations showing the variation in brightness of the system (from Winn, 2010). In the light curve and during the transit, the flux diminishes proportionally to the planet to star surface ratio. Near the occultation, it is possible to measure the stellar light reflected on the planet (dayside phases). . . . 9

1.6 Sketch of radial velocity and position variations due to an unseen planetary companion. The cross represents the centre of mass of the system to which both bodies orbit, while stars symbols represents the background reference-stars. The target star presents a wobble to the observer: in radial velocities this is translated into a regular decrease and increase, while the star position describes a loop pattern projected in the sky plane. The amplitude of the RV signal and how close is the loop pattern depends (in part) on the angle between the orbital and sky planes). . . . 10

1.7 The left panel shows a scheme of the microlensing technique, where under the presence of a foreground planet system acting as a gravitational lens, the transient light curve of the background star shows a perturbation. The right panel illustrates the direct imaging technique consisting on a correct treatment of a stellar image to unveil the presence of young planets in wide orbits. . . . 11

1.8 The planet mass as a function its separation to the parent star. Each detection technique fills different parts of the diagram, showing that each of them favoured the detection of planets of different mass regimes and configuration. As a reference, Earth- to super-Earth mass planets fill the regions between 0.003 and 0.03 Jupiter masses. . . . 13

1.9 Summary of equations allowing the detection of exoplanets from different techniques. Credit: Somewhere in the net. . . . 13

1.10 Representation in 3-dimensions of a Keplerian orbit. Each body orbits the centre of mass (CM, red cross) following the black ellipse (star), and the grey one (planet); for clarity, only the stellar periastron is represented (p). The z-axis is from the centre of mass toward the observer (the observer line of sight). 15
1.11 The effect of the eccentricity and the longitude of periastron on the shape of the radial velocity signal. The semi-amplitude K, the period P and the periastron passage t_0 are constants. 17
1.12 Sketch showing the result from cross correlating (CCF, right panels) a binary mask (box shaped emission lines shifted at different velocities from top to bottom, left panels) with an observed spectra (left panels). 18
1.13 From Queloz (1995). 19
1.14 Blueshift excess due to convection cells. Snapshot from a simulation of solar convective flows. The green volume rendering indicates swirling flows near the optical solar surface, which is color-coded with vertical flow velocity (downflows in red and upflows in blue). The size of the box shown is 4800 km x 4800 km horizontally and 1400 km in depth. The optical surface is hidden in the lower right quadrant, uncovering the swirling structure in the subsurface layers. Credits: `http://www.mps.mpg.de/1764720/Solar-MHD` 21

2.1 The Hertzsprung-Russell diagram showing some well known stars of different spectral types. M dwarfs are located at the bottom-right corner. Credit: http://www.eso.org/public/images/ 32
2.2 Spectra for a G8.5V star (HD 10700, top) and a M2.5V (Gl 436, bottom) star. The M dwarf spectrum shows plenty of absorption lines due to the presence of atmospheric molecules, which is translated into a lack of continuum. In the other hand, the spectrum of the G dwarf shows deep and sharp absorption lines, these are atomic lines allowing a well defined continuum. 33
2.3 The evolution for different low mass objects in the HR diagram. From a 0.06 Brown dwarf to a 0.25 M dwarf. From Laughlin et al. (1997) 34
2.4 Radial velocity variations due to stellar oscillations. Different spectral types are showed from top to bottom (K1V, G8V, G5IV-V and G2IV). Note how changes the frequency of the oscillations for the different spectral types. From Mayor et al. (2003). 35
2.5 Resulting from MHD simulations, these histograms shows the granule area (left panel) and the vertical velocity averaged over the area as a function of spectral type. From Beeck et al. (2013). 35
2.6 Expected semi-amplitudes (K) as a function of stellar masses ($M_\odot$) and for different periods ranging from 10 to 350 days. For this exercise, I consider 100% edge-on and circular orbits for all curves. Solid curves represent a $1M_\oplus$ planetary mass, while dashed curves depict M_{pl}=$5M_\oplus$. Red horizontal lines are instrumental detection limits (without accounting for the number of data, their Doppler uncertainty or stellar jitter) for *HARPS* ($\sim 1\ m\,s^{-1}$) and *ESPRESSO* ($\sim 0.1\ m\,s^{-1}$). The curves are labeled with different orbital periods, in day units. 36
2.7 The habitable zone as a function of stellar mass. From `http://phl.upr.edu/library/media/thehabitablezone` 38

3.1 Schema of the Ω- and α-process transforming a poloidal field into a toroidal one, and vice versa. Credits: `http://www.konkoly.hu/solstart/stellar_activity.html` 44

3.2 Sketch showing the impact of stellar spots on line shapes, which affects the radial velocity extraction. 46

4.1 Examples of a G (top) and M dwarf (bottom) spectra. While a well defined continuum is present in the G dwarf spectrum, the one corresponding to the M dwarf is densely populated by molecular features. A binary mask used by the HARPS pipeline to perform the CCF in M dwarfs is represented in grey. 71

4.2 Sketch showing the χ^2-minimisation process (χ^2, right panels) using a stellar template (middle spectrum in left panels, which is shifted at different velocities from top to bottom). An observed spectrum (the top one) and the telluric template (the bottom one) are represented in left panels. The telluric template is used to discard telluric zones. 73

4.3 Three spectra of Gl 436 acquired in different epochs and shifted to the rest frame. From top to bottom $BERV = -26.7, 0.2, 25.2$ $[km\,s^{-1}]$. Red vertical line indicates a stellar feature and blue vertical lines indicate the shifted position of a telluric feature. 75

4.4 *Top:* The stellar-template obtained from the first iteration is represented by the red curve and the black step-curve depicts an observed spectrum. The telluric spectrum is embedded in the residuals coming from the ratio between the black and red curves. *Middle:* The telluric-template derived in the first iteration (black curve). The blue curve is the estimated continuum while the two green curves are $\pm 3\sigma$, where σ is computed from the telluric spectra set. Grey points represent an estimation of zones affected by telluric, which are used to built a binary telluric-template. *Bottom:* Black and grey points are the standard deviation of re-sampled spectrum in the first step ($N^{i,j}_{resamp}$) and the third step ($N^{i,j}_{resamp^*,clean}$) along the i-axis. This example comes from Gl 436, where 127 spectra were used. 76

4.5 Histogram of the residuals – and its Gaussian fits – for the order 66 of two spectra of Gl 436 acquired with air-masses of 1.78 (black curve) and 2.24 (grey curve). The stellar-template was scaled to each observed spectrum using Eq. (4.4) (left panel) and Eq. (4.6) (right panel). Printed arrows depicts the difference between the peaks of the black and grey distributions; such difference is 39.1 $[e^-]$ in the left panel, while when we improve the scale factor (right panel) this difference is 18.7 $[e^-]$. In the right panel black and grey distributions have σ=77.9 and 43.9. 78

4.6 Example (Gl 436) of the χ^2-minimisation from the first step in 4.1.3, where the snapshot corresponds to a RV_s near the χ^2-minimum. The upper left panel shows the χ^2-profile; the upper right panel shows the distribution of the residuals (black) and a Gaussian fit to it (red), just below is the difference between the residuals and the Gaussian fit; middle panel shows the residuals normalised by the uncertainties and bottom panel shows the squared normalised residuals. 82

4.7 *Top left panel* shows the dispersion of the RVs residuals (σ_{O-C}) – when subtracting the signal from Gl 436b – as a function of different $R_{\partial X/\partial\lambda}$ limits (see Eq. 4.10); σ_{O-C} remains constant for $[R_{\partial X/\partial\lambda}]_{lim} \geq 7.5$. Normalised periodograms for the RVs residuals are shown in *top right and bottom panels* for different $[R_{\partial X/\partial\lambda}]_{lim}$. Peaks at 90, 120 and 180 days in *top right panel* come from telluric effects; these peaks decrease drastically in *bottom left panel* and completely disappear in *bottom right panel*, demonstrating that the procedure is efficient in removing telluric. In the latter panel the dominant peak comes from stellar activity (see Sect. 4.1.5 below). 83

4.8 *Top panels:* Normalised periodogram for (Gl 436) RVs residuals with and without 5σ-clipping. Two peaks are associated to Gl 436 surface inhomogeneities at 4.7 and 48 days (see Sect. 4.1.5). We note a significant decrease in the 4.7 d peak when performing a 5σ-clipping. *Bottom panels:* The *left panel* shows, for the cases of Gl 436 and GJ 1214, the dispersion of RVs residuals as a function of how many pixels are added to either side of those satisfying $(O-C)^{i}_{norm} > 5$; the *right panel* is the periodogram of Gl 436 RVs residuals when 5 pixels are added to either side of 5σ-clipped zones, in that case the power of both peaks at 4.7 and 48 days are the lowest. 84

4.9 Example (Gl 436) of the χ^2-minimisation from the second step in 4.1.3, where the snapshot corresponds to a RV_s near the χ^2-minimum. Description panels are the same as in figure 4.6. 85

4.10 These panels show the full χ^2-profile and its Voigtian- (blue) and Gaussian fit (red) – second step; the black cross at the bottom represents the inferred RV (centroid of the Gaussian fit). Black points in left panel represent RVs which step is $ps/2$ while red points have a RV-step of $ps/10$ (the Gaussian is fitted only to these points; right panel shows a zoom to the bottom part of the χ^2-profile). 85

4.11 This example shows the comparison between the bisector-span derived by the CCF (red) and the experimental RV_{χ^2-bis} (black) from NAIRA. Left panel corresponds to data from Gl 674 ($P_{rot} \approx 35\ d$), a star with a planetary companion – which signal was removed – and an active region; the *RMS* of the linear fits are 1.27 (CCF) and 1.18 (NAIRA). In the right panel I used data from the very active star Gl 388 (AD Leo, $P_{rot} \approx 2.24\ d$), in this case the *RMS* of the linear fits are 2.54 (CCF) and 1.94 (NAIRA). 87

4.12 Flowchart of the algorithm. The top panel is firstly performed, and then, the bottom one. The *Init* label represents the starting point and dashed rectangles highlight final results. . 89

4.13 *Top panels:* Periodograms of the residuals when subtracting the Gl 436b signal from the RVs derived with NAIRA *(top left)* and with the CCF *(top right)*. Both periodograms show power excess – $p = 0.174$ (*left panel*), 0.169 (*right panel*) – at about 4.7 d. Horizontal lines represent 3σ ($0.3\%FAP$, *solid line*), 2σ ($4.6\%FAP$, *dashed line*), 1σ ($31.7\%FAP$, *dotted line*) confidence limits. *Bottom panel* shows the residuals phased with a period of 4.7 d, where black points depict RVs from NAIRA ($\sigma_e = 1.43\,m\,s^{-1}$) and grey points represent RVs from the CCF ($\sigma_e = 1.70\,m\,s^{-1}$). 92

4.14 Periodograms for the RVs after subtract the Gl 436b signal (*left panel*) and the S-index (*right panel*). The first, second and third rows correspond to epochs 2007, 2008 and 2009, respectively; vertical dashed lines depict the 4.7 d period. We note the variability of the 4.7 d peak in the periodograms of the RVs residuals and the S-index from 2008 show power excess at 4.7 d. In the RVs periodogram from 2007 it is visible the peak (48 d) associated to the stellar rotation. 92

4.15 *Top panels:* Periodograms of the residuals for RVs extracted with NAIRA *(top left)* and with the CCF *(top right)*. No relevant peak appears, horizontal lines are as in Fig 4.13. *Bottom panel* shows the residuals phased with GJ 1214b period, where black points depict RVs from NAIRA ($\sigma_e = 4.18\,m\,s^{-1}$) and grey points represent RVs from the CCF ($\sigma_e = 5.43\,m\,s^{-1}$). 94

List of Tables

1.1 Expected RVs semi-amplitude K and required number of observations (N) for a $S/N_{v_r} = 20$ detection with different RV uncertainties σ_{v_r}. N is not given when a very low number of observations allows the detection. Properties for the last three entries from `http://exoplanet.eu` and `http://phl.upr.edu/projects/habitable-exoplanets-catalog` 17

4.1 Percentage of rejected pixels in Gl 436 and GJ 1214 RVs extraction. 88
4.2 One-Keplerian fit for Gl 436 using RVs from CCF and NAIRA. 91
4.3 One-Keplerian fit for GJ 1214 using 74 or 21 RVs from CCF, HARPS-TERRA and NAIRA. 94
4.4 Comparison between RVs derived from CCF and NAIRA for GJ 3293, GJ 3341 and GJ 3543. 108

Contents

1 Introduction **1**
- 1.1 Where are we? . . . 1
- 1.2 A new era in Astronomy: extra-solar planets . . . 3
  - 1.2.1 First ideas...then the detection . . . 3
  - 1.2.2 Current techniques . . . 8
- 1.3 The radial velocity method . . . 14
  - 1.3.1 Orbital parameters . . . 14
  - 1.3.2 Doppler spectroscopy and the cross-correlation function . . . 17
  - 1.3.3 Limitations and difficulties of the radial velocities method . . . 20
  - 1.3.4 Radial velocities surveys . . . 22

2 Search for planets around M dwarfs **31**
- 2.1 Basic properties of M dwarfs . . . 31
  - 2.1.1 M dwarfs activity . . . 32
  - 2.1.2 Extra-solar planets around M dwarfs . . . 35
- 2.2 This thesis . . . 39

3 The R'_{HK}-index in M dwarfs **43**
- 3.1 Dynamo processes . . . 43
- 3.2 Stellar activity diagnostics . . . 44
- 3.3 Stellar activity and planets detection . . . 45
- 3.4 Calibrating the R'_{HK}-index (paper) . . . 45

4 Optimise radial velocity extraction **70**
- 4.1 χ^2-minimisation method . . . 72
  - 4.1.1 Read data . . . 72
  - 4.1.2 Building the stellar template . . . 74
  - 4.1.3 Calculating radial velocities: χ^2-minimisation . . . 79
  - 4.1.4 Fraction of rejected wavelength region . . . 87
  - 4.1.5 Performances . . . 90
- 4.2 Applications . . . 95
  - 4.2.1 Telluric correction . . . 95
  - 4.2.2 A complete analysis of the radial velocities of GJ 3293, GJ 3341 and GJ 3543 . . . 107

5 Conclusions and future prospects **131**

A Publications related to this thesis **134**

Chapter 1

Introduction

1.1 Where are we?

Nowadays we talk with relative naturalness that the Universe is populated with an unimaginable quantity of galaxies, each having billions of stars, which in turn are orbited by planets - extra-solar planets or exoplanets. But to reach this point, humanity has come a long path and I can not start without very briefly recall it from an historical point of view.

The Sun, the Moon and stars have been influencing humanity forever. Since the first civilisations, time and calendars naturally emerges using the movements of the Moon and the Sun. Babylonian were familiar about the existence of five stars with a peculiar erratic movement that differs from other stars; these five "wandering stars" (planets) are Venus, Mercury, Mars, Jupiter and Saturn. Around 1900 BC they already knew the synodic period of Venus and they also estimated the synodic period of Mercury with an error of only five days. They were familiar with the fact that the relative positions of planets and the Moon follows the ecliptic.

Where is our place? In the ancient Greece we found some answers to this question. The Milesian school (600 BC) gave different explanations of how the world is organised (Thales, Anaximander, Anaximenes), proposing that the Earth is flat like a disc immersed in a essential substance and there is a semi-spherical envelope enclosing the stars. Around 500 BC, Pythagoras of Samos or Parmenides of Elea are the first to propose a spherical Earth in the centre of a series of spherical shells, while Anaxagoras gave an order to astronomical objects: the Moon, the Sun, and then the five known planets. Imaginative ideas were proposed by Philolaus, with a fire in the centre of Cosmos where the Earth and planets moves around it. The Earth rotates around this hypothetical fire in 24 hours, an anti-Earth hides the central fire, the Moon and the Sun also rotates this central fire. At that time, the basis to explain the erratic movement of planets was the use of uniform and circular movements (Plato's problem). To elucidate the apparent planetary paths, Eudoxus of Cnidus (400 BC) fixed each planet in one rotating spherical shell centred on Earth, whose poles are in turn fixed to other rotating shells and so on up to four spherical shells, whereas three spherical shells explains the movement of the Moon and the Sun. Therefore, in this relatively complex homocentric schema of Eudoxus, the Cosmos is represented by twenty-seven spheres, twenty for the five known planets, six for the Moon and the Sun and one for the fixed stars. This conception was adopted by Aristotle (350 BC), but ending with fifty-four shells to describe the Cosmos. In the other hand, one of Aristotle greatest achievement was to estimate the size of the Earth, equivalent of 400,000 stadiums - around 60% bigger than the true value.

A fact against the homocentric shell system is that it could not explains the brightness variation of planets; this issue was addressed by Heraclides of Pontus, although with the Earth still placed at the centre, around 350 BC he proposed that Venus and Mercury orbit the Sun. Another model addressing this issue was proposed by Aristarchus of Samos (300 BC), who suggested that the Sun represents the centre

of the planetary system, with the Earth orbiting it and spinning (translation and rotation movements). Unfortunately, his ideas were avoided for eighteen centuries and the model of Claudius Ptolemy (100 AC) prevailed. Ptolemy used a geocentric mathematical model which makes use of epicycles to describe the positions of the Moon, the Sun and planets, as well as their brightness variation.

An heliocentric model came back with Nicolaus Copernicus (1500 AC); he took observations of Ptolemy and Hipparcos (mostly) to develop a model with a centre close to the Sun, the Earth with more than one motion (translation and rotation) and the Moon orbiting the Earth. A description of the Cosmos based on an uniform and circular movements (following Plato) was still present in Copernicus model, which is constituted by the combination of 48 spheres. The heliocentric model was fully established by Galileo Galilei and Johannes Kepler around 1600 AC. The telescope was not invented by Galileo, but he was the first to point it to the sky. On January 7, 1910, he surprisingly found four satellites orbiting Jupiter (Io, Europa, Ganymede, and Callisto); then, in September 1910, he observed the phases of Venus. In the other hand, Kepler revolutionised our understanding of the Cosmos based on observations of Mars acquired by Tycho Brahe. His findings were revolutionaries in the sense that he banished the two millennial use of - divine - circular movements to describe the observations of planets. He introduced the concept of elliptical orbits and the *driving soul*, which is a force of motion placed in the Sun and responsible of movements.

Christiaan Huygens in 1655 and Giovanni Casinni in 1671 discovered Titan and Iapetus orbiting Saturn, respectively. Cassini also applied Kepler laws to find a most accurate value for the Earth-Sun distance. One of the biggest revolution arrives in 1687, when Isaac Newton published his majestic *Principia*; there he joined the celestial mechanics of Kepler with the terrestrial mechanics of Galileo in one unique law. The solar system was still growing with the discovery of Uranus by William Herschel (observations) and Anders Lexell (orbital parameters) in 1781. The new model culminated by the prediction of Neptune by Urbain Jean Leverrier in November, 1845, (or John Couch Adams in September, 1845) thanks to irregularities observed in the movement of Uranus; Neptune was observed (close to the position predicted by Leverrier) by Johann Gottfried Galle in September 1846.

Now regarding greater distances, Herschel was the first to make the analysis of the spatial distribution of stars. Thanks to his observations he determined the star density as a function of sky direction, and he proposed that the stars are distributed along a disc where the diameter is five times the thickness, with the presence of an indent. This conception was first suggested by Thomas Wright in 1750 and by Emanuel Kant in 1755. Kant go beyond proposing that the Universe is populated by millions of galaxy like the Milky Way. The nature of *spiral nebulae* (galaxies) and our position in the Milky Way were addressed by Herver Curtis and Harlow Shapley around 1920. Shapley proposed a diameter of 300,000 light-years for our galaxy and located the Sun at 60,000 light-years from the galactic centre; but he thought that *spiral nebulae* were part of our galaxy. While Curtis said that *spiral nebulae* are beyond our galaxy. 170 years after Kant's conception of the Universe, it was finally confirmed by the observations of Edwin Hubble that *spiral nebulae* are other galaxies located outside the Milky Way.

Today, we know that we are surrounded by stars where the majority of them harbour planets (Fig. 1.1; Mayor et al., 2011; Bonfils et al., 2013); we know that we are located in a banal place near the edge of the Milky Way, which is a typical galaxy among the vast quantity of others galaxies (Fig. 1.2); we know that the Milky Way is part of a gravitationally bound system (the Local Group) containing tens of galaxies (Fig. 1.3) and that the Local Group is embedded in a larger structure with a diameter of about 33 Mpc called the Virgo Supercluster, which contains a hundred of galaxy groups (Fig. 1.4)...and so on. Now, having in mind the immense amount of stars in a galaxy and the huge quantity of galaxy in the vastness

of the Universe, try to imagine the amount of planets there are.

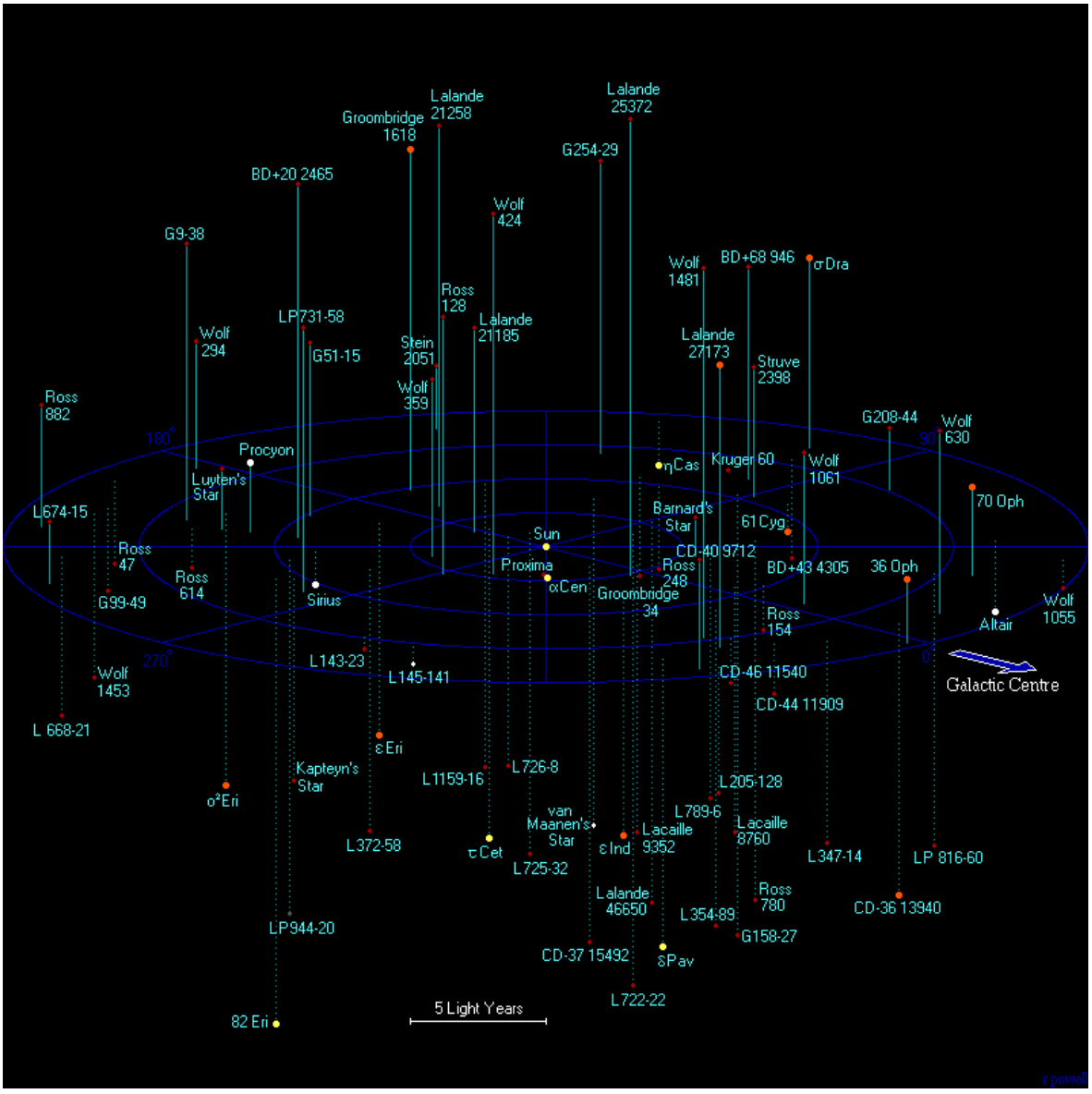

Figure 1.1: Diagram of the stars in the (20 light-years) Solar neighbourhood.
Credits: http://holtz.org/Library/Natural%20Science/Astronomy/Cosmology/Cosmic%20Atlas%20by%20Richard%20Powell/

1.2 A new era in Astronomy: extra-solar planets

1.2.1 First ideas...then the detection

Having in mind our place in the Universe, next natural questions are: how many worlds like our are there? Are we alone? We already found some speculations about these questions in the ancient Greece. Although the philosopher Epicurus (300 BC) said that everything should be demonstrated through observations or

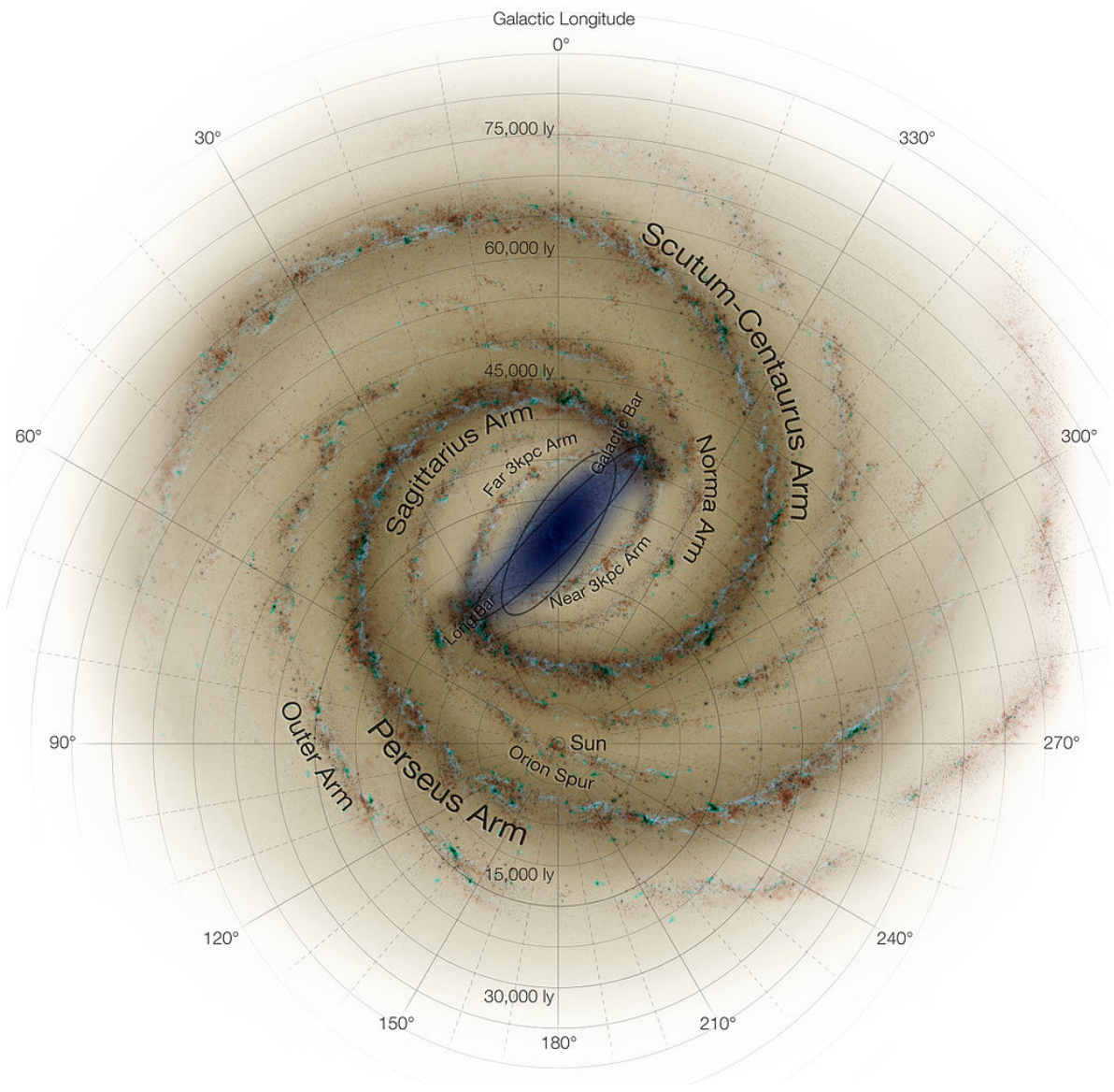

Figure 1.2: Artist's conception of the Milky Way with the Sun's position. During the last decade it was clearly established that the Milky Way is a barred spiral galaxy (Burton, 1988; Dame et al., 2001; Benjamin et al., 2005). Credits: `http://en.wikipedia.org`

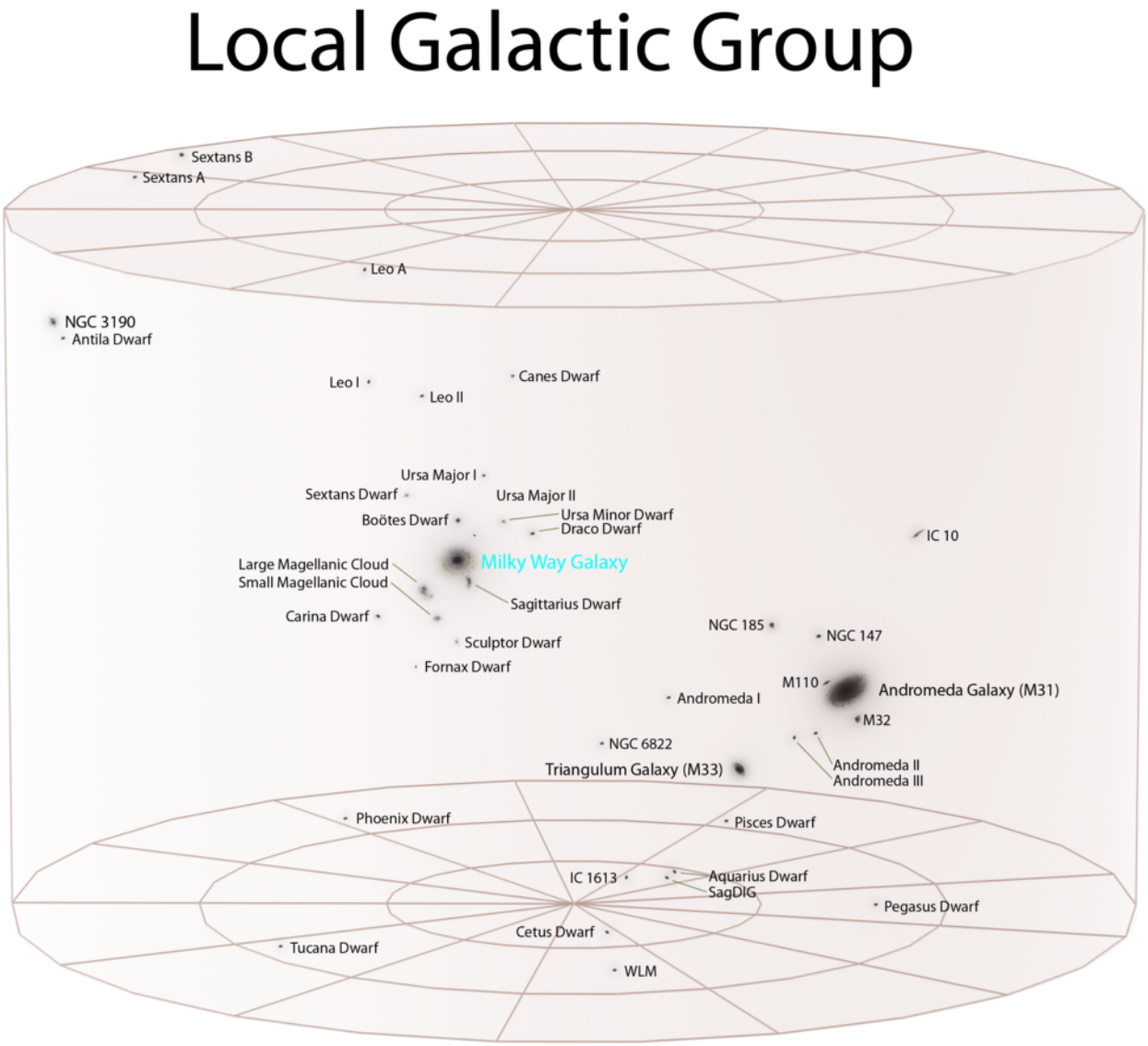

Figure 1.3: Diagram of the galaxies in the Local Group relative to the Milky Way. Andrew Z. Colvin, Credits: http://en.wikipedia.org

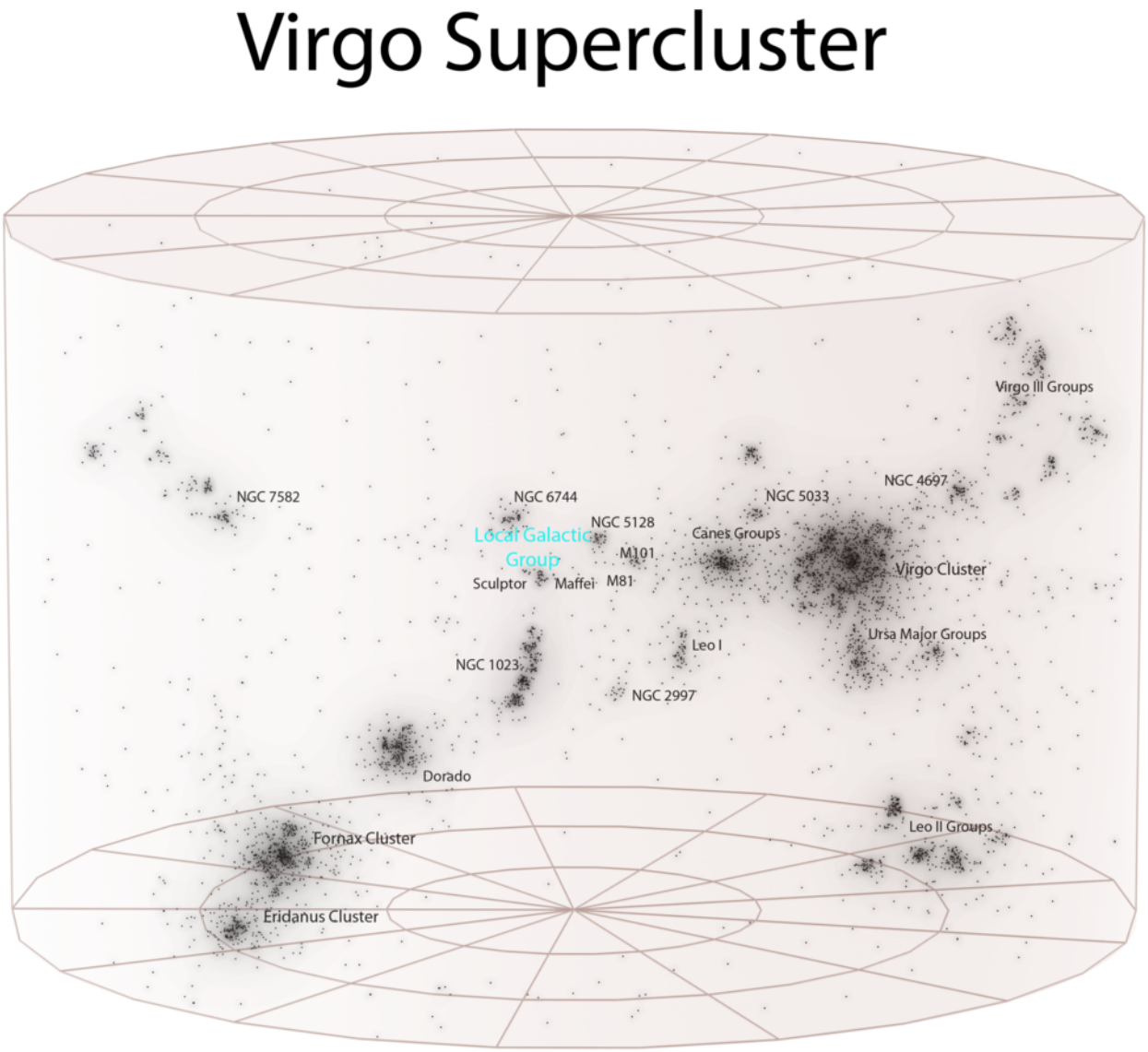

Figure 1.4: The position of the Local Group within the Virgo Supercluster. Andrew Z. Colvin, Credits: http://en.wikipedia.org

logical deduction, he stated that there are infinite worlds like and unlike ours, and those worlds harbour living creatures and other things we see in our world. Fifteen centuries later, around 1200, history shows that the Catholic bishop Albertus Magnus wondered about the existence of other worlds, asserting that this is one of the most noble and exalted question in the study of Nature. Then, the french philosopher Jean Buridan (1300) speculated about the possibility that there are other inhabited worlds; he also rejected Ptolemy epicycles in favour of eccentric orbits. The existence of other stars and worlds were also advocated by Nicola de Cusa around 1400. The controversial ideas - at that time - of Giordano Bruno (1600) also point to the idea that we are not alone; he pondered that if we suppose that the Sun is like other stars, why there would be no more planets around other stars? In *Cosmotheoros* (1695), Christiaan Huygens speculate on how would be the sky to inhabitants of other worlds. Later, in 1761, in addition to predicting that stars forms galaxies, and these last form galaxy clusters, Johann Heinrich Lambert wrote that each star is like the Sun, surrounded by their own planets.

In a less speculative way and with the aid of better telescopes, in 1844 Friedrich Bessel measured anomalies in the position of Sirius. He was able to conclude that this bright star is pulled by an unseen companion (Bessel, 1844), which was observed almost twenty years later and found to be a white dwarf. This event was the introduction and success of precise astrometry. Claims of unseen companions with planetary nature were announced around 70 Ophiuchi, 61 Cygni and Barnard's star (GJ 699), but they all were disproved (Jacob, 1855; Strand, 1944; van de Kamp, 1963; Gatewood and Eichhorn, 1973; Moulton, 1899; Heintz, 1978).

Struve (1952) proposed two different techniques to indirectly detect short-period Jupiter-like companions orbiting other stars than the Sun; these techniques were high-precision radial-velocity and transits. The radial-velocities technique looks for Doppler wobbles induced by orbiting planets in the spectra of their hosts stars. Transit observations search for regular eclipses caused by planets transiting the stellar disk. In the case of radial velocities (RVs), an important key element to achieve high precision is the accuracy of wavelength calibration of spectra. Initially, telluric spectral lines were used as the reference but the required precision was not achieved at this time to detect Jupiter-mass companions (Griffin, 1973). The next key step, achieving an increase of an order-of magnitude in precision, came with Campbell and Walker (1979). They proposed to use a gas-cell (hydrogen fluoride) to generate reference absorption lines. A first success appeared ten years later, with the discovery of a periodic RV variations produced by an unseen companion (for details of the technique, see 1.2.2). Around HD 114762, Latham et al. (1989) estimated that the HD 114762b has a mass in the lower edge of brown dwarfs. It is to note that with a minimum mass of $m\,sin(i)$=10.98M$_{Jup}$, HD 114762b could be classified as a very massive planet or a brown dwarf following the inclination i of the system. Then, in 1992 it was discovered the two very first planets outside the Solar-system; Wolszczan and Frail (1992) announced the detection around a pulsar of objects with masses of 2.8M$\oplus$ and 3.4M$\oplus$ by measuring pulsar-timing variations (these planets are so-called dead-planets, because they orbit dead stars). Despite this astonishing finding, the community was waiting for the detection of planets around main-sequence stars. The wait was not too long, only three years later came the amazing announcement by Mayor and Queloz (1995) of Jupiter-mass planet orbiting the Sun-like star (51Peg). But the surprise was double, because the RV variations have a periodicity of only 4.2 days, challenging the accepted planetary formation models, which were not able at this time to explain the formation of planets so close to their parent star. Since then, many other planets were detected by different groups (e.g. Marcy and Butler, 1996). In the other hand, the transit technique waited a little bit more. A regular light dimming was detected in the Sun-like star HD 209458 (Henry

et al., 2000; Charbonneau et al., 2000), corresponding to an unseen planetary companion previously detected by RV (Mazeh et al., 2000). The planet shadow was also previously seen by the HIPPARCOS satellite (Soderhjelm, 1999). HD 209458b has a periodicity of 3.5 days for a light dimming consistent with a Jupiter-like planet.

1.2.2 Current techniques

The detection of the first exoplanets (Wolszczan and Frail, 1992; Mayor and Queloz, 1995; Marcy and Butler, 1996) answered the ancient question about the existence of other worlds, and in addition it shows that planetary systems may be very different in comparison to the Solar-system. This enormous advance triggered huge efforts to search for more exoplanets to answer new questions: What is the occurrence of planets? Around which type of stars? How are their populations in terms of mass and size? How do they form and eventually migrate? What are the characteristics of their atmospheres? What is the nature of their composition (superficial and internal structure)? What are the properties of their host star? Can they support life?

The main techniques or methods used to detect these worlds are extreme development of previous techniques applied to the study of stellar binary systems: spectroscopy (Doppler effect) or astrometry to detect reflex motions, photometry to detect transits or occultations, and high-contrast imaging to directly detect companions. Only visual high-contrast imaging is a direct method, the other techniques are indirect in the sense that we do not directly detect photons from the companion (only detected through the human genius). In addition, there are the timing and microlensing techniques. Each technique has its own pros and cons, here I will discuss the principles of each of them. Only the radial velocity technique will be described with more details, as it is in the focus of this thesis.

Definition of methods

Transits: In some cases the orbital plane of an exoplanet is aligned with the line of sight connecting the host-star and the observer, in this configuration the planet will pass in front of the star blocking part of the stellar light (a transit). In addition, the planet will also pass behind the stellar disc (an occultation, Fig. 1.5). During a transit, the light dimming is proportional to the ratio of the planet and star surfaces, therefore assuming a known stellar radii, it is possible to infer the planet radii. Such an event will be repeated periodically, unveiling the orbital period; from this method it is also possible to derive the orbital semi-major axis and the angle between the sky and orbital planes, however the planetary mass remains unknown (which can be inferred from the combination of this method with RVs). The probability that a given planet shows transits is proportional to the stellar radii and inversely proportional to the semi-major axis and, therefore, this technique is largely biased toward short periods. Specially relevant is that, from this technique, it is possible to characterise the atmosphere of the planet through absorption spectroscopy, if there is any. Indeed, under the presence of an atmosphere the light dimming will be wavelength dependent according to the atmospheric composition. For a detailed description of this method see, e.g., Winn (2010).

Radial velocities: In a system of bodies, each orbits a common centre of mass, where position depends on the body's masses. The semi-major axis of the orbit of the more massive object (the host star) is smaller than the one of the less massive object (the planet). We can thus infer the presence of a planet by measuring the reflex motion that is induced on the parent star (Fig 1.6). This reflex motion is measured using the Doppler effect: the spectral lines of the star appear shifted by an amount proportional

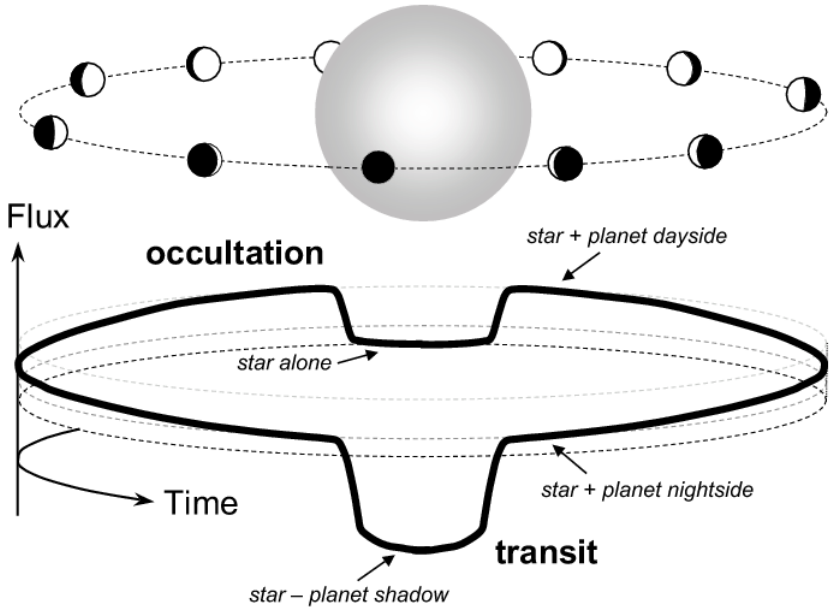

Figure 1.5: Diagram of transits and occultations showing the variation in brightness of the system (from Winn, 2010). In the light curve and during the transit, the flux diminishes proportionally to the planet to star surface ratio. Near the occultation, it is possible to measure the stellar light reflected on the planet (dayside phases).

to the radial velocity. The periodic variation of the RV reveal the presence of the planetary companion and, from such a variation it is possible to infer the orbital period, the minimum mass of the planet (assuming that the stellar mass is known), the eccentricity and the semi-major axis. This technique measures the minimum mass ($m\,sin(i)$, i being the angle between the orbital and sky planes) because the angle between the orbital and sky planes remains unknown (only one component of the stellar motion is measured), the planet radii is also unknown. At the end of the XX^{th}-century, the radial velocity technique was biased to Jupiter-like planets due to the typical RV precision of 10-20 $m\,s^{-1}$. But now with the development of stable and precise spectrographs, Earth-like planets orbiting low-mass stars are accessible. This technique will be reviewed in detail below.

Astrometry: In the same way as described in the radial velocity technique, this method aims to quantify the wobble of the parent star around the common centre of mass; this time, by measuring with an exquisite precision the position of the target star with respect the background stars (Fig 1.6). One of the biggest advantages of this method is that it measures two components (projected in the sky plane) of the stellar motion, allowing to infer all orbital parameters, including the planetary mass (assuming that the stellar mass is known). This method, as the radial velocity method, is biased to massive planets orbiting low-mass stars in close orbits, but also to the closest systems because the astrometric motion is directly proportional to the distance to the system. Unfortunately, today, no detection have been made with this technique. The astrometry method is detailed in, e.g. Quirrenbach (2011).

Microlensing: A foreground star passing close to the line of sight connecting a background star and the observer produces a microlensing event. The effect is provoked by bending of light due to the gravitational field of the foreground star. If this star has a companion, a perturbation will appear while the background star is being magnified (Fig 1.7). Such perturbation will depends on the planetary mass and the planet-star separation. This technique is sensitive to Earth-mass planets at large separation but

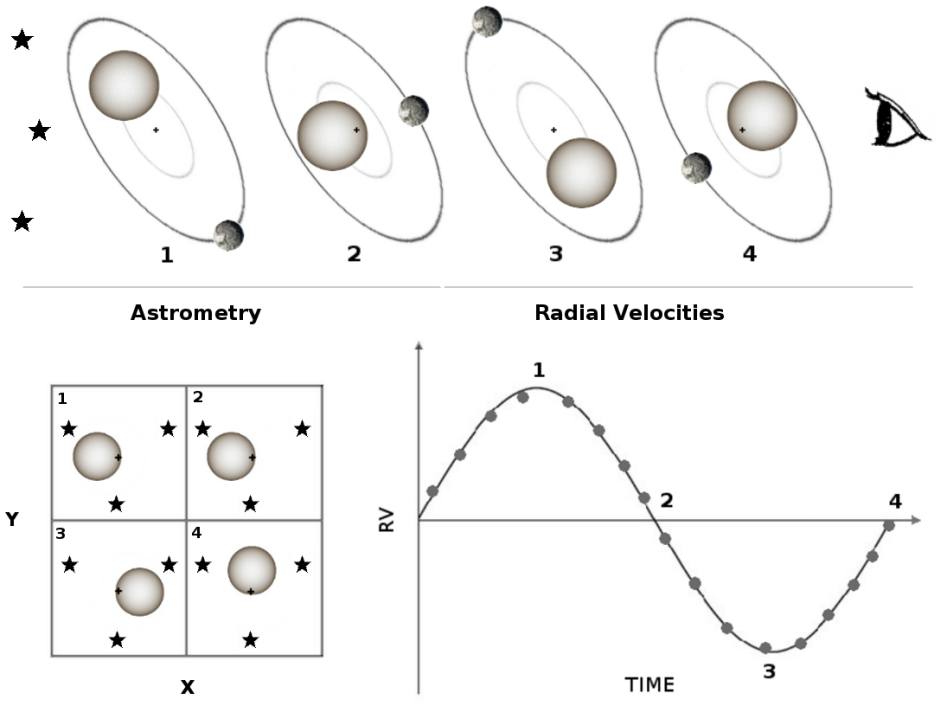

Figure 1.6: Sketch of radial velocity and position variations due to an unseen planetary companion. The cross represents the centre of mass of the system to which both bodies orbit, while stars symbols represents the background reference-stars. The target star presents a wobble to the observer: in radial velocities this is translated into a regular decrease and increase, while the star position describes a loop pattern projected in the sky plane. The amplitude of the RV signal and how close is the loop pattern depends (in part) on the angle between the orbital and sky planes).

the event is transient, which is the main disadvantage of the method. The technique is fully described in Gaudi (2011).

Direct imaging: This technique is to spatially resolves the planet in a high contrast image, where the main difficulty is to get rid of the stellar brightness. The stars radiation is several orders of magnitude greater than the planet radiation (as an example, Jupiter emits a few 10^{-9} of the solar luminosity), under this scenario, this method masks the star light using an adapted coronograph and perform a correct treatment of residuals (Fig 1.7). Some advantages of this method is that it is possible to directly derive physical and chemical properties of the planet (like its effective temperature or atmosphere composition) and also unveil the presence of debris disks; however, it is currently limited to young and nearby systems. For further details see, e.g., Traub and Oppenheimer (2011).

Timing: This technique reveals the presence of planets by measuring perturbations in periodic events, like variations in pulsars timing, in pulsating stars, or the central time of transits. The mass of the companion dynamically affects the periodic event, hence, allowing us to quantify the planetary mass. In the case of pulsars timing, the huge precision in measuring the timing gives access to planets with the lowest mass (or even large asteroids). Further details can be found in Wolszczan and Kuchner (2011); Silvotti et al. (2007); Nesvorný et al. (2013).

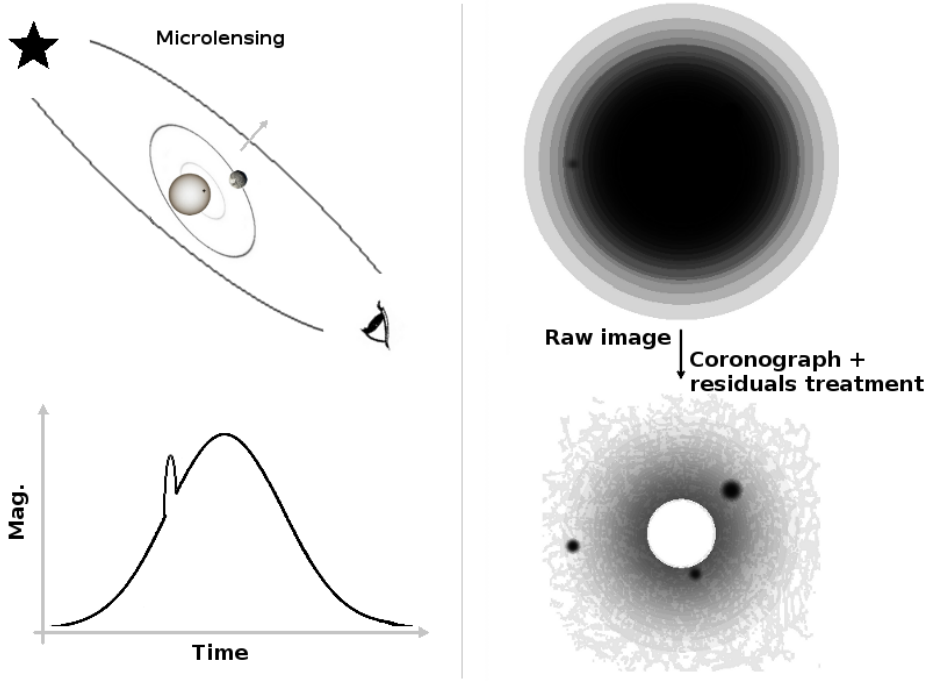

Figure 1.7: The left panel shows a scheme of the microlensing technique, where under the presence of a foreground planet system acting as a gravitational lens, the transient light curve of the background star shows a perturbation. The right panel illustrates the direct imaging technique consisting on a correct treatment of a stellar image to unveil the presence of young planets in wide orbits.

Instruments

I had briefly described the detection techniques, which are complementary in the search for exoplanets. This is shown in figure 1.8, where we visualise the diversity of known planets. At the date, more than 1500 exoplanets are known (transits: 1061; RV: 439; timing: 61; microlensing: 16; imaging: 8)[1] and there are about 3000 transiting candidates from the *Kepler* mission. Great technological challenges were – and are – addressed to reach this quantity.

In the search for transiting exoplanets, the expected $\sim$ 1% light dimming of Jupiter-sized planets transiting Sun-like stars is accessible from the ground (where it is worth the use of reference stars). Since the first discovery made by radial velocities, several ground-based projects took place to constantly scan the sky in the search for the appreciate light dimming – e.g. TrES, Alonso et al. (2004); WASP, Pollacco et al. (2006); or *Mearth* (searching for planets transiting low-mass stars, Nutzman and Charbonneau, 2008). However, a great advantage is the use of space-based observatories because the lack of variations introduced by Earth's atmosphere. Indeed, golden times arrived with space missions like *COROT* (with a photometric precision of 0.01% which allows to detect transiting super-Earths, Barge et al., 2006) or the *Kepler* mission to search for transiting Earth-sized planets (achieving a 0.001% precision, Borucki et al., 2009). With its fixed field-of-view, *Kepler* confirmed planets exceeds 1000 and its candidates are around three times this number. The field is very promising with future spacecrafts dedicated to search for transits (*TESS, PLATO*) or even the non-dedicated mission *JWST*. This is also the case for searches from the ground, with even more dedicated surveys like *NGTS* or *ExTrA*, where the latter will be specially dedicated to search for planets transiting cool-stars in the *nIR* (previous and current surveys

[1] http://exoplanets.org/; February 5, 2015

operates in the optical).

The radial velocity semi-amplitude ranges from $\sim 50\ m\,s^{-1}$ for a hot-Jupiter orbiting a Sun-like star to $\sim 10\ cm\,s^{-1}$ for a Earth-like planets orbiting the same type of stars in a 1 yr period. In section 1.3.3 I review some of the characteristics of dedicated spectrographs that pushed the RV precision to lower values, here I highlight some instruments. *CORAVEL* was a spectrophotometer installed at the Haute-Provence Observatory (OHP), it achieved a RV precision of $\sim 200\ m\,s^{-1}$. Such precision was improved with the stabilised and high-resolution spectrograph *ELODIE* (OHP, Baranne et al., 1996, and its copy *CORALIE* on the Euler telescope at La Silla) with an instrumental velocity error of $\sim 13\ m\,s^{-1}$ (low enough to detect the signal of 51Pegb, Mayor and Queloz, 1995). Based on the experience and success of *ELODIE*, a second generation of super-stable velocimeter see the light with the High Accuracy Radial velocity Planet Searcher (*HARPS*) mounted in a 3.6 telescope (ESO). *HARPS* reaches the $m\,s^{-1}$ precision, or even the sub-$m\,s^{-1}$ when bright stars data are acquired with simultaneous reference lamps. The instrumental stability is $\sim 1\ m\,s^{-1}$ over several years (Mayor et al., 2003), giving access to super-Earth planets orbiting low-mass stars. Even more, the near future is very promising with the next generation instrument *ESPRESSO* (Pepe et al., 2010), that will be installed in a 8m-class telescope (VLT, ESO). *ESPRESSO* is an ultra-stable, high-resolution spectrograph conceived to break the 10 $cm\ s^{-1}$ precision, giving access the to domain of Earth-like planets orbiting Sun-like stars. Cool-stars are also in the target of future instruments designed for the hunt of extrasolar planets, as is the case of *SPIRou*, a nIR high-precision velocimeter and spectropolarimeter to be mounted in the CFHT (Delfosse et al., 2013). The exoplanet hunt is part of the science case for the upcoming generation of extreme large telescopes, as an example, *CODEX@E-ELT* (Pasquini et al., 2008) was designed to be an ultra-stable spectrograph that envisages the 2 $cm\ s^{-1}$ precision.

The combination of adaptive-optics and coronographs allows the direct imaging of exoplanets in the nIR. *NACO* is a camera mounted in a 8m-class telescope (VLT-ESO) used for the first imaged exoplanet $\beta Picb$ (Lagrange et al., 2009); this event encourages even more the design of specialised instruments with extreme adaptive-optics like *SPHERE* (Beuzit et al., 2008) or *GPI* (Macintosh et al., 2008), which will allows the direct detection of Jupiter-like planets. The era of Extreme large telescopes, of course, envisages the integration of this kind of instruments, as is the case of *METIS@E-ELT*. Finally, astro-engineering is not exempt to address the technique of astrometry; *GAIA* (ESA), with its micro-arcsecond precision, will surely gives excellent news for this technique.

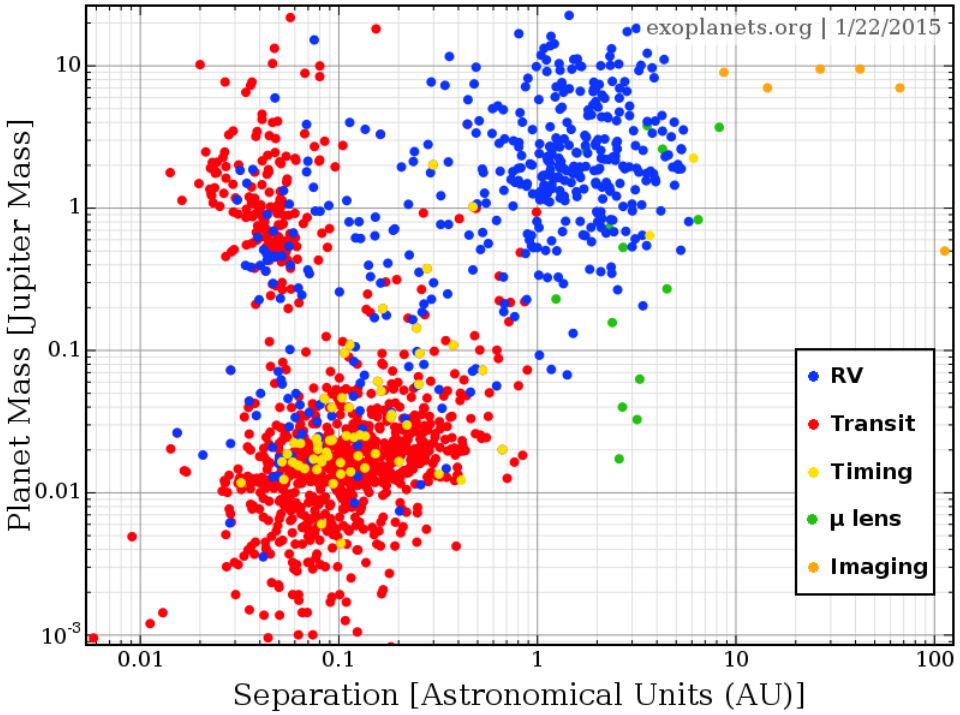

Figure 1.8: The planet mass as a function its separation to the parent star. Each detection technique fills different parts of the diagram, showing that each of them favoured the detection of planets of different mass regimes and configuration. As a reference, Earth- to super-Earth mass planets fill the regions between 0.003 and 0.03 Jupiter masses.

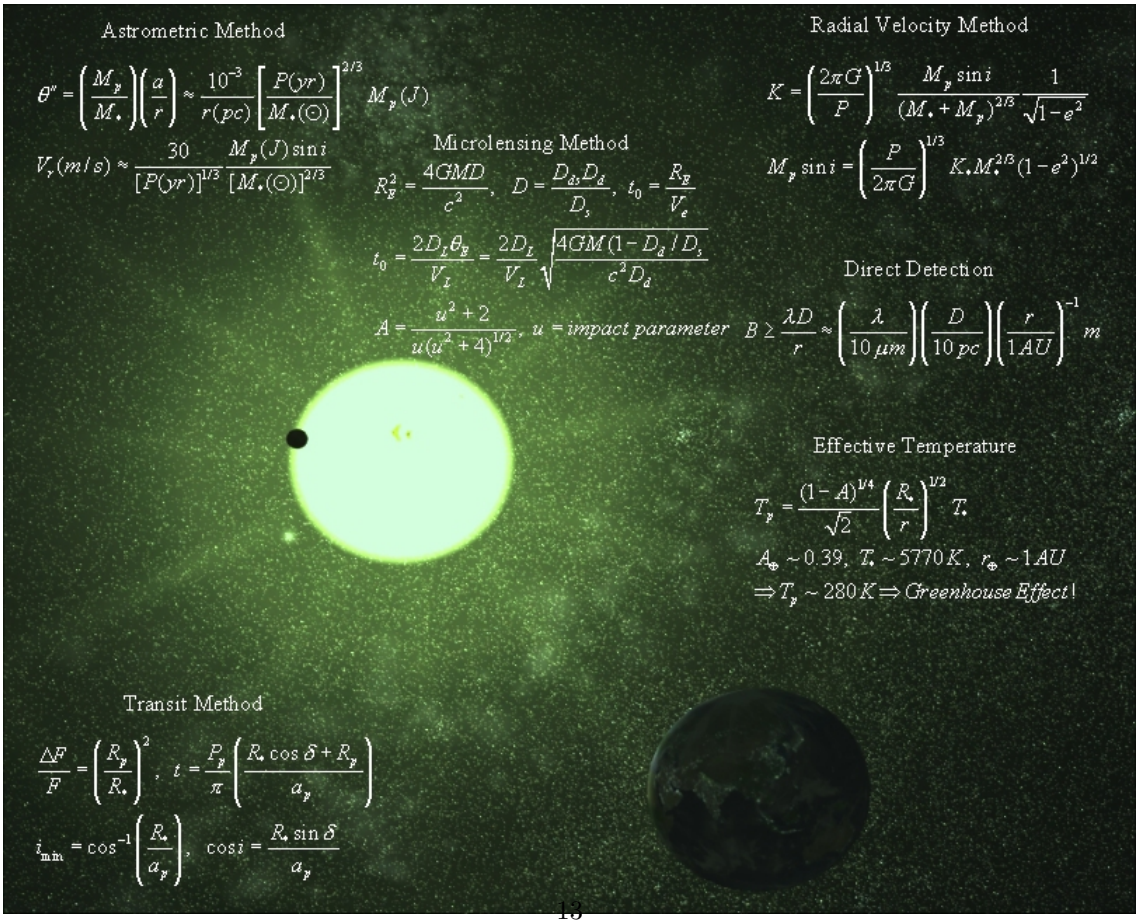

Figure 1.9: Summary of equations allowing the detection of exoplanets from different techniques. Credit: Somewhere in the net.

1.3 The radial velocity method

This thesis focuses on the detection of exoplanets by the radial velocity method. The principles of the method were briefly described above, and the general solution of the two-body problem is addressed in, e.g., Murray and Correia (2011) and concretely for radial velocities in, e.g., Lovis and Fischer (2011). Here I will directly discuss how orbital parameters and the (minimum) planetary mass is derived from the RV measurements.

1.3.1 Orbital parameters

In the two-body problem, each object orbits the common centre of mass and it is natural to locate the origin of the reference frame in this point. Considering a star with mass $M_\star$ and a planet with mass m_p, each body follow its own elliptical orbit whit the focus located in the centre of mass (Fig. 1.10), they shared the same period P and eccentricity e, their periastron (the orbital point of least distance to the centre of mass) differs by an angle of π, and their semi-major axis scale as

$$a_\star = \frac{m_p}{M_\star + m_p} \cdot a \quad ; \quad a_p = \frac{M_\star}{M_\star + m_p} \cdot a \tag{1.1}$$

where a is the semi-major axis of the relative orbit (maximum separation between the star and the planet, $a = a_\star + a_p$). Figure 1.10 shows the configuration of the system, where the $\hat{z}$ axis points toward the observer (the line of sight); we are interested in the star velocity vector projected into the line of sight. Firstly we define:

- the line of nodes as the intersection between the orbital and sky planes, passing through the centre of mass CM
- the ascending node Ψ, which is the point where the star crosses it toward us,
- i as the angle between the orbital and sky planes
- p is the periastron of the stellar orbit (the periastron of the planetary orbit differs from π)
- the argument of the periastron ω is the fixed angle between the line of nodes and periastron ($\Omega\widehat{CM}p$)
- the true anomaly ν is the time dependent angle between the periastron and $\vec{r}$ ($p\widehat{CM}r$), where $\vec{r}$ is the vector connecting the centre of mass and the star position

Once some parameters were defined, the seven parameters that fully define an orbit are: the period P, the semi-major axis a, the eccentricity e, the angle i between the orbital plane and the plane of sky, the longitude of periastron ω, the passage of periastron t_0, and the longitude of the ascending node Ω.

As we are interested in the radial component of motion, from trigonometry, we write the star's z-coordinate

$$z = r(t)\ cos(\nu + \omega)\ sin(i) \tag{1.2}$$

and then, we compute the derivative of eq. 1.2 with respect time, giving

$$v_r = r\frac{d\nu}{dt}\ cos(\nu + \omega)\ sin(i)\ +\ \frac{dr}{dt}\ sin(\nu + \omega)\ sin(i) \tag{1.3}$$

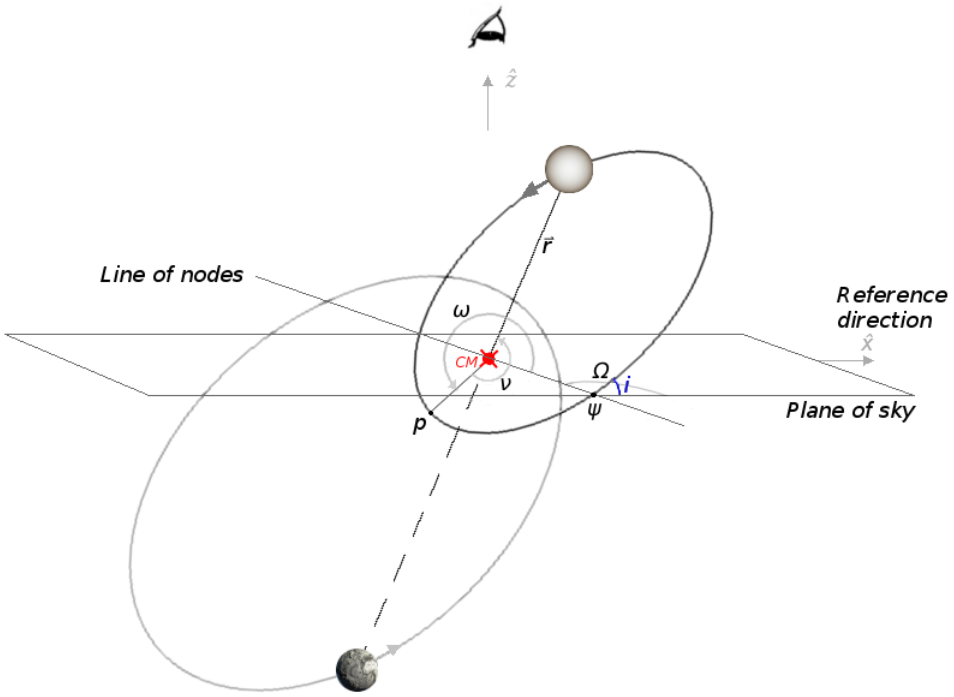

Figure 1.10: Representation in 3-dimensions of a Keplerian orbit. Each body orbits the centre of mass (CM, red cross) following the black ellipse (star), and the grey one (planet); for clarity, only the stellar periastron is represented (p). The z-axis is from the centre of mass toward the observer (the observer line of sight).

In equation 1.3, we obtain dr/dt using the general equation of the ellipse[2] and $d\nu/dt$ from Kepler's 2^{nd} law[3]

$$\begin{aligned} \frac{dr}{dt} &= \frac{r\ e\ sin(\nu)}{1+e\ cos(\nu)}\ \frac{d\nu}{dt} \\ r\ \frac{d\nu}{dt} &= \frac{2\ \pi\ a_\star^2\ \sqrt{1-e^2}}{r\ P} \end{aligned}$$

where the relation $A = \pi\ a^2\ \sqrt{1-e^2}$ was used. Now, to write the right hand side of above equations without the terms r and $d\nu/dt$, the equation of the ellipse is used again, then rearranging

$$\frac{dr}{dt} = \frac{2\ \pi\ a_\star\ e\ sin(\nu)}{P\ \sqrt{1-e^2}} \tag{1.4}$$

$$r\ \frac{d\nu}{dt} = \frac{2\ \pi\ a_\star\ [1+e\ cos(\nu)]}{P\ \sqrt{1-e^2}} \tag{1.5}$$

and substituting eq. (1.4) and (1.5) in eq. (1.3)

$$v_r = \frac{2\ \pi\ a_\star\ sin(i)}{P\ \sqrt{1-e^2}}\ [cos(\omega+\nu) + e\ cos(\nu)\ cos(\omega+\nu) + sin(\omega+\nu)]$$

2 $r = \frac{a\ (1-e^2)}{1+e\ cos(\nu)}$

3 $\frac{dA}{dt} = \frac{1}{2} r^2 \frac{d\nu}{dt}$, with A the swept out area in a time dt.

Manipulating above equation with trigonometric identities, it simplify as

$$\begin{aligned} v_r &= \frac{2\,\pi\,a_\star\,sin(i)}{P\,\sqrt{1-e^2}}\,\left[cos(\omega+\nu)+e\,cos(\omega)\right] \\ &= \frac{2\,\pi\,a\,sin(i)}{P\,\sqrt{1-e^2}}\,\frac{m_p}{M_\star+m_p}\left[cos(\omega+\nu)+e\,cos(\omega)\right] \end{aligned}$$

where the eq. (1.1) for the stellar semi-major axis was used. Finally, using Kepler's 3^{rd} law[4] in the precedent equation and assuming $m_p << M_\star$

$$v_r = \left(\frac{2\,\pi\,G}{P}\right)^{1/3}\frac{1}{\sqrt{1-e^2}}\,\frac{m_p\,sin(i)}{M_\star^{2/3}}\,\left[cos(\omega+\nu)+e\,cos(\omega)\right] \tag{1.6}$$

In equation (1.6) it is convenient to use the concept of semi-amplitude K, which is defined as

$$K = \left(\frac{2\,\pi\,G}{P}\right)^{1/3}\frac{1}{\sqrt{1-e^2}}\,\frac{m_p\,sin(i)}{M_\star^{2/3}} \tag{1.7}$$

Additionally, it is important to note that the whole system may have a general motion, in that case the centre of mass has a radial component γ which is added to v_r. This results in

$$v_r = \gamma + K\,\left[cos(\omega+\nu)+e\,cos(\omega)\right] \tag{1.8}$$

The bracketed term in equation (1.8) gives the shape of the signal (see figure 1.11) and K the strength of the signal. We note that assuming the stellar mass $M_\star$ and deriving the eccentricity from the shape of the curve, we derive the planetary minimum mass $m_p\,sin(i)$; combining the radial velocity method with the transits method allows to infer the true mass.

Generally speaking and from equation (1.7), we note that $K \propto m_p\,M_\star^{-2/3}\,P^{-1/3}$, which means that the radial velocity method is more sensitive to massive planets, lower stellar mass plays a considerable role and it has some sensitivity to shorter periods. In terms of detectability, a RV signal will be detectable depending on the amplitude of the signal K, the overall RV uncertainty σ_{v_r} and the number of RV measurements N; assuming a circular (or almost circular) orbit, the shape of the signal will have a low impact on its detectability (see Fig. 1.11). With this in mind, a RV signal-to-noise ratio can be expressed as

$$S/N_{v_r} \approx \sqrt{N}\,\frac{K}{\sigma_{v_r}} \tag{1.9}$$

In equation (1.9) one assumes an uniform sampling of RV measurements along several periods. An interesting exercise is to estimate the semi-amplitude of Solar-system and others outstanding planets detected by transits. I suppose a detection[5] with $S/N_{v_r} = 20$, without any additional source of noise (stellar, instrumental, etc). As we see from table 1.1, true Mars-like planets are beyond the capabilities of the RV method even if an accuracy of 10 $cm\,s^{-1}$ is reached. A reasonable upper limit of data is around 300, with this, it is evident how important is to achieve precision of $cm\,s^{-1}$ to access to Earth-like planets.

[4] $P^2 = \frac{4\,\pi^2}{G\,(m_1+m_2)}\,a^3$, with G the gravitational constant

[5] Estimated from the detection of GJ 1214b, with $K = 15\ m\,s^{-1}$, $\sigma_{v_r} = 3.5\ m\,s^{-1}$ and using 21 measurements (see section 4.1.5)

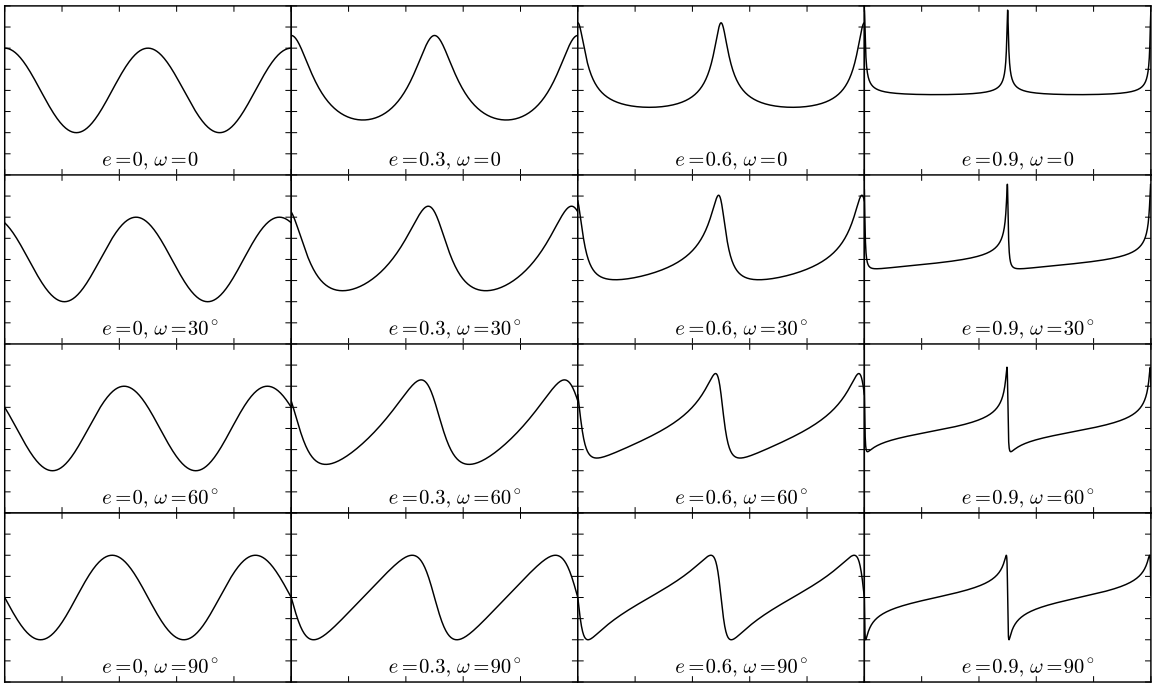

Figure 1.11: The effect of the eccentricity and the longitude of periastron on the shape of the radial velocity signal. The semi-amplitude K, the period P and the periastron passage t_0 are constants.

Table 1.1: Expected RVs semi-amplitude K and required number of observations (N) for a $S/N_{v_r} = 20$ detection with different RV uncertainties σ_{v_r}. N is not given when a very low number of observations allows the detection. Properties for the last three entries from http://exoplanet.eu and http://phl.upr.edu/projects/habitable-exoplanets-catalog

	K $[m\,s^{-1}]$	$N(\sigma_{v_r} = 3[m\,s^{-1}])$	$N(\sigma_{v_r} = 1[m\,s^{-1}])$	$N(\sigma_{v_r} = 0.1[m\,s^{-1}])$
Earth	0.09	4.4×10^5	4.9×10^4	500
Mars	0.008	5.6×10^7	6.2×10^6	6.2×10^4
Jupiter	12.5	25	–	–
Saturn	2.8	460	50	–
Uranus	0.3	4×10^4	4.5×10^3	45
Kepler-438b (1.3$M_\oplus$)	0.38	2.5×10^4	2.8×10^3	28
Kepler-22b (20.4$M_\oplus$)	2.01	900	100	–
EPIC-201367065d (3.7$M_\oplus$)	0.94	4×10^3	450	–

1.3.2 Doppler spectroscopy and the cross-correlation function

I described how to detect exoplanets by the radial velocities and derive the orbital parameters (Sect. 1.3.1). But how we measure the stellar radial velocity? The answer comes from stellar absorption lines, which are shifted according to the relative velocity between the star and the observer. First, it is convenient to define the Solar-system barycenter as the standard reference frame (IAU). Once in the standard reference

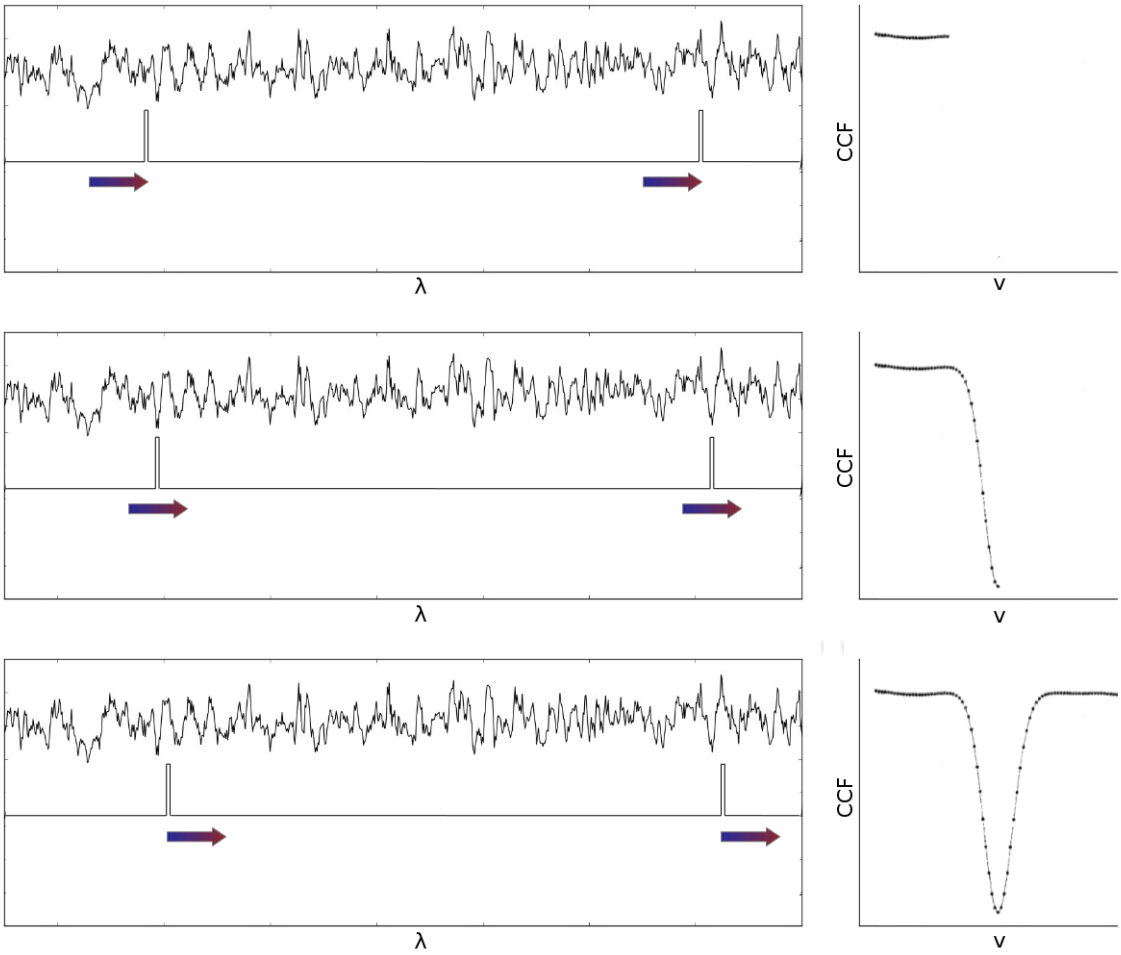

Figure 1.12: Sketch showing the result from cross correlating (CCF, right panels) a binary mask (box shaped emission lines shifted at different velocities from top to bottom, left panels) with an observed spectra (left panels).

frame and neglecting relativistic effects, the radial Doppler effect gives the wavelength shift, which is written as

$$\lambda = \lambda_0 \left(1 + \frac{v_r}{c}\right) \tag{1.10}$$

where λ is the wavelength measured by the observer, λ_0 is the wavelength at the source and c is the speed of light. Here we immediately notice the challenges of measuring the Doppler shift induced by a 1 $m\,s^{-1}$ differential RV; indeed, for example at 5500Å this corresponds to a wavelength shift of about 1.8×10^{-5}Å to be measured in a resolution element of 0.055 Å (for a high instrumental resolution of $R = 100000$). So, how to achieve precision of the order of $m\,s^{-1}$? The Doppler information is contained in each stellar spectral line, so instead of measuring the position of each line independently, ones can increase the signal-to-noise by accumulating the Doppler information of thousands absorption lines in a one unique line, which is the idea behind cross correlating; therefore, one wants a wide spectral domain (cross-dispersed echelle spectrographs). Initially, physical masks with holes tracking the position of most favourable lines were proposed (Fellgett, 1955) and used (Griffin, 1967; Baranne et al., 1979),

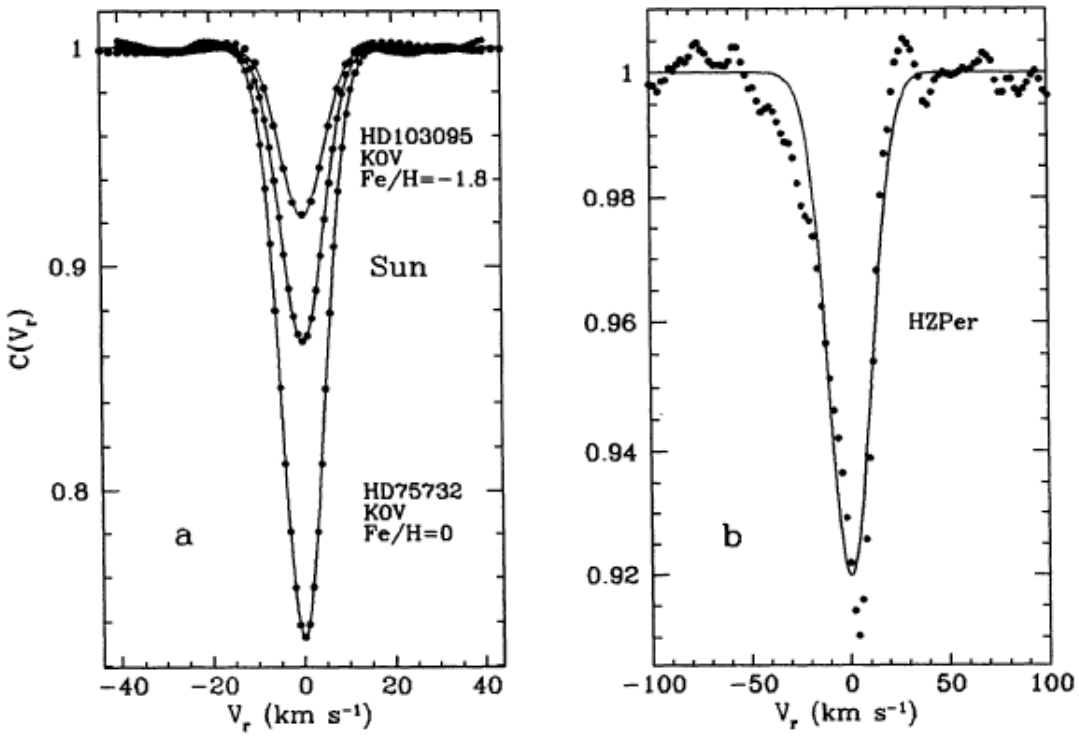

Fig. 1. CCFs for stars with various temperatures and metallicities (dots). The CCFs reproduce well the average behavior of the majority of lines matchmg the template (neutral lines). The solid lines represent the fitted Gaussians and it is worth noticing that they approximate the CCFs very well. b) CCF of a Cepheid star at a particular pulsating phase where the lines are asymmetric.

Figure 1.13: From Queloz (1995).

where the physical mask is cross-correlated with the observed spectra. Then, the cross-correlation was improved in accuracy and spectral type adaptability by using a numerical mask (Queloz, 1995) and fibre-fed spectrographs (SOPHIE, Baranne et al., 1996). The numerical mask (binary template M) has box-shaped emission lines strategically placed in most prominent lines, and it is shifted in velocity space to search the minimum of the correlation. This writes as

$$C(\epsilon) = \frac{R(\epsilon)}{R(\infty)} \; ; \quad R(\epsilon) = \int_{-\infty}^{\infty} S(v)\, M(v-\epsilon)\, dv \tag{1.11}$$

where C is the cross-correlation function (CCF), S the stellar spectrum and we look for the value of ϵ which minimises C (the procedure is detailed in, e.g. Queloz, 1995; Baranne et al., 1996, see figure 1.12 showing a sketch of the procedure). The – approximately Gaussian – shape of the CCF represents the overall shape of spectral lines, hence, its symmetry will depends on stellar lines symmetry; and its full-width at half-maximum ($FWHM$) is representative of the stellar rotation. The stellar radial velocity corresponds to the centre of a Gaussian fit performed to the CCF, while the error is estimated from

Monte-Carlo simulations (see Fig. 1.13). Bouchy et al. (2001) gives a procedure to estimate the RV error directly from spectrum (although is not suitable for low signal-to-noise spectra). Bouchy et al. (2001) showed that the RV – photon – precision depends on the spectrum signal-to-noise ratio and the $FWHM$ and depth of stellar lines, that is, narrow and deep lines contain more Doppler information than spread and weak ones. Accordingly, Pepe et al. (2002) proposed a weighted CCF, where the weight of prominent lines is greater; in addition, they found an improvement in RVs when rejecting stellar lines close by ± 30 $[km\,s^{-1}]$ (annual Earth's motion) to telluric lines.

For example, this technique is today used by the "official" pipeline of *HARPS* (ESO) and *SOPHIE* (OHP). As I describe in section 2.2, one of the goal of my thesis is to propose and implement another methodology to extract accurate RV from spectra.

1.3.3 Limitations and difficulties of the radial velocities method

Instrumental

Of course, one of the first limitations in precise RVs is the need of high signal-to-noise spectra, which is limited by the star's luminosity and its distance. Therefore, efficient spectrographs and large telescopes are needed to analyse faint objects. Also required are high-resolution ($R > 50000$) spectrographs with a wide spectral coverage, because the needs to sample stellar lines with enough accuracy and to accumulate the Doppler information from a vast number of lines.

A key step in the radial velocity technique was the fine wavelength calibration of spectra, allowing precision from tens of $m\,s^{-1}$ to few $m\,s^{-1}$ with the introduction of the gas-cell or ThAr lamps. Iodine-gas cell located at the spectrograph entrance slit superimpose catalogued absorption lines (mostly between 5000-6200 Å) to the stellar spectrum, improving RV precision around 2 $m\,s^{-1}$. However, caution is needed because changes in the internal pressure of the gas cell may introduce spurious variations of the wavelength calibration; in addition, there is a loss of light when using gas cells and the domain of iodine lines makes almost impossible to use it for M dwarfs. Another method for wavelength calibration is the use of ThAr lamps, which have a similar RV precision than iodine cells. These lamps emit lines in a wider spectral domain (from the optical to nIR) than I_2, however, their lines are affected by a drift when the lamp ages and its internal pressure change. Such drift affects Th and Ar lines in a different way, allowing a correction for a stable RV precision (Lovis and Pepe, 2007). Another approach to push the limits of wavelength calibration is the use of laser frequency comb that generates emission lines arranged in a regular way, enabling a wavelength calibration of the order of 0.01 $m\,s^{-1}$ (Murphy et al., 2007). Fabry-Perot etalon are also used for the wavelength calibration (e.g. HARPS; Wildi et al., 2011, demonstrated that 10 $cm\,s^{-1}$ was achieved during a night and a 1 $m\,s^{-1}$ stability was reached over 60 days), and will certainly be combined with the laser frequency comb (to overcome the high-frequency peaks that spectrographs can not resolve at $R \sim 100000$).

A deep understanding and monitoring of the instrument profile is required. To illustrate the difficulties, a pixel of the *HARPS* CCD along the dispersion direction of the spectrograph, represents about 1 $km\,s^{-1}$. To ensure RV precision of 1 $m\,s^{-1}$ it is thus necessary to monitor the spectrum position at a level of $1/1000^{th}$ pixel, i.e., in the case of *HARPS* at a level of 15 nm on the detector (for a 10 μm pixel size). By the use of fibres, the spectrograph can be placed in a vacuum vessel with a fine temperature control (stable environment) avoiding thermal or mechanical effects. Additionally, fibre-fed instruments overcomes the problem of illumination variations of slit spectrographs. However, variation of the light injection is observed as a function of the centering of the star in the fiber entrance, degrading the stability

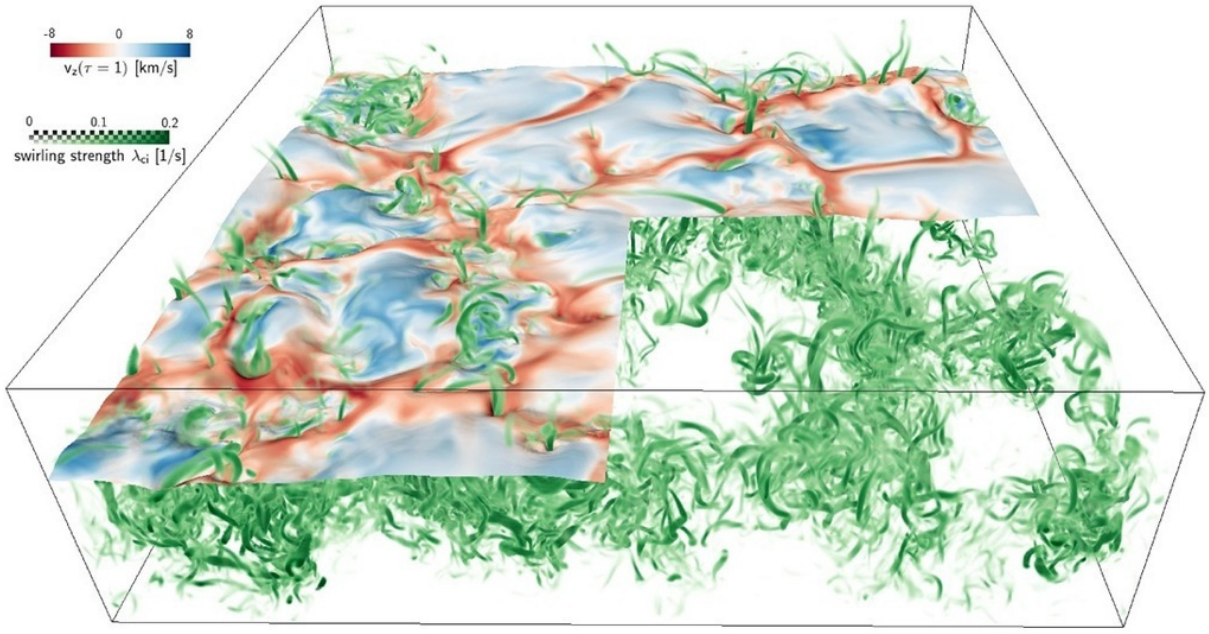

Figure 1.14: Blueshift excess due to convection cells. Snapshot from a simulation of solar convective flows. The green volume rendering indicates swirling flows near the optical solar surface, which is color-coded with vertical flow velocity (downflows in red and upflows in blue). The size of the box shown is 4800 km x 4800 km horizontally and 1400 km in depth. The optical surface is hidden in the lower right quadrant, uncovering the swirling structure in the subsurface layers. Credits: http://www.mps.mpg.de/1764720/Solar-MHD

of the spectrograph. This point was resolved first by adding a double scrambler in the fiber link and then by using octagonal fiber (Perruchot et al., 2011), which have a high scrambling power and average illumination inhomogeneities at the fiber output. Moreover, it is common that fibre-fed spectrographs have two fibres, with the possibility to directly monitor the RV drift of the spectrograph (due to mechanical flexure or thermal contraction/dilatation) by doing the wavelength calibration simultaneously to the science exposure.

Charge-Coupled Device (CCD) also affect the extraction of RVs. The size, arrangement and sensibility of CCD pixels is not perfectly uniform. For example, inter pixel size variations introduces jump discontinuities in the wavelength solution, affecting the wavelength calibration. A high density sampling of pixels (with a Fabry-Perot cavity or laser frequency comb) is able to correct for this issue.

Non Instrumental

Now we turn to difficulties non related to the instrument. I start quoting the effects of telluric lines affecting spectra acquired from the ground. Contrary to stellar lines and neglecting wind effects, telluric lines are in rest in the observer frame or Doppler shifted in the Solar-system barycenter due to the Earth motion. These telluric features introduce a one year signal in RVs, and therefore spectral zones containing tellurics should be avoided or corrected.

Depending on the sky transparency, diffuse moon-light may affect RVs. In fact, as the Moon reflects the Sun-light, observing near the Moon may introduce a solar spectrum (shifted according to the Moon's RV) in the spectra of our target star. Therefore, one should avoid to observe near the Moon position and check that there is enough difference between the Moon and stellar radial velocities.

One of the most problematic effect in RVs come from the star itself. Stars are far to be static objects and many dynamic phenomena occur on their surface. Stellar activity and its impact on RVs will be revised below (chapter 3), here I give some basics. Oscillating pressure modes (p-modes) take place in convective stars, and introduce RV variations as they produce slight variations on the stellar radii. Pressure waves are responsible of RV variations of the order of 10-100 $cm\,s^{-1}$ with 3-30 mn periodicity in solar-type stars (Bouchy and Carrier, 2001). Several measures or long exposure times can average the effect of oscillating p-modes (Dumusque et al., 2011).

The stellar convection moves the plasma upward and inward, introducing a limiting in the radial velocity method. Surface granulation (the surface signature of convective cells) results from the upward material, which is responsible of a blueshift of spectral lines, while the downward material in inter-granular regions produces a redshift in stellar lines; averaging over several granules results in an overall blueshift (Fig. 1.14). The unbalance between the two components comes from a difference of size and plasma temperature between blue- and red-shifted part of the photosphere. For detecting planets, a problem appears when convection is inhibited under the presence of strong local magnetic fields, which is translated into a change in the line profiles inducing RVs variations. The CCF bisector span is an indicator of stellar convection, and it need to be monitored to search for any correlation between its value and RVs (e.g. Queloz et al., 2001; Meunier and Lagrange, 2013).

Difficulties also arise due to inhomogeneities in the stellar surface due to the presence of magnetic fields. Dark spots and bright plages are responsible of RVs variations when they cross the stellar disc, as the star rotates; these RVs variations can mimic the signature of planetary companions. Some stellar lines can be used to trace the stellar surface magnetic activity, like Ca II H&K lines, Hα or the sodium doublet. Any correlation between one of these activity indicators and RVs warn us about the nature of a RVs signal (e.g. Bonfils et al., 2007; Lagrange et al., 2010; Dumusque et al., 2014). Inhomogeneities on the stellar surface and the inhibition of convection will mainly produce RV variation at the rotation period of the star (or one of its harmonic, Boisse et al., 2011) and/or at the period of the stellar magnetic cycle. For this reason I work on the determination of rotation periods of M dwarfs (Sect. 2.2).

Any variation in radial velocities not due to a planetary companion but to intrinsic effects of the star, is known as stellar *jitter*. Relatively quiet stars will show a low dispersion in RVs, while active stars show high RVs dispersion. Characterising stellar activity, theoretically or empirically, is a fundamental step to detect – by radial velocities – low-mass planets orbiting stars with moderate activity.

1.3.4 Radial velocities surveys

To detect planets with the radial velocity method needs a constant monitoring of a sample of stars, this is a huge effort in human resources and telescope time. In the late 80s-early 90s, the hunt for planets orbiting other stars than the Sun was the focus of several groups.

A survey to propose RV standards monitored a few dozen of stars using facilities from Oak Ridge, Whippler and OHP (*CORAVEL*) observatories. After more than ten years of monitoring, Latham et al. (1989) reported the discovery of a very massive planet ($m\,sin(i) = 11.98\mathrm{M}_{Jup}$) orbiting HD 114762. A program to search for exoplanets started in 1985 at Steward Observatory (University of Arizona); McMillan et al. (1994) reported six years of observation for 20 stars and, although they did not detect any massive planet, they announced the first detection of p-mode oscillations in a star other than the Sun (Smith et al., 1987). Two-years after the Lick Observatory survey to search for brown dwarfs and massive planets started, Marcy and Butler (1992) published the analysis of data; neither brown dwarfs nor

Jupiter-mass planets were unveiled with the echelle spectrograph mounted with an iodine-gas cell in a 3m-telescope. Cochran and Hatzes (1994) describes their search for Jupiter-like planets around 33 G-dwarfs, their McDonald Observatory Planetary Search survey used an iodine-cell placed in the entrance slit of a 2.7m-telescope; they found no traces of massive planets. In 1995, Walker et al. published a summary of a 12-years RV survey monitoring 21 stars; using a iodine-gas cell at the focus of the Canada France Hawaii Telescope, they found no evidences of planet companions in an upper limit of 1-3 Jupiter masses for orbital periods out to 15 years. Just after, came the discovery of 51-Pegb (Mayor and Queloz, 1995), announced a year and a half after Mayor and Queloz started their *ELODIE@OHP* (1.93m-telescope) survey of 142 GK-stars.

More recent surveys[6] have been increasing the number of known exoplanets (to the date, 589 detected by RVs[7]), to give some examples: AFOE@Mt. Hopkins Observatory (Noyes et al., 1997) – 3 detections; UCLES@Anglo-Australian Telescope (Butler et al., 2001) – 28 detections; CORALIE@Leonard Euler Swiss telescope Udry et al. (2000) – 7 detections; ELODIE@OHP 1m93-telescope (Mayor and Queloz, 1995) – 4 detection; Exoplanet Tracker@Kitt Peak National Observatory 0.9m-telescope (Ge et al., 2006) – 1 detection; *HARPS*@La Silla 3.6m-telescope – more than 125 detections until 2011, e.g The *HARPS* search for southern extra-solar planets series; The Lick-Carnegie Exoplanet Survey and The California Planet Survey, HIRES@Keck and HRS@HET (Howard et al., 2010; Meschiari et al., 2011); The McDonald Observatory Planet Search Projects (Endl et al., 2004); SOPHIE@OHP 1m93-telescope – 15 detections.

[6] http://exoplanet.eu/research/
[7] http://exoplanet.eu

References

Alonso, R., Brown, T. M., Torres, G., Latham, D. W., Sozzetti, A., Mandushev, G., Belmonte, J. A., Charbonneau, D., Deeg, H. J., Dunham, E. W., O'Donovan, F. T., Stefanik, R. P., 2004. TrES-1: The Transiting Planet of a Bright K0 V Star. ApJ 613, L153–L156, astro-ph/0408421.

Baranne, A., Mayor, M., Poncet, J. L., 1979. CORAVEL - A new tool for radial velocity measurements. Vistas in Astronomy 23, 279–316.

Baranne, A., Queloz, D., Mayor, M., Adrianzyk, G., Knispel, G., Kohler, D., Lacroix, D., Meunier, J.-P., Rimbaud, G., Vin, A., 1996. ELODIE: A spectrograph for accurate radial velocity measurements. A&AS 119, 373–390.

Barge, P., Léger, A., Ollivier, M., Rouan, D., Schneider, J., Exoplanet COROT Team, 2006. Photometric Search for Transiting Planets. In: Fridlund, M., Baglin, A., Lochard, J., Conroy, L. (Eds.), ESA Special Publication. Vol. 1306 of ESA Special Publication. p. 83.

Benjamin, R. A., Churchwell, E., Babler, B. L., Indebetouw, R., Meade, M. R., Whitney, B. A., Watson, C., Wolfire, M. G., Wolff, M. J., Ignace, R., Bania, T. M., Bracker, S., Clemens, D. P., Chomiuk, L., Cohen, M., Dickey, J. M., Jackson, J. M., Kobulnicky, H. A., Mercer, E. P., Mathis, J. S., Stolovy, S. R., Uzpen, B., 2005. First GLIMPSE Results on the Stellar Structure of the Galaxy. ApJ 630, L149–L152, astro-ph/0508325.

Bessel, F. W., 1844. On the variations of the proper motions of Procyon and Sirius. MNRAS 6, 136–141.

Beuzit, J.-L., Feldt, M., Dohlen, K., Mouillet, D., Puget, P., Wildi, F., Abe, L., Antichi, J., Baruffolo, A., Baudoz, P., Boccaletti, A., Carbillet, M., Charton, J., Claudi, R., Downing, M., Fabron, C., Feautrier, P., Fedrigo, E., Fusco, T., Gach, J.-L., Gratton, R., Henning, T., Hubin, N., Joos, F., Kasper, M., Langlois, M., Lenzen, R., Moutou, C., Pavlov, A., Petit, C., Pragt, J., Rabou, P., Rigal, F., Roelfsema, R., Rousset, G., Saisse, M., Schmid, H.-M., Stadler, E., Thalmann, C., Turatto, M., Udry, S., Vakili, F., Waters, R., 2008. SPHERE: a 'Planet Finder' instrument for the VLT. In: Society of Photo-Optical Instrumentation Engineers (SPIE) Conference Series. Vol. 7014 of Society of Photo-Optical Instrumentation Engineers (SPIE) Conference Series. p. 18.

Boisse, I., Bouchy, F., Hébrard, G., Bonfils, X., Santos, N., Vauclair, S., 2011. Disentangling between stellar activity and planetary signals. A&A 528, A4.

Bonfils, X., Delfosse, X., Udry, S., Forveille, T., Mayor, M., Perrier, C., Bouchy, F., Gillon, M., Lovis, C., Pepe, F., Queloz, D., Santos, N. C., Ségransan, D., Bertaux, J.-L., 2013. The HARPS search for southern extra-solar planets. XXXI. The M-dwarf sample. A&A 549, A109, 1111.5019.

Bonfils, X., Mayor, M., Delfosse, X., Forveille, T., Gillon, M., Perrier, C., Udry, S., Bouchy, F., Lovis, C., Pepe, F., Queloz, D., Santos, N. C., Bertaux, J.-L., 2007. The HARPS search for southern extra-solar planets. X. A m sin i = 11 $M_{\oplus}$ planet around the nearby spotted M dwarf GJ 674. A&A 474, 293–299, 0704.0270.

Borucki, W., Koch, D., Batalha, N., Caldwell, D., Christensen-Dalsgaard, J., Cochran, W. D., Dunham, E., Gautier, T. N., Geary, J., Gilliland, R., Jenkins, J., Kjeldsen, H., Lissauer, J. J., Rowe, J., 2009. KEPLER: Search for Earth-Size Planets in the Habitable Zone. In: Pont, F., Sasselov, D., Holman, M. J. (Eds.), IAU Symposium. Vol. 253 of IAU Symposium. pp. 289–299.

Bouchy, F., Carrier, F., 2001. Catching the sounds of stars. Asteroseismology, the right tool to understand stellar interiors. The Messenger 106, 32–37.

Bouchy, F., Pepe, F., Queloz, D., 2001. Fundamental photon noise limit to radial velocity measurements. A&A 374, 733–739.

Burton, W. B., 1988. The structure of our Galaxy derived from observations of neutral hydrogen. pp. 295–358.

Butler, R. P., Tinney, C. G., Marcy, G. W., Jones, H. R. A., Penny, A. J., Apps, K., 2001. Two New Planets from the Anglo-Australian Planet Search. ApJ 555, 410–417.

Campbell, B., Walker, G. A. H., 1979. Precision radial velocities with an absorption cell. PASP 91, 540–545.

Charbonneau, D., Brown, T. M., Latham, D. W., Mayor, M., 2000. Detection of Planetary Transits Across a Sun-like Star. ApJ 529, L45–L48, astro-ph/9911436.

Cochran, W. D., Hatzes, A. P., 1994. A high-precision radial-velocity survey for other planetary systems. Ap&SS 212, 281–291.

Dame, T. M., Hartmann, D., Thaddeus, P., 2001. The Milky Way in Molecular Clouds: A New Complete CO Survey. ApJ 547, 792–813, astro-ph/0009217.

Delfosse, X., Donati, J.-F., Kouach, D., Hébrard, G., Doyon, R., Artigau, E., Bouchy, F., Boisse, I., Brun, A. S., Hennebelle, P., Widemann, T., Bouvier, J., Bonfils, X., Morin, J., Moutou, C., Pepe, F., Udry, S., do Nascimento, J.-D., Alencar, S. H. P., Castilho, B. V., Martioli, E., Wang, S. Y., Figueira, P., Santos, N. C., 2013. World-leading science with SPIRou - The nIR spectropolarimeter / high-precision velocimeter for CFHT. In: Cambresy, L., Martins, F., Nuss, E., Palacios, A. (Eds.), SF2A-2013: Proceedings of the Annual meeting of the French Society of Astronomy and Astrophysics. pp. 497–508.

Dumusque, X., Boisse, I., Santos, N. C., 2014. SOAP 2.0: A Tool to Estimate the Photometric and Radial Velocity Variations Induced by Stellar Spots and Plages. ApJ 796, 132, 1409.3594.

Dumusque, X., Udry, S., Lovis, C., Santos, N. C., Monteiro, M. J. P. F. G., 2011. Planetary detection limits taking into account stellar noise. I. Observational strategies to reduce stellar oscillation and granulation effects. A&A 525, A140, 1010.2616.

Endl, M., Cochran, W. D., McArthur, B., Allende Prieto, C., Hatzes, A. P., Paulson, D. B., 2004. The McDonald Observatory Planet Search Projects. In: Beaulieu, J., Lecavelier Des Etangs, A., Terquem, C. (Eds.), Extrasolar Planets: Today and Tomorrow. Vol. 321 of Astronomical Society of the Pacific Conference Series. p. 105.

Fellgett, P., 1955. A Proposal for a Radial Velocity Photometer. Optica Acta 2, 9–16.

Gatewood, G., Eichhorn, H., 1973. An unsuccessful search for a planetary companion of Barnard's star BD +4 3561. AJ 78, 769–776.

Gaudi, B. S., 2011. Microlensing by Exoplanets. pp. 79–110.

Ge, J., van Eyken, J., Mahadevan, S., DeWitt, C., Kane, S. R., Cohen, R., Vanden Heuvel, A., Fleming, S. W., Guo, P., Henry, G. W., Schneider, D. P., Ramsey, L. W., Wittenmyer, R. A., Endl, M., Cochran, W. D., Ford, E. B., Martín, E. L., Israelian, G., Valenti, J., Montes, D., 2006. The First Extrasolar Planet Discovered with a New-Generation High-Throughput Doppler Instrument. ApJ 648, 683–695, astro-ph/0605247.

Griffin, R., 1973. On the possibility of determining stellar radial velocities to 0.01 km s^{-1}. MNRAS 162, 243–253.

Griffin, R. F., 1967. A Photoelectric Radial-Velocity Spectrometer. ApJ 148, 465.

Heintz, W. D., 1978. Reexamination of suspected unresolved binaries. ApJ 220, 931–934.

Henry, G. W., Marcy, G. W., Butler, R. P., Vogt, S. S., 2000. A Transiting "51 Peg-like" Planet. ApJ 529, L41–L44.

Howard, A. W., Johnson, J. A., Marcy, G. W., Fischer, D. A., Wright, J. T., Bernat, D., Henry, G. W., Peek, K. M. G., Isaacson, H., Apps, K., Endl, M., Cochran, W. D., Valenti, J. A., Anderson, J., Piskunov, N. E., 2010. The California Planet Survey. I. Four New Giant Exoplanets. ApJ 721, 1467–1481, 1003.3488.

Jacob, W. S., 1855. On certain Anomalies presented by the Binary Star 70 Ophiuchi. MNRAS 15, 228.

Lagrange, A.-M., Desort, M., Meunier, N., 2010. Using the Sun to estimate Earth-like planets detection capabilities . I. Impact of cold spots. A&A 512, A38, 1001.1449.

Lagrange, A.-M., Gratadour, D., Chauvin, G., Fusco, T., Ehrenreich, D., Mouillet, D., Rousset, G., Rouan, D., Allard, F., Gendron, É., Charton, J., Mugnier, L., Rabou, P., Montri, J., Lacombe, F., 2009. A probable giant planet imaged in the β Pictoris disk. VLT/NaCo deep L'-band imaging. A&A 493, L21–L25, 0811.3583.

Latham, D. W., Stefanik, R. P., Mazeh, T., Mayor, M., Burki, G., 1989. The unseen companion of HD114762 - A probable brown dwarf. Nature 339, 38–40.

Lovis, C., Fischer, D., 2011. Radial Velocity Techniques for Exoplanets. pp. 27–53.

Lovis, C., Pepe, F., 2007. A new list of thorium and argon spectral lines in the visible. A&A 468, 1115–1121, astro-ph/0703412.

Macintosh, B. A., Graham, J. R., Palmer, D. W., Doyon, R., Dunn, J., Gavel, D. T., Larkin, J., Oppenheimer, B., Saddlemyer, L., Sivaramakrishnan, A., Wallace, J. K., Bauman, B., Erickson, D. A., Marois, C., Poyneer, L. A., Soummer, R., 2008. The Gemini Planet Imager: from science to design to construction. In: Society of Photo-Optical Instrumentation Engineers (SPIE) Conference Series. Vol. 7015 of Society of Photo-Optical Instrumentation Engineers (SPIE) Conference Series. p. 18.

Marcy, G. W., Butler, R. P., 1992. Precision radial velocities with an iodine absorption cell. PASP 104, 270–277.

Marcy, G. W., Butler, R. P., 1996. A Planetary Companion to 70 Virginis. ApJ 464, L147.

Mayor, M., Marmier, M., Lovis, C., Udry, S., Ségransan, D., Pepe, F., Benz, W., Bertaux, J. ., Bouchy, F., Dumusque, X., Lo Curto, G., Mordasini, C., Queloz, D., Santos, N. C., 2011. The HARPS search for southern extra-solar planets XXXIV. Occurrence, mass distribution and orbital properties of super-Earths and Neptune-mass planets. ArXiv e-prints 1109.2497.

Mayor, M., Pepe, F., Queloz, D., Bouchy, F., Rupprecht, G., Lo Curto, G., Avila, G., Benz, W., Bertaux, J.-L., Bonfils, X., Dall, T., Dekker, H., Delabre, B., Eckert, W., Fleury, M., Gilliotte, A., Gojak, D., Guzman, J. C., Kohler, D., Lizon, J.-L., Longinotti, A., Lovis, C., Megevand, D., Pasquini, L., Reyes, J., Sivan, J.-P., Sosnowska, D., Soto, R., Udry, S., van Kesteren, A., Weber, L., Weilenmann, U., 2003. Setting New Standards with HARPS. The Messenger 114, 20–24.

Mayor, M., Queloz, D., 1995. A Jupiter-mass companion to a solar-type star. Nature 378, 355–359.

Mazeh, T., Naef, D., Torres, G., Latham, D. W., Mayor, M., Beuzit, J.-L., Brown, T. M., Buchhave, L., Burnet, M., Carney, B. W., Charbonneau, D., Drukier, G. A., Laird, J. B., Pepe, F., Perrier, C., Queloz, D., Santos, N. C., Sivan, J.-P., Udry, S., Zucker, S., 2000. The Spectroscopic Orbit of the Planetary Companion Transiting HD 209458. ApJ 532, L55–L58, astro-ph/0001284.

McMillan, R. S., Moore, T. L., Perry, M. L., Smith, P. H., 1994. Long, accurate time series measurements of radial velocities of solar-type stars. Ap&SS 212, 271–280.

Meschiari, S., Laughlin, G., Vogt, S. S., Butler, R. P., Rivera, E. J., Haghighipour, N., Jalowiczor, P., 2011. The Lick-Carnegie Survey: Four New Exoplanet Candidates. ApJ 727, 117, 1011.4068.

Meunier, N., Lagrange, A.-M., 2013. Using the Sun to estimate Earth-like planets detection capabilities. IV. Correcting for the convective component. A&A 551, A101.

Moulton, F. R., 1899. The limits of temporary stability of satellite motion, with an application to the question of the existence of an unseen body in the binary system 70 Ophiuchi. AJ 20, 33–37.

Murphy, M. T., Udem, T., Holzwarth, R., Sizmann, A., Pasquini, L., Araujo-Hauck, C., Dekker, H., D'Odorico, S., Fischer, M., Hänsch, T. W., Manescau, A., 2007. High-precision wavelength calibration of astronomical spectrographs with laser frequency combs. MNRAS 380, 839–847, astro-ph/0703622.

Murray, C. D., Correia, A. C. M., 2011. Keplerian Orbits and Dynamics of Exoplanets. pp. 15–23.

Nesvorný, D., Kipping, D., Terrell, D., Hartman, J., Bakos, G. Á., Buchhave, L. A., 2013. KOI-142, The King of Transit Variations, is a Pair of Planets near the 2:1 Resonance. ApJ 777, 3, 1304.4283.

Noyes, R., Jha, S., Korzennik, S., Krockenberger, M., Nisenson, P., Brown, T., Kennelly, E., Horner, S., 1997. The AFOE Program of Extra-Solar Planet Research. In: Soderblom, D. (Ed.), Planets Beyond the Solar System and the Next Generation of Space Missions. Vol. 119 of Astronomical Society of the Pacific Conference Series. p. 119.

Nutzman, P., Charbonneau, D., 2008. Design Considerations for a Ground-Based Transit Search for Habitable Planets Orbiting M Dwarfs. PASP 120, 317–327, 0709.2879.

Pasquini, L., Avila, G., Dekker, H., Delabre, B., D'Odorico, S., Manescau, A., Haehnelt, M., Carswell, B., Garcia-Lopez, R., Lopez, R., Osorio, M. T., Rebolo, R., Cristiani, S., Bonifacio, P., D'Odorico, V., Molaro, P., Spanò, P., Zerbi, F., Mayor, M., Dessauges, M., Megevand, D., Pepe, F., Queloz, D., Udry, S., 2008. CODEX: the high-resolution visual spectrograph for the E-ELT. In: Society of Photo-Optical Instrumentation Engineers (SPIE) Conference Series. Vol. 7014 of Society of Photo-Optical Instrumentation Engineers (SPIE) Conference Series. p. 1.

Pepe, F., Mayor, M., Galland, F., Naef, D., Queloz, D., Santos, N. C., Udry, S., Burnet, M., 2002. The CORALIE survey for southern extra-solar planets VII. Two short-period Saturnian companions to HD 108147 and HD 168746. A&A 388, 632–638, astro-ph/0202457.

Pepe, F. A., Cristiani, S., Rebolo Lopez, R., Santos, N. C., Amorim, A., Avila, G., Benz, W., Bonifacio, P., Cabral, A., Carvas, P., Cirami, R., Coelho, J., Comari, M., Coretti, I., De Caprio, V., Dekker, H., Delabre, B., Di Marcantonio, P., D'Odorico, V., Fleury, M., García, R., Herreros Linares, J. M., Hughes, I., Iwert, O., Lima, J., Lizon, J.-L., Lo Curto, G., Lovis, C., Manescau, A., Martins, C., Mégevand, D., Moitinho, A., Molaro, P., Monteiro, M., Monteiro, M., Pasquini, L., Mordasini, C., Queloz, D., Rasilla, J. L., Rebordão, J. M., Santana Tschudi, S., Santin, P., Sosnowska, D., Spanò, P., Tenegi, F., Udry, S., Vanzella, E., Viel, M., Zapatero Osorio, M. R., Zerbi, F., 2010. ESPRESSO: the Echelle spectrograph for rocky exoplanets and stable spectroscopic observations. In: Society of Photo-Optical Instrumentation Engineers (SPIE) Conference Series. Vol. 7735 of Society of Photo-Optical Instrumentation Engineers (SPIE) Conference Series. p. 0.

Perruchot, S., Bouchy, F., Chazelas, B., Díaz, R. F., Hébrard, G., Arnaud, K., Arnold, L., Avila, G., Delfosse, X., Boisse, I., Moreaux, G., Pepe, F., Richaud, Y., Santerne, A., Sottile, R., Tézier, D., 2011. Higher-precision radial velocity measurements with the SOPHIE spectrograph using octagonal-section fibers. In: Society of Photo-Optical Instrumentation Engineers (SPIE) Conference Series. Vol. 8151 of Society of Photo-Optical Instrumentation Engineers (SPIE) Conference Series. p. 15.

Pollacco, D. L., Skillen, I., Collier Cameron, A., Christian, D. J., Hellier, C., Irwin, J., Lister, T. A., Street, R. A., West, R. G., Anderson, D. R., Clarkson, W. I., Deeg, H., Enoch, B., Evans, A., Fitzsimmons, A., Haswell, C. A., Hodgkin, S., Horne, K., Kane, S. R., Keenan, F. P., Maxted, P. F. L., Norton, A. J., Osborne, J., Parley, N. R., Ryans, R. S. I., Smalley, B., Wheatley, P. J., Wilson, D. M., 2006. The WASP Project and the SuperWASP Cameras. PASP 118, 1407–1418, astro-ph/0608454.

Quanz, S. P., 2006. Book review: New Light on Dark Stars - Red Dwarfs, Low-Mass Stars, Brown Dwarfs / Springer, Heidelberg, 34 + 560 pp., ISBN 3-540-25124-3. Sterne und Weltraum 45 (11), 97–98.

Queloz, D., 1995. Echelle Spectroscopy with a CCD at Low Signal-To-Noise Ratio. In: Philip, A. G. D., Janes, K., Upgren, A. R. (Eds.), New Developments in Array Technology and Applications. Vol. 167 of IAU Symposium. p. 221.

Queloz, D., Henry, G. W., Sivan, J. P., Baliunas, S. L., Beuzit, J. L., Donahue, R. A., Mayor, M., Naef, D., Perrier, C., Udry, S., 2001. No planet for HD 166435. A&A 379, 279–287, astro-ph/0109491.

Quirrenbach, A., 2006. Detection and Characterization of Extrasolar Planets. In: Queloz, D., Udry, S., Mayor, M., Benz, W., Cassen, P., Guillot, T., Quirrenbach, A. (Eds.), Saas-Fee Advanced Course 31: Extrasolar planets. pp. 1–242.

Quirrenbach, A., 2011. Astrometric Detection and Characterization of Exoplanets. pp. 157–174.

Seager, S., Lissauer, J. J., 2011. Introduction to Exoplanets. pp. 3–13.

Silvotti, R., Schuh, S., Janulis, R., Solheim, J.-E., Bernabei, S., Østensen, R., Oswalt, T. D., Bruni, I., Gualandi, R., Bonanno, A., Vauclair, G., Reed, M., Chen, C.-W., Leibowitz, E., Paparo, M., Baran, A., Charpinet, S., Dolez, N., Kawaler, S., Kurtz, D., Moskalik, P., Riddle, R., Zola, S., 2007. A giant planet orbiting the 'extreme horizontal branch' star V391 Pegasi. Nature 449, 189–191.

Smith, P. H., McMillan, R. S., Merline, W. J., 1987. Evidence for periodic radial velocity variations in Arcturus. ApJ 317, L79–L84.

Soderhjelm, S., 1999. Possible detection of the planet transits of HD 209458 in the Hipparcos photometry. Information Bulletin on Variable Stars 4816, 1.

Strand, K. A., 1944. The astrometric study of unseen companions in double stars. AJ 51, 12–13.

Struve, O., 1952. Proposal for a project of high-precision stellar radial velocity work. The Observatory 72, 199–200.

Torres, G., Kipping, D. M., Fressin, F., Caldwell, D. A., Twicken, J. D., Ballard, S., Batalha, N. M., Bryson, S. T., Ciardi, D. R., Henze, C. E., Howell, S. B., Isaacson, H. T., Jenkins, J. M., Muirhead, P. S., Newton, E. R., Petigura, E. A., Barclay, T., Borucki, W. J., Crepp, J. R., Everett, M. E., Horch, E. P., Howard, A. W., Kolbl, R., Marcy, G. W., McCauliff, S., Quintana, E. V., 2015. Validation of Twelve Small Kepler Transiting Planets in the Habitable Zone. ArXiv e-prints 1501.01101.

Traub, W. A., Oppenheimer, B. R., 2011. Direct Imaging of Exoplanets. pp. 111–156.

Udry, S., Mayor, M., Naef, D., Pepe, F., Queloz, D., Santos, N. C., Burnet, M., Confino, B., Melo, C., 2000. The CORALIE survey for southern extra-solar planets. II. The short-period planetary companions to HD 75289 and HD 130322. A&A 356, 590–598.

van de Kamp, P., 1963. Astrometric study of Barnard's star from plates taken with the 24-inch Sproul refractor. AJ 68, 515–521.

Walker, G. A. H., Walker, A. R., Irwin, A. W., Larson, A. M., Yang, S. L. S., Richardson, D. C., 1995. A search for Jupiter-mass companions to nearby stars. Icarus116, 359–375.

Wildi, F., Pepe, F., Chazelas, B., Lo Curto, G., Lovis, C., 2011. The performance of the new Fabry-Perot calibration system of the radial velocity spectrograph HARPS. In: Society of Photo-Optical Instrumentation Engineers (SPIE) Conference Series. Vol. 8151 of Society of Photo-Optical Instrumentation Engineers (SPIE) Conference Series. p. 1.

Winn, J. N., 2010. Transits and Occultations. ArXiv e-prints 1001.2010.

Wolszczan, A., Frail, D. A., 1992. A planetary system around the millisecond pulsar PSR1257 + 12. Nature 355, 145–147.

Wolszczan, A., Kuchner, M., 2011. Planets Around Pulsars and Other Evolved Stars: The Fates of Planetary Systems. pp. 175–190.

Chapter 2

Search for planets around M dwarfs

2.1 Basic properties of M dwarfs

Not only the vast majority ($> 70\%$) of our galaxy is populated by low-mass stars, but they also contribute the most ($\sim 80\%$) to the stellar population of other elliptical galaxies (van Dokkum and Conroy, 2010). M dwarfs are low-mass and cool-stars with an effective temperature ranging between 3600 to 1600 K, and therefore their spectral energy distribution peaks in the nIR. In terms of core temperature, the latest M dwarfs (or may be the earlier L dwarfs) defines the hydrogen-burning limit: under this limit the only thermonuclear fusion may be a temporal lithium- or deuterium-burning (in some Brown-dwarfs). This situation place the mass lower edge around $0.07\mathrm{M}_{\odot}$, while the upper edge is around $0.6\mathrm{M}_{\odot}$ (Delfosse et al., 2000); the radii of M dwarfs ranges between $0.1\mathrm{R}_{\odot}$ and $0.8\mathrm{R}_{\odot}$ (Demory et al., 2009). The corresponding luminosities are in the $3 \times 10^{-4} < L/L_{\odot} < 1 \times 10^{-1}$ domain, placing these cold, small and faint stars at the end of the main-sequence, that is, at the bottom-right corner of the Hertzsprung-Russell diagram (see figure 2.1).

As the temperature gradient of stars interior goes up, as is the case of these kind of stars, the opacity increases and therefore the radiative energy transfer slow down, which is translated in a more efficient convective energy transfer. For this reason M dwarfs have a large convective zone; when the star's temperature drops more and more (enhanced temperature gradients) the radiative zone shrinks until a certain limit, where the stars become entirely convective. M dwarfs are fully convective at around $0.35\mathrm{M}_{\odot}$ (Chabrier and Baraffe, 2000).

M dwarfs surface gravity are $log(g) \approx 5$ and can reach levels of about $log(g) \approx 5.5$ for the latest ones (in cgs units and for solar metallicities), which means that their atmospheres are relatively compressed. Compared to hotter stars, the greater photosphere density and lower temperatures allow the formation of molecules in their atmospheres and even condensates (aerosoles and dust) for the late M dwarfs. Dusty clouds may be composed, among other, of $CaTiO_3, Mg_2SiO_4, NaCl, H_2O, NH_3$, while in the gaseous state the oxygen is mostly trapped in molecules like TiO, VO (the bands of these metal-oxides are the principal indicator of this spectral type) or H_2O, metal-hydrides are in the form of, for example, FeH, CaH or MgH (Allard et al., 2011). The above facts imply that M dwarfs spectra looks very different from spectra from hotter stars; the spectra of these cool-stars is crowded with absorption lines which are mostly due to molecules with some atomic features (H, K, Ca, Na, Mg, etc). For this reason, contrary to earlier spectral types, no continuum is visible in the optical spectrum of M dwarfs (Fig. 2.2). M dwarfs are so-called red dwarfs, indeed: as they are cooler stars, their energy distribution is shifted toward redder domains and, further more, molecules and dust have large opacities at optical wavelengths, making them looking even redder. As an example, the $B-V$ colour-index for M0 to M7 dwarfs is $1.35 < B-V < 2.10$;

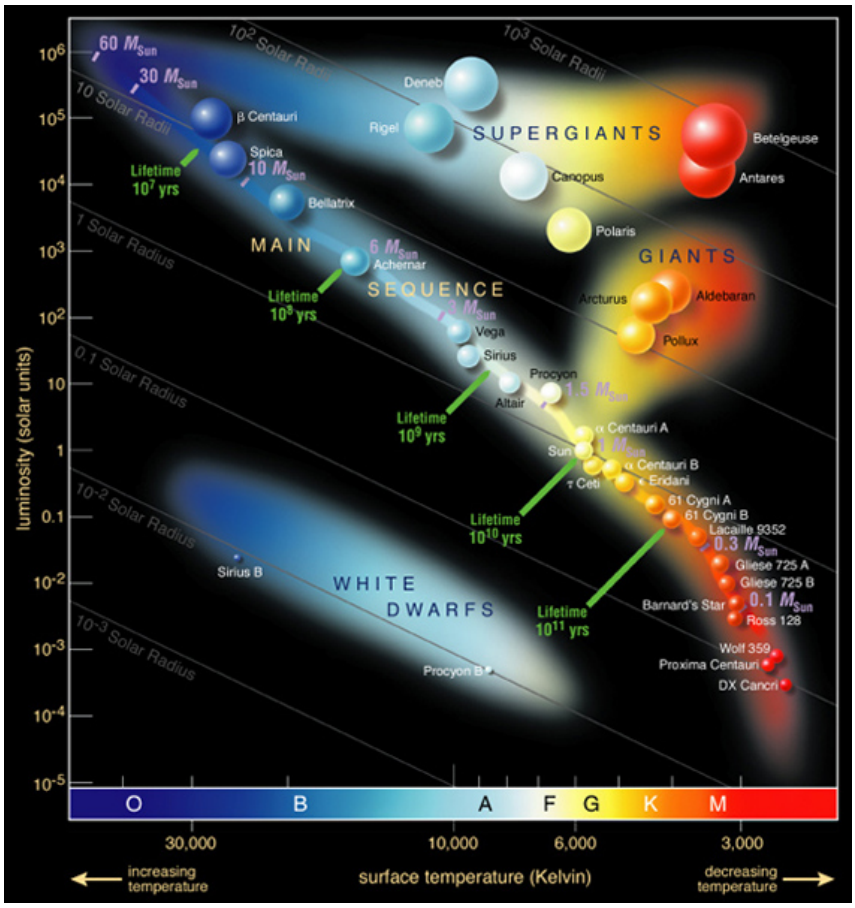

Figure 2.1: The Hertzsprung-Russell diagram showing some well known stars of different spectral types. M dwarfs are located at the bottom-right corner. Credit: http://www.eso.org/public/images/

but as the flux in the B-band is low for these stars, other colour-indices like $V - K$ are more suitable. Spectral types from M0 to M9 have $3.47 < V - K < 8.90$ (Leggett, 1992).

Stellar evolution is mass dependent in such a way that the lower the mass, slower the evolution. Low mass stars evolve so slowly (in time scales of trillion of years) that their lifetime in the main-sequence may be longer than the age of the Universe ($\sim 13.8\,Gyr$, Planck Collaboration et al., 2014). This means that at some point the only stars in the Universe will be those with the lowest mass. According to Laughlin et al. (1997) stars with masses below $0.16M_{\odot}$ remain fully convective until $\sim 6\times10^{12}\ yr$, where a radiative core takes place, although their radii grows a little (they will not become giants), their luminosity increase due to a rise in the surface temperature; however, they will not proceed to burn helium. The situation is somewhat different for stars with masses around $0.2M_{\odot}$, which substantially increase in size (up to five time their main-sequence radii), becoming red giants hotter than their main-sequence stage (Fig. 2.3).

2.1.1 M dwarfs activity

In section 1.3.3, I presented some stellar activity effects limiting the planet detection by radial velocities. Here, I start addressing stellar oscillations, which are due to pressure modes corresponding to waves travelling in the interior or stellar surface. Stellar seismic waves are generated by perturbations that occurs in stars having a convective envelope, which is the case of M dwarfs. As a mechanical wave, seismic

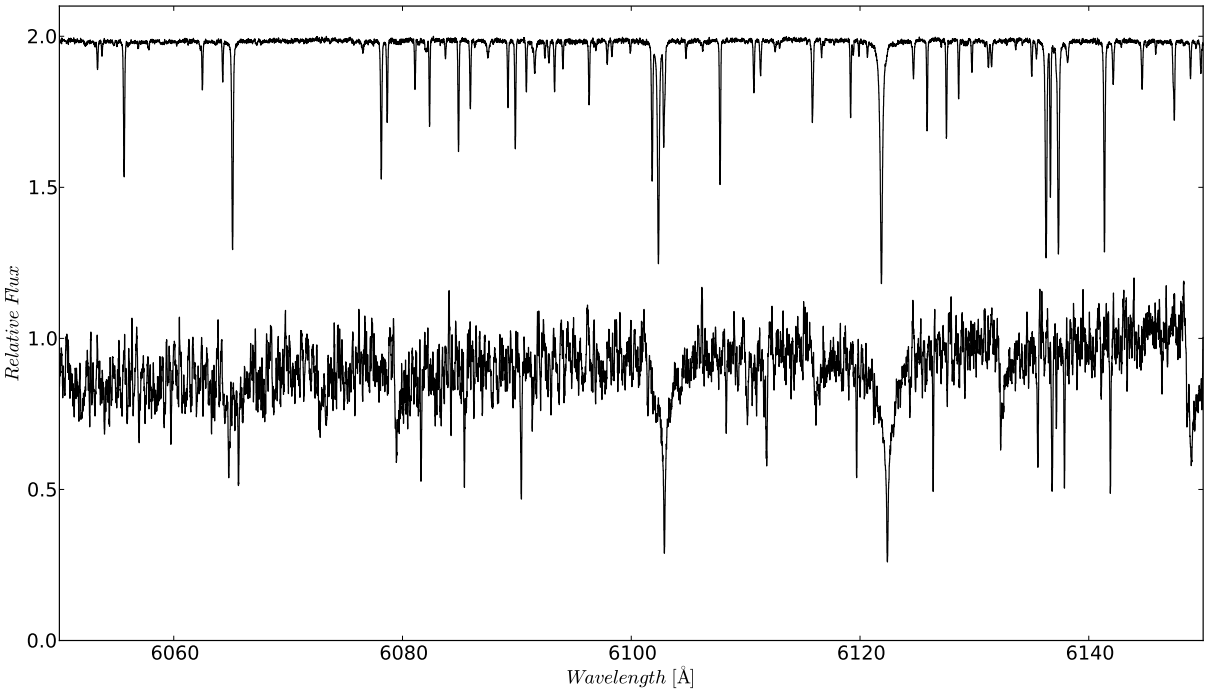

Figure 2.2: Spectra for a G8.5V star (HD 10700, top) and a M2.5V (Gl 436, bottom) star. The M dwarf spectrum shows plenty of absorption lines due to the presence of atmospheric molecules, which is translated into a lack of continuum. In the other hand, the spectrum of the G dwarf shows deep and sharp absorption lines, these are atomic lines allowing a well defined continuum.

waves propagation depends on the nature of the medium (density, temperature, plasma motions or other properties). M dwarfs are denser than more massive stars, and therefore in low-mass stars we expect higher frequencies and lower amplitudes of such oscillations (e.g. Fig. 2.4; Christensen-Dalsgaard, 2004). Accordingly, stellar ocillations are not considered as a limitation to obtain accurate RV measurements of M dwarfs.

The Sun is the only possible case where we can directly observe the effect of convection (granulation). However, for other stars it is possible to characterise the convection using complex magneto-hydrodynamic (MHD) simulations or through the shape of spectral lines, as the shape of spectral line is not only driven by the temperature, gravity, micro-turbulence or metallicity, but also by the blue-shift and red-shift due to upward and downward material. The unbalance is quantified through the *"C"* shaped line bisector (e.g. Dravins et al., 1981). Convection is the main energy transport process for M dwarfs. The granules (top part of convective cells) are smaller in comparison to earlier-spectral types ($\sim 5\,Mm$ and $\sim 0.3, Mm$ for a F3V and a M2V, respectively); with respect to granules size, the dark intergranular lanes are thinner and have a greater variation in contrast than those of G or K dwarfs. The plasma vertical velocity in convective cells is also lower for M dwarfs than latter spectral types (see Fig. 2.5 Beeck et al., 2013). This is translated in greater turnover times for low-mass stars (Kim and Demarque, 1996).

The knowlendge of magnetic activity is crucial for RV studies. The majority of M dwarfs present core emission in certain spectral lines sensitive to stellar magnetic activity, main analysed lines are the

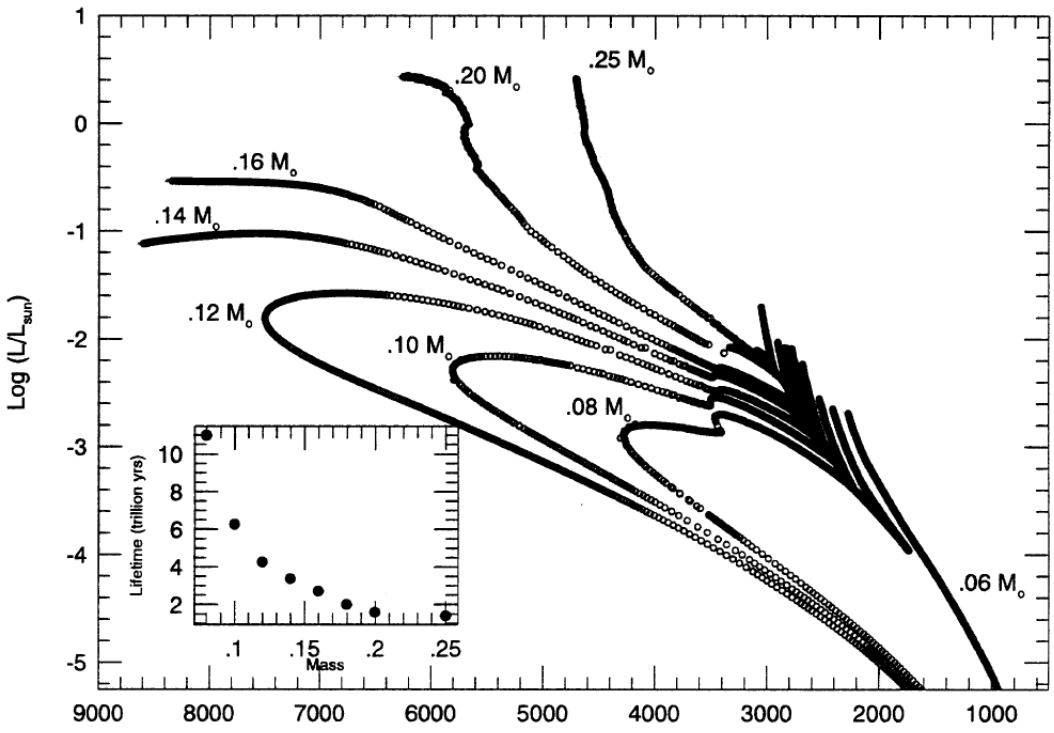

Figure 2.3: The evolution for different low mass objects in the HR diagram. From a 0.06 Brown dwarf to a 0.25 M dwarf. From Laughlin et al. (1997)

Ca II H&K resonance lines and the Balmer series. However, only some of them exhibit emission in the hydrogen series, Joy and Abt (1974) catalogued those with (resp. without) detectable hydrogen emission as dMe (resp. dM) stars. These emissions are due to mechanisms associated to strong magnetic fields heating the chromosphere. Direct magnetic field measurements for some M dwarfs show strengths which are comparable with those measured in sunspots (e.g. Morin et al., 2010). The dependency of magnetic activity with stellar rotation rates for main-sequence stars, including M dwarfs, is well known. The latter spectral type generally shows more intense chromospheric activity than more massive stars for equal rotation rates (at the same age), which is reflected by a higher flux at the wavelengths affected by magnetic activity. To allow the comparison of the level of activity between different spectral types, the flux in chromospherical emission lines need to be scaled to the bolometric flux (through a bolometric calibration). For FGK stars, Ca II H&K lines has been widely used as the main indicator when relating activity and rotation. But unfortunately, the bolometric calibration has not been done for M dwarfs. I did the first calibration of this activity-index (see Sect. 2.2). But fortunately, it is still possible to use other indicators like $H\alpha$ or X-rays (Reiners et al., 2009; Wright et al., 2011). M dwarfs present flare events more frequently than more massive stars, as shown in sudden increases in brightness and a huge emission in Ca II H&K lines, the Balmer series of hydrogen, X-rays or even gamma-rays (e.g. Hawley et al., 2014; Fender et al., 2015).

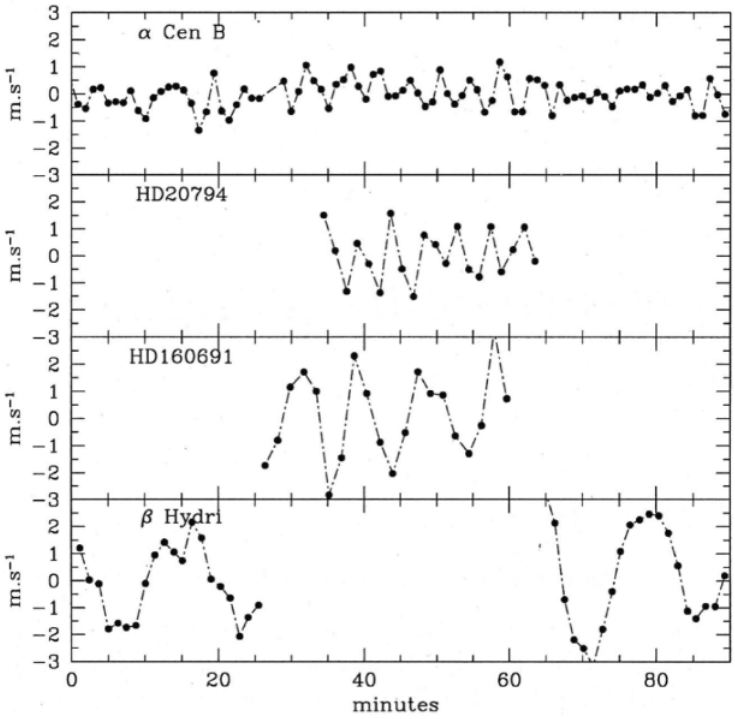

Figure 2.4: Radial velocity variations due to stellar oscillations. Different spectral types are showed from top to bottom (K1V, G8V, G5IV-V and G2IV). Note how changes the frequency of the oscillations for the different spectral types. From Mayor et al. (2003).

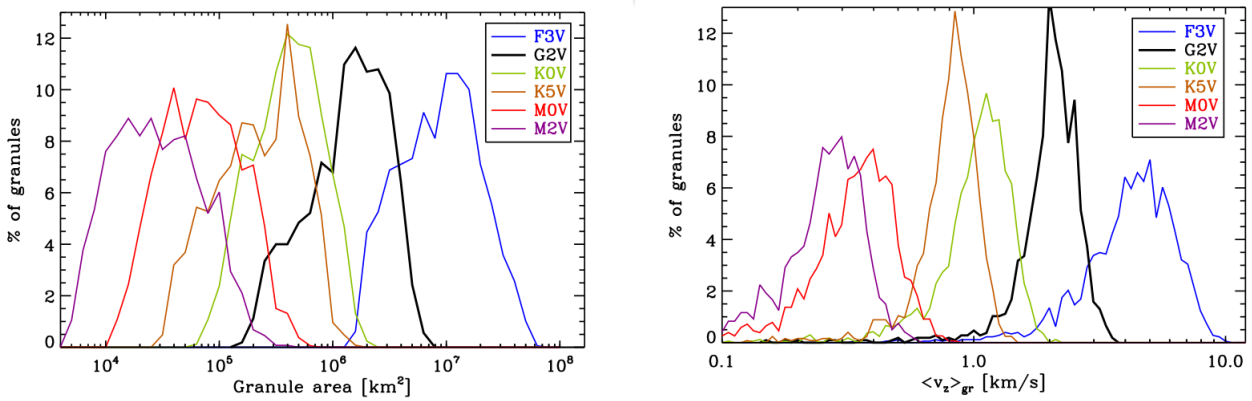

Figure 2.5: Resulting from MHD simulations, these histograms shows the granule area (left panel) and the vertical velocity averaged over the area as a function of spectral type. From Beeck et al. (2013).

2.1.2 Extra-solar planets around M dwarfs

Detectability

Why is it interesting and encouraging to search for planets orbiting M dwarfs? Firstly, because it is easier to detect low-mass planets. I described the radial velocity method in section 1.3.1, where I quoted

that the centre of mass position depends on the involved masses in the system. Fixing the planetary mass in a star-planet system, the centre of mass is further from the centre of the stars as lower is its mass, implying a greater orbit of the host star and therefore, the RV semi-amplitude is larger – Eq. (1.8). This means that for a given radial velocity precision and telescope time, it is easier to detect low-mass planets orbiting M dwarfs than solar-type stars. Furthermore, regarding the transit method and for a given photometric precision, as the transit depth scales with the planet to star surface ratio, it is easier to detected a small planet (for a fixed planetary size) orbiting M dwarfs.

Figure 2.6 shows the expected semi-amplitude (K) for a system with a super-Earth ($5M_\oplus$) or a Earth-mass ($1M_\oplus$) planet as a function of the parent star mass. From the figure we note that if we consider an orbit producing a $K \sim 1\ m\,s^{-1}$, with current instrumentation (like *HARPS*), a super-Earth in a 1 year period (resp. 50 days) is detectable around a M dwarf of $0.35M_\odot$ (resp. a K dwarf of $0.8M_\odot$). The situation is more critical for a Earth-like planets, where only short periods (P<10 d) are detectable around M dwarfs. With the advent of *ESPRESSO*, detection of a Earth-like planet orbiting a Sun-like star in a one year orbit will be possible, although this remains challenging.

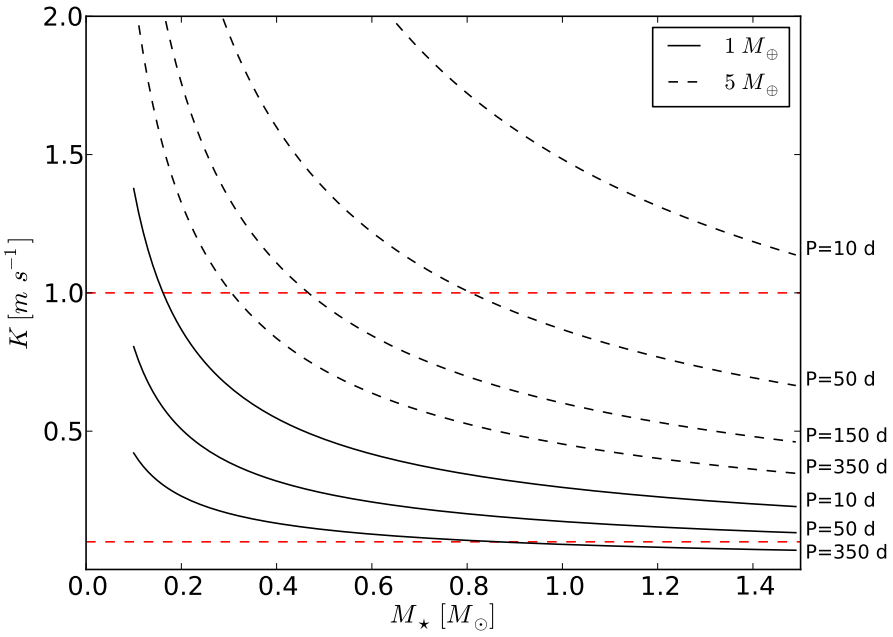

Figure 2.6: Expected semi-amplitudes (K) as a function of stellar masses ($M_\odot$) and for different periods ranging from 10 to 350 days. For this exercise, I consider 100% edge-on and circular orbits for all curves. Solid curves represent a $1M_\oplus$ planetary mass, while dashed curves depict M_{pl}=$5M_\oplus$. Red horizontal lines are instrumental detection limits (without accounting for the number of data, their Doppler uncertainty or stellar jitter) for *HARPS* ($\sim 1\ m\,s^{-1}$) and *ESPRESSO* ($\sim 0.1\ m\,s^{-1}$). The curves are labeled with different orbital periods, in day units.

Habitability

Considering current radial velocities precision, another exciting fact justifying the search for planets around low-mass stars come from Astrobiology. There are several factors involved in the development of life as it is known on Earth. One conditioning factor is the presence of liquid water. Although such

condition is not sufficient as, for example, the presence of a planetary magnetic field (to protect its atmosphere from stellar wind) is also supposed to be a key parameter. With respect to the condition of liquid water existence, the next question arises: What kind of planets can maintain liquid water on their surface? To answer this question, the concept of the *habitable zone* is defined.

The habitable zone is the range of distances from the pattern star where the planet equilibrium temperature allows liquid water to flow on its surface. Accounting for the greenhouse effect of the planet (which depends on the atmosphere composition), the needed equilibrium temperature allowing the water to be liquid ranges between 175 K to 270 K. The equilibrium temperature depends on the nature of the planetary atmosphere, where the planetary mass plays an important role. Two necessary conditions constraining the habitability of a planet are if its orbit is within the habitable zone and if its mass ranges between $0.5M_\oplus$ and $10M_\oplus$. For a planetary mass below $0.5M_\oplus$ the expected gravity is too low to avoid escape processes and retain an atmosphere where liquid water is sustainable; while a planetary mass above $10M_\oplus$ is supposed to have a too dense atmosphere (composed mainly of hydrogen and helium) with a surface pressure too high to allow liquid water (Selsis et al., 2007).

The star luminosity depends on its mass, and as low-mass stars are fainter, their habitable zone is closer (Fig. 2.7). The effort in telescope time to detect an extrasolar planet in the habitable zone is therefore lower for M dwarfs, because such a planet has a typical orbital period of about 50 days compared to a 1 year orbit for a Sun-like star. Thus, an exo-Earth in the habitable zone produces a much larger RV wobble (4× to 8× for a M4 and M6 respectively) compared to the same planet orbiting a Sun-like star.

True Goldilocks planets are those with a mass ranging 0.5-$10M_\oplus$, orbiting in the habitable zone and transiting their host star. Nowadays, it is feasible to detect and produce a sample of these kind of planets orbiting M dwarfs (at least super-Earths), and once discovered, we want to derive their bulk density (determining the fraction of rocky/ocean/ice planets, at least for the brightest *Kepler* candidates) and characterise their atmospheres (with future facilities like JWST or ELT). It is particularly important to characterise the atmospheres of Goldilocks planets because our experience on the atmosphere of habitable planets is limited (for the time being) to the Solar system. The knowledge about the complex processes defining the nature and evolution of these atmospheres is mainly based on models and missions to planets of the Solar system (e.g. see Forget and Leconte, 2014), and of course, it will be an opportunity to verify (and elaborate, if needed) that our models are compatible with the atmopshere of Goldilocks planets.

Formation and statistics

Giant or terrestrial planets are formed by the accretion of material from a protoplanetary disk by planetesimals (core-accretion), although giant planets formation may also be explained by the collapse of self-graviting clumps in the protoplanetary disk (e.g. Roberge and Kamp, 2011, and references therein). M dwarfs protoplanetary disks are less massive than the ones of more massive stars, implying that the mass of planets are correlated with the mass of host stars; hence, the formation of massive planets is not expected to be frequent around very low-mass stars (e.g. Ida and Lin, 2005; Kennedy and Kenyon, 2008). This statement is statistically true as very few Jupiter-like planets have been detected around M dwarfs (e.g. Delfosse et al., 1998; Johnson et al., 2007), in comparison to Neptune-like or super-Earth planets, which are more abundant for this kind of stars (Bonfils et al., 2013). Indeed, Bonfils et al. (2013) found that for $P < 100$ d only $2\%^{+3}_{-2}$ of M dwarfs are orbited by giant planets, while for super-Earths this frequency rises to $88\%^{+30}_{-15}$.

Around 100 exoplanets have been detected around M dwarfs. Radial velocities establish that $88\%^{+55}_{-19}$

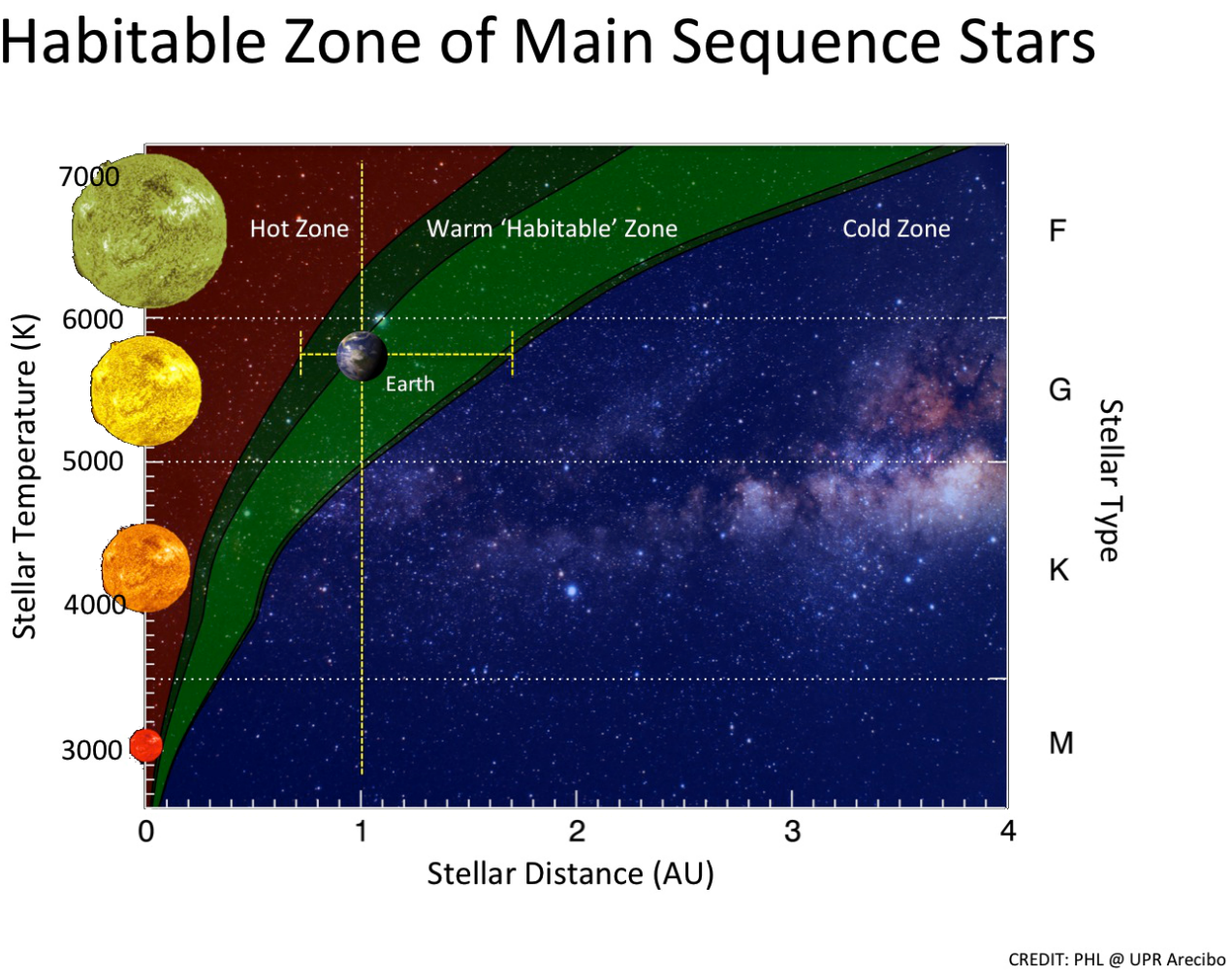

Figure 2.7: The habitable zone as a function of stellar mass. From http://phl.upr.edu/library/media/thehabitablezone

of M dwarfs have planets with an orbital period under 100 days. Transits establish that $90\%^{+4}_{-3}$ of stars with temperatures below 4000 K harbour super-Earths- or Earth-size planets with periods below 50 days. From the *Kepler* sample $51\%^{+6}_{-5}$ of stars with $T_{eff} < 4000$ K have Earth-size planets (0.5-1.4R$_\oplus$), while the occurrence rate decreases for cooler stars when entering in the super-Earth size domain (planets with radii between 1.4-4R$_\oplus$ have an occurrence of $61\%^{+8}_{-6}$ for stars with $3723 < T_{eff}[K] < 4000$, and for stars with $3122 < T_{eff}[K] < 3723$ the occurrence decreases to $19\%^{+7}_{-5}$).

The first estimation of the occurrence of planets orbiting within the habitable zone was done for M dwarfs. Bonfils et al. (2013) estimated from radial velocities that the frequency of planets with masses between $1 < M/M_\oplus < 10$ orbiting the habitable zone of M dwarfs is $41\%^{+54}_{-13}$; where they used the recent Venus and early Mars criteria to define the edges of the habitable zone (Selsis et al., 2007). From *Kepler* transit data, Dressing and Charbonneau (2013) obtained that $15\%^{+13}_{-6}$ (resp. $4\%^{+6}_{-2}$) of stars with $T_{eff} < 4000$ K have planets between 0.5-1.4R$_\oplus$ (resp. 1.4-4R$_\oplus$) orbiting in the habitable zone; they derived the habitable zone from Kasting et al. (1993). From the same *Kepler* transit data, Kopparapu

(2013) obtained $48\%^{+12}_{-24}$ (resp. $61\%^{+7}_{-15}$) by using a moist/max greenhouse effect (resp. recent Venus and early Mars) to derive the habitable zone edges (Kopparapu et al., 2013).

2.2 This thesis

The understanding and characterisation of chromospheric activity is of great importance in the detection of low-mass planets, because magnetic activity of late-type stars is actually the principal limit of such detections. One of the best methods to characterise stellar activity is the R'_{HK}-index (a true measurement of activity through the Ca II H&K lines). One goal of this thesis is to properly calibrate the R'_{HK}-index for M dwarfs, which opens the possibility to compare this activity index for low-mass stars of different spectral types, allowing to infer the dependence of magnetic activity as a function of stellar properties. I will also establish for the first time the R'_{HK} vs. P_{rot} relationship for M dwarfs. It is crucial to determine at which periods RV variations are due to stellar activity.

On the other hand, it had been demonstrated that the extraction of radial velocities by the traditional cross-correlation function (CCF) is not optimised, at least in the case of M dwarfs. The need to optimise the extraction of RV from M dwarf spectra is justified to push RV precision to lower limits, enabling the detection of low-mass planets which are not accessible by the traditional cross-correlation function (CCF).

To achieve these objectives, I benefit of the *HARPS* spectral database (is really a benefit because the hunt for exoplanets produces a huge amount of high quality data). Among others, the Grenoble exoplanet team is world leading in the detection of planets orbiting M dwarfs, therefore, a direct access to M dwarf data is warranted. I also used data of latter spectral type stars, GK dwarfs data were provided by the Geneva exoplanet/instrumentation team thanks to a collaboration between Geneva and Grenoble. Furthermore, I feel very lucky because the feedback I received from Geneva about the *HARPS* reduced data or the procedure of the CCF to extract RV from spectra.

From the stellar activity work, I'm the first author of a forthcoming paper which is ready and will be promptly submitted. This paper describes and gives the calibration of the R'_{HK}-index for the latter spectral type stars. But most interesting, using the *HARPS* M dwarf database, it shows the relationships between this activity index and stellar rotation, masses and activity variability. This part of the work is described section 3.

I implemented the first version of an optimised pipeline to extract RVs which is ready and usable. I published a paper about the detection of three (or maybe four) new planets orbiting M dwarfs. These planets are in the range of Neptune- and super-Earth-masses, where a RV precision near the m/s is needed, and therefore, it shows that the pipeline works well – of course, after many previous tests. A future paper will describe the algorithm and performances of this new pipeline. I describe this work in chapter 4.

This thesis triggered many collaborations. Concretely with Christophe Lovis (Geneva) in the stellar activity work; in a publication led by Audrey Lanotte (Liège) about a deep analysis of Gl 436, where I calculated the RVs; with Etienne Artigau (Montreal) in the study of extract RVs when telluric features are corrected (SPIE paper), where I was in charge of testing the applied corrections; with Alexandre Santerne (Porto) about the K2 follow-up, where I compute RVs of KOIs observed with *SOPHIE* and *HARPS*-N. In addition, I joined the *SOPHIE* and *HARPS* consortiums as an observer. During my thesis (3 years), I travelled many times to the Observatoire de Haute-Provence and to La Silla Observatory, corresponding to 45 nights observing with these two spectrographs.

References

Allard, F., Homeier, D., Freytag, B., 2011. Model Atmospheres From Very Low Mass Stars to Brown Dwarfs. In: Johns-Krull, C., Browning, M. K., West, A. A. (Eds.), 16th Cambridge Workshop on Cool Stars, Stellar Systems, and the Sun. Vol. 448 of Astronomical Society of the Pacific Conference Series. p. 91.

Beeck, B., Cameron, R. H., Reiners, A., Schüssler, M., 2013. Three-dimensional simulations of near-surface convection in main-sequence stars. II. Properties of granulation and spectral lines. A&A 558, A49, 1308.4873.

Bonfils, X., Delfosse, X., Udry, S., Forveille, T., Mayor, M., Perrier, C., Bouchy, F., Gillon, M., Lovis, C., Pepe, F., Queloz, D., Santos, N. C., Ségransan, D., Bertaux, J.-L., 2013. The HARPS search for southern extra-solar planets. XXXI. The M-dwarf sample. A&A 549, A109, 1111.5019.

Chabrier, G., Baraffe, I., 2000. Theory of Low-Mass Stars and Substellar Objects. ARA&A 38, 337–377, astro-ph/0006383.

Christensen-Dalsgaard, J., 2004. Physics of solar-like oscillations. Sol. Phys. 220, 137–168.

Delfosse, X., Forveille, T., Mayor, M., Perrier, C., Naef, D., Queloz, D., 1998. The closest extrasolar planet. A giant planet around the M4 dwarf GL 876. A&A 338, L67–L70, astro-ph/9808026.

Delfosse, X., Forveille, T., Ségransan, D., Beuzit, J.-L., Udry, S., Perrier, C., Mayor, M., 2000. Accurate masses of very low mass stars. IV. Improved mass-luminosity relations. A&A 364, 217–224, astro-ph/0010586.

Demory, B.-O., Ségransan, D., Forveille, T., Queloz, D., Beuzit, J.-L., Delfosse, X., di Folco, E., Kervella, P., Le Bouquin, J.-B., Perrier, C., Benisty, M., Duvert, G., Hofmann, K.-H., Lopez, B., Petrov, R., 2009. Mass-radius relation of low and very low-mass stars revisited with the VLTI. A&A 505, 205–215, 0906.0602.

Dravins, D., Lindegren, L., Nordlund, A., 1981. Solar granulation - Influence of convection on spectral line asymmetries and wavelength shifts. A&A 96, 345–364.

Dressing, C. D., Charbonneau, D., 2013. The Occurrence Rate of Small Planets around Small Stars. ApJ 767, 95, 1302.1647.

Fender, R. P., Anderson, G. E., Osten, R., Staley, T., Rumsey, C., Grainge, K., Saunders, R. D. E., 2015. A prompt radio transient associated with a gamma-ray superflare from the young M dwarf binary DG CVn. MNRAS 446, L66–L70, 1410.1545.

Forget, F., Leconte, J., 2014. Possible climates on terrestrial exoplanets. Royal Society of London Philosophical Transactions Series A 372, 30084, 1311.3101.

Hawley, S. L., Davenport, J. R. A., Kowalski, A. F., Wisniewski, J. P., Hebb, L., Deitrick, R., Hilton, E. J., 2014. Kepler Flares. I. Active and Inactive M Dwarfs. ApJ 797, 121, 1410.7779.

Ida, S., Lin, D. N. C., 2005. Toward a Deterministic Model of Planetary Formation. III. Mass Distribution of Short-Period Planets around Stars of Various Masses. ApJ 626, 1045–1060, astro-ph/0502566.

Johnson, J. A., Butler, R. P., Marcy, G. W., Fischer, D. A., Vogt, S. S., Wright, J. T., Peek, K. M. G., 2007. A New Planet around an M Dwarf: Revealing a Correlation between Exoplanets and Stellar Mass. ApJ 670, 833–840, 0707.2409.

Joy, A. H., Abt, H. A., 1974. Spectral Types of M Dwarf Stars. ApJS 28, 1.

Kasting, J. F., Whitmire, D. P., Reynolds, R. T., 1993. Habitable Zones around Main Sequence Stars. Icarus101, 108–128.

Kennedy, G. M., Kenyon, S. J., 2008. Planet Formation around Stars of Various Masses: The Snow Line and the Frequency of Giant Planets. ApJ 673, 502–512, 0710.1065.

Kim, Y.-C., Demarque, P., 1996. The Theoretical Calculation of the Rossby Number and the "Nonlocal" Convective Overturn Time for Pre-Main-Sequence and Early Post-Main-Sequence Stars. ApJ 457, 340.

Kopparapu, R. K., 2013. A Revised Estimate of the Occurrence Rate of Terrestrial Planets in the Habitable Zones around Kepler M-dwarfs. ApJ 767, L8, 1303.2649.

Kopparapu, R. K., Ramirez, R., Kasting, J. F., Eymet, V., Robinson, T. D., Mahadevan, S., Terrien, R. C., Domagal-Goldman, S., Meadows, V., Deshpande, R., 2013. Habitable Zones around Main-sequence Stars: New Estimates. ApJ 765, 131, 1301.6674.

Kopparapu, R. K., Ramirez, R. M., SchottelKotte, J., Kasting, J. F., Domagal-Goldman, S., Eymet, V., 2014. Habitable Zones around Main-sequence Stars: Dependence on Planetary Mass. ApJ 787, L29, 1404.5292.

Laughlin, G., Bodenheimer, P., Adams, F. C., 1997. The End of the Main Sequence. ApJ 482, 420–432.

Leggett, S. K., 1992. Infrared colors of low-mass stars. ApJS 82, 351–394.

Lunine, J. I., Fischer, D., Hammel, H., Henning, T., Hillenbrand, L., Kasting, J., Laughlin, G., Macintosh, B., Marley, M., Melnick, G., Monet, D., Noecker, C., Peale, S., Quirrenbach, A., Seager, S., Winn, J., 2008. Worlds Beyond: A Strategy for the Detection and Characterization of Exoplanets. ArXiv e-prints 0808.2754.

Mayor, M., Pepe, F., Queloz, D., Bouchy, F., Rupprecht, G., Lo Curto, G., Avila, G., Benz, W., Bertaux, J.-L., Bonfils, X., Dall, T., Dekker, H., Delabre, B., Eckert, W., Fleury, M., Gilliotte, A., Gojak, D., Guzman, J. C., Kohler, D., Lizon, J.-L., Longinotti, A., Lovis, C., Megevand, D., Pasquini, L., Reyes, J., Sivan, J.-P., Sosnowska, D., Soto, R., Udry, S., van Kesteren, A., Weber, L., Weilenmann, U., 2003. Setting New Standards with HARPS. The Messenger 114, 20–24.

Morin, J., Donati, J.-F., Petit, P., Delfosse, X., Forveille, T., Jardine, M. M., 2010. Large-scale magnetic topologies of late M dwarfs. MNRAS 407, 2269–2286, 1005.5552.

Planck Collaboration, Ade, P. A. R., Aghanim, N., Alves, M. I. R., Armitage-Caplan, C., Arnaud, M., Ashdown, M., Atrio-Barandela, F., Aumont, J., Aussel, H., et al., 2014. Planck 2013 results. I. Overview of products and scientific results. A&A 571, A1, 1303.5062.

Reiners, A., Basri, G., Browning, M., 2009. Evidence for Magnetic Flux Saturation in Rapidly Rotating M Stars. ApJ 692, 538–545, 0810.5139.

Roberge, A., Kamp, I., 2011. Protoplanetary and Debris Disks. pp. 269–295.

Selsis, F., Kasting, J. F., Levrard, B., Paillet, J., Ribas, I., Delfosse, X., 2007. Habitable planets around the star Gliese 581? A&A 476, 1373–1387, 0710.5294.

van Dokkum, P. G., Conroy, C., 2010. A substantial population of low-mass stars in luminous elliptical galaxies. Nature 468, 940–942, 1009.5992.

Vidotto, A. A., Jardine, M., Morin, J., Donati, J.-F., Lang, P., Russell, A. J. B., 2013. Effects of M dwarf magnetic fields on potentially habitable planets. A&A 557, A67, 1306.4789.

Wright, N. J., Drake, J. J., Mamajek, E. E., Henry, G. W., 2011. The Stellar-activity-Rotation Relationship and the Evolution of Stellar Dynamos. ApJ 743, 48, 1109.4634.

Chapter 3

The R'_{HK}-index in M dwarfs

Almost all the knowledge we have about stellar properties has its starting point on the Sun. Of course, this is the case of the study of stellar magnetic fields. In the early XX^{th} century much interest aroused with several discoveries related to the solar magnetism, such as the measurement of the magnetic field strength in sunspots, the movement in latitude of sunspots or they polarity, and the solar cycle (∼1850). At the same time, the idea of a dynamo process that generates such magnetism quickly arise.

3.1 Dynamo processes

Stellar dynamo processes transform the kinematic energy of the conducting plasma into magnetic energy. In 1919[1] the action of a dynamo was proposed to generate solar magnetic fields. The role of differential rotation, and then of the toroidal and poloidal decomposition, was introduced to describe the magnetic field (firstly for the Earth's magnetic filed, Elsasser, 1946). Such decomposition supports the active role of differential rotation since it is shown that the toroidal field could be enhanced by differential rotation with latitude (the Ω-effect, which transforms the poloidal into a toroidal field). But how is regenerated the poloidal component? Parker (1955) proposed that the Coriolis force can regenerate the poloidal field as it twists the magnetic field (helical component) under the presence of a stratified and rotating turbulent medium, then called the α-effect. Latter, seismology revealed the existence of a layer with strong shears, located between the convective and radiative zones. This thin layer, called the tachocline, was rapidly incorporated into magnetic models as the place where the toroidal field are magnified (e.g. Charbonneau and MacGregor, 1997). The – hydromagnetic self-sustained – $\alpha\Omega$-dynamo model (Fig. 3.1), involving the tachocline and magnetic diffusive coefficients due to turbulence, explains the displacement of sunspots (in latitude), which is cyclic and results in the stellar – long-term – magnetic cycle. This cycle corresponds to the 22-yr solar cycle, and analogue cycles had been discovered in other stars (e.g. Baliunas et al., 1995; Lovis et al., 2011).

The $\alpha\Omega$-dynamo process explains observed magnetic fields under the presence of stellar (differential) rotation and a convective envelope surrounding a radiative envelope (partly convective stars): as a result, a strong correlation between the strength of magnetic fields and stellar rotation is expected. This is the case for a wide range of stellar masses. However, under $0.35 M_\odot$ the radiative zone vanishes, yielding fully convective stars (this is also the case for T-tauri stars). Hence, it is expected that these stars generate magnetic fields without an Ω-effect. Magnetic fields produced at the scale of plasma motions were proposed by Durney et al. (1993), where stellar rotation is not essential. Then, it was proposed that the α-effect could be responsible for both the toroidal and poloidal magnetic components (the α^2-dynamo) of fully convective stars. Finally, when differential rotation is weak, an $\alpha^2\Omega$-dynamo may explains the presence of large scale magnetic fields. It suggests that both the α-effect and differential

[1] Larmor, J. Report of the British Association for the Advancement of Science (87th Meeting, 1919).

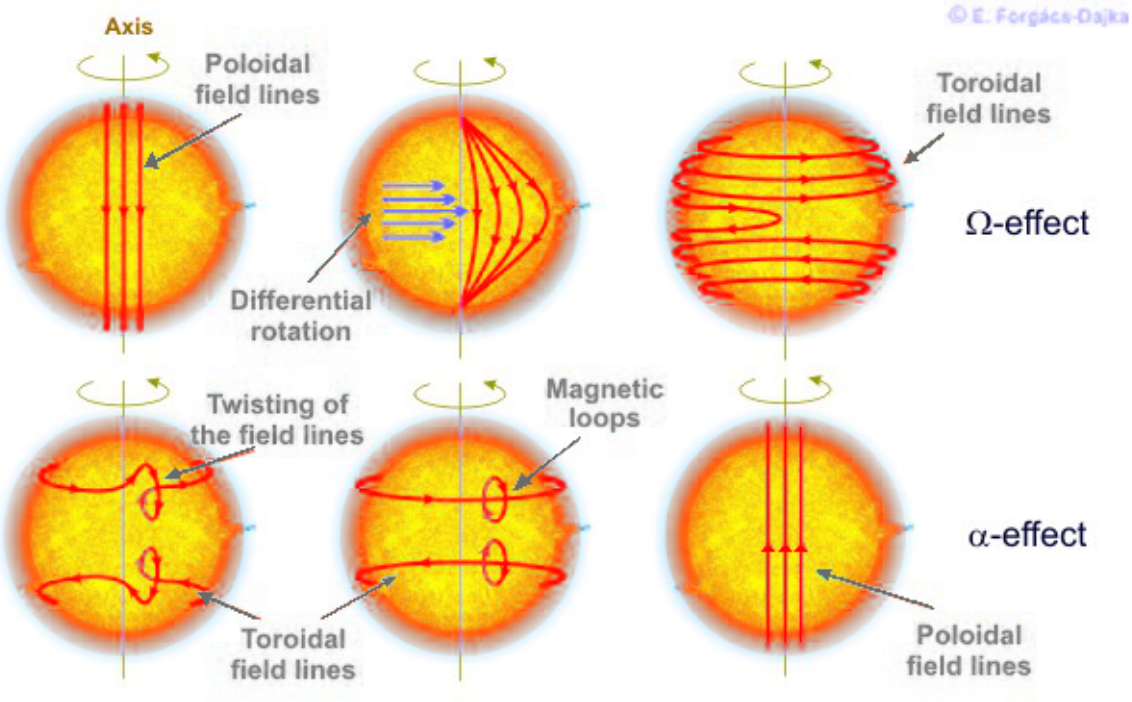

Figure 3.1: Schema of the Ω- and α-process transforming a poloidal field into a toroidal one, and vice versa. Credits: http://www.konkoly.hu/solstart/stellar_activity.html

rotation generates the toroidal magnetic field.

On the section 6 of the paper "Magnetic activity on the HARPS M dwarfs sample" I give a summary of the state of the art of the knowledge of M dwarf magnetic fields.

3.2 Stellar activity diagnostics

Characterising the magnetic activity of stars different than the Sun is not a trivial task, as we rarely resolve them. Several tracers are used to trace the stellar magnetic activity. The more direct tracer comes from the Zeeman effect, allowing a direct measurements of magnetic fields in the stellar photosphere. This consists in measuring the splitting of spectral lines that occurs under the presence of magnetic fields, where the amount of splitting depends on the modulus of the magnetic field. From the same basis, another approach is to observe the different polarisation components of the Zeeman-split.

Stellar magnetic activity also affects outer layers. Coronal activity is traced at X-ray wavelengths, and M dwarfs are in general more luminous at those wavelength than G dwarfs. For such a comparison, it is necessary to compute the ratio between the X-ray luminosity and the bolometric luminosity (L_X/L_{bol}), and once done, we have a true measure of X-ray activity. For M dwarfs, a correlation between L_X/L_{bol} and rotation has been observed (e.g. Pizzolato et al., 2003), showing also a mass dependence (Kiraga and Stepien, 2007). This confirms the magnetic activity–rotation dependence in fully convective stars. Through this activity indicator, it is also shown that at a certain rotation period ($\sim 10\ d$) a saturation level is reached (Wright et al., 2011).

Now we turn to the chromospheric activity. Between the photosphere and the corona is situated the chromosphere, a zone where the temperature increases up to the transition region, at which the corona

starts (and the temperature increases much more; e.g. Hawley and Fisher, 1992; Mauas and Falchi, 1994). The presence of enhanced magnetic fields may provoke departures from the radiative equilibrium and heat the chromosphere. Several indicators are used to infer magnetic activity in this region, among them the Ca II H&K resonance lines and the $H\alpha$ (or lines from the Balmer series) line are the most used. While the former is a good diagnostic for chromospheric plages, the latter traces filaments that appear as dark features in $H\alpha$ (e.g. Wilson, 1978; Baliunas et al., 1995; Meunier and Delfosse, 2011). Modulation of these indicators reveals the stellar rotation period. In addition, Gomes da Silva et al. (2011) performed an activity analysis in M dwarfs using several chromospheric activity indicators (Ca II H&K, $H\alpha$, He I D3, and Na I D1D2 lines). As is the case for X-ray activity, $H\alpha$ has also shown evidence of saturation at a certain level of rotation rates (Delfosse et al., 1998; Reiners et al., 2009). Last but not least, the Ca II IRT-triplet is a good activity tracer in the near-infrared.

Finally, as I quoted in section 2.1.1, the bisector is used to trace granules. The stellar convection is inhibited under the presence of strong magnetic fields, which is reflected by the variations in the line shapes and detectable through variations in the bisector. Spots on the stellar surface (also linked to strong magnetic fields) are detectable by photometry variations, unveiling the stellar rotation (e.g. Irwin et al., 2011).

3.3 Stellar activity and planets detection

In the context of planet detection, stellar activity introduces "noise" on data, affecting almost all detection methods. As I mentioned in section 1.3.3, such stellar noise is seen as a RV *jitter*, not only because the dispersion it introduces on RV measurements, but more worrisome, such dispersion may variate periodically, In that case, the stellar activity mimics RV variations of genuine planetary companions (e.g. Queloz et al., 2001; Bonfils et al., 2007; Forveille et al., 2009; Robertson et al., 2014).

Strong local magnetic fields inhibit the convection and produce bright plages or dark photospheric spots on the star's surface. The brightness of a magnetically active zone differs from the rest of the photosphere due to a temperature contrast. Such temperature contrast is greater for spots than plages. Because the star rotates, a spot (or plage) shows different RVs as it crosses the stellar disc, breaking the balance between red- and blue-shifted light (fig. 3.2 second row). This photospheric effect deforms line shapes, affecting the calculation of their centroids, which is translated in a wrong extraction of the RV (this photospheric effect is grater for spots than plages). Figure 3.2 shows the spurious effects on RV by the presence of a spot. The other effect producing RV variations come from the inhibition of the convection. The raising material (hotter than the downward plasma in lanes) in convection cells produces an overall blueshift when averaging over several granules. Similarly to the photospheric effect described above, the convection inhibition affects the line shapes producing differences in the determination of the line centroids. A close monitoring of activity indices (like the described above) is necessary to reject false detection. Any RV signal with a periodicity close to the stellar rotation period (or any of its harmonics, Boisse et al., 2011) warns us about stellar activity as the nature of the RV variations. Modulation of activity indices or photometric follow-up may be used to determine such stellar rotation periods.

3.4 Calibrating the R'_{HK}-index (paper)

The emission in the Ca II H&K resonance lines is quantified by the S-index, which is the ratio between the the integrated flux in triangular pass-bands centred on both Ca lines (H&K bands) and the integrated flux

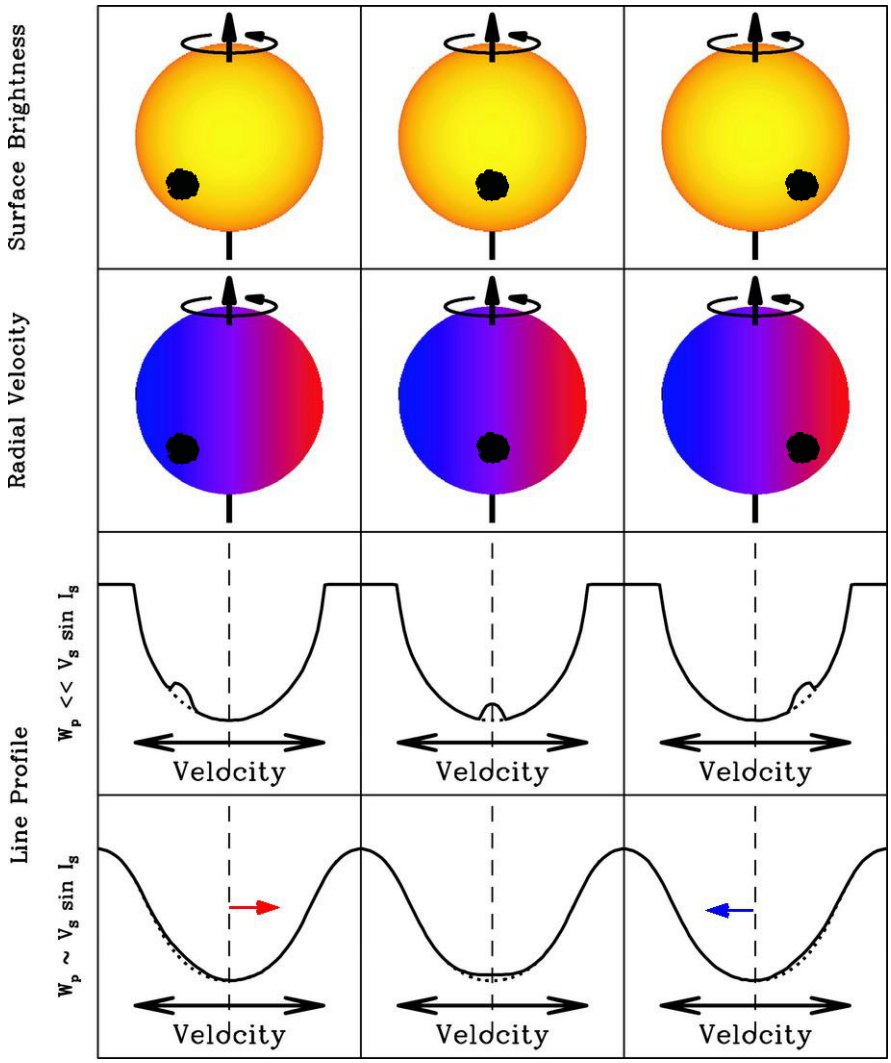

Figure 3.2: Sketch showing the impact of stellar spots on line shapes, which affects the radial velocity extraction.

in adjacent rectangular pass-bands (V&R bands, an estimation of the continuum, or pseudo-continuum in the case of M dwarfs). However, this continuum varies with spectral type, precluding any relationship between the S-index and properties of stars of different spectral type. To settle this point and fully benefit of the potential of the S-index, one needs to scale the S-index with respect the bolometric flux. This is the idea behind the R_{HK}-index, which is the ratio between the flux in the core of Ca II H&K lines and the bolometric flux. The bolometric flux is derived through the integrated flux in the visual band and the bolometric correction. But to be even more precise in measuring the stellar activity through this tracer, one needs to subtract the photospheric component (photospheric factor), resulting in the so-called R'_{HK}-index (Linsky and Ayres, 1978; Middelkoop, 1982; Rutten, 1984). To scale the S-index to the bolometric luminosity, a wavelength dependent bolometric factor is derived. Such factor was already obtained for FGK dwarfs (we say that the R'_{HK}-index is calibrated for those stars). Thanks to this calibration, a relationship between R'_{HK} and stellar rotation was derived, showing the correlation between magnetic activity and rotation rates (e.g. Noyes et al., 1984).

However, neither the bolometric factor nor the photospheric factor have been properly calibrated for

M dwarfs, making impossible a suitable analysis between R'_{HK} and M dwarfs properties. Calibrating these factors is the goal of the following paper, and once done, I analyses the R'_{HK}-index with respect to stellar properties such as rotation or mass. In the context of the search for exoplanets around low-mass stars, such a calibration will also open the possibility to analyse the relation between the R'_{HK}-index and the dispersion excess in RV (when planetary signals, if there is, are previously removed).

Astronomy & Astrophysics manuscript no. Rhk˙v1-1
February 12, 2015

Magnetic activity on the HARPS M dwarfs sample⋆

Calibrating R'_{HK} for low-mass stars and a rotation-activity relation

N. Astudillo-Defru[1,2], X. Delfosse[1,2], X. Bonfils[1,2], T. Forveille[1,2], C. Lovis[3], J. Rameau[1,2,4]

[1] Univ. Grenoble Alpes, IPAG, F-38000 Grenoble, France
[2] CNRS, IPAG, F-38000 Grenoble, France
[3] Observatoire de Genève, Université de Genève, 51 ch. des Maillettes, 1290 Sauverny, Switzerland
[4] Département de Physique, Université de Montréal, C.P. 6128 Succ. Centre-Ville, Montréal, QC H3C 3J7, Canada

ABSTRACT

Context. A flux excess in Ca II H&K lines is produced in the chromosphere due to enhanced magnetic fields. Since the Mount Wilson program, these spectral lines have been widely used to trace stellar magnetic activity and to link it to age or stellar rotation period. Moreover, monitoring stellar activity is essential in the search for extra-solar planets to reject false-positives. Much work have been done to characterise Ca II H&K flux for FGK dwarfs in using the R'_{HK}-index which, expresses the emission relative to bolometric flux. However M dwarfs, the most numerous stars of the Galaxy, were not included in this analysis, R'_{HK} being not defined for M dwarfs to date.
Aims. We aim to characterise the magnetic activity in low-mass stars using the R'_{HK}-index. A relationship between this activity index and stellar rotation is specially relevant to warn for false-positives, because it can be used as a proxy when the rotation period is unknown for a given star.
Methods. We calibrated the bolometric and photospheric factors for M dwarfs to properly transform the S-index into the R'_{HK}. We monitored magnetic activity through the Ca II H&K emission lines in the HARPS M dwarf sample.
Results. We determine the bolometric and photospheric factors which allows to derive reliable R'_{HK} values for M dwarfs. We provide a R'_{HK}-rotation relationship which, analogously to L_X/L_{bol}, shows saturated and unsaturated activity regimes for rotation periods under or above ten days respectively. The unsaturated regime shows a decrease in magnetic activity as rotation period increase, as expected. We find an activity-mass dependence where R'_{HK} decrease for masses from 0.6M$_\odot$ to 0.35M⊙, under the limit of fully-convective stars and above 0.6M$_\odot$ the R'_{HK} defines a constant basal activity. The activity short-term variability is larger for M dwarfs above the lower envelope defined in the activity-mass relationship. The most active stars are those that have the greatest R'_{HK} variability, as is the case for earlier spectral types.

Key words. Stars: activity – Stars: late-type – Stars : planetary systems – Techniques: spectroscopic

1. Introduction

Stellar activity comprises all the effects resulting from the concentration of enhanced magnetic fields in the stellar surface, chromosphere and corona. This is a proxy of the dynamo process and characterise it on a wide range of spectral type and ages allows to probe inner process according to the mass and rotational period. The advent of a large spectroscopic program to search for extrasolar planets reinforces the interest of this topics firstly because they provide a large amount of data which can be used to determine spectroscopic activity index for a large sample.

A correlation between activity and stellar mass is well established since a long time. M dwarfs, on average, are much more active than solar-like stars. This results from the combination of two effects: lower mass stars have much longer braking times for stellar rotation (Delfosse et al. 1998; Barnes 2003; Delorme et al. 2011), and for the same rotation period they are more active (Kiraga & Stepien 2007). Magnetic field topology is also directly obtained thanks to spectropolarimetry measurements and reveals that massive active M dwarfs (more massive than 0.5 M$_\odot$) host strong toroidal component of the magnetic field which can be reminiscent of active K and G dwarfs while M dwarfs of lower mass exhibit a mainly poloidal magnetic field (Morin et al. 2008; Donati et al. 2008). As this transition takes place when the stars become fully convective (M∼0.35M$_\odot$) this raises the question of the difference of generation of magnetic field for stars with and without tachocline.

A knowledge of all the effects of the stellar activity is also essential to not confuse them with the existence of a planet. Indeed stellar magnetic activity complicates the detection of extra-solar planets using the RV method, inhomogeneities in the stellar surface – convection inhibition, spots and/or plages – deforms the spectral line shapes and centroid introducing a RV *jitter*. Such RV *jitter* may induces RVs variation which can mimic the signal of a planetary companion (Queloz et al. 2001; Bonfils et al. 2007; Robertson et al. 2014). Much work have been done to better understand such an effect and propose methods to filter out the RV signal due to stellar activity. Several stellar activity proxies are widely used to try to disentangle signals produced by the star or by a planetary companion and the analysis of the variability in the Ca II H&K lines is frequently used on RVs surveys (Dumusque et al. 2011b,a; Boisse et al. 2011, 2012; Lagrange et al. 2010; Meunier et al. 2010; Meunier & Lagrange 2013; Tuomi et al. 2014). However, due to the complexity of the ef-

⋆ Based on observations made with the HARPS instrument on the ESO 3.6 m telescope under the program IDs 072.C-0488(E), 183.C-0437(A), 072.C-0488, 183.C-0972 and 083.C-1001 at Cerro La Silla (Chile).

fects that magnetic activity produces on the stellar surface, it is still not clear how to recognise the RV dependence upon some of these activity proxies – e.g. linear correlation, loop pattern – and different groups leads to different conclusions (Santos et al. 2014; Jenkins & Tuomi 2014).

Stellar magnetic activity play also an essential role on the evolution of planets. At the younger age of the system the central star is very active (Ribas et al. 2005) and close-in planets are subject to stellar X-ray and UV radiation, as well as coronal mass ejections (CMEs) which could potentially cause a major atmospheric escape (Scalo et al. 2007; Lammer et al. 2009; Ehrenreich & Désert 2011; Vidotto et al. 2014). This point is crucial for planetary system around M dwarfs, as the habitable zone is close to the star, because of its low temperature, and since these stars have a longer high-activity phase.

All this topics justify the determination of activity estimators along all the HR diagram. One of these is the non-thermal heating in the chromosphere that produces superficial bright plages, which can be traced by spectroscopic activity indicators. The reversal emission in the Ca II H&K resonance lines (396.8 nm and 393.4 nm respectively) is a widely known activity indicator. This activity proxy was intensively monitored by the Mount Wilson program,

Historical Mt. Wilson program standardised a quantity to measure the stellar activity: the S-index. Vaughan et al. (1978) defined as the ratio of the integrated flux through a triangular band-pass (with a FWHM of 1.09 Å) centred in the Ca II H&K cores over two 20 Å-wide rectangular band-pass in the violet (V, centred at 3901 Å) and red (R, centred at 4001 Å) side of the emission lines (Fig. 1). The S-index is a relative quantity that does not represent a true measurement of stellar activity, as it depends on the spectral-type. This is due to intrinsic variations in the continuum level of stars of different spectral type. To address this limitation, it was introduced the C_{cf}. This factor (Middelkoop 1982; Rutten 1984) is a correction to transform the S-index into the fraction of stellar luminosity which comes from the Ca II H&K lines. To date such calibration is focused on FGK dwarfs and covers imperfectly the domain of M dwarfs. Moreover the colour index choose by numerous author to express C_{cf} along the HR diagram is $B-V$, such index is not a nice proxy for M dwarfs due to the faint part of their energy emitted in the B-passband and to the metallicity dependence of their V-emission (see for example Delfosse et al. 2000). The large scatter of C_{cf} seen for $B-V > 1.2$ (late-K), in the figure 3 of (Vaughan & Preston 1980), illustrate this point.

Another limitation is that the integrated flux over the pass-band centred in the Ca II H&K not only account for the chromospheric emission, but also has a photosphere contribution. Two corrections were proposed by Blanco et al. (1974) and Linsky & Ayres (1978), but a more accepted photospheric correction – for details see Appendix of Noyes et al. (1984) – was later introduced by Hartmann et al. (1984). This later work compute the S-index but only considering the photospheric flux when integrating over the band-pass centred in Ca II H&K lines, which is known as S_{phot}. Finally, they transform this correction factor in the Middelkoop (1982) calibration to obtain a colour dependent photospheric factor $R_{phot}(B-V)$. This results in the $R'_{HK} = R_{HK} - R_{phot}$ activity index which was calibrated for spectral classes F5 to K1. R'_{HK} is thus the ratio between the energy emitted in the CaII H&K chromospheric lines and the bolometric energy, representing an absolute measurement of stellar activity.

Numerous works uses the R'_{HK}-index in the colour domain where the transformation from S to absolute flux was calibrated – FGK dwarfs – (Henry et al. 1996; Santos et al. 2000; Wright et al. 2004; Hall et al. 2007; Isaacson & Fischer 2010; Lovis et al. 2011). To extend activity studies to later dwarfs some authors extrapolate the conversion factor C_{cf} and R_{phot} in a colour domain where there validity is not demonstrated (Strassmeier et al. 2000; Tinney et al. 2002; Jenkins et al. 2006). Two studies propose a calibration of an absolute Ca II H&K index extended to M dwarfs. Browning et al. (2010) determine a L_{Ca}/L_{bol} through the Ca II H&K equivalent widths for a sample of M dwarfs, but their index is not anchored to the Mount Wilson R'_{HK}. Mittag et al. (2013) computed the S to R'_{HK} conversion making use of synthetic spectra but they calibrate it in using the $B-V$ colour index which is source of large scattering for M dwarfs.

The aim of the present work is to calibrate C_{cf} and R_{phot} for early to mid-M dwarfs (Sect. 3, 4 and 5). Then, we focused in the magnetic activity dependence with stellar rotation in section 6 and the overall analysis of R'_{HK} against stellar parameters of the HARPS M dwarf sample is described in section 7.

2. Observations and data reduction

2.1. HARPS spectrum

We used data from the High Accuracy Radial velocity Planets Searcher (HARPS) installed on the ESO's 3.6m telescope at La Silla observatory in Chile. HARPS is a fiber-fed, cross-dispersed echelle spectrograph covering from 380 to 630 nm and with a resolving power of 115,000. The stellar light is injected in a science fiber and a second fiber can be illuminated with a wavelength calibration lamp, simultaneously or not (Mayor et al. 2003).

We use spectra of M dwarfs to calibrate C_{cf} and R_{phot} for this spectral type and GK dwarfs spectra as standards (see below for a definition of a standard). The total stellar sample comprises GKM stars which was originally selected to search for exoplanet through high-precision RVs (Lovis et al. 2011; Bonfils et al. 2012, 2013). The selection criteria was described in detail in the aforecited papers, here we just highlight some points. GK dwarfs are closer than 50 pc and projected rotational velocity $v\ sin\, i < 3-4\ kms^{-1}$; their spectra usually reach a signal-to-noise (S/N) ratio above 100 per pixel at 550 nm. M dwarfs sample are volume-limited to 11 pc with $v\ sin\, i \leq 6.5\ kms^{-1}$. All spectroscopic binaries were discarded and also visual pairs with separation $< 5''$ for M dwarfs data.

The HARPS pipeline (Lovis & Pepe 2007) automatically reduces raw data to 1D and 2D spectra making use of a wavelength solution which is done through nightly calibrations. In addition, the pipeline gives the RV by cross-correlating a binary mask with spectra. The cross-correlation function (CCF) also provide its full-width at half-maximum, the contrast and the bisector-span. The data used in this work are 1D spectra which are corrected from the barycentric Earth RV and the background was subtracted. We later recenter data to the rest frame making use of the stellar RV provided by the pipeline. Finally, we computed the instrumental transmittance (normalised to one) as the ratio between the theoretical energy distribution of the bright (V=6.88) G dwarf HD 223171 computed with the BT-settle model (Allard 2014) and the observed energy distribution which results from stacking 20 – 1D – spectra; subsequently, all spectra were divided by the instrumental transmittance. This is a first order correction as it does not take into account temporal variability.

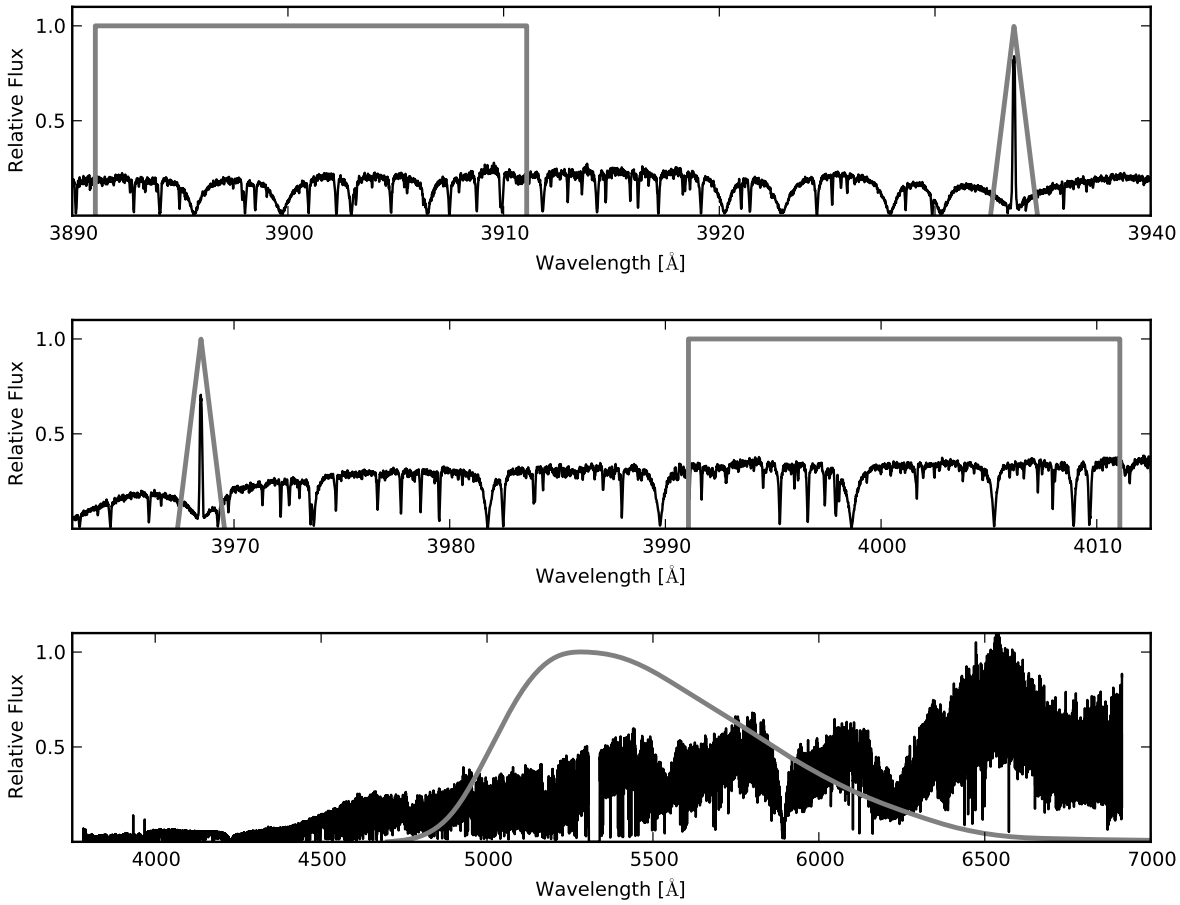

Fig. 1. An example (Gl 699) of a median spectrum obtained with HARPS where the V, K (top panel), H, R (middle panel) and visual (bottom panel) pass-bands are represented (grey lines) in the rest frame.

2.2. Data from literature

The present work makes use BVIK photometry and parallaxes. The photometry was obtained from different sources and homogenised to Johnson-Cousins-Cit system using Carpenter (2001)'s transformations when needed. For M dwarfs photometry, ordered by priority, were obtained from Leggett (1992), Gaidos et al. (2014), Cutri et al. (2003); while photometry for GK dwarfs comes from Ducati et al. (2001) and/or Cutri et al. (2003). Parallaxes (π) were recovered, by priority order, from van Leeuwen (2007), van Altena et al. (1995), Perryman & ESA (1997), Hawley et al. (1997) and/or the Research Consortium on Nearby Stars (RECONS) parallax program[1]. We also used effective temperature, radii, masses and metallicities. For GK dwarfs we adopted these stellar parameters from Sousa et al. (2008); for M dwarfs, metallicities were obtained from Neves et al. (2013), effective temperatures and radii were computed using Boyajian et al. (2012) V-K/metallicity relationships, while stellar masses were derived from Delfosse et al. (2000) K-band absolute magnitude relationship, which we extrapolated up to $0.8M_{\odot}$ – since it was derived using masses from $0.093M_{\odot}$ to $0.713M_{\odot}$.

[1] http://www.recons.org/publishedpi.2014.0720

3. Scaling the S-index from HARPS observations

The S-index was originally introduced in the stellar activity Mt. Wilson program. This huge campaign, targeted to measure it for several FGK dwarfs, started using the Coudé scanner at the 100-inch telescope (HKP-1) (Wilson 1968, 1978) and later the photometer at the 60-inch telescope (HKP-2) (Vaughan et al. 1978). This activity indicator is defined as

$$S = \alpha \cdot \frac{f_H + f_K}{f_V + f_R} \tag{1}$$

where α is a calibration constant to match HKP-1 and HKP-2 activity indexes and it was estimated to be 2.4; f_H, f_K, f_V, and f_R are the total flux in each pass-band described above (see Sec. 1 and Fig. 1).

To compute the S-index with HARPS we must consider that the spectrophotometer used in the Mt. Wilson program exposes 8 times more flux in the H and K bands than in the V and R bands; also, we considered to work with the mean flux per wavelength interval (Lovis et al. 2011). So the HARPS calibration constant α_H is

$$\alpha_H = \alpha \cdot 8 \cdot \frac{1.09\,\text{Å}}{20\,\text{Å}} \sim 1$$

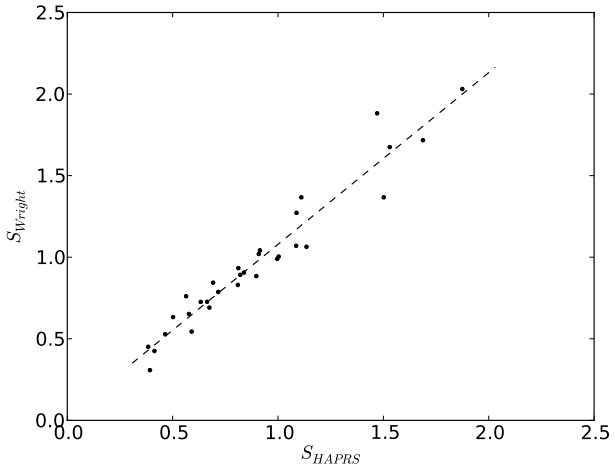

Fig. 2. Median HARPS S-index values for our 31 targets in common with Wright et al. (2004). The solid line represents the least-square linear fit (Eq. 3) used to scale our S measurements to the Mount Wilson program.

Therefore, equation (1) for HARPS data is

$$S = \frac{20}{1.09} \cdot \frac{f_H + f_K}{f_V + f_R} \tag{2}$$

We do not have common targets with the Mt. Wilson program to verify our S measurements consistency. However, Wright et al. (2004) scaled their Keck and Lick S-index measurements to the Mt. Wilson ones. We have 31 targets in common with Wright et al. (2004, Fig. 2) allowing us to establish a transformation relating Mt. Wilson and HARPS S-index[2]. Our linear fit which better scale our S measurements to Mt. Wilson program is

$$S_{M.W.} = 1.053 \cdot S + 0.026 \tag{3}$$

The root-main-square of S about the fit gives 0.080. Besides calibration errors, it is expected that intrinsic stellar variability is the main responsible of scatter.

Once we scaled HARPS S-index to the Mt. Wilson one, R'_{HK} is obtained by

$$\begin{aligned} R'_{HK} &= R_{HK} - R_{phot} \\ &= K \cdot \sigma^{-1} \cdot 10^{-14} \cdot C_{cf} \cdot (S - S_{phot}) \end{aligned} \tag{4}$$

where 10^{-14} is scaling factor, σ is the Stefan-Boltzmann constant, the C_{cf} is calibrated for 0.44<B-V<0.82 – spectral classes F5 to K1 and, therefore, its use is not reliable for M dwarfs (B-V>1.35; Leggett 1992) – and K is a parameter which converts the surface fluxes in arbitrary units to absolute surface fluxes (for a detailed description see, e.g. Rutten 1984, section 2.d). Middelkoop (1982), Rutten (1984), and Hall et al. (2007) found respectively $K = 0.76{\times}10^6$, $1.29{\times}10^6$, $1.07{\times}10^6$ [$erg\,cm^{-2}\,s^{-1}$] for a 1.09Å triangular band pass, respectively, while Mittag et al. (2013) derived K as a B-V dependent relation involving the absolute flux in the V and R pass bands ($\mathcal{F}_{VR}$), the C_{cf} and the effective temperature (T_{eff}). However, they computed T_{eff} from Gray (2005)'s B-V relationship which is not reliable for M dwarfs. Here we prefer to use K from Hall et al. (2007) because it is calibrated with recent solar data : $K \cdot \sigma^{-1} \cdot 10^{-14} = 1.887 \times 10^{-4}$. Finally, S_{phot} – or R_{phot} – stands for the photospheric contribution which needs to be subtracted in order to measure the genuine flux excess in the Ca II H&K lines (see Sect. 5 below).

[2] the common targets are Gl 465, Gl 357, Gl 1, Gl 581, Gl 87, Gl 667C, Gl 486, Gl 686, Gl 436, Gl 105B, Gl 699, Gl 526, Gl 433, Gl 273, Gl 555, Gl 628, Gl 413.1, GJ 2066, Gl 701, Gl 393, Gl 876, Gl 849, Gl 536, Gl 887, Gl 514, Gl 176, Gl 678.1A, Gl 229, Gl 846, Gl 880, and Gl 382

4. The bolometric factor C_{cf}

The HARPS wavelength domain covers only the bluer part of the spectral energy distribution of M dwarfs. For this reason, we cannot directly obtain the bolometric apparent luminosity and then link it with the flux over the V and R pass-bands. Nevertheless, the bolometric flux can be obtained through the visual band and the bolometric correction. In addition, the instrumental plus sky transmittance is variable (e.g. over time) and, in consequence, our first order transmittance correction (described in section 2) does not allow to accurately calibrate the flux in the V and R pass bands to the bolometric flux.

To decrease the effects of such transmittance variation we use spectra of G and K dwarfs acquired in the same conditions as M dwarfs spectra. Namely, GK dwarfs represents standards (*Std*) whose spectra were acquired just before or after the observation of a M dwarf and with similar airmass. This is done by restricting the use of data satisfying

- the time lapse between the observation of a M dwarf and a standard should be less than 30 min
- the difference in airmass between the observation of a M dwarf and the observation of a standard should be less than 0.05
- data recorded with an airmass below 1.4
- at least 5 spectra per target
- we estimate the night quality (Σ) by the ratio between the measured and the theoretical fluxes in the visual band ($\Sigma = f_v/[t_{exp}10^{-0.4m_v}]$). We selected data having $\Sigma_{Std}/\Sigma_M - 1 \leq 0.2$

From the HARPS M dwarf sample, only 14 M dwarfs fulfil above restrictions.

The bolometric factor for M dwarfs ($C_{cf,M}$) and for standards ($C_{cf,Std}$) is defined as

$$C_{cf,M} \equiv \frac{(f_V + f_R)_M}{f_{bol,M}} \tag{5}$$

$$C_{cf,Std} \equiv \frac{(f_V + f_R)_{Std}}{f_{bol,Std}} \tag{6}$$

where f_V and f_R are the same as in eq. (1), while f_{bol} is the apparent bolometric flux of the star.

The number of counts (N) on the detector depends on the stellar flux (f_λ) and transmittance – which, in turn, both are wavelength (λ) dependent – plus atmospheric variations in time (t) and airmass (A_z) that, indeed, are part of the transmittance. Relatively stable instrumental parameters (e.g. mirror reflectance and CCD quantum efficiency) are also involved in N but are not taken into account in the following analysis.

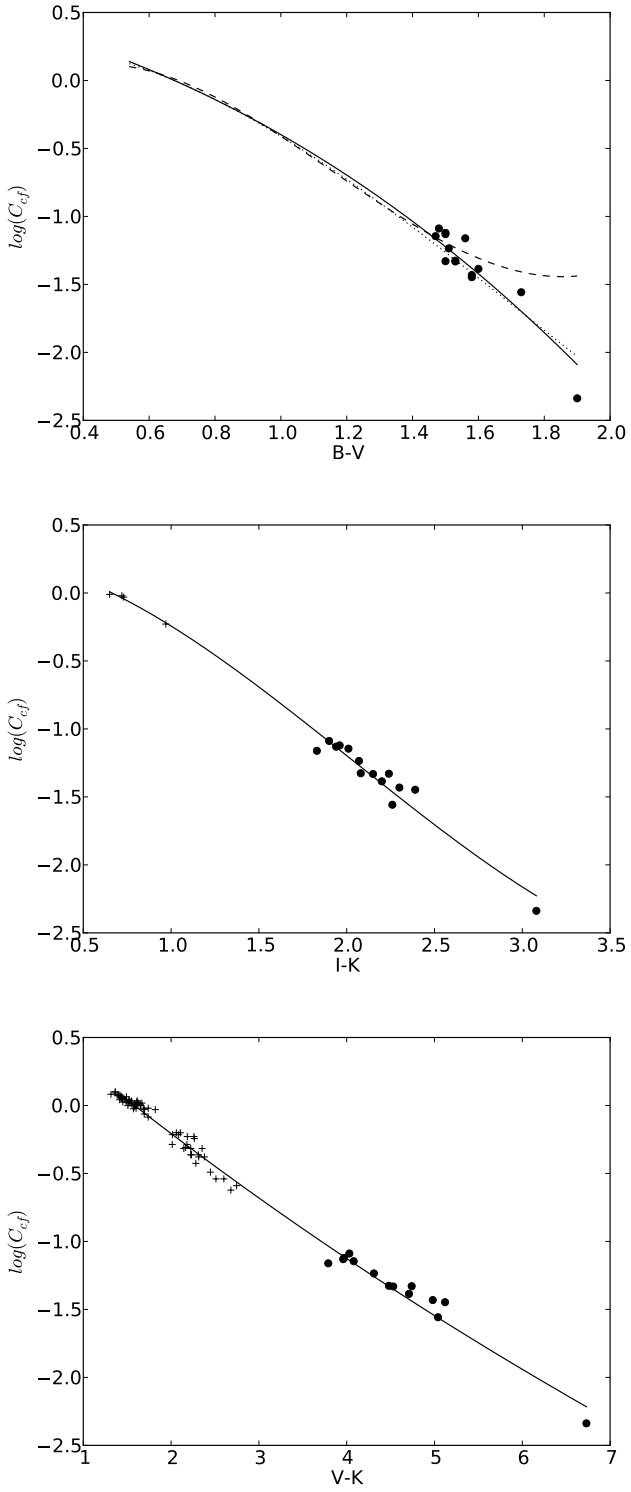

Fig. 3. The bolometric factor against $B-V$ (top panel), $I-K$ (middle panel), and $V-K$ (bottom panel) colour indices. Black dots and crosses represents the $C_{cf,M}$ median and the $C_{cf,Std}$, respectively. Solid lines represents the least-square fits described in equations (15), (16), and (17). In the top panel we omitted the 125 $C_{cf,Std}(B-V)$ points to clearly visualise the fits from Middelkoop (1982) and Rutten (1984) that are represented by dashed and dotted lines, respectively.

Representing the transmittance as $T(\lambda,\, t,\, A_z)$, the number of counts in the V and R pass bands can be written

$$N_V + N_R = \int T(\lambda,\, t,\, A_z)\cdot(T_V + T_R)_\lambda \cdot f_\lambda \, d\lambda \tag{7}$$

where T_V, T_R represent the V, R box shaped pass bands, respectively. Now, as spectra are corrected – to first order – for transmittance in wavelength (as is described in section 2), we have $\int T(\lambda,\, t,\, A_z)\, d\lambda \approx T(t,\, A_z)$ and hence eq. (7) gives

$$\begin{aligned} N_V + N_R &= T(t,\, A_z)\sum_\lambda (T_V + T_R)_\lambda \cdot f_\lambda \\ &= T(t,\, A_z)\cdot(f_V + f_R) \end{aligned} \tag{8}$$

In the same way for the visual band, we have

$$\begin{aligned} N_\upsilon &= \int T(\lambda,\, t,\, A_z)\cdot T_{\upsilon,\lambda}\cdot f_\lambda \, d\lambda \\ &= T(t,\, A_z)\cdot f_\upsilon \end{aligned} \tag{9}$$

with $T_{\upsilon,\lambda}$ representing the transmission of the visual filter and f_υ the corresponding filtered flux.

On the other hand, the apparent bolometric flux ratio between standards and M dwarfs is obtained in terms of the apparent visual magnitude m_υ and the bolometric correction BC_υ

$$\frac{f_{bol,Std}}{f_{bol,M}} = 10^{-0.4(\Delta m_\upsilon + \Delta BC_\upsilon)} \tag{10}$$

where

$$\Delta BC_\upsilon = BC_{\upsilon,Std} - BC_{\upsilon,M}$$

and

$$\Delta m_\upsilon = m_{\upsilon,Std} - m_{\upsilon,M} = -2.5\, log\left(\frac{f_{\upsilon,Std}}{f_{\upsilon,M}}\right) \tag{11}$$

Now using eq. (9) and assuming – given our restrictions in selected data described above – that $T(t,\, A_z)_M \approx T(t,\, A_z)_{Std}$, eq. (11) becomes in

$$\Delta m_\upsilon = -2.5\, log\left(\frac{N_{\upsilon,Std}}{N_{\upsilon,M}}\right) \tag{12}$$

and then replacing eq. (12) in eq. (10) gives

$$\frac{f_{bol,Std}}{f_{bol,M}} = \frac{N_{\upsilon,Std}}{N_{\upsilon,M}} 10^{-0.4\Delta BC_\upsilon} \tag{13}$$

Finally, using eq. (8) and (13) and combining eq. (5) and (6) we obtain

$$C_{cf,M} \approx C_{cf,Std}\cdot\frac{(N_V + N_R)_M}{(N_V + N_R)_{Std}}\cdot\frac{N_{\upsilon,Std}}{N_{\upsilon,M}}\cdot 10^{-0.4\Delta BC_\upsilon} \tag{14}$$

where $C_{cf,Std}$ is derived from Middelkoop (1982) relationship; the bolometric correction for the standards $BC_{\upsilon,Std}$ is obtained from Flower (1996), while the bolometric correction for M dwarfs $BC_{\upsilon,M}$ is determined from Leggett et al. (2001) [3].

Restricting to have at least 5 spectra per target allow us to decrease the effect of our above assumptions as well as possible flares phenomena (e.g. Gl 551) by computing the median of $C_{cf,M}$. These median values are listed in Table A.1 and $C_{cf,Std}$ values are listed in Table A.2. Figure 3 shows the C_{cf} derived

[3] $BC_\upsilon = BC_K + m_K - m_\upsilon$

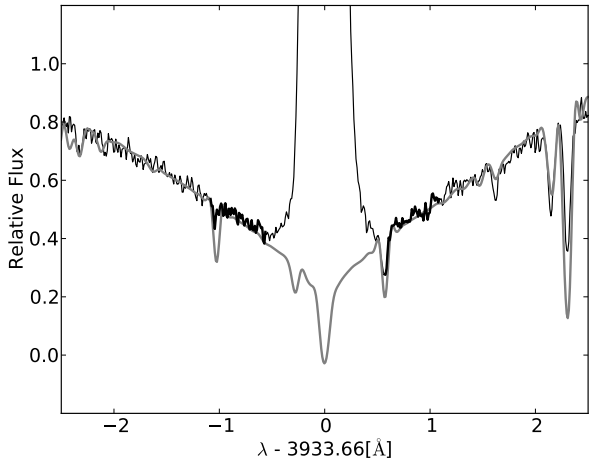

Fig. 4. Gl 205 Ca II K region where the thin black and bold grey lines are the observed and the corresponding theoretical spectrum from BT-Settl (T_{eff} = 3800 [K], $log(\ g\ [cm/s])$ = 4.5, Fe/H = 0.0). The bold black line represents the zones falling inside the triangular shaped pass band (K) where the inner boundaries corresponds to the estimation of the minimum (K1) used to determine the photospheric flux in K.

with equation (14) against B-V, I-K, and V-K, as well as their third order least-square polynomial fit. These fits are given by

$$log(C_{cf}) = -0.053\,(B-V)^3 - 0.341\,(B-V)^2 - \\ -0.545\,(B-V) + 0.541 \quad (15)$$

$$log(C_{cf}) = 0.071\,(I-K)^3 - 0.434\,(I-K)^2 - \\ -0.150\,(I-K) + 0.270 \quad (16)$$

$$log(C_{cf}) = 0.018\,(V-K)^2 - 0.554\,(V-K) + \\ +0.835 \quad (17)$$

where the colour boundaries for the equations (15), (16), and (17) are 0.54<B-V<1.9, 0.72<I-K<3.08, and 1.45<V-K<6.73, respectively, which corresponds to spectral classes from G0 to M6. The rms considering only M dwarf gives 0.130, 0.078, and 0.055 for the B-V, I-K, and V-K fits respectively.

Jenkins et al. (2006) computed R'_{HK} for B-V>0.9 by an extrapolation to C_{cf} Middelkoop (1982)'s relationship, however, from top panel of Fig. 3 we note that big discrepancies arises for B-V>1.5 and therefore such extrapolation leads to overestimate R_{HK} up to a factor of three. Including the latest main sequence stars, Rutten (1984) conversion and our updated C_{cf}-colour relationship matches quite well and allows to properly transform S to R_{HK}.

5. The photospheric factor R_{phot}

The photospheric flux falling inside the two 1.09Å triangular pass-bands needs to be estimated and then subtracted to properly measure the chromospheric flux excess present in the Ca II H&K lines (see Fig. 1). Different approaches were performed to correct for the photospheric contribution of GK dwarfs. Noyes et al. (1984) summarizes these approaches in their appendix and here we recall their generalities. These approaches are to perform a parabolic fit or to interpolate the Ca II H&K wings into the lines cores, while another option is to identify the minimum formed by the reversal emission together with the wings (commonly known as H1 and K1 points). It is clear that the flux between these points are produced in the stellar chromosphere while the flux outside H1 and K1 are formed on the photosphere, see Fig. 4. However, the determination of the K1 and H1 points is ambiguous as Hartmann et al. (1984) noted; by this option they quantified the photospheric correction accuracy around 10%.

Table 1. Determined stellar parameters and used BT-Settl grids. In this table $\log g$ is computed with mass and radius respectively from the relationship of Delfosse et al. (2000); Boyajian et al. (2012); T_{eff} from Boyajian et al. (2012) and [Fe/H] from Neves et al. (2013)

Name	log(g [cm s^{-1}]) Det. / Used	T_{eff} [K] Det. / Used	Fe/H Det. / Used
Gl 1	5.00 / 5.0	3458 / 3500	-0.45 / -0.5
Gl 191	5.25 / 4.5	3134 / 3300	-0.88 / -1.0
Gl 205	4.70 / 4.5	3780 / 3800	+0.22 / -0.0
Gl 229	4.82 / 5.0	3643 / 3700	-0.10 / -0.0
Gl 393	4.75 / 5.0	3639 / 3600	-0.22 / -0.0
Gl 551	4.94 / 5.0	2659 / 2800	-0.00 / -0.0
Gl 581	4.92 / 5.0	3327 / 3500	-0.21 / -0.0
Gl 588	4.70 / 4.5	3519 / 3500	+0.07 / -0.0
Gl 628	4.80 / 5.0	3364 / 3400	-0.02 / -0.0
Gl 674	4.91 / 5.0	3374 / 3400	-0.25 / -0.5
Gl 699	5.30 / 5.0	3088 / 3300	-0.52 / -0.5
Gl 849	4.59 / 4.5	3519 / 3500	+0.24 / -0.0
Gl 876	4.69 / 4.5	3421 / 3400	+0.15 / -0.0
Gl 887	4.89 / 5.0	3686 / 3700	-0.24 / -0.0

To derive a colour dependent relation for the photospheric factor S_{phot} (or R_{phot}) we do not follow this procedure. As previous authors (Walkowicz & Hawley 2009; Mittag et al. 2013) we prefer use a theoretical grids of spectral model (here BT-Settl/CIFIST2011bc Allard 2013)[4] to fit the photospheric contribution. As showed in Fig. 4, the spectrum is locally reproduced very accurately by these models.

For each target we selected grids based on their corresponding stellar parameters: effective temperature, gravity and metallicity. When large differences between theoretical and observed spectrum were visually found we tested grids with $T_{eff} \pm 200$ [K] and/or $log(g) \pm 0.5$ [$cm\,s^{-1}$] and finally selected the grid which better match the observed spectrum. Table 1 lists the stellar parameters and the used grids.

We focused on the region 3880-4022 Å for 1D spectra and the used grids. The average spectra for each target was computed to improve the S/N, then the averaged and synthetic spectra were normalised around the Ca II H&K lines. For the observed spectra (averaged and normalised) we replace the 2 Å region centred in the Ca II H&K lines by the appropriate synthetic spectrum (Fig. 4). Then, we used equations (2) and (3) to compute S_{phot} and equations (17) to finally compute the photospheric contribution

$$R_{phot} = 1.887 \times 10^{-4} \cdot C_{cf} \cdot S_{phot} \quad (18)$$

Next, for each target we calculated the median of R_{phot} – listed in Table A.1 – and then computed a third order least-square polynomials for B-V, I-K, and V-K. These fits results in

$$log(R_{phot}) = 0.364\,(B-V)^3 - 1.270\,(B-V)^2 + \\ +0.249\,(B-V) - 4.304 \quad (19)$$

[4] To shift spectra from vacuum to air and to work with absolute fluxes we followed instructions from the PHOENIX website: http://phoenix.ens-lyon.fr/Grids/

$$log(R_{phot}) = 0.112\,(I-K)^3 - 0.495\,(I-K)^2 + \\ +0.005\,(I-K) - 4.485 \quad (20)$$

$$log(R_{phot}) = 0.001\,(V-K)^3 + 0.038\,(V-K)^2 - \\ -0.608\,(V-K) - 3.730 \quad (21)$$

where the rms for each fits gives 0.107, 0.078, and 0.066 for B-V, I-K, and V-K colour indexes, respectively; the colour boundaries are 0.54<B-V<1.9, 0.65<I-K<3.08, and 1.45<V-K<6.73 (i.e. up to M6 spectral type). Figure 5 shows the photospheric factor against the colour indexes and the corresponding fits, where we note that a systematic offset appears between our fit and Hartmann et al. (1984) or Noyes et al. (1984) R_{phot} relations. The offset could be explained by the fact that the intensity go to zero in a narrow zone of the Ca II H&K lines (fig. 4) compared to the whole width of the emission zone. Therefore a photospheric component may be still present in their estimation of the reversal emissions, which results in an underestimated R_{phot} (or the minimum photospheric factor as they call).

6. R'_{HK} and rotation periods

We show that C_{cf} and R_{phot} are more accurately determined when they are expressed in function of $V-K$ colour index rather than $B-V$ or $I-K$. In this section, all our value of R'_{HK} will be computed with our $\log C_{cf}(V-K)$ and $\log R_{phot}(V-K)$ relationships.

It is demonstrated that magnetic activity scales with rotation period for stars having a radiative zone surrounded by a convective envelope where a thin layer exposed to strong shears is present (the tachocline). In that scenario an $\alpha\Omega$ dynamo-process explains the formation of magnetic fields and, therefore, rotation plays a crucial role (e.g. Parker 1955). In the other hand, for fully convective M-dwarfs (later the M4V; e.g., Bercik et al. 2005), theoretical 3D global numerical simulation (Gastine et al. 2013; Schrinner et al. 2014) point similarities with planetary dynamo. In such case the ratio between inertia and Coriolis force (approximated by the ratio of the rotation period to the convective turnover time) is know to play a major role. Observational data obtained with Zeeman Doppler Imaging demonstrate that magnetic topology change when stars are largely convective. Partly convective early-M dwarfs present complex multi-polar magnetic feature (Donati et al. 2008) while the majority of fully convective stars of short rotational period has a strong dipolar magnetic field (Morin et al. 2008). For late-M dwarfs a bi-stability is observed (Morin et al. 2010).

However the correlation between rotational period and proxies of integral field (average field strengths Reiners & Basri 2007; Reiners et al. 2009) or of activity (e.g. L_X Kiraga & Stepien 2007) does not highlight a significant change when the stars become fully convective. Here we analyse the dependence of the R'_{HK} upon rotation periods for 31 M dwarfs (M1 to M6) with well known stellar rotation periods. These periods were inferred from photometry or S-index periodic modulations. All the rotational period are obtained from the literature (see Table 2) at the exception of Gl 514 for which we determine P_{rot} from a clear peak in the Ca II H&K periodogram of the HARPS data at a ∼30 days period.

For solar like stars Noyes et al. (1984) found that the scatter diminish when plotting $log(R'_{HK})$ against the Rossby number ($Ro = P_{obs}/\tau_c$, where τ_c is the convective overturn time) instead of P_{rot} alone. This is in concordance to the fact that the strength of an $\alpha\Omega$ dynamo-process is proportional with the inverse square of Ro; thenceforth Ro was widely used when relating magnetic activity with rotation rates. τ_c can be determined empirically (e.g. Noyes et al. 1984) or theoretically (e.g Ventura et al. 1998), however, for M dwarfs the determination of τ_c in

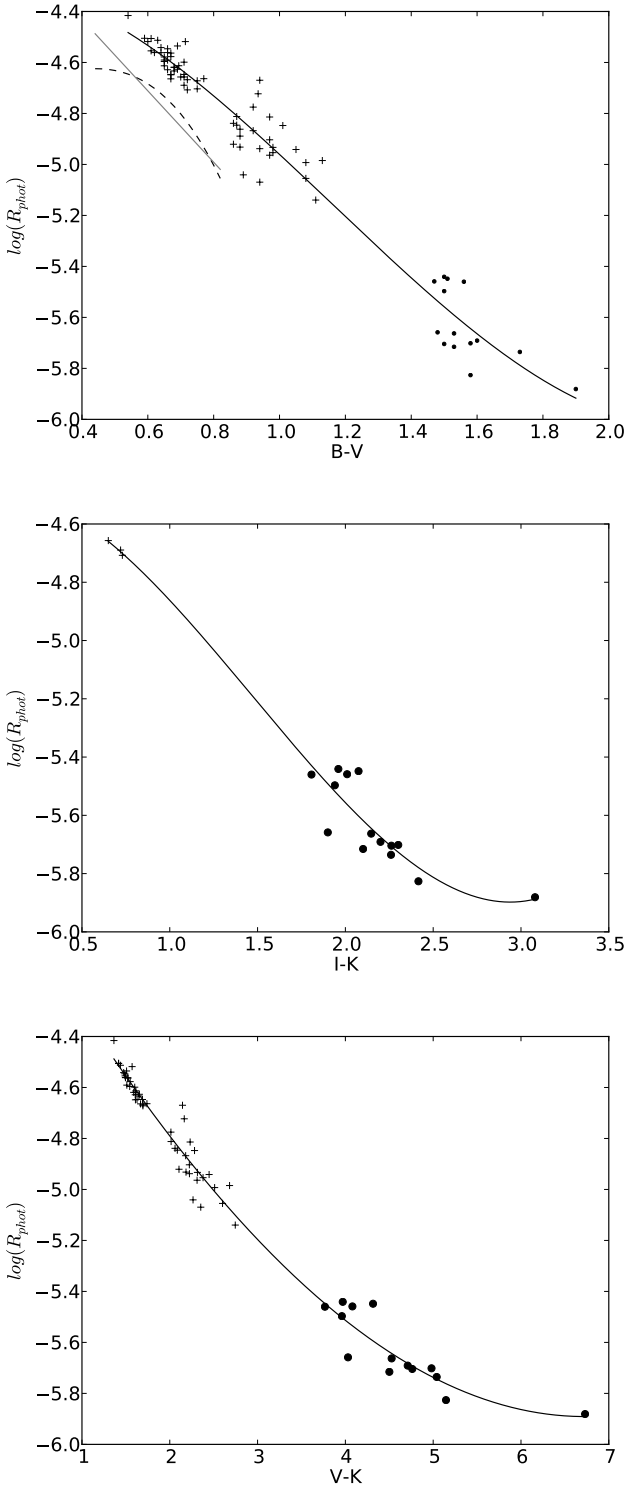

Fig. 5. From top to bottom the photospheric factor as function of B-V, I-K, and V-K colour indices. Black dots and crosses represents the R_{phot} for M dwarfs and GK dwarfs, respectively. The solid lines are from equations (19), (20), and (21). We also plot in the top panel the photospheric factor from Hartmann et al. (1984) and Noyes et al. (1984) represented by black dashed line and grey solid line, respectively.

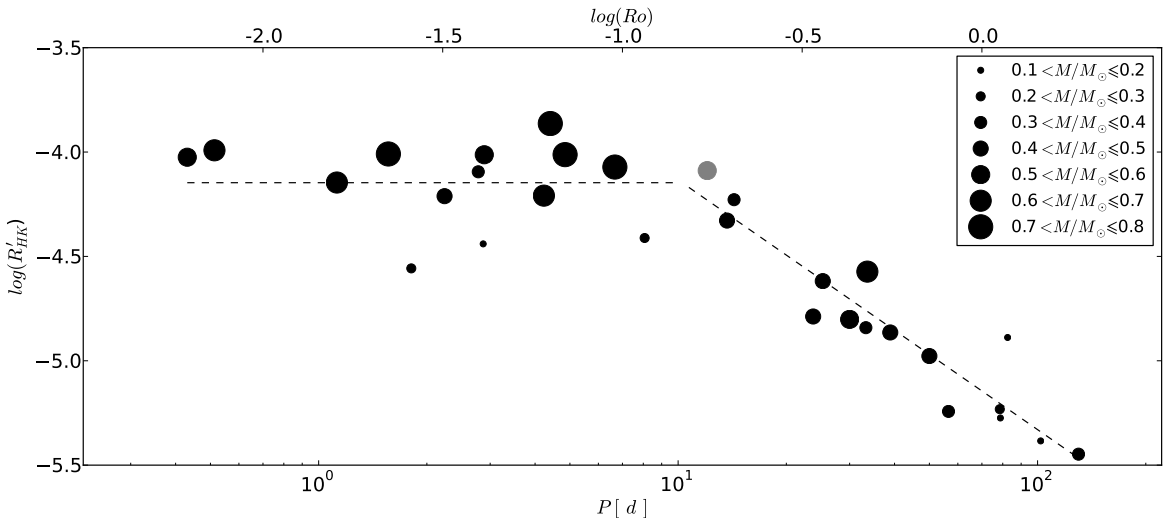

Fig. 6. $log(R'_{HK})$ vs. $log(P_{rot})$ where the size of filled circles represents the masses. As a reference, the second x-axis shows the Rossby number ($Ro = P_{rot}/\tau_c$) using τ_c = 70 d. A linear correlation fits the points corresponding to P_{rot} > 10 d, under this rotation rate $log(R'_{HK})$ is distributed along a plateau, which is translated as saturated regime. A single point is flagged (grey point) as it is derived from photometric parallax (Lépine & Gaidos 2011) with a large uncertainty – large mass uncertainty.

either ways is uncertain. Additionally, a debate arose about if *Ro* is the best option for linking the stellar activity to rotation rates; some authors argues that P_{rot} should be used over *Ro* (Stepien 1993; Reiners et al. 2014). Fig. 6 demonstrate that, for M dwarfs, the use of $log(P_{rot})$ allows to encompass stellar masses from $0.1M_\odot$ to $0.8M_\odot$ in an unique linear relation linking $log(R)$ to $log(P_{rot})$ while the scatter remains low.

Figure 6 clearly shows that above a stellar rotation of around ten days the activity decreases with increasing rotation periods, as expected. While under rotation periods of around ten days the points defines a plateau which means that the stellar activity reaches the saturated regime. The $log(R'_{HK})$-$log(P_{rot})$ dependence can be described with the following relation

$$log(R'_{HK}) = \begin{cases} -1.196 \cdot log(P_{rot}) - 2.937 & \text{if } P_{rot}[d] > 10 \\ -4.147 & \text{if } P_{rot}[d] < 10 \end{cases} \quad (22)$$

The saturated regime is also observed for M dwarfs in using another activity proxies like $L_{H\alpha}/L_{bol}$, L_X/L_{bol} or B_f (e.g. Delfosse et al. 1998; Kiraga & Stepien 2007; Reiners et al. 2009, 2012). Activity tracers saturates at certain rotation neither because magnetic fields can not growth indefinitely due to a saturation in dynamo processes, or because the stellar surface is completely covered by active regions (f=1) while magnetic field still grows. For M dwarfs, the R'_{HK} saturation level is reached at $Ro \approx 0.1$ (adopting $\tau_c = 70\,d$ as in Reiners et al. 2009). The saturation regime occurs at the same $Ro \approx 0.1$ when linking L_X/L_{bol} or Bf to *Ro* (Kiraga & Stepien 2007; Reiners et al. 2009).

Regarding the unsaturated region, the $log(R'_{HK})$ vs. $log(P_{rot})$ show a linear regime for rotational period ranging from 10 to ∼100 days. FGK-dwarfs relation show similar behaviour (Noyes et al. 1984; Mamajek & Hillenbrand 2008)

One third of our M dwarf sample (11) have masses under $0.35M_\odot$, where a fully-convective dynamo process is invoked to describe magnetic fields for stars without a tachocline. No significant change in the $log(R'_{HK})$ vs. $log(P_{rot})$ seem to occur at this transition, indicating that that stellar rotation continue to drives activity in fully convective stars. However, it is to note in the Fig 6 that the three lowest mass stars of our sample in the saturated regime have lower $log(R'_{HK})$ that more massive M-dwarfs in the same regime. Such behaviour need to be confirmed with a larger sample.

7. An overall view of R'_{HK} from the HARPS M dwarfs sample

We computed R'_{HK} for 403 stars of the HARPS M dwarf sample (Bonfils et al. 2012, 2013). For this, eq. (4) was used, where the C_{cf} was obtained by eq. (17) when V-K colour index exists in the literature, or by eq. (15) if we only found B-V colour index. In the same way, R_{phot} was derived through eq. (21) when V-K is available or by eq. (19) if only B-V was found. The median of R'_{HK} for each stars was used for the following analysis.

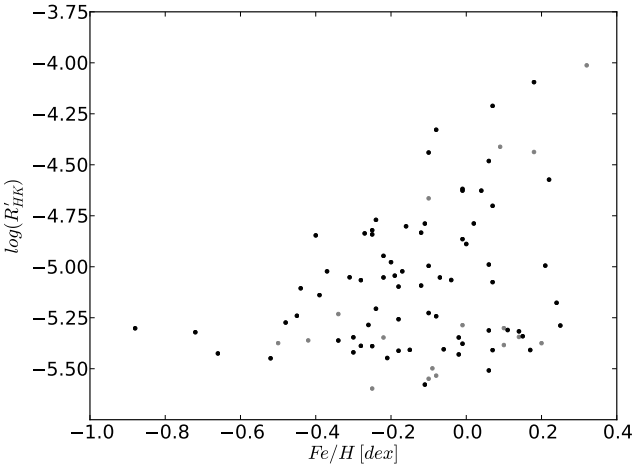

Fig. 7. $log(R'_{HK})$ as a function of metallicity where no trend in the lower envelope is visible. Black points represent targets with more than six measurements and $S/N_{VR,\,pix}$ ≥5, while grey dots depict targets having less than six measurements or $S/N_{VR,\,pix}$ <5.

Table 2. Rotation periods and median $\log(R'_{HK})$. The rotation periods for the 31 M dwarfs are from (1) Kiraga & Stepien (2007), (2) Bonfils et al. (2013), (3) Morin et al. (2008), (4) Irwin et al. (2011), (5) Robertson et al. (2014), and (6) This work. V-K colour and stellar mass are tabulated as well.

Name	V-K [mag]	M [$M_\odot$]	P_{rot} [d]	P_{ref}	$\log(R'_{HK})$
GJ 1264	4.288	0.74	6.67	(1)	-4.072
Gl 699	5.040	0.16	130.00	(1)	-5.449
Gl 569A	4.416	0.48	13.68	(1)	-4.328
GJ 182	3.680	0.79	4.41	(1)	-3.863
GJ 890	3.852	0.57	0.43	(1)	-4.025
GJ 867A	4.716	0.63	4.23	(1)	-4.209
GJ 841A	4.769	0.68	1.12	(1)	-4.146
Gl 803	4.230	0.74	4.85	(1)	-4.012
Gl 729	5.080	0.17	2.87	(1)	-4.440
Gl 618A	4.686	0.38	56.52	(1)	-5.236
Gl 551	6.730	0.12	82.53	(1)	-4.883
GJ 494	4.150	0.60	2.89	(1)	-4.013
GJ 431	4.980	0.37	14.31	(1)	-4.228
GJ 3367	3.817	0.54	12.05	(1)	-4.089
GJ 1054A	3.949	0.66	0.51	(1)	-3.992
GJ 103	3.941	0.75	1.56	(1)	-4.009
Gl 205	4.080	0.63	33.61	(1)	-4.573
Gl 358	4.660	0.42	25.26	(1)	-4.618
Gl 176	4.509	0.49	38.92	(1)	-4.864
Gl 674	4.480	0.34	33.29	(1)	-4.841
Gl 479	4.640	0.43	23.75	(2)	-4.788
Gl 526	4.010	0.49	50.00	(2)	-4.977
Gl 388	4.710	0.42	2.24	(3)	-4.211
Gl 12	4.809	0.22	78.50	(4)	-5.447
G 141-29	5.235	0.24	8.07	(4)	-4.412
GJ 3379	5.334	0.23	1.81	(4)	-4.557
GJ 1057	5.950	0.18	102.00	(4)	-5.384
LHS 1610	5.783	0.17	78.80	(4)	-5.048
Gl 285	5.420	0.31	2.78	(4)	-4.095
Gl 581	4.710	0.31	130.00	(5)	-5.448
Gl 514	3.990	0.52	30.00	(6)	-4.802

7.1. R'_{HK} and metallicity

First, we paid attention to the how behave R'_{HK} in terms of metallicity. For solar-like stars it is known that metallicity can affect R'_{HK} measurements because, at a given T_{eff}, fluxes in the V and R pass-bands are weaker for metal-poor stars, producing larger S values; besides S, metallicity could also affects the C_{cf} as its derivation involves the flux in the visual band, which in turn is affected by metallicity. Lovis et al. (2011) noticed this effect characterised by a systematic increase of R'_{HK} while Fe/H decreases, defining a linear trend in the lower envelope. They performed an efficient correction in taking in account the variation of the bolometric flux in function of Fe/H (see their Fig. 3). In the case of M dwarfs we does not see evidence of such a trend in the lower envelope (Fig. 7) and therefore we do not applied any metallicity correction to R'_{HK}. Additionally, we also notice that the majority of active M dwarfs are located in the "metallic" part of the Fig. 7. In comparison to earlier spectral type, M dwarfs with solar-type metallicity and beyond are, up to a factor of about two, more active than GK dwarfs. This is certainly the effect of the larger slowdown timescale of M-dwarfs.

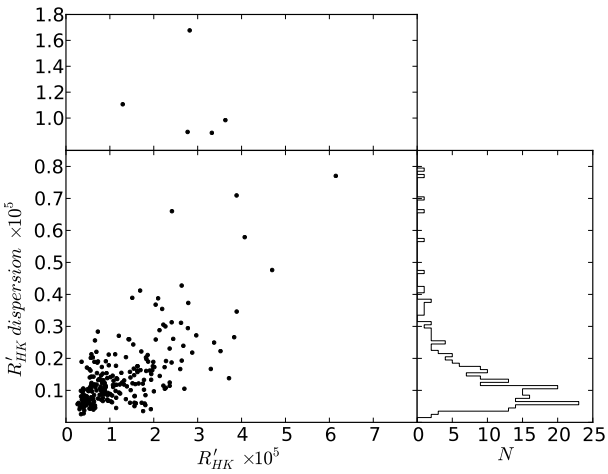

Fig. 8. The R'_{HK}-index and its short-term variability. R'_{HK} presents more dispersion as stars are more active, such a dispersion is representative of intrinsic stellar variability under the selection criteria described in the text. The y-axis has two scales for clarity (upper and bottom panels). This sub-sample contains 248 M dwarfs. The distribution of the R'_{HK} dispersion is also showed on the right side panel.

7.2. R'_{HK} dispersion

R'_{HK} dispersion accounts for intrinsic stellar activity variability but they can also originate from instrumental errors, which in some cases may dominate dispersion due to the low S/N in the Ca II H&K lines. Lovis et al. (2011) demonstrated the high precision reached by HARPS through the analysis of τ Ceti's R'_{HK} dispersion. This precision, evidently, depends on data S/N and they found that when photon errors become smaller than ∼0.007 an instrumental noise floor is reached. We proceed, in the same way as Lovis et al. (2011), to plot the normalised standard deviations as a function of the average S/N per pixel in the V and R calcium continuum bands ($S/N_{VR,\,pix}$), where a systematic raise of the lower envelope is observed for $S/N_{VR,\,pix} \lesssim 5$. We attribute this effect to instrumental errors, where in addition, under this limit the background subtraction may not be reliable. We therefore selected targets with $S/N_{VR,\,pix} \geq 5$ and at least six measurements to characterise short-term stellar variability.

Here we focus on the short-term variability of stars in the lower end of the main sequence. Figure 8 shows that more active M dwarfs present higher R'_{HK} variability – which is also true for GK dwarfs (e.g. Lovis et al. 2011) – where many stars showing high variability are flare-stars (Gl 551, Gl 54.1, Gl 729, GJ 3379, GJ 234A, and GJ 3148A). The same figure also shows that the distribution of M dwarfs R'_{HK} dispersion peaks at 0.6×10^{-6}, while the same distribution for GK dwarfs peaks at $0.2{\times}10^{-6}$ and it is also narrower. Compared to more massive stars, M dwarfs higher variability and spreader distribution could be due to their lower spin evolution rate, although instrumental effects may not be discarded despite our selection criteria.

7.3. R'_{HK}, stellar masses and V-K

We now turn our attention to the relation between magnetic activity and stellar mass. We consider three groups of stars with masses $M/M_\odot \leq 0.4$, $0.4 < M/M_\odot \leq 0.6$, or $0.6 < M/M_\odot < 0.8$. The $log(R'_{HK})$ distribution for each group is plotted in Fig. 9, where it is shown that the peak of distribution is shifted toward lower R'_{HK} values as the group contains less massive stars. Indeed, for

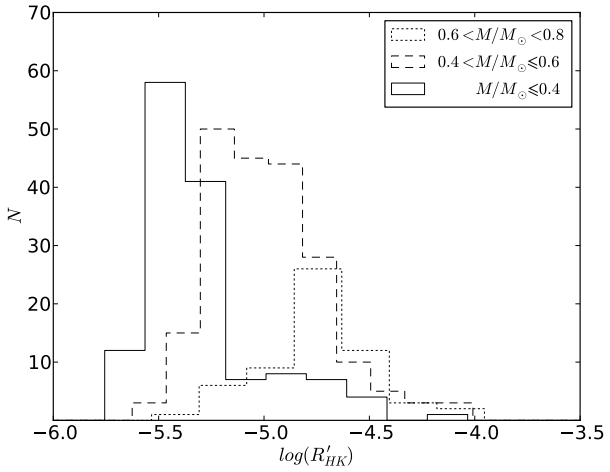

Fig. 9. Distribution of the median $log(R'_{HK})$ for M dwarfs grouped in different mass regime. The total sample is 403 stars with 138 less massive than 0.4M$_\odot$, 206 with masses between 0.4M$_\odot$ and 0.6M$_\odot$, while 59 have masses greater 0.6M$_\odot$. The distribution is shifted toward lower activity levels as the sub-sample it represents contains stars with lower masses.

stars more massive than 0.6M$_\odot$ the distribution peaks at -4.74 – GK dwarfs peaks at -4.95, Lovis et al. (2011); stars ranging from 0.4M$_\odot$ to 0.6M$_\odot$ present the highest peaks of distribution at -5.22; while stars with masses lower than 0.4M$_\odot$ have a high predominant peak at -5.47. Another remark is that the 0.4≤M/M$_\odot$ group exhibits a large tail toward greater $log(R'_{HK})$ values. Figure 10 shows R'_{HK} as a function of mass, where the dependence between magnetic activity and mass is visible in a more uniform way. A decrease in R'_{HK} lower envelope from $M \sim 0.6M_\odot$ and toward lower masses is visible until a mass of 0.35M$_\odot$, below this mass the pattern is better described by a constant lower enveloppe at $R_{HK} = 0.44 \times 10^{-5}$ (this is even more visible plotting $log(R'_{HK})$, but with this choice the dispersion is not displayed correctly). The change in the pattern is particularly interesting because the transition from partially to fully convective stars occurs around this mass (Chabrier & Baraffe 2000). Additionally, the scatter is higher toward more active regimes and also more active targets also present more R'_{HK} variability. This suggests that the magnetic variability decreases with age and then when mean activity level decrease also.

Regarding the R'_{HK} index in terms of V-K (Fig. 11), analogously to the activity-mass relation, a decrease in activity toward redder stars is clearly observable. Instead of a uniform pattern, there it is shown two populations forming two trends, one less active (89.9% of the sample) and another more with active stars (10.1%); the two populations may be explained by the manner the sample was built – selecting less active M dwarfs – and by targets without or with Hα emission (dM and dMe stars), although an Hα analysis is beyond the scope of this paper. This finding is in agreement with Rauscher & Marcy (2006) and Mittag et al. (2013). In a R'_{HK} vs. B-V (from 0.45 to 1.6) plot Mittag et al. (2013) noticed an activity rise in the 1.1≤B-V≤1.3 range followed by a decrease when 1.3≤B-V≤1.5, although whether the decrease stops or not is not well established in their work (latest spectral type is M3). They ruled out a statistical fluctuation to explain such an effect. In the other hand, Rauscher & Marcy (2006) found an increase in the Ca II H&K full-with at half-maximum with brighter υ-band absolute magnitude in the region from $M_\upsilon \sim 11$ to $M_\upsilon \sim 8$, and here we

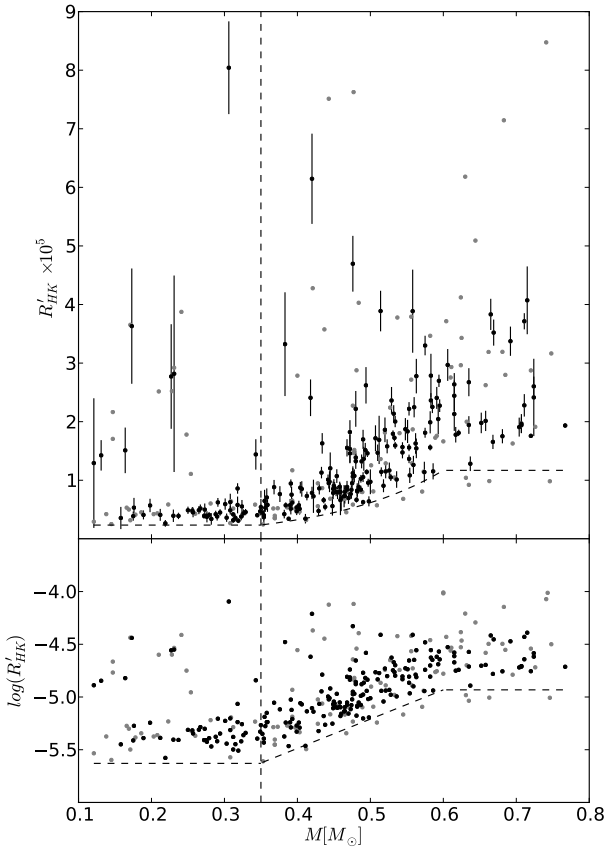

Fig. 10. R'_{HK} and its dispersion as a function of stellar mass. All points satisfy $\delta\pi/\pi < 0.1$ to avoid large mass errors. Targets with S/N$_{VR,\,pix}$ >5 and more than six measurements are represented with black dots. Grey dots represent stars with S/N$_{VR,\,pix}$ <5 or less than six measurements. A decrease of activity is visible as the mass decrease until the star becomes fully convective (0.35M$_\odot$, represented by the vertical dashed line). Interestingly, M dwarfs departing further from the lower envelope (dashed curve) are those which present higher variability.

found that the R'_{HK} decreases in the same M_υ range. The figure 5 of Browning et al. (2010), showing L_{Ca}/L_{Bol} in function spectral type for M dwarfs, shows similar behaviour same if it is less clear than in our Fig. 11.

The nature of this effect it is still uncertain. However, it is not seen when tracing stellar activity through $L_{H\alpha}/L_{bol}$ as this activity index remains constant for spectral type from M0 to M5 and it declines at M5-M6 (West et al. 2004). We recall that Ca II H&K and Hα traces different chromosphere heights and that they do not correlate for intermediate or weak activity stars, while active stars show a positive correlation (Rauscher & Marcy 2006; Walkowicz & Hawley 2009).

8. Conclusions

We used high-resolution spectra from the HARPS M dwarf sample to analyse the magnetic activity against stellar rotation, mass, and colour-indices. For this purpose we used the R'_{HK}-index, and thus, we firstly updated the bolometric C_{cf} and photospheric R_{phot} calibration factors by extending their B-V relationships up to B-V=1.90, corresponding to spectral type M6. We determine C_{cf} and R_{phot} in function of I-K and V-K and show that the results is more accurate for this last case. These new calibrations

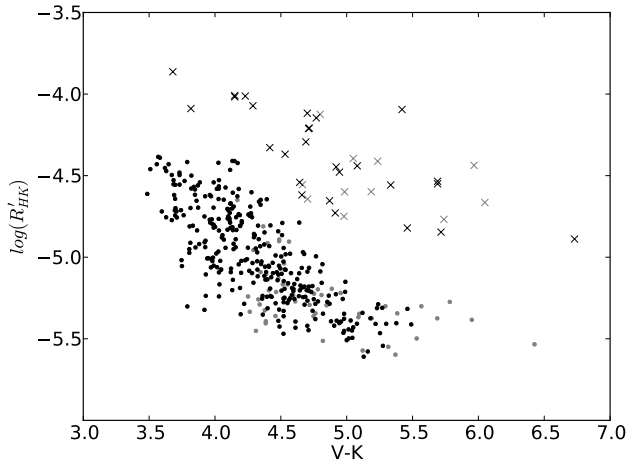

Fig. 11. $log(R'_{HK})$ as a function of V-K color index. Black and gray represents targets with $S/N_{VR,\,pix}$ greater and lower than 5 respectively. Dots and crosses stands for an estimation of less active and more active stars.

were made, in the case of C_{cf}, by using GK dwarfs as standards which were observed in the same conditions as M dwarfs and, in the case of R_{phot}, by using PHOENIX synthetic spectra to replace Ca II H&K chromospheric emission by models accounting only the photosphere. These updated calibrations allows a confident transformation from the S-index to R'_{HK} for M dwarfs. Extrapolating Rutten (1984) C_{cf}–B-V relationship to redder domains gives close values to our calibrated relationship, however, an extrapolation to the relationship given by Middelkoop (1982) or Noyes et al. (1984) shows considerable differences, producing overestimated R'_{HK} values (e.g. Tinney et al. 2002; Jenkins et al. 2006).

On analysing $log(R'_{HK})$ vs. $log(P_{rot})$, two regime are show for M0-M6 dwarfs. A saturation regime is reached for $P < 10\,d$ ($Ro \approx 0.1$, in using $\tau_c = 70\,d$) while a linear regime is present for longer rotational period (activity decrease when rotational period increase). For this last case, we noticed that the relationship linking R'_{HK} to P_{rot} has a slope which is close to what was observed with other activity tracers (like L_X/L_{bol} or Bf, Kiraga & Stepien 2007; Reiners et al. 2009). This result is the expected behaviour in a canonical picture where as a star ages, it loses angular momentum, and hence, its rotation slows weakening the magnetic activity. The foregoing assertion is well understood in an $\alpha\Omega$-dynamo process, however, it is still unclear why the magnetic activity of fully convective stars – explained by a turbulent-dynamo process – exhibit a rotation dependence.

The magnetic activity shows a mass dependence for M dwarfs. The R'_{HK} describes a lower envelope decreasing with decreasing stellar mass until $M \sim 0.35 M_{\odot}$, corresponding to the transition from partially convective to fully convective stars. Below this mass limit, the lower envelope remains constant. Over these lower envelopes describing the two regimes, some points spread toward higher activity levels while, in comparison to points near the lower envelopes, the activity short-term variability is larger. This finding shows that M dwarfs R'_{HK} basal values are mass dependent, and this dependence is in the opposite direction when compared to K dwarfs, as according to Mittag et al. (2013) this kind of stars shows that R'_{HK} increases with decreasing mass. The presence of a dent in the basal R'_{HK} ($S_{M.W.}$) vs. colour-index (mass) plot is not understood, however in the corresponding colour-index (spectral type), it seems to match the curve profile shape of main-sequence stars in the Hertzsprung-Russell diagram.

Besides the study of surface magnetic fields itself, our relation (22) furnishing an estimation of P_{rot} in function of R'_{HK}, gains importance in the context of extra-solar planet searches. Stellar rotation plays an important role to reject false-positives. Indeed, stellar activity can mimic the RV signature of a planetary companion (e.g. Bonfils et al. 2007; Robertson et al. 2014) and serious doubts about the nature of RVs signatures arise when the stellar rotation period – or one of its harmonics (Boisse et al. 2011) – is near the RV periodicity. In this scenario eq.(22) can be used as a proxy when stellar rotation is not known for RVs analysis.

Acknowledgements. The authors acknowledge Nadège Meunier for her precious advises and insights. N. A. acknowledges support from CONICYT Becas-Chile 72120460. X. B., X. D., and T. F. acknowledge the support of the French Agence Nationale de la Recherche (ANR), under the program ANR-12-BS05-0012 Exo-atmos.

References

Allard, F. 2013, in Proceedings of the International Astronomical Union, Vol. 8, Exploring the Formation and Evolution of Planetary Systems, 271–272
Allard, F. 2014, in IAU Symposium, Vol. 299, IAU Symposium, ed. M. Booth, B. C. Matthews, & J. R. Graham, 271–272
Barnes, S. A. 2003, ApJ, 586, 464
Bercik, D. J., Fisher, G. H., Johns-Krull, C. M., & Abbett, W. P. 2005, ApJ, 631, 529
Blanco, C., Catalano, S., Marilli, E., & Rodonò, M. 1974, A&A, 33, 257
Boisse, I., Bonfils, X., & Santos, N. C. 2012, A&A, 545, A109
Boisse, I., Bouchy, F., Hébrard, G., et al. 2011, A&A, 528, A4
Bonfils, X., Delfosse, X., Udry, S., et al. 2013, A&A, 549, A109
Bonfils, X., Gillon, M., Udry, S., et al. 2012, A&A, 546, A27
Bonfils, X., Mayor, M., Delfosse, X., et al. 2007, A&A, 474, 293
Boyajian, T. S., von Braun, K., van Belle, G., et al. 2012, ApJ, 757, 112
Browning, M. K., Basri, G., Marcy, G. W., West, A. A., & Zhang, J. 2010, AJ, 139, 504
Carpenter, J. M. 2001, AJ, 121, 2851
Chabrier, G. & Baraffe, I. 2000, ARA&A, 38, 337
Cutri, R. M., Skrutskie, M. F., van Dyk, S., et al. 2003, VizieR Online Data Catalog, 2246, 0
Delfosse, X., Forveille, T., Perrier, C., & Mayor, M. 1998, A&A, 331, 581
Delfosse, X., Forveille, T., Ségransan, D., et al. 2000, A&A, 364, 217
Delorme, P., Collier Cameron, A., Hebb, L., et al. 2011, MNRAS, 413, 2218
Donati, J.-F., Morin, J., Petit, P., et al. 2008, MNRAS, 390, 545
Ducati, J. R., Bevilacqua, C. M., Rembold, S. B., & Ribeiro, D. 2001, ApJ, 558, 309
Dumusque, X., Santos, N. C., Udry, S., Lovis, C., & Bonfils, X. 2011a, A&A, 527, A82
Dumusque, X., Udry, S., Lovis, C., Santos, N. C., & Monteiro, M. J. P. F. G. 2011b, A&A, 525, A140
Ehrenreich, D. & Désert, J.-M. 2011, A&A, 529, A136
Flower, P. J. 1996, ApJ, 469, 355
Gaidos, E., Mann, A. W., Lépine, S., et al. 2014, MNRAS, 443, 2561
Gastine, T., Morin, J., Duarte, L., et al. 2013, A&A, 549, L5
Gray, D. F. 2005, The Observation and Analysis of Stellar Photospheres
Hall, J. C., Lockwood, G. W., & Skiff, B. A. 2007, AJ, 133, 862
Hartmann, L., Soderblom, D. R., Noyes, R. W., Burnham, N., & Vaughan, A. H. 1984, ApJ, 276, 254
Hawley, S. L., Gizis, J. E., & Reid, N. I. 1997, AJ, 113, 1458
Henry, T. J., Soderblom, D. R., Donahue, R. A., & Baliunas, S. L. 1996, AJ, 111, 439
Irwin, J., Berta, Z. K., Burke, C. J., et al. 2011, ApJ, 727, 56
Isaacson, H. & Fischer, D. 2010, ApJ, 725, 875
Jenkins, J. S., Jones, H. R. A., Tinney, C. G., et al. 2006, MNRAS, 372, 163
Jenkins, J. S. & Tuomi, M. 2014, ArXiv e-prints
Kiraga, M. & Stepien, K. 2007, Acta Astron., 57, 149
Lagrange, A.-M., Desort, M., & Meunier, N. 2010, A&A, 512, A38
Lammer, H., Bredehöft, J. H., Coustenis, A., et al. 2009, A&A Rev., 17, 181
Leggett, S. K. 1992, ApJS, 82, 351
Leggett, S. K., Allard, F., Geballe, T. R., Hauschildt, P. H., & Schweitzer, A. 2001, ApJ, 548, 908
Lépine, S. & Gaidos, E. 2011, AJ, 142, 138

Linsky, J. L. & Ayres, T. R. 1978, ApJ, 220, 619
Lovis, C., Dumusque, X., Santos, N. C., et al. 2011, ArXiv e-prints
Lovis, C. & Pepe, F. 2007, A&A, 468, 1115
Mamajek, E. E. & Hillenbrand, L. A. 2008, ApJ, 687, 1264
Mayor, M., Pepe, F., Queloz, D., et al. 2003, The Messenger, 114, 20
Meunier, N., Desort, M., & Lagrange, A.-M. 2010, A&A, 512, A39
Meunier, N. & Lagrange, A.-M. 2013, A&A, 551, A101
Middelkoop, F. 1982, A&A, 107, 31
Mittag, M., Schmitt, J. H. M. M., & Schröder, K.-P. 2013, A&A, 549, A117
Morin, J., Donati, J.-F., Petit, P., et al. 2008, MNRAS, 390, 567
Morin, J., Donati, J.-F., Petit, P., et al. 2010, MNRAS, 407, 2269
Neves, V., Bonfils, X., Santos, N. C., et al. 2013, A&A, 551, A36
Noyes, R. W., Hartmann, L. W., Baliunas, S. L., Duncan, D. K., & Vaughan, A. H. 1984, ApJ, 279, 763
Parker, E. N. 1955, ApJ, 122, 293
Perryman, M. A. C. & ESA, eds. 1997, ESA Special Publication, Vol. 1200, The HIPPARCOS and TYCHO catalogues. Astrometric and photometric star catalogues derived from the ESA HIPPARCOS Space Astrometry Mission
Queloz, D., Henry, G. W., Sivan, J. P., et al. 2001, A&A, 379, 279
Rauscher, E. & Marcy, G. W. 2006, PASP, 118, 617
Reiners, A. & Basri, G. 2007, ApJ, 656, 1121
Reiners, A., Basri, G., & Browning, M. 2009, ApJ, 692, 538
Reiners, A., Joshi, N., & Goldman, B. 2012, AJ, 143, 93
Reiners, A., Schüssler, M., & Passegger, V. M. 2014, ApJ, 794, 144
Ribas, I., Guinan, E. F., Güdel, M., & Audard, M. 2005, ApJ, 622, 680
Robertson, P., Mahadevan, S., Endl, M., & Roy, A. 2014, Science, 345, 440
Rutten, R. G. M. 1984, A&A, 130, 353
Santos, N. C., Mayor, M., Naef, D., et al. 2000, A&A, 361, 265
Santos, N. C., Mortier, A., Faria, J. P., et al. 2014, A&A, 566, A35
Scalo, J., Kaltenegger, L., Segura, A. G., et al. 2007, Astrobiology, 7, 85
Schrinner, M., Petitdemange, L., Raynaud, R., & Dormy, E. 2014, A&A, 564, A78
Sousa, S. G., Santos, N. C., Mayor, M., et al. 2008, A&A, 487, 373
Stepien, K. 1993, in IAU Symposium, Vol. 157, The Cosmic Dynamo, ed. F. Krause, K. H. Radler, & G. Rudiger, 141
Strassmeier, K., Washuettl, A., Granzer, T., Scheck, M., & Weber, M. 2000, A&AS, 142, 275
Tinney, C. G., McCarthy, C., Jones, H. R. A., et al. 2002, MNRAS, 332, 759
Tuomi, M., Anglada-Escude, G., Jenkins, J. S., & Jones, H. R. A. 2014, ArXiv e-prints
van Altena, W. F., Lee, J. T., & Hoffleit, E. D. 1995, The general catalogue of trigonometric [stellar] parallaxes
van Leeuwen, F. 2007, A&A, 474, 653
Vaughan, A. H. & Preston, G. W. 1980, PASP, 92, 385
Vaughan, A. H., Preston, G. W., & Wilson, O. C. 1978, PASP, 90, 267
Ventura, P., Zeppieri, A., Mazzitelli, I., & D'Antona, F. 1998, A&A, 334, 953
Vidotto, A. A., Jardine, M., Morin, J., et al. 2014, MNRAS, 438, 1162
Walkowicz, L. M. & Hawley, S. L. 2009, AJ, 137, 3297
West, A. A., Hawley, S. L., Walkowicz, L. M., et al. 2004, AJ, 128, 426
Wilson, O. C. 1968, ApJ, 153, 221
Wilson, O. C. 1978, ApJ, 226, 379
Wright, J. T., Marcy, G. W., Butler, R. P., & Vogt, S. S. 2004, ApJS, 152, 261

Appendix A: Tables

Table A.1. Median values for C_{cf} and for R_{phot} for M dwarfs. N is the number of spectra satisfying restrictions described in Sect. 4. C_{cf} values are derived from eq. (14); R_{phot} is obtained with equations (2), (3), (4), and (17) after the reversal Ca II H&K emission was replaced by the corresponding BT-Settl spectrum.

Name	N	B-V	I-K	V-K	BC_v	$\log(C_{cf})$	$\log(R_{phot})$
Gl 1	28	1.48	1.900	4.030	-1.278	-1.089	-5.659
Gl 191	3	1.56	1.807	3.767	-1.492	-1.161	-5.460
Gl 205	34	1.47	2.010	4.080	-1.698	-1.145	-5.459
Gl 229	7	1.50	1.960	3.970	-1.487	-1.121	-5.441
Gl 393	3	1.51	2.075	4.315	-1.888	-1.235	-5.448
Gl 551	17	1.90	3.080	6.730	-3.808	-2.338	-5.881
Gl 581	50	1.60	2.200	4.710	-2.283	-1.385	-5.691
Gl 588	4	1.53	2.147	4.527	-1.864	-1.331	-5.663
Gl 628	10	1.58	2.301	4.981	-2.064	-1.431	-5.702
Gl 674	38	1.53	2.101	4.501	-2.049	-1.326	-5.715
Gl 699	3	1.73	2.260	5.040	-2.392	-1.558	-5.736
Gl 849	17	1.50	2.262	4.762	-2.357	-1.329	-5.704
Gl 876	17	1.58	2.416	5.146	-3.808	-1.447	-5.826
Gl 887	31	1.50	1.940	3.960	-1.402	-1.131	-5.497

Table A.2. C_{cf} and median R_{phot} for standards. C_{cf} values are derived from Middelkoop (1982)'s relation. R_{phot} is obtained in the same way as is described in table A.1.

Name	B-V	I-K	V-K	BC_v	$\log(C_{cf})$	$\log(R_{phot})$	Name	B-V	I-K	V-K	BC_v	$\log(C_{cf})$	$\log(R_{phot})$
BD-013125	1.24	–	–	-0.671	-0.813	–	HD 20868	1.04	–	–	-0.422	-0.469	–
BD-044138	1.19	–	–	-0.601	-0.723	–	HD 208704	0.64	–	1.475	-0.085	0.042	-4.542
HD 10180	0.63	–	1.438	-0.079	0.050	-4.513	HD 209449	0.72	–	–	-0.138	-0.028	–
HD 10700	0.72	0.730	–	-0.139	-0.03	-4.708	HD 210752	0.54	–	1.364	-0.03	0.101	-4.416
HD 109271	0.66	–	–	-0.097	0.028	–	HD 210918	0.65	–	1.544	-0.091	0.034	-4.596
HD 114613	0.70	0.650	–	-0.124	-0.01	-4.657	HD 211038	0.89	–	–	-0.277	-0.243	–
HD 114747	0.92	–	2.013	-0.304	-0.287	-4.775	HD 212708	0.73	–	–	-0.146	-0.041	–
HD 11505	0.64	–	1.521	-0.085	0.042	-4.561	HD 213042	1.08	–	2.511	-0.471	-0.54	-4.993
HD 115617	0.71	–	–	-0.132	-0.02	-4.657	HD 213240	0.60	–	1.432	-0.063	0.069	-1.729
HD 123180	1.02	–	–	-0.406	-0.447	–	HD 213575	0.67	–	1.609	-0.104	0.017	-4.648
HD 124364	0.67	–	1.627	-0.104	0.017	-4.647	HD 214867	0.66	–	1.535	-0.099	0.025	–
HD 124785	0.57	–	–	-0.047	0.086	–	HD 215152	0.97	–	2.311	-0.352	-0.363	-4.964
HD 125455	0.87	–	2.015	-0.259	-0.215	-4.812	HD 217221	0.94	–	–	-0.324	-0.32	–
HD 125595	1.11	–	–	-0.502	-0.585	–	HD 217395	0.58	–	–	-0.052	0.080	–
HD 125612	0.63	–	–	-0.078	0.051	–	HD 21749	1.13	–	2.681	-0.528	-0.623	-4.985
HD 126525	0.68	–	1.611	-0.111	0.009	-4.619	HD 220339	0.88	–	2.185	-0.268	-0.229	-4.932
HD 126999	1.19	–	–	-0.594	-0.715	–	HD 220456	0.63	–	–	-0.077	0.053	–
HD 127339	1.40	–	–	-0.926	-1.061	–	HD 220507	0.69	–	1.595	-0.117	-0.001	–
HD 128674	0.67	–	1.667	-0.104	0.017	-4.664	HD 221503	1.29	–	–	-0.736	-0.887	–
HD 129191	0.68	–	–	-0.112	0.007	–	HD 221580	0.69	–	–	-0.116	0.000	–
HD 129642	0.94	–	2.224	-0.322	-0.317	-4.938	HD 223121	0.94	–	2.145	-0.322	-0.317	-4.67
HD 132569	0.89	–	–	-0.277	-0.243	–	HD 223171	0.66	–	1.511	-0.098	0.026	-4.591
HD 134060	0.62	–	1.430	-0.073	0.057	-1.729	HD 224063	0.73	–	–	-0.149	-0.045	–
HD 134088	0.60	–	–	-0.06	0.072	–	HD 24633	0.83	–	–	-0.223	-0.158	–
HD 134440	0.88	0.970	2.260	-0.268	-0.229	–	HD 27063	0.67	–	1.524	-0.104	0.017	-4.563
HD 134664	0.66	–	1.488	-0.098	0.026	-4.546	HD 28821	0.68	–	1.589	-0.111	0.009	-4.619
HD 135625	0.62	–	–	-0.071	0.059	–	HD 290327	0.76	–	–	-0.169	-0.075	–
HD 136352	0.65	–	–	-0.091	0.034	-4.59	HD 30177	0.77	–	–	-0.178	-0.089	–
HD 136713	0.97	–	2.223	-0.352	-0.363	-4.903	HD 31527	0.61	–	1.417	-0.067	0.064	-4.506
HD 13808	0.87	–	2.086	-0.259	-0.215	-4.846	HD 31822	0.58	–	1.315	-0.05	0.082	-1.729
HD 144411	0.98	–	2.379	-0.361	-0.378	-4.954	HD 3220	0.60	–	–	-0.062	0.069	–
HD 144585	0.66	–	1.496	-0.098	0.026	-4.561	HD 323631	0.93	–	–	-0.313	-0.302	–
HD 144628	0.86	–	2.105	-0.25	-0.201	-4.921	HD 323684	1.27	–	–	-0.703	-0.85	–
HD 145377	0.62	–	–	-0.075	0.055	–	HD 330075	0.94	–	2.165	-0.317	-0.309	-4.723
HD 1461	0.67	–	1.549	-0.104	0.017	-4.577	HD 36003	1.11	–	2.746	-0.505	-0.59	-5.14
HD 146233	0.65	–	–	-0.091	0.034	-4.578	HD 36379	0.56	–	1.362	-0.039	0.093	-1.729
HD 147512	0.72	–	1.694	-0.139	-0.03	-4.668	HD 3823	0.56	–	–	-0.039	0.093	-1.729
HD 147642	0.57	–	–	-0.046	0.087	–	HD 38973	0.59	–	1.386	-0.055	0.077	-1.729
HD 147935	0.73	–	–	-0.148	-0.044	–	HD 40307	0.94	–	2.353	-0.322	-0.317	-5.07
HD 148211	0.55	–	–	-0.036	0.096	–	HD 40865	0.63	–	–	-0.077	0.053	–
HD 148303	0.98	–	2.315	-0.361	-0.378	-4.933	HD 44420	0.69	–	1.508	-0.117	-0.001	-4.535
HD 148577	0.66	–	–	-0.10	0.023	–	HD 44573	0.92	–	2.181	-0.304	-0.287	-4.868
HD 149396	0.70	–	–	-0.127	-0.014	–	HD 45184	0.62	–	1.495	-0.073	0.057	-4.561
HD 153950	0.56	–	–	-0.042	0.090	–	HD 457	0.62	–	–	-0.073	0.057	–
HD 154577	0.89	–	2.265	-0.277	-0.243	-5.041	HD 47186	0.71	–	1.601	-0.132	-0.02	-4.599
HD 156411	0.61	–	–	-0.069	0.061	–	HD 4915	0.66	–	1.607	-0.098	0.026	-4.629
HD 157338	0.59	–	1.402	-0.055	0.077	-1.729	HD 52919	1.08	–	2.601	-0.471	-0.54	-5.055
HD 160691	0.69	–	–	-0.12	-0.005	-4.613	HD 564	0.59	–	–	-0.058	0.074	–
HD 16280	1.06	–	–	-0.448	-0.507	–	HD 59468	0.69	–	1.654	-0.117	-0.001	-4.627
HD 163436	0.92	–	–	-0.303	-0.285	–	HD 69830	0.75	–	–	-0.161	-0.063	-4.704
HD 166724	0.86	–	2.060	-0.25	-0.201	-4.839	HD 7134	0.59	–	1.417	-0.055	0.077	-4.505
HD 16714	0.71	–	1.689	-0.132	-0.02	-4.647	HD 71835	0.77	–	1.740	-0.176	-0.086	-4.664
HD 171028	0.61	–	–	-0.067	0.064	–	HD 8326	0.97	–	2.232	-0.352	-0.363	-4.814
HD 172513	0.75	–	1.694	-0.161	-0.063	-4.672	HD 8638	0.68	–	1.649	-0.111	0.009	-4.633
HD 181433	1.01	–	2.282	-0.392	-0.426	-4.847	HD 92588	0.88	–	–	-0.268	-0.229	-4.889
HD 188559	1.05	–	2.448	-0.437	-0.491	-4.941	HD 9578	0.61	–	–	-0.068	0.063	–
HD 191797	0.91	–	–	-0.291	-0.266	–	HD 967	0.65	–	1.614	-0.091	0.034	-4.613
HD 192310	0.88	–	–	-0.268	-0.229	-4.862	HD 96700	0.61	–	1.491	-0.067	0.064	-4.554
HD 199960	0.64	–	1.415	-0.085	0.042	-1.729	HIP 102964	1.01	–	–	-0.392	-0.426	–
HD 200538	0.61	–	–	-0.065	0.067	–	HIP 107758	1.37	–	–	-0.86	-1.008	–
HD 202206	0.71	–	1.571	-0.135	-0.024	-4.518	HIP 117865	1.10	–	–	-0.492	-0.57	–
HD 202871	0.56	–	–	-0.04	0.092	–	HIP 5158	1.08	–	–	-0.469	-0.537	–
HD 20794	0.71	0.720	–	-0.132	-0.02	-4.689	HD 207129	0.60	–	–	-0.061	0.070	-4.518

Table A.3. The Ca II H&K analysis for the HARPS M dwarf sample. We listed the V magnitude, B-V, V-K colour-indexes and their references (Ref. Phot., see below); the parallax (π), its uncertainty (σ_π) and the references (Ref. π, see below); the stellar masses; the number of spectra used in the analysis for a given target (N_{mes}); the median of the S-index and its dispersion (σ_S); the median of the R'_{HK} and its dispersion ($\sigma_{R'_{HK}}$); the rotation period derived from eq. 22; and the averaged S/N in the violet and red bands. References: (1) : Leggett (1992); (2) : Gaidos et al. (2014); (3) : van Leeuwen (2007); (4) : van Altena et al. (1995); (5) : RECONS; (6) : Lépine & Gaidos (2011).

Name	V	B-V	V-K	π	σ_π	Ref.	M	N_{mes}	S	σ_S	$log(R'_{HK})$	$\sigma_{R'_{HK}}$	P_{rot}	S/N_{VR}
				[mas]	[mas]	Phot, π	M/M$_\odot$					$\times 10^5$	[d]	
Gl551	11.09	1.90	6.730	771.64	2.60	(3),(1)	0.12	76	11.265	9.641	-4.888	1.107	43	7.5
Gl388	9.32	1.53	4.710	204.60	2.80	(4),(1)	0.42	41	8.690	1.089	-4.211	0.770	12	28.3
LHS3746	11.82	1.54	5.078	134.29	1.31	(5),(2)	0.24	6	0.783	0.109	-5.408	0.054	116	7.2
HIP74261	10.73	1.28	3.558	41.26	2.31	(3),(2)	0.60	5	1.685	0.079	-4.430	0.175	18	12.4
HD329868	10.81	1.21	3.698	46.39	3.65	(3),(2)	0.56	6	1.452	0.154	-4.556	0.295	23	10.4
HD329879	11.25	1.34	3.731	36.84	2.45	(3),(2)	0.58	12	1.506	0.202	-4.555	0.373	23	10.1
LHS1134	13.05	1.59	5.316	113.90	34.20	(6),(2)	0.17	6	0.665	0.452	-5.549	0.110	152	3.2
GJ163	11.82	1.52	4.680	66.69	1.82	(3),(1)	0.40	179	0.703	0.135	-5.291	0.098	93	9.4
HIP19394	11.90	1.37	4.741	66.69	1.82	(3),(2)	0.40	20	0.684	0.094	-5.328	0.064	100	9.3
BD-12066	10.12	1.25	3.648	45.28	1.97	(3),(2)	0.71	8	1.846	0.069	-4.430	0.138	18	17.4
BD-12052	10.92	1.24	3.672	33.76	1.88	(3),(2)	0.68	3	1.626	0.110	-4.496	0.216	20	8.4
BD-09095	10.41	1.33	4.115	50.80	3.74	(3),(2)	0.69	5	1.292	0.084	-4.788	0.106	35	11.2
BD-12617	10.27	1.23	3.848	45.00	2.68	(3),(2)	0.72	21	1.583	0.101	-4.585	0.167	24	15.2
Gl832	8.66	1.50	4.180	201.87	1.01	(3),(1)	0.45	62	0.765	0.097	-5.044	0.114	58	38.0
Gl887	7.34	1.50	3.960	305.26	0.70	(3),(1)	0.49	76	1.155	0.111	-4.770	0.163	34	48.3
LTT9759	10.34	1.09	4.767	100.07	1.05	(3),(2)	0.54	11	1.512	0.211	-4.994	0.142	52	14.4
GJ1001	12.85	1.62	5.089	76.86	3.97	(5),(2)	0.26	15	0.867	0.156	-5.368	0.077	108	4.1
Gl1	8.55	1.48	4.030	230.42	0.90	(3),(1)	0.39	48	0.419	0.077	-5.240	0.106	84	44.0
L225-57	12.61	1.53	5.275	97.00	29.10	(6),(2)	0.25	11	0.687	0.146	-5.543	0.061	151	5.6
Gl145	11.59	1.44	4.659	93.11	1.94	(3),(2)	0.32	7	1.158	0.121	-5.066	0.090	60	10.0
GJ1061	13.06	1.83	6.426	271.92	1.34	(5),(2)	0.12	6	1.963	0.337	-5.534	0.050	148	3.1
Gl191	8.84	1.56	3.790	255.66	0.91	(3),(1)	0.27	31	0.286	0.060	-5.302	0.104	95	38.8
HIP31293	10.60	1.36	4.714	110.88	2.25	(3),(2)	0.43	9	1.222	0.147	-5.065	0.104	60	14.2
HIP31292	11.50	1.51	4.918	115.19	10.61	(3),(2)	0.30	19	1.021	0.166	-5.227	0.096	82	7.3
Gl358	10.72	1.49	4.660	105.63	1.64	(3),(1)	0.42	37	3.246	0.422	-4.618	0.313	25	16.4
Gl367	10.29	1.33	4.486	101.31	3.18	(3),(2)	0.48	25	1.010	0.128	-5.053	0.112	59	22.1
GJ1123	13.16	1.61	5.688	110.92	2.02	(5),(2)	0.20	5	1.477	0.320	-5.375	0.092	109	2.4
Gl803	8.81	1.45	4.230	100.91	1.06	(3),(1)	0.74	4	8.637	0.323	-4.012	0.363	10	32.1
LHS3583	11.60	1.52	4.750	94.72	2.38	(5),(2)	0.32	6	0.812	0.162	-5.257	0.110	87	6.4
Gl908	8.98	1.47	3.930	167.29	1.23	(3),(1)	0.42	89	0.518	0.069	-5.106	0.105	65	36.8
Gl54.1	12.16	1.74	5.716	271.01	8.36	(3),(2)	0.13	15	5.115	0.933	-4.846	0.260	39	5.9
Gl105B	11.66	1.61	5.050	137.00	27.40	(3),(1)	0.25	21	0.715	0.253	-5.430	0.057	121	9.1
GJ1057	13.79	1.82	5.950	105.80	5.10	(2),(1)	0.18	6	1.828	0.501	-5.384	0.113	111	3.1
GJ1065	12.87	1.65	5.095	105.40	21.10	(2),(2)	0.18	7	0.914	0.406	-5.347	0.200	103	4.2
Gl176	10.14	1.35	4.509	107.83	2.85	(3),(2)	0.49	71	1.593	0.238	-4.864	0.204	41	20.8
LHS1723	12.22	1.70	5.460	187.92	1.26	(5),(2)	0.16	7	4.298	1.108	-4.821	0.389	38	5.4
Gl205	7.95	1.47	4.080	176.77	1.18	(3),(1)	0.64	103	2.050	0.184	-4.573	0.239	23	43.9
Gl213	11.53	1.64	5.160	171.55	3.99	(3),(1)	0.22	19	0.571	0.123	-5.578	0.057	161	8.3
Gl229	8.12	1.50	3.970	173.81	0.99	(3),(1)	0.58	24	1.624	0.086	-4.627	0.125	26	57.6
Gl250B	10.25	1.31	4.503	114.80	0.40	(2),(2)	0.44	12	1.171	0.102	-4.996	0.088	53	19.5
Gl273	9.86	1.57	4.980	262.98	1.39	(3),(1)	0.29	98	0.765	0.110	-5.377	0.060	110	24.4
Gl285	11.15	1.61	5.420	167.88	2.31	(3),(1)	0.31	7	22.068	2.173	-4.095	0.792	10	7.8
Gl299	12.83	1.72	5.190	148.70	6.00	(2),(1)	0.14	23	0.880	0.419	-5.374	0.167	109	3.4
Gl300	12.19	1.62	5.461	125.60	0.97	(5),(2)	0.26	39	1.374	0.171	-5.317	0.060	97	9.1
Gl357	11.02	1.50	4.521	110.82	1.92	(3),(2)	0.33	51	0.510	0.127	-5.362	0.067	106	13.4
Gl382	9.26	1.50	4.170	127.08	1.90	(3),(1)	0.53	33	1.979	0.193	-4.627	0.231	26	29.5
Gl393	9.65	1.51	4.310	141.50	2.22	(3),(1)	0.43	29	1.087	0.094	-4.947	0.098	48	28.9
Gl876	10.18	1.58	5.120	213.28	2.12	(3),(1)	0.33	184	0.949	0.111	-5.341	0.053	102	18.9
Gl12	12.64	1.63	4.809	85.85	2.57	(5),(2)	0.22	5	0.911	0.229	-5.232	0.147	83	4.7
Gl83.1	12.41	1.72	5.738	217.70	8.60	(2),(2)	0.15	25	6.244	1.516	-4.768	0.414	34	4.8
LHS1610	13.86	1.70	5.783	101.57	2.07	(5),(2)	0.17	2	2.028	0.170	-5.274	0.045	90	2.5
LHS1731	11.83	1.54	4.870	108.61	2.66	(3),(2)	0.27	9	0.853	0.112	-5.285	0.068	92	7.8
Gl203	12.49	1.55	4.924	113.50	5.01	(3),(2)	0.19	10	0.698	0.251	-5.389	0.077	112	5.2
G108-21	12.12	1.53	4.762	77.90	2.80	(2),(2)	0.31	4	0.768	0.096	-5.286	0.065	92	7.4
LHS1935	11.80	1.53	4.713	94.31	3.31	(3),(2)	0.29	8	0.883	0.106	-5.206	0.075	79	7.7
GJ2066	10.23	1.42	4.440	109.62	1.54	(3),(2)	0.45	8	0.872	0.078	-5.097	0.071	64	21.5
Gl87	10.04	1.45	3.990	96.02	1.66	(3),(1)	0.46	25	0.622	0.062	-5.052	0.088	59	21.0
LHS1481	12.71	1.71	4.487	95.50	10.90	(2),(2)	0.17	9	0.525	0.328	-5.321	0.171	98	5.1
GJ1125	11.80	1.46	4.905	103.46	3.94	(3),(2)	0.29	9	0.647	0.116	-5.420	0.068	119	10.2
GJ1129	12.50	1.60	5.219	90.93	3.78	(5),(2)	0.28	6	0.890	0.108	-5.409	0.047	116	5.1
Gl402	11.65	1.65	5.230	147.92	3.52	(3),(1)	0.25	6	1.123	0.143	-5.312	0.062	97	8.9
Gl880	8.66	1.49	4.130	146.09	1.00	(3),(1)	0.58	27	1.602	0.152	-4.701	0.189	30	32.1

Table A.3. continued.

Name	V	B-V	V-K	π [mas]	σ_π [mas]	Ref. Phot./π	M M/M$_\odot$	N_{mes}	S	σ_S	$log(R'_{HK})$	$\sigma_{R'_{HK}}$ $\times 10^5$	P_{rot} [d]	S/N_{VR}
LHS543	11.77	1.41	5.239	91.00	2.89	(3),(2)	0.39	7	1.196	0.228	-5.288	0.098	92	9.2
HIP38594	9.89	1.21	3.697	51.52	1.46	(3),(2)	0.71	17	1.190	0.100	-4.642	0.192	27	16.5
Gl433	9.82	1.51	4.200	112.58	1.44	(3),(1)	0.47	86	0.819	0.074	-5.022	0.085	55	23.4
Gl849	10.38	1.50	4.740	109.94	2.07	(3),(1)	0.48	51	0.968	0.066	-5.177	0.046	74	19.8
GJ1265	13.67	1.73	5.531	96.00	3.90	(2),(2)	0.17	5	0.964	0.184	-5.498	0.061	138	2.8
LHS3799	13.31	1.80	5.967	138.17	1.87	(5),(2)	0.17	2	16.407	3.145	-4.437	0.700	18	2.6
HIP6097	11.87	1.40	4.296	45.20	3.50	(3),(2)	0.48	6	1.257	0.124	-4.878	0.131	42	7.3
HIP12961	10.38	1.27	3.620	43.45	1.72	(3),(2)	0.67	46	1.701	0.108	-4.453	0.223	19	18.1
HIP31148	11.49	1.25	3.672	37.57	2.29	(3),(2)	0.51	6	0.860	0.210	-4.772	0.412	34	12.5
HIP34785	10.51	1.19	3.596	37.47	1.93	(3),(2)	0.70	15	0.899	0.076	-4.720	0.162	31	18.8
BD-08258	9.57	0.90	3.789	68.69	1.29	(3),(2)	0.67	18	2.196	0.153	-4.417	0.266	17	16.9
HIP48502	10.30	1.24	3.708	41.45	1.55	(3),(2)	0.73	1	1.010	0.000	-4.719	0.000	31	12.9
HD304043	11.67	1.39	4.611	78.91	2.60	(3),(2)	0.35	18	0.519	0.112	-5.395	0.087	113	10.2
HIP27323	9.9	1.16	3.582	48.18	0.98	(3),(2)	0.71	10	1.892	0.269	-4.390	0.579	16	13.8
BD-09307	10.32	1.33	4.264	81.00	1.91	(3),(2)	0.53	6	1.647	0.054	-4.747	0.059	33	19.2
Gl514	9.05	1.49	3.990	130.62	1.05	(3),(1)	0.52	16	1.107	0.084	-4.802	0.120	36	36.1
Gl555	11.31	1.63	5.300	164.99	3.29	(3),(1)	0.27	14	0.960	0.115	-5.408	0.047	116	11.1
LHS3056	12.90	1.49	5.294	79.60	23.90	(6),(2)	0.27	6	1.223	0.194	-5.301	0.079	95	4.9
Gl581	10.56	1.60	4.710	154.66	2.62	(5),(1)	0.32	248	0.505	0.078	-5.447	0.055	125	16.2
Gl588	9.31	1.53	4.530	168.66	1.30	(3),(1)	0.47	42	1.001	0.091	-5.075	0.077	61	33.3
Gl846	9.17	1.47	3.730	97.61	1.53	(3),(1)	0.57	55	1.782	0.090	-4.482	0.167	20	28.4
GJ1256	13.34	1.83	5.567	114.50	3.20	(2),(2)	0.17	5	1.570	0.731	-5.301	0.233	95	2.5
LP816-60	11.60	1.55	5.377	175.03	3.40	(3),(2)	0.23	7	1.039	0.279	-5.405	0.106	115	10.1
Gl479	10.66	1.55	4.640	103.18	2.31	(3),(1)	0.43	58	2.155	0.232	-4.788	0.175	35	19.8
LHS337	12.78	1.68	5.370	156.78	1.99	(5),(2)	0.14	10	0.663	0.291	-5.597	0.111	167	4.6
Gl480.1	12.29	1.65	4.853	128.52	3.90	(3),(2)	0.18	10	0.863	0.270	-5.274	0.166	90	5.3
Gl526	8.47	1.43	4.010	185.49	1.10	(3),(1)	0.49	34	0.753	0.060	-4.977	0.084	51	43.7
Gl536	9.87	1.25	4.163	99.72	1.57	(3),(2)	0.51	20	1.222	0.117	-4.833	0.140	38	26.5
Gl569A	10.21	1.38	4.416	103.59	1.72	(3),(2)	0.48	23	5.004	0.507	-4.328	0.476	15	15.4
Gl628	10.08	1.58	4.980	232.98	1.60	(3),(1)	0.29	44	0.821	0.101	-5.347	0.055	103	22.7
Gl618A	10.66	1.47	4.686	119.85	2.52	(3),(2)	0.38	20	0.790	0.069	-5.243	0.050	85	18.1
Gl643	11.77	1.69	5.030	148.92	4.00	(3),(1)	0.21	10	0.783	0.195	-5.388	0.102	112	7.1
Gl674	9.38	1.53	4.480	220.24	1.42	(3),(1)	0.34	48	1.633	0.294	-4.841	0.260	39	32.0
Gl682	10.95	1.65	5.270	196.90	2.15	(3),(1)	0.27	21	1.170	0.163	-5.310	0.068	96	12.0
Gl693	10.86	1.52	4.820	171.48	2.31	(3),(2)	0.26	12	0.708	0.129	-5.346	0.082	103	11.6
Gl701	9.37	1.50	4.030	128.89	1.43	(3),(1)	0.47	31	1.063	0.115	-4.836	0.158	39	27.0
GJ1224	13.90	1.16	6.049	126.54	1.05	(5),(2)	0.15	5	10.455	5.401	-4.665	1.118	28	2.3
G141-29	12.81	1.58	5.235	90.09	1.91	(5),(2)	0.24	4	8.967	3.392	-4.412	1.465	17	2.7
Gl729	10.47	1.72	5.080	336.72	2.03	(3),(1)	0.17	8	7.278	1.973	-4.440	0.984	18	12.5
GJ1232	13.31	1.01	5.384	97.40	2.50	(2),(2)	0.19	5	1.202	0.402	-5.344	0.152	103	2.6
Gl413.1	10.59	1.34	4.469	93.00	1.69	(3),(2)	0.46	19	0.907	0.115	-5.092	0.102	63	19.7
Gl465	11.29	1.61	4.490	112.98	2.51	(3),(1)	0.28	22	0.430	0.109	-5.425	0.095	120	10.9
Gl486	11.38	1.56	5.000	119.47	2.69	(3),(1)	0.32	12	0.577	0.076	-5.509	0.041	141	9.1
Gl680	10.26	1.39	4.407	102.83	2.75	(3),(2)	0.47	38	0.936	0.109	-5.052	0.103	59	18.6
Gl678.1A	9.65	1.10	4.204	100.23	1.07	(3),(2)	0.56	32	1.410	0.152	-4.788	0.176	35	27.1
Gl686	9.62	1.53	4.040	123.67	1.61	(3),(1)	0.44	20	0.700	0.068	-5.022	0.092	55	22.5
Gl752A	9.12	1.50	4.460	170.36	1.00	(3),(1)	0.49	24	1.140	0.073	-4.989	0.065	52	37.3
GJ1236	12.46	1.60	4.748	96.90	1.30	(2),(2)	0.21	8	0.638	0.060	-5.361	0.041	106	4.0
HIP95903	11.38	1.29	3.486	28.89	2.73	(3),(2)	0.61	36	1.029	0.110	-4.612	0.261	25	9.0
HIP10688	11.48	1.31	3.805	43.61	2.54	(3),(2)	0.48	7	0.653	0.068	-4.950	0.117	48	12.0
HIP10049	10.69	1.30	3.697	51.58	1.92	(3),(2)	0.54	5	0.942	0.037	-4.744	0.071	32	15.5
BD-03569	10.45	1.19	3.569	45.24	2.05	(3),(2)	0.62	1	1.890	0.000	-4.385	0.000	16	17.0
BD-22621	10.91	1.32	3.769	41.22	2.64	(3),(2)	0.61	3	1.648	0.043	-4.533	0.076	22	14.6
Gl438	10.48	1.37	4.136	91.70	2.05	(5),(2)	0.42	24	0.588	0.230	-5.139	0.284	69	34.2
HIP85126	11.70	1.41	4.157	41.78	4.12	(3),(2)	0.52	8	0.952	0.097	-4.939	0.117	47	8.2
HD162283	10.25	1.30	3.685	45.89	2.18	(3),(2)	0.69	5	1.444	0.205	-4.553	0.396	22	18.1
HIP73194	11.55	1.25	3.690	40.81	4.60	(3),(2)	0.47	3	1.247	0.102	-4.619	0.198	25	13.3
Gl447	11.12	1.76	5.490	298.04	2.30	(3),(1)	0.17	12	1.133	0.228	-5.412	0.078	117	11.5
Gl452.1	12.88	1.61	4.984	88.30	3.70	(2),(2)	0.21	13	4.609	0.848	-4.599	0.463	25	3.6
Gl436	10.66	1.52	4.560	98.61	2.33	(3),(1)	0.44	171	0.668	0.070	-5.263	0.057	88	12.8
HIP55119	9.95	1.18	3.731	56.52	1.28	(3),(2)	0.66	5	1.724	0.238	-4.496	0.440	20	16.7
HIP57459	11.77	1.42	4.677	50.02	3.10	(3),(2)	0.53	5	1.434	0.049	-4.980	0.036	51	11.8
BD-06395	10.28	1.30	3.685	51.64	1.76	(3),(2)	0.62	5	1.530	0.131	-4.528	0.254	21	17.1
BD-07415	10.64	1.36	4.273	71.95	1.88	(3),(2)	0.52	5	1.680	0.346	-4.742	0.373	32	14.5
HIP85647	9.95	1.03	4.101	60.79	1.62	(3),(2)	0.71	43	1.519	0.104	-4.712	0.133	30	16.1
HIP11442	11.46	1.27	3.509	30.28	2.44	(3),(2)	0.58	3	1.495	0.084	-4.460	0.194	19	10.5

Table A.3. continued.

Name	V	B-V	V-K	π [mas]	σ_π [mas]	Ref. Phot./π	M $M/M_\odot$	N_{mes}	S	σ_S	$log(R'_{HK})$	$\sigma_{R'_{HK}}$ $\times 10^5$	P_{rot} [d]	S/N_{VR}
Gl234	11.20	1.62	5.690	242.32	3.12	(3),(2)	0.23	4	10.240	0.777	-4.535	0.222	22	16.9
Gl494	9.76	1.47	4.150	85.54	1.53	(3),(1)	0.60	1	8.044	0.000	-4.009	0.000	10	28.8
Gl699	9.55	1.73	5.040	548.31	1.51	(3),(1)	0.16	102	0.687	0.366	-5.449	0.189	126	21.3
GJ7	11.76	1.44	3.880	42.65	2.65	(3),(2)	0.45	11	0.756	0.170	-4.919	0.271	45	9.6
GJ46	11.86	1.45	4.944	80.95	3.21	(3),(2)	0.37	4	0.696	0.136	-5.404	0.077	115	10.3
GJ1009	11.23	1.39	4.421	55.62	2.32	(3),(2)	0.54	12	1.677	0.089	-4.805	0.083	36	13.9
GJ1036	11.35	1.41	4.388	61.68	3.43	(3),(2)	0.47	1	0.841	0.000	-5.091	0.000	63	13.8
GJ27.1	11.53	1.38	4.112	41.69	2.80	(3),(2)	0.55	50	1.481	0.150	-4.728	0.190	31	11.3
GJ3082	11.17	1.39	4.180	60.38	1.81	(3),(2)	0.47	42	1.542	0.172	-4.739	0.203	32	9.8
GJ3110	11.24	1.31	3.814	42.82	2.36	(3),(2)	0.53	12	1.177	0.057	-4.698	0.097	30	12.8
GJ3098	11.26	1.39	4.136	55.98	1.91	(3),(2)	0.48	1	1.187	0.000	-4.834	0.000	39	13.5
GJ2003	11.72	1.45	4.001	43.11	3.75	(3),(2)	0.47	41	1.087	0.173	-4.814	0.243	37	9.3
GJ1293	10.87	1.29	3.629	31.13	2.21	(3),(2)	0.72	7	0.856	0.017	-4.755	0.035	33	17.5
GJ56.1	11.87	1.40	4.296	45.20	3.50	(3),(2)	0.48	7	1.316	0.107	-4.857	0.112	40	9.8
GJ3084	11.02	1.31	3.976	48.83	10.75	(3),(2)	0.55	5	1.181	0.049	-4.768	0.071	34	14.8
GJ3103	11.67	1.36	4.322	49.44	3.00	(3),(2)	0.49	7	0.817	0.065	-5.076	0.067	61	11.9
GJ70	10.95	1.51	4.410	87.62	2.00	(3),(2)	0.40	9	0.926	0.104	-5.059	0.098	59	15.2
GJ3138	10.98	1.29	3.710	33.44	2.17	(3),(2)	0.68	20	0.927	0.064	-4.757	0.121	33	15.1
GJ84.1A	11.02	1.21	3.832	43.03	2.08	(3),(2)	0.58	8	0.934	0.030	-4.807	0.051	37	18.7
GJ91	10.46	1.34	4.343	79.68	1.69	(3),(2)	0.53	26	1.158	0.135	-4.933	0.136	47	18.8
GJ1046	11.65	1.47	4.595	71.06	3.23	(3),(2)	0.39	7	0.784	0.088	-5.208	0.070	79	11.5
GJ1050	11.81	1.52	4.481	87.70	2.38	(5),(2)	0.28	10	0.462	0.054	-5.390	0.048	112	10.5
GJ130	11.57	1.46	4.361	79.60	9.70	(4),(2)	0.33	8	0.585	0.215	-5.237	0.213	84	28.9
GJ93	11.48	1.31	3.805	43.61	2.54	(3),(2)	0.48	11	0.619	0.085	-4.973	0.146	50	12.6
GJ114.1A	10.80	1.40	4.281	77.19	1.64	(3),(2)	0.46	48	0.746	0.137	-5.097	0.146	64	17.2
GJ118	11.49	1.46	4.637	85.87	1.99	(3),(2)	0.36	20	0.762	0.074	-5.238	0.056	84	9.6
GJ126	11.68	1.30	3.926	32.81	2.29	(3),(2)	0.59	32	0.758	0.091	-4.938	0.138	47	10.7
GJ3260	11.51	1.38	4.029	47.80	14.40	(6),(2)	0.47	6	1.921	0.312	-4.579	0.428	24	6.8
GJ173	10.49	1.36	4.375	90.10	1.74	(3),(2)	0.47	16	0.785	0.088	-5.115	0.086	66	19.5
GJ3218	11.40	1.43	4.393	53.60	16.10	(6),(2)	0.52	46	2.360	0.313	-4.645	0.300	27	12.0
GJ3256	11.32	1.45	4.346	54.60	16.40	(6),(2)	0.52	29	2.089	0.386	-4.678	0.388	29	9.6
GJ155.1	11.15	1.41	4.016	59.36	2.42	(3),(2)	0.45	12	0.625	0.072	-5.061	0.100	60	13.2
GJ3307	11.31	1.36	4.254	60.00	18.00	(6),(2)	0.46	18	1.662	0.146	-4.738	0.161	32	12.2
GJ3313	11.40	1.40	3.925	39.80	11.90	(6),(2)	0.56	6	1.552	0.075	-4.627	0.114	26	12.4
GJ3321	11.39	1.38	4.133	54.90	16.50	(6),(2)	0.46	5	1.233	0.087	-4.816	0.107	37	14.1
GJ3344	11.78	1.28	4.394	46.14	1.46	(5),(2)	0.51	1	0.597	0.000	-5.242	0.000	85	12.3
GJ180	11.02	1.42	4.398	82.52	2.40	(3),(2)	0.41	37	0.766	0.078	-5.136	0.074	69	16.0
GJ182	10.07	1.41	3.680	38.64	2.54	(3),(1)	0.80	3	7.032	0.321	-3.863	0.626	10	23.2
GJ3328	11.60	1.36	4.141	46.90	14.10	(6),(2)	0.49	8	0.985	0.076	-4.918	0.093	45	10.9
GJ3340	11.66	1.38	4.118	44.54	4.06	(3),(2)	0.49	10	1.206	0.097	-4.819	0.122	37	11.1
GJ206	11.53	1.63	4.920	78.16	3.70	(3),(1)	0.44	1	6.168	0.000	-4.447	0.000	18	11.5
GJ207.1	11.58	1.42	4.701	62.75	4.02	(3),(2)	0.48	1	10.690	0.000	-4.118	0.000	10	14.1
GJ3362	11.50	1.29	4.277	59.90	18.00	(6),(2)	0.43	2	2.327	1.546	-4.602	1.662	25	9.5
GJ3369	11.07	1.33	3.762	37.39	2.24	(3),(2)	0.62	9	1.009	0.030	-4.743	0.054	32	17.3
GJ3379	11.40	1.57	5.334	190.93	1.89	(5),(2)	0.23	16	7.027	2.264	-4.557	0.893	23	7.5
GJ218	10.74	1.46	4.080	66.54	1.43	(3),(1)	0.49	9	0.876	0.034	-4.942	0.045	47	18.2
GJ9206	11.36	1.31	3.920	35.48	2.09	(3),(2)	0.62	8	1.162	0.087	-4.750	0.133	33	13.8
GJ2049	10.86	1.24	3.872	40.00	3.15	(3),(2)	0.66	55	1.254	0.108	-4.696	0.173	30	13.9
GJ3367	11.00	1.30	3.817	47.10	14.10	(6),(2)	0.54	5	4.805	0.649	-4.089	1.100	10	8.2
GJ234A	11.20	1.62	5.690	242.32	3.12	(3),(2)	0.23	16	9.880	5.880	-4.550	1.677	22	9.5
GJ1097	11.51	1.46	4.782	81.38	2.49	(3),(2)	0.40	8	0.811	0.065	-5.271	0.043	89	11.9
GJ1135	10.13	1.28	4.113	61.21	1.52	(3),(2)	0.67	22	1.311	0.096	-4.781	0.122	35	24.1
GJ1100	11.56	1.30	3.807	34.57	2.79	(3),(2)	0.56	32	0.902	0.098	-4.811	0.168	37	11.5
GJ3440	11.84	1.44	4.268	40.80	12.30	(6),(2)	0.53	26	1.884	0.339	-4.690	0.368	29	5.0
GJ298	11.73	1.51	4.320	60.68	2.48	(3),(1)	0.39	7	0.917	0.068	-5.025	0.070	56	9.6
GJ3501A	11.27	1.29	4.067	37.95	2.70	(3),(2)	0.64	11	0.970	0.094	-4.892	0.125	43	12.3
GJ330	10.59	1.53	4.030	58.79	2.72	(3),(1)	0.57	1	0.589	0.000	-5.093	0.000	63	10.2
GJ3528	11.87	1.33	4.536	51.25	3.72	(3),(2)	0.47	13	1.002	0.182	-5.077	0.152	61	8.0
GJ3530	11.69	1.42	4.353	57.50	17.20	(6),(2)	0.43	24	0.943	0.071	-5.026	0.071	56	9.2
GJ3543	10.85	1.40	4.334	65.50	19.60	(6),(2)	0.53	81	2.156	0.349	-4.659	0.355	28	15.7
GJ3555	11.68	1.38	4.029	36.81	2.49	(3),(2)	0.56	2	1.980	0.164	-4.566	0.225	23	7.5
GJ361	10.36	1.50	4.190	88.81	1.68	(3),(1)	0.47	104	1.327	0.126	-4.809	0.148	37	16.4
GJ377	11.54	1.38	4.816	61.39	2.55	(3),(2)	0.52	11	1.417	0.172	-5.043	0.110	58	9.9
GJ386	11.12	1.33	4.644	73.30	2.62	(3),(2)	0.49	7	0.831	0.053	-5.203	0.040	78	18.5
GJ390	10.17	1.54	4.120	81.00	1.91	(3),(1)	0.53	40	1.704	0.116	-4.670	0.145	28	22.7
GJ399	11.37	1.45	4.528	60.80	3.14	(3),(2)	0.50	8	0.760	0.102	-5.194	0.086	77	11.5

Table A.3. continued.

Name	V	B-V	V-K	π [mas]	σ_π [mas]	Ref. Phot./π	M $M/M_\odot$	N_{mes}	S	σ_S	$log(R'_{HK})$	$\sigma_{R'_{HK}}$ $\times 10^5$	P_{rot} [d]	S/N_{VR}
GJ401A	11.14	1.37	3.864	49.95	2.26	(3),(2)	0.50	7	0.902	0.038	-4.836	0.061	39	17.3
GJ422	11.67	1.39	4.611	78.91	2.60	(3),(2)	0.35	20	0.476	0.124	-5.432	0.096	122	8.7
GJ2085	11.28	1.38	4.095	46.81	2.39	(3),(2)	0.54	8	1.147	0.078	-4.831	0.101	38	10.3
GJ443	11.69	1.50	4.570	50.02	3.10	(3),(1)	0.53	12	1.298	0.078	-4.979	0.063	51	10.5
GJ452A	11.95	1.44	4.481	51.10	3.58	(3),(2)	0.45	9	0.889	0.120	-5.106	0.106	65	8.5
GJ9381	11.57	1.35	4.203	38.05	2.85	(3),(2)	0.60	2	1.440	0.145	-4.779	0.168	35	9.4
GJ3695	11.90	1.37	4.302	41.35	2.81	(3),(2)	0.51	2	1.299	0.012	-4.866	0.012	41	8.3
GJ3671	11.25	1.42	3.970	56.38	2.04	(3),(2)	0.44	7	0.671	0.123	-5.011	0.178	54	10.2
GJ3708A	11.77	1.51	4.702	79.43	2.36	(3),(2)	0.35	25	0.760	0.197	-5.266	0.140	88	9.2
GJ476	11.41	1.43	4.260	54.69	3.05	(3),(1)	0.48	12	0.755	0.113	-5.083	0.123	62	11.9
GJ3778	12.05	1.41	4.350	48.60	14.60	(6),(2)	0.43	19	0.908	0.191	-5.042	0.191	57	6.3
GJ513	12.12	1.44	4.570	62.90	12.60	(6),(1)	0.35	8	0.692	0.053	-5.252	0.043	86	8.7
GJ508.3	11.89	1.32	3.813	27.96	3.61	(3),(2)	0.59	9	0.720	0.070	-4.912	0.118	45	9.6
GJ510	11.08	1.43	4.180	59.72	2.43	(3),(2)	0.49	13	2.217	0.263	-4.582	0.311	24	11.6
GJ3823	12.24	1.60	4.376	64.20	19.30	(6),(2)	0.30	3	1.454	0.089	-4.848	0.086	40	5.2
GJ618.4	11.89	1.37	4.229	41.77	3.59	(3),(2)	0.50	8	0.850	0.060	-5.019	0.068	55	8.4
GJ606	10.64	1.36	4.273	71.95	1.88	(3),(2)	0.52	18	1.725	0.195	-4.730	0.211	32	16.2
GJ618.1	10.80	1.27	3.695	29.92	2.69	(3),(2)	0.77	8	1.008	0.022	-4.714	0.041	31	14.5
GJ620	10.22	1.47	3.840	60.83	2.06	(3),(1)	0.59	22	1.628	0.063	-4.569	0.105	23	18.6
GJ724	10.75	1.34	4.180	61.15	2.07	(3),(2)	0.55	26	1.551	0.167	-4.737	0.197	32	14.4
GJ431	11.51	1.55	4.980	96.56	2.39	(3),(1)	0.37	4	0.645	0.107	-5.452	0.059	126	6.2
GJ477	11.20	1.37	4.332	52.67	3.05	(3),(2)	0.56	2	1.267	0.015	-4.889	0.015	43	10.6
GJ3759	11.01	1.37	4.052	58.94	2.40	(3),(2)	0.49	12	0.986	0.088	-4.879	0.118	42	10.6
GJ480	11.50	1.48	4.810	69.59	2.79	(3),(1)	0.47	37	1.083	0.155	-5.157	0.100	72	9.0
GJ494	9.76	1.47	4.150	85.54	1.53	(3),(1)	0.60	1	7.901	0.000	-4.017	0.000	10	16.1
GJ3799	12.14	1.41	4.135	30.00	9.00	(6),(2)	0.57	3	2.012	0.129	-4.605	0.160	25	6.7
GJ3804	11.94	1.49	5.014	97.62	5.03	(3),(2)	0.30	18	0.680	0.134	-5.442	0.071	124	8.2
GJ3813	11.73	1.41	4.562	71.00	21.30	(6),(2)	0.37	18	1.528	0.194	-4.905	0.158	44	4.8
GJ3822	10.76	1.31	4.030	50.36	2.04	(3),(2)	0.61	64	2.165	0.198	-4.528	0.272	21	11.5
GJ637	11.37	1.41	4.122	62.97	1.99	(3),(2)	0.41	17	0.681	0.105	-5.070	0.132	61	7.0
GJ634	11.65	1.45	4.292	57.40	6.60	(2),(2)	0.42	43	0.659	0.112	-5.156	0.118	72	8.7
GJ3707	12.14	1.51	5.253	77.93	2.41	(5),(2)	0.39	8	0.806	0.061	-5.465	0.026	130	9.0
GJ469	12.16	1.50	5.180	75.85	3.99	(3),(2)	0.38	10	0.929	0.161	-5.374	0.073	109	7.1
GJ3846	12.31	1.55	4.696	70.03	4.89	(3),(2)	0.31	6	0.875	0.199	-5.203	0.143	78	5.5
GJ3838	11.63	1.36	4.327	60.50	18.20	(6),(2)	0.41	6	1.526	0.080	-4.806	0.082	37	8.1
GJ552	10.66	1.49	4.250	71.39	2.10	(3),(1)	0.52	8	1.037	0.070	-4.942	0.077	47	13.3
GJ3871	11.65	1.38	4.511	80.90	24.30	(6),(2)	0.33	33	1.895	0.189	-4.790	0.162	35	7.3
GJ3874	11.34	1.27	3.928	40.78	2.48	(3),(2)	0.56	23	0.832	0.102	-4.899	0.155	44	10.9
GJ553.1	12.00	1.53	5.015	92.44	3.94	(3),(2)	0.31	9	0.599	0.089	-5.498	0.047	138	8.3
GJ570B	8.09	1.48	4.160	168.77	21.54	(3),(1)	0.64	2	1.458	0.128	-4.755	0.154	33	43.3
GJ676A	9.95	1.03	4.101	60.79	1.62	(3),(2)	0.71	80	1.539	0.128	-4.706	0.163	30	20.2
GJ4079	10.86	1.36	4.132	61.75	2.07	(3),(2)	0.51	15	3.138	0.279	-4.410	0.346	17	10.8
GJ3915	11.73	1.37	4.141	55.40	16.60	(6),(2)	0.40	20	0.913	0.173	-4.951	0.213	48	8.4
GJ3885	12.32	1.50	4.864	48.00	14.40	(6),(2)	0.48	12	0.951	0.202	-5.236	0.123	83	5.6
GJ3892	11.56	1.39	4.678	69.19	2.60	(3),(2)	0.44	9	0.905	0.072	-5.180	0.053	75	9.9
GJ3916	11.35	1.46	4.583	66.21	3.18	(3),(2)	0.48	3	0.732	0.108	-5.233	0.087	83	10.1
GJ611.3	11.69	1.30	4.101	28.17	7.39	(3),(2)	0.69	7	1.391	0.080	-4.750	0.102	33	7.2
GJ1203	12.22	1.35	4.521	59.63	3.55	(3),(2)	0.35	6	0.553	0.078	-5.329	0.066	100	7.2
GJ3962	11.60	1.34	3.885	28.12	3.55	(3),(2)	0.67	27	1.816	0.138	-4.541	0.218	22	7.9
GJ644A	9.34	1.25	4.913	161.41	5.64	(3),(2)	0.56	1	3.202	0.000	-4.729	0.000	31	23.9
GJ3973	10.99	1.37	4.192	54.86	2.18	(3),(2)	0.55	7	1.335	0.053	-4.807	0.061	37	14.9
GJ3998	10.95	1.40	4.110	56.20	2.26	(3),(2)	0.53	6	1.362	0.048	-4.763	0.061	34	12.2
GJ2128	11.56	1.48	4.430	67.08	2.69	(3),(2)	0.40	6	0.618	0.085	-5.243	0.078	85	8.8
GJ4001	10.70	1.29	3.961	51.86	2.49	(3),(2)	0.59	19	1.639	0.127	-4.619	0.187	25	12.8
GJ654	10.08	1.45	4.120	94.59	1.85	(3),(1)	0.48	18	0.646	0.070	-5.092	0.087	63	23.0
GJ3987	10.95	1.37	3.981	52.83	1.98	(3),(2)	0.53	7	1.107	0.041	-4.798	0.060	36	13.6
GJ4254	10.27	1.23	3.848	45.00	2.68	(3),(2)	0.72	11	1.468	0.402	-4.617	0.660	25	22.6
GJ855	10.82	1.33	4.066	52.22	2.17	(3),(2)	0.58	30	1.702	0.079	-4.648	0.105	27	13.1
GJ863	10.37	1.51	3.990	78.68	2.69	(3),(1)	0.48	5	1.063	0.060	-4.819	0.085	37	18.3
GJ800A	10.82	1.32	4.057	55.72	2.38	(3),(2)	0.55	28	1.023	0.054	-4.865	0.073	41	16.5
GJ821	10.87	1.54	3.930	82.18	2.17	(3),(1)	0.36	11	0.383	0.078	-5.237	0.118	84	12.8
GJ1264	9.96	1.10	4.288	61.29	1.54	(3),(2)	0.74	1	7.972	0.000	-4.072	0.000	10	12.9
GJ4206	10.76	1.34	4.094	47.06	2.55	(3),(2)	0.65	23	1.538	0.136	-4.704	0.176	30	13.3
GJ841A	10.67	1.28	4.769	62.61	2.92	(3),(2)	0.68	1	10.685	0.000	-4.146	0.000	10	12.3
GJ867A	9.54	0.97	4.716	115.01	1.32	(3),(2)	0.63	1	8.790	0.000	-4.209	0.000	12	33.0
GJ842	9.97	1.21	4.189	83.43	1.77	(3),(2)	0.57	8	1.546	0.073	-4.742	0.085	32	23.4

Table A.3. continued.

Name	V	B-V	V-K	π [mas]	σ_π [mas]	Ref. Phot./π	M M/M$_\odot$	N_{mes}	S	σ_S	$log(R'_{HK})$	$\sigma_{R'_{HK}}$ $\times 10^5$	P_{rot} [d]	S/N_{VR}
GJ735	10.11	1.53	4.690	84.94	1.72	(3),(1)	0.64	1	7.062	0.000	-4.293	0.000	14	13.9
GJ740	9.21	1.46	3.820	91.68	1.54	(3),(1)	0.61	55	1.559	0.114	-4.579	0.193	24	28.3
GJ4092	10.92	1.27	3.742	38.50	2.30	(3),(2)	0.64	13	1.062	0.083	-4.712	0.151	30	15.6
GJ672.1	11.70	1.41	4.157	41.78	4.12	(3),(2)	0.52	4	1.051	0.466	-4.890	0.085	43	5.7
GJ4004	12.21	1.50	4.887	79.95	1.82	(5),(2)	0.31	3	1.072	0.289	-5.193	0.173	77	3.1
GJ4082	12.10	1.50	4.487	38.60	4.10	(3),(2)	0.54	2	1.465	0.119	-4.892	0.104	43	3.6
GJ739	11.23	1.36	4.506	70.95	2.56	(3),(2)	0.46	14	0.919	0.130	-5.102	0.112	64	9.6
GJ747.4	11.43	1.41	4.028	45.99	3.33	(3),(2)	0.51	11	1.250	0.161	-4.765	0.222	34	7.8
GJ762	12.14	1.35	4.346	38.72	1.34	(5),(2)	0.50	5	0.806	0.298	-5.092	0.300	63	4.5
GJ781.1A	12.55	1.50	5.129	67.08	5.02	(3),(2)	0.35	5	0.515	0.079	-5.610	0.038	171	5.6
GJ1252	12.25	1.41	4.311	50.53	2.14	(5),(2)	0.37	5	0.340	0.342	-5.452	0.356	126	4.2
GJ808	11.91	1.41	4.222	56.93	2.12	(5),(2)	0.37	5	0.407	0.197	-5.286	0.129	92	5.0
GJ9724	12.09	1.51	4.399	67.55	3.74	(3),(2)	0.31	6	0.510	0.076	-5.313	0.073	97	5.0
GJ9732	11.00	1.34	4.142	48.82	2.20	(3),(2)	0.59	8	1.666	0.211	-4.689	0.259	29	12.3
GJ838.6	12.02	1.50	4.420	68.33	3.84	(3),(2)	0.32	8	0.619	0.153	-5.238	0.143	84	7.5
GJ4293	11.50	1.36	4.026	39.90	3.04	(3),(2)	0.56	1	2.755	0.000	-4.421	0.000	17	11.2
GJ874	12.03	1.43	4.380	50.70	11.30	(2),(2)	0.42	5	0.900	0.128	-5.058	0.124	59	6.4
GJ4273	12.08	1.46	4.412	53.65	3.15	(3),(2)	0.39	3	1.242	0.176	-4.932	0.166	46	5.5
GJ865	11.48	1.61	5.050	75.87	5.83	(3),(1)	0.48	1	7.853	0.000	-4.395	0.000	17	4.4
GJ4303	11.59	1.40	4.148	40.34	2.84	(3),(2)	0.56	72	3.186	0.582	-4.410	0.709	17	7.3
GJ4332	11.12	1.36	4.014	37.92	2.23	(3),(2)	0.66	2	1.883	0.273	-4.581	0.380	24	7.1
GJ3025	11.09	1.30	3.821	28.93	1.91	(3),(2)	0.75	2	1.873	0.472	-4.500	0.797	20	6.0
GJ1012	12.17	1.47	4.957	75.40	5.10	(2),(2)	0.34	9	0.720	0.050	-5.395	0.028	113	8.7
GJ1032	12.30	1.46	4.668	44.29	3.02	(3),(2)	0.48	10	1.459	0.150	-4.969	0.111	50	7.3
GJ1030	11.53	1.42	4.347	45.23	2.29	(3),(2)	0.56	6	2.239	0.172	-4.648	0.173	27	8.4
GJ78	11.85	1.42	4.195	60.36	3.08	(3),(2)	0.35	7	0.384	0.066	-5.350	0.077	104	7.7
GJ3135	12.25	1.61	4.668	107.81	2.92	(3),(2)	0.20	11	0.774	0.155	-5.244	0.114	85	6.4
GJ3148A	12.10	1.50	4.945	69.81	3.10	(3),(2)	0.38	63	5.869	1.564	-4.478	0.886	19	5.8
GJ3139	11.86	1.46	4.577	50.68	2.53	(3),(2)	0.49	5	0.995	0.074	-5.097	0.060	64	7.6
GJ1051	11.98	1.38	4.034	36.41	4.51	(3),(2)	0.50	3	0.499	0.023	-5.166	0.032	73	7.8
GJ103	8.85	1.33	3.941	86.18	0.78	(3),(2)	0.75	1	0.656	0.000	-5.007	0.000	54	26.2
GJ3141	12.27	1.54	4.520	71.53	1.64	(5),(2)	0.28	12	0.400	0.116	-5.469	0.099	131	6.1
GJ1054A	10.34	1.19	3.949	52.08	2.13	(3),(2)	0.66	2	0.664	0.046	-5.006	0.068	54	14.4
GJ3212	11.69	1.42	3.985	29.00	8.70	(6),(2)	0.65	12	0.693	0.062	-5.003	0.089	53	10.0
GJ3131	11.27	1.32	4.475	64.10	19.20	(6),(2)	0.48	2	0.815	0.030	-5.141	0.027	70	10.3
GJ3160	12.12	1.38	4.515	38.45	3.15	(3),(2)	0.55	1	0.800	0.000	-5.166	0.000	73	3.2
GJ43	12.46	1.46	4.329	27.99	4.08	(3),(2)	0.58	7	0.539	0.206	-5.259	0.210	87	4.0
GJ3263	12.44	1.44	4.975	56.18	1.06	(5),(2)	0.41	18	0.625	0.148	-5.464	0.081	129	5.7
GJ3205	11.88	1.28	4.324	59.12	4.68	(3),(2)	0.38	20	0.744	0.132	-5.117	0.135	66	8.1
GJ3221	12.25	1.49	4.664	54.70	2.40	(2),(2)	0.40	28	3.769	0.707	-4.555	0.522	23	4.7
GJ3029	12.27	1.50	4.799	51.80	4.40	(3),(2)	0.44	1	11.559	0.000	-4.124	0.000	10	2.5
GJ3032	11.95	1.43	4.551	50.82	2.74	(3),(2)	0.47	4	0.827	0.152	-5.167	0.125	73	4.2
GJ1022	12.20	1.39	4.339	48.62	1.39	(5),(2)	0.40	9	0.508	0.111	-5.290	0.113	93	4.8
GJ3090	11.49	1.40	4.172	44.71	2.57	(3),(2)	0.54	1	3.171	0.000	-4.423	0.000	17	7.0
GJ9201	12.26	1.33	4.243	35.25	2.65	(3),(2)	0.50	10	0.876	0.191	-5.012	0.212	54	6.4
GJ143.3	12.39	1.44	4.459	43.71	6.44	(3),(2)	0.43	5	0.485	0.272	-5.360	0.244	106	3.7
GJ155.3	12.17	1.37	4.198	38.99	2.92	(3),(2)	0.47	12	0.691	0.085	-5.096	0.099	64	8.8
GJ3279	11.83	1.46	4.596	61.90	18.60	(6),(2)	0.41	11	0.809	0.082	-5.195	0.065	77	9.3
GJ3455	12.48	1.45	4.701	61.92	0.98	(5),(2)	0.32	12	0.533	0.089	-5.420	0.064	119	6.3
GJ333	12.16	1.57	4.190	72.50	16.30	(2),(1)	0.25	11	0.554	0.101	-5.188	0.119	76	7.1
GJ3500	11.94	1.55	5.043	72.80	1.30	(5),(2)	0.41	2	0.621	0.068	-5.494	0.035	137	7.4
GJ3020	11.66	1.38	4.524	43.89	4.39	(3),(2)	0.58	2	1.083	0.013	-5.038	0.011	57	4.6
GJ3009	12.15	1.53	4.731	57.10	17.10	(6),(2)	0.41	10	0.883	0.293	-5.213	0.203	80	5.0
GJ3293	12.03	1.42	4.520	42.60	12.80	(6),(2)	0.52	161	1.108	0.163	-5.027	0.138	56	6.6
GJ3563	12.04	1.50	4.521	63.47	3.54	(3),(2)	0.36	12	0.625	0.082	-5.276	0.069	90	8.7
GJ3527	11.90	1.38	4.819	73.70	22.10	(6),(2)	0.38	1	0.481	0.000	-5.513	0.000	142	4.1
GJ372	10.69	1.37	4.536	62.33	2.15	(6),(2)	0.63	1	1.247	0.000	-4.982	0.000	51	10.8
GJ3005	12.05	1.46	4.399	42.73	150.0	(6),(2)	0.49	1	1.277	0.000	-4.914	0.000	45	3.7
GJ3006	12.24	1.49	4.585	59.85	2.64	(3),(2)	0.35	7	0.812	0.237	-5.189	0.189	76	6.9
GJ179	11.96	1.59	4.990	81.38	4.04	(3),(1)	0.36	21	1.302	0.284	-5.151	0.154	71	7.7
GJ204.2	12.11	1.48	4.649	56.80	6.50	(2),(2)	0.41	10	0.894	0.146	-5.174	0.110	74	7.9
GJ3356	11.93	1.43	4.970	80.60	9.80	(2),(2)	0.36	10	1.003	0.081	-5.256	0.045	87	7.7
GJ3341	12.14	1.38	4.383	43.18	1.40	(5),(2)	0.46	134	0.752	0.196	-5.137	0.190	69	6.3
GJ1088	12.29	1.57	4.954	87.03	1.28	(5),(2)	0.28	3	1.075	0.478	-5.219	0.268	81	4.1
GJ238	11.62	1.55	4.520	60.77	1.94	(3),(1)	0.45	8	0.658	0.191	-5.253	0.162	86	7.9
GJ3404A	12.12	1.53	4.762	77.90	2.80	(2),(2)	0.31	11	0.620	0.056	-5.379	0.037	110	7.1

Table A.3. continued.

Name	V	B-V	V-K	π [mas]	σ_π [mas]	Ref. Phot./π	M $M/M_\odot$	N_{mes}	S	σ_S	$log(R'_{HK})$	$\sigma_{R'_{HK}}$ $\times 10^5$	P_{rot} [d]	S/N_{VR}
GJ297.2B	11.88	1.46	4.438	44.50	8.90	(2),(2)	0.51	16	1.006	0.167	-5.034	0.154	57	7.4
GJ3470	12.38	1.40	4.367	44.60	13.40	(6),(2)	0.40	90	1.569	0.343	-4.811	0.337	37	4.3
GJ369	10.20	1.28	4.026	72.92	1.82	(3),(2)	0.55	45	0.787	0.095	-4.965	0.130	50	23.6
GJ3817	12.31	1.64	4.847	88.40	11.50	(2),(2)	0.26	9	0.817	0.169	-5.295	0.105	93	3.6
GJ660.1	11.71	1.34	3.749	50.10	3.62	(3),(2)	0.37	27	0.486	0.068	-5.054	0.123	59	9.6
GJ3598	12.51	1.49	4.464	35.90	10.80	(6),(2)	0.49	7	0.683	0.105	-5.213	0.094	80	4.3
GJ1212	12.04	1.52	4.763	53.41	4.76	(3),(2)	0.47	1	0.674	0.000	-5.344	0.000	103	4.9
GJ3634	11.99	1.46	4.496	50.55	1.55	(5),(2)	0.45	76	0.982	0.144	-5.069	0.125	61	7.7
GJ3918	12.54	1.51	4.685	62.30	18.70	(6),(2)	0.31	28	0.909	0.297	-5.182	0.215	75	4.9
GJ4005	12.16	1.51	4.481	51.60	15.50	(6),(2)	0.41	4	0.841	0.355	-5.130	0.313	68	3.9
GJ4056	11.93	1.46	4.419	73.20	22.00	(6),(2)	0.31	11	0.686	0.124	-5.192	0.116	77	9.6
GJ4088	11.51	1.33	3.921	36.20	10.90	(6),(2)	0.58	14	0.808	0.059	-4.909	0.090	44	11.8
GJ2121	12.34	1.42	4.718	44.58	5.36	(3),(2)	0.48	24	0.727	0.260	-5.292	0.182	93	4.6
GJ4016	12.28	1.53	4.409	47.50	14.30	(6),(2)	0.40	5	0.663	0.234	-5.203	0.221	78	4.3
GJ4065	12.37	1.42	4.979	95.40	1.90	(2),(2)	0.25	6	3.245	0.744	-4.750	0.408	33	3.0
GJ3643	12.43	1.51	4.609	50.90	4.58	(3),(2)	0.39	23	0.688	0.228	-5.271	0.178	89	4.2
GJ629.3	12.44	1.40	4.251	46.51	170.0	(3),(2)	0.36	15	0.519	0.241	-5.241	0.216	84	4.3
GJ4024	10.77	1.39	4.115	50.09	2.48	(3),(2)	0.63	2	2.721	0.565	-4.465	0.712	19	6.9
GJ2138	11.30	1.47	4.427	77.60	2.79	(3),(2)	0.39	7	0.812	0.146	-5.123	0.135	67	8.1
GJ4100	12.19	1.51	4.116	26.60	2.60	(2),(2)	0.61	8	1.693	0.229	-4.671	0.288	28	6.1
GJ1207	12.33	1.54	5.186	115.39	1.51	(5),(2)	0.23	1	5.579	0.000	-4.598	0.000	24	4.0
GJ9600	12.13	1.41	4.044	40.80	11.90	(2),(2)	0.42	1	0.619	0.000	-5.078	0.000	62	11.5
GJ723	11.23	1.81	3.746	30.49	7.89	(3),(2)	0.68	10	0.527	0.037	-5.018	0.068	55	11.5
GJ4077	12.11	1.46	4.528	72.80	21.80	(6),(2)	0.30	8	0.671	0.239	-5.248	0.201	85	5.0
GJ754.1B	11.73	1.48	4.292	91.30	4.00	(2),(2)	0.25	1	0.372	0.674	-4.956	0.000	49	4.7
GJ3700	12.40	1.41	4.505	55.70	16.70	(6),(2)	0.34	11	0.724	0.063	-5.205	0.054	79	8.7
GJ660A	11.48	1.46	4.800	98.19	12.09	(3),(2)	0.34	13	1.259	0.267	-5.087	0.173	63	6.1
GJ696	10.16	1.43	3.630	45.89	2.18	(3),(1)	0.69	33	1.646	0.122	-4.472	0.249	19	18.7
GJ4129	11.97	1.59	4.385	63.40	12.70	(3),(2)	0.35	4	0.407	0.111	-5.405	0.107	116	4.9
GJ4038	12.29	1.49	4.752	83.30	25.00	(6),(2)	0.27	1	0.879	0.000	-5.224	0.000	82	2.3
GJ730	10.73	1.45	3.870	47.08	2.12	(3),(1)	0.61	3	1.713	0.075	-4.560	0.120	23	10.6
GJ1248	12.27	1.47	4.378	73.80	1.90	(2),(2)	0.26	9	0.485	0.241	-5.326	0.234	99	3.9
GJ890	10.99	1.31	3.852	44.88	2.30	(3),(2)	0.57	1	0.701	0.000	-4.940	0.000	47	11.1
GJ891	11.34	1.46	4.321	62.17	3.27	(3),(2)	0.45	28	1.040	0.114	-4.970	0.117	50	11.4
GJ4331	11.32	1.34	3.990	29.93	2.52	(3),(2)	0.72	1	2.015	0.000	-4.541	0.000	22	6.0
GJ4310	10.86	1.22	4.027	49.22	2.02	(3),(2)	0.59	10	1.653	0.079	-4.643	0.108	27	14.3
GJ889.1	11.06	1.34	3.969	63.06	2.15	(3),(2)	0.43	3	0.595	0.079	-5.062	0.115	60	10.9
GJ4231	12.19	1.45	4.781	32.79	5.65	(3),(2)	0.66	1	0.961	0.000	-5.197	0.000	77	2.8
GJ4241	11.15	1.28	4.281	48.80	2.12	(3),(2)	0.59	4	1.642	0.067	-4.755	0.072	33	10.0
GJ4195	11.70	1.50	4.131	40.70	5.90	(2),(2)	0.53	4	0.507	0.148	-5.202	0.183	78	5.3
GJ4180	12.22	1.48	4.487	40.03	3.67	(3),(2)	0.50	6	1.432	0.246	-4.901	0.216	44	4.7
GJ4213	12.17	1.44	4.703	48.02	3.36	(3),(2)	0.48	2	3.192	0.694	-4.643	0.494	27	3.6
GJ9773	12.09	1.45	4.594	66.84	4.41	(3),(2)	0.34	5	0.739	0.233	-5.233	0.184	83	3.5
GJ843	12.09	1.47	4.881	78.20	11.70	(2),(2)	0.33	4	0.673	0.078	-5.393	0.047	113	5.9
GJ4249	12.10	1.47	4.264	48.42	4.51	(3),(2)	0.40	6	0.426	0.230	-5.334	0.250	101	4.4
GJ4253	12.45	1.45	4.386	42.30	12.70	(6),(2)	0.41	3	0.419	0.329	-5.393	0.318	113	4.0
GJ4262	12.23	1.42	4.388	45.10	13.50	(6),(2)	0.43	1	0.816	0.000	-5.104	0.000	65	3.6
GJ895.1	11.38	1.30	3.989	27.28	2.85	(3),(2)	0.75	4	1.410	0.109	-4.696	0.156	30	9.9
GJ4353	12.05	1.43	4.532	53.54	3.52	(3),(2)	0.42	4	5.100	1.263	-4.369	1.059	16	5.4
GJ817	11.45	1.49	3.920	52.16	2.92	(3),(1)	0.43	7	0.307	0.177	-5.323	0.081	99	7.5
GJ4197	12.26	1.42	4.603	64.30	19.30	(6),(2)	0.33	2	0.708	0.058	-5.256	0.046	87	5.1
GJ4383	11.80	1.44	4.713	59.47	2.70	(3),(2)	0.46	9	0.936	0.363	-5.180	0.256	75	6.4
GJ912	11.26	1.33	4.521	53.77	2.88	(3),(2)	0.57	8	1.344	0.208	-4.943	0.177	48	8.0
GJ4364	11.47	1.37	3.963	31.00	9.30	(6),(2)	0.67	11	1.113	0.107	-4.788	0.157	35	8.9
GJ828.2	11.17	1.47	3.980	61.18	2.39	(3),(2)	0.43	4	0.658	0.033	-5.023	0.048	55	12.0
GJ1099	11.98	1.48	4.522	68.70	13.70	(3),(2)	0.34	6	0.843	0.220	-5.146	0.187	70	6.6
GJ3508	11.90	1.32	4.555	52.74	3.69	(3),(2)	0.46	7	0.845	0.269	-5.159	0.220	72	7.2
GJ319C	11.76	1.54	4.460	66.96	3.91	(3),(1)	0.37	5	0.581	0.075	-5.282	0.068	91	7.8
GJ3492	11.96	1.46	4.639	66.70	20.00	(6),(2)	0.37	7	1.053	0.174	-5.099	0.131	64	6.1
GJ333.2A	12.39	1.41	4.550	47.70	8.00	(2),(2)	0.41	5	0.635	0.095	-5.281	0.078	91	6.8
GJ1077	11.90	1.53	4.660	65.35	1.91	(5),(1)	0.39	5	0.876	0.044	-5.187	0.033	76	5.9
GJ317	12.04	1.50	4.988	94.20	18.80	(5),(2)	0.30	23	1.127	0.085	-5.213	0.046	80	8.1
GJ816	11.34	1.43	4.624	69.53	2.93	(3),(2)	0.47	17	0.957	0.172	-5.134	0.132	69	9.0
GJ4149	11.70	0.64	4.047	37.20	10.98	(3),(2)	0.55	4	0.624	0.082	-5.075	0.111	61	5.0
GJ4155	12.10	0.50	4.374	47.60	14.30	(6),(2)	0.43	1	1.224	0.000	-4.922	0.000	46	5.9
GJ2033	11.04	1.42	4.285	46.82	4.32	(3),(2)	0.64	3	0.864	0.124	-5.036	0.132	57	6.9

Table A.3. continued.

Name	V	B-V	V-K	π [mas]	σ_π [mas]	Ref. Phot./π	M $M/M_\odot$	N_{mes}	S	σ_S	$log(R'_{HK})$	$\sigma_{R'_{HK}}$ $\times 10^5$	P_{rot} [d]	S/N_{VR}
GJ4362	12.41	1.52	4.643	41.25	1.55	(5),(2)	0.48	4	3.815	0.438	-4.541	0.331	22	6.6
GJ4159	11.55	1.39	3.860	36.36	3.15	(3),(2)	0.55	10	1.366	0.071	-4.654	0.115	27	8.1
GJ811.1	11.61	1.36	4.702	65.29	3.19	(3),(2)	0.46	2	1.144	0.133	-5.089	0.095	63	8.6
GJ864	9.99	1.44	3.700	58.42	1.79	(3),(1)	0.63	3	1.047	0.056	-4.699	0.107	30	19.2
GJ4265	11.91	1.33	4.170	37.67	3.50	(3),(2)	0.53	1	1.877	0.000	-4.650	0.000	27	4.9
GJ899	11.21	1.47	4.358	71.54	3.27	(3),(2)	0.43	5	0.561	0.018	-5.254	0.018	86	11.8
GJ4352	11.39	1.46	4.363	74.10	22.20	(6),(2)	0.38	4	0.450	0.072	-5.352	0.071	104	10.3
GJ4304A	11.36	1.32	4.096	40.89	2.12	(3),(2)	0.59	4	1.344	0.103	-4.763	0.133	34	9.3
GJ791	11.49	1.40	4.602	67.38	3.01	(3),(2)	0.45	2	0.873	0.035	-5.164	0.027	73	7.2
GJ810A	12.51	1.57	5.121	77.59	1.49	(5),(2)	0.31	2	0.558	0.294	-5.572	0.141	159	3.1
GJ812A	11.96	1.53	4.870	56.54	3.92	(3),(1)	0.48	9	3.651	0.503	-4.654	0.305	27	5.4

References

Baliunas, S. L., Donahue, R. A., Soon, W. H., Horne, J. H., Frazer, J., Woodard-Eklund, L., Bradford, M., Rao, L. M., Wilson, O. C., Zhang, Q., Bennett, W., Briggs, J., Carroll, S. M., Duncan, D. K., Figueroa, D., Lanning, H. H., Misch, T., Mueller, J., Noyes, R. W., Poppe, D., Porter, A. C., Robinson, C. R., Russell, J., Shelton, J. C., Soyumer, T., Vaughan, A. H., Whitney, J. H., 1995. Chromospheric variations in main-sequence stars. ApJ 438, 269–287.

Boisse, I., Bouchy, F., Hébrard, G., Bonfils, X., Santos, N., Vauclair, S., 2011. Disentangling between stellar activity and planetary signals. A&A 528, A4.

Bonfils, X., Mayor, M., Delfosse, X., Forveille, T., Gillon, M., Perrier, C., Udry, S., Bouchy, F., Lovis, C., Pepe, F., Queloz, D., Santos, N. C., Bertaux, J.-L., 2007. The HARPS search for southern extra-solar planets. X. A m sin i = 11 $M_{\oplus}$ planet around the nearby spotted M dwarf GJ 674. A&A 474, 293–299, 0704.0270.

Charbonneau, P., MacGregor, K. B., 1997. Solar Interface Dynamos. II. Linear, Kinematic Models in Spherical Geometry. ApJ 486, 502–520.

Delfosse, X., Forveille, T., Mayor, M., Perrier, C., Naef, D., Queloz, D., 1998. The closest extrasolar planet. A giant planet around the M4 dwarf GL 876. A&A 338, L67–L70, astro-ph/9808026.

Durney, B. R., De Young, D. S., Roxburgh, I. W., 1993. On the generation of the large-scale and turbulent magnetic fields in solar-type stars. Sol. Phys. 145, 207–225.

Elsasser, W. M., 1946. Induction Effects in Terrestrial Magnetism Part I. Theory. Physical Review 69, 106–116.

Forveille, T., Bonfils, X., Delfosse, X., Gillon, M., Udry, S., Bouchy, F., Lovis, C., Mayor, M., Pepe, F., Perrier, C., Queloz, D., Santos, N., Bertaux, J.-L., 2009. The HARPS search for southern extra-solar planets. XIV. Gl 176b, a super-Earth rather than a Neptune, and at a different period. A&A 493, 645–650, 0809.0750.

Gomes da Silva, J., Santos, N. C., Bonfils, X., Delfosse, X., Forveille, T., Udry, S., 2011. Long-term magnetic activity of a sample of M-dwarf stars from the HARPS program. I. Comparison of activity indices. A&A 534, A30, 1109.0321.

Hawley, S. L., Fisher, G. H., 1992. X-ray-heated models of stellar flare atmospheres - Theory and comparison with observations. ApJS 78, 565–598.

Irwin, J., Berta, Z. K., Burke, C. J., Charbonneau, D., Nutzman, P., West, A. A., Falco, E. E., 2011. On the Angular Momentum Evolution of Fully Convective Stars: Rotation Periods for Field M-dwarfs from the MEarth Transit Survey. ApJ 727, 56, 1011.4909.

Kiraga, M., Stepien, K., 2007. Age-Rotation-Activity Relations for M Dwarf Stars. Acta Astron.57, 149–172, 0707.2577.

Linsky, J. L., Ayres, T. R., 1978. Stellar model chromospheres. VI - Empirical estimates of the chromospheric radiative losses of late-type stars. ApJ 220, 619–628.

Lovis, C., Dumusque, X., Santos, N. C., Bouchy, F., Mayor, M., Pepe, F., Queloz, D., Ségransan, D., Udry, S., 2011. The HARPS search for southern extra-solar planets. XXXI. Magnetic activity cycles in solar-type stars: statistics and impact on precise radial velocities. ArXiv e-prints 1107.5325.

Mauas, P. J. D., Falchi, A., 1994. Atmospheric models of flare stars: The quiescent state of AD Leonis. A&A 281, 129–138, astro-ph/9308010.

Meunier, N., Delfosse, X., 2011. Filaments and the magnetic configuration. I. Observation of the solar case. A&A 532, A18.

Middelkoop, F., 1982. Magnetic structure in cool stars. IV - Rotation and CA II H and K emission of main-sequence stars. A&A 107, 31–35.

Noyes, R. W., Hartmann, L. W., Baliunas, S. L., Duncan, D. K., Vaughan, A. H., 1984. Rotation, convection, and magnetic activity in lower main-sequence stars. ApJ 279, 763–777.

Parker, E. N., 1955. Hydromagnetic Dynamo Models. ApJ 122, 293.

Pizzolato, N., Maggio, A., Micela, G., Sciortino, S., Ventura, P., 2003. The stellar activity-rotation relationship revisited: Dependence of saturated and non-saturated X-ray emission regimes on stellar mass for late-type dwarfs. A&A 397, 147–157.

Queloz, D., Henry, G. W., Sivan, J. P., Baliunas, S. L., Beuzit, J. L., Donahue, R. A., Mayor, M., Naef, D., Perrier, C., Udry, S., 2001. No planet for HD 166435. A&A 379, 279–287, astro-ph/0109491.

Reiners, A., Basri, G., Browning, M., 2009. Evidence for Magnetic Flux Saturation in Rapidly Rotating M Stars. ApJ 692, 538–545, 0810.5139.

Robertson, P., Mahadevan, S., Endl, M., Roy, A., 2014. Stellar activity masquerading as planets in the habitable zone of the M dwarf Gliese 581. Science 345, 440–444, 1407.1049.

Rutten, R. G. M., 1984. Magnetic structure in cool stars. VII - Absolute surface flux in CA II H and K line cores. A&A 130, 353–360.

Wilson, O. C., 1978. Chromospheric variations in main-sequence stars. ApJ 226, 379–396.

Wright, N. J., Drake, J. J., Mamajek, E. E., Henry, G. W., 2011. The Stellar-activity-Rotation Relationship and the Evolution of Stellar Dynamos. ApJ 743, 48, 1109.4634.

Chapter 4

Extracting radial velocities by maximum likelihood

The cross-correlation function is widely used to derive radial velocities (see section 1.3.2), however, the binary mask used to cross-correlate misses Doppler information since all spectral features are not taken in account by the mask. Although the majority of spectral lines are considered in a binary mask when extracting Doppler information in warm stars (FGK dwarfs) and for which a spectral continuum is well defined, the scenario is different in the coolest stars of the main sequence. M dwarfs spectra contain many lines that, for someone unfamiliar with them, may seem dominated by noise (Fig. 4.1). Nevertheless, this apparent noise is actually a huge amount of overlapping stellar molecular lines. The binary mask used to extract radial velocities in M dwarfs only targets well defined features (in strength and symmetry), and therefore the mask makes sub-optimal use of the available Doppler information.

Under these circumstances it make sense to correlate spectral data with a true stellar template. This procedure can be performed in the Fourier space (e.g. Chelli, 2000; Galland et al., 2005) or in the wavelength domain (e.g. Zucker and Mazeh, 2006; Anglada-Escudé and Butler, 2012). In this thesis I focused the later procedure, below I will briefly recall how proceeds (in the wavelength domain) some previous works, and how we address the template matching method.

The basic idea behind this method is to search for the parameters that adjust the template to match a true stellar spectrum as much as possible, avoiding Earth's atmosphere. Although synthetic spectra are commonly used to infer certain stellar fundamental parameters (like the effective temperature, e.g. Mann et al., 2013), the use of templates derived from observations is favoured over the ones derived from theoretical models. This is because some spectral regions remains imperfectly modelled implying the loss of Doppler information, and in addition, the method becomes more complex when using synthetic spectra as free parameters (e.g. effective temperature, gravity or abundances) are added. A scaling factor may be added to the parameter space to properly scale both the template and the spectrum to the same flux level. Such method was first developed by Howarth et al. (1997) to determine stellar rotation of OB stars. They applied rotational broadening to a stellar template to derive stellar rotations. The template was a spectrum from a O-star with low rotation rate. In their procedure, they masked-out P-Cygni profiles (OB-stars) and interstellar lines; next, they normalise by dividing with polynomial fits; finally, they cross-correlate and measure the width of the correlation profile (by fitting a Gaussian), this width was previously calibrated by a relationship between the full-width at half-maximum of the correlation and $v\sin i$. Although they correlate their template to stars of different spectral type, their results agree with those previously reported in the literature.

The rationale behind the template matching was also applied by Zucker and Mazeh (2006) to derive relative Doppler shifts between a set of spectra from single-lined spectroscopic binaries. In their work, after normalisation of the spectra, they produce several correlation matrices for different relative shifts,

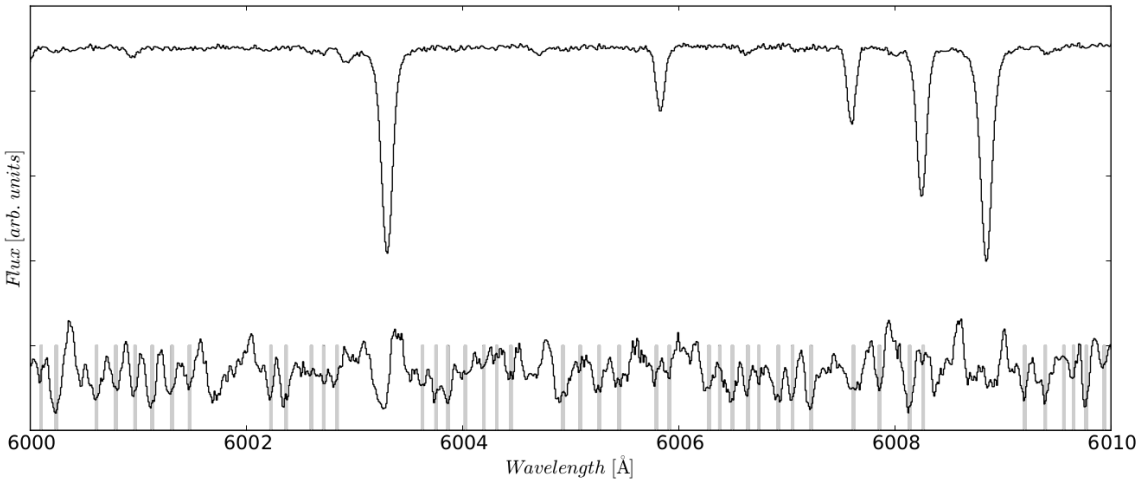

Figure 4.1: Examples of a G (top) and M dwarf (bottom) spectra. While a well defined continuum is present in the G dwarf spectrum, the one corresponding to the M dwarf is densely populated by molecular features. A binary mask used by the HARPS pipeline to perform the CCF in M dwarfs is represented in grey.

where the entries in each correlation matrix are the correlation coefficients obtained from a pair of spectra and a relative shift between them; that is, each spectrum is used as a template to be cross-correlated with all other spectra. Then, they optimise over the different relative shifts (the optimised parameter is $\rho = (\lambda_M - 1)/(n-1)$, where λ_M is the maximum eigenvalue of the each correlation matrix and n is the number of spectra) and the relative radial velocity is obtained from fitting parabolas to the peak. In the correct alignment, all spectra can be modelled by one principal component, where the eigenvector corresponding to the eigenvalue λ_M is used to produce an effective template.

I finally briefly describe the template matching method implemented by Anglada-Escudé and Butler (2012). They compute the RV separately for each echelle order (their final RV is the weighted mean of the RVs of all the orders) masking-out telluric using an atmospheric synthetic spectrum. Then, they compute the difference (R) between a stellar template (evaluated in several Doppler factors $\alpha_v = 1 - v_r/c$) and the observed spectrum multiplied by a normalisation polynomial (whose coefficients $[\alpha_0, ..., \alpha_M]$ are free parameters; that is, they derive a relationship for the blaze function). Next, they minimise the quantity

$$\chi^2 = \sum_{i=1}^{pix} \omega_i R[\lambda_i; \hat{\alpha}]^2$$

to infer the free parameters $\hat{\alpha} = [\alpha_v, \alpha_0, ..., \alpha_M]$, where ω_i are weights for each λ_i. These weights are derived in an iteration as

$$\omega_i = (\sqrt{< f >}/\sigma_{<R>})^2/f_i$$

with $\sqrt{< f >}$ the mean photon uncertainty of the observed flux f_i and $\sigma_{<R>}$ is the rms of R (they justify the use of such weights claiming that Poisson statistics never apply in realistic situations; I stress on this part because I will show that $\sqrt{< f >}/\sigma_{<R>} \approx 1$). Their stellar template is, in a first step, the highest signal-to-noise spectrum (S/N) and once they compute values for the free parameters $\hat{\alpha}$, they co-add all available spectra to derive a stellar template with better S/N and they iterate with this improved

template. The derived radial velocity ($v_{e,a}$, from the Doppler factor) and its uncertainty ($\sigma_{e,a}$, from the covariance matrix) – with the subscript e and a referring to each epoch and aperture respectively – are then used to compute the weights and a zero point for each aperture; these weights are finally used to compute the radial velocity of each epoch.

As we see, the common idea is to explore the parameter space to infer the most probable parameters that constraint the model. When data responds to a Gaussian distribution, maximise the probability density function – in the context of a maximum likelihood method – is analogous to minimise χ^2.

4.1 The χ^2-minimisation method using a stellar template

One of the objectives of this thesis is to optimise the extraction of radial velocities from spectra. In this topic, the works described above have shown an improvement compared to the traditional cross-correlation function technique. Accordingly, I implemented our own algorithm[1] – NAIRA (New Algorithm to Infer RAdial-velocities)[2], which extracts radial velocities by a χ^2-minimisation approach.

Our model is a stellar template built with all available spectra for a given target In principle, the template may be used with different targets of the same spectral type, however, parameters like metallicity, abundances or stellar rotation may degrades the result; on this point, it is necessary to conduct performance/effectiveness tests. For now, the template is only used to compute radial velocity of the target from which it is derived.

Telluric regions are discarded to ensure the best matching between the template and the spectrum of a given epoch. To recognise these regions, I exploit the fact that telluric lines are shifted according to the radial velocity of the observer in the Solar-system barycenter. Thereby, a telluric-template is derived from observations (figure 4.2 shows a sketch of the χ^2-minimisation). In our implementation, the coincidence between the template and the spectrum of a given epoch only depends on the Doppler shift; that is, we deal with only one free parameter and therefore the complexity of the implementation is minimal. In the following I will address the algorithm implementation details (a flowchart is given after the algorithm description).

4.1.1 Read data

Several science and calibration files are required to build the template, while others are optional. The (*main*) algorithm loads data previously saved in a folder for a given target. I implemented a dedicated script which receives the *id* of a star and scans the whole database to copy in a folder (this folder is created by the script) all the *.fits* files related to the star. Once the folder containing data for a given star is created, the *main* algorithm loads the following files

– 2D extracted spectra acquired in the science fibre ($*\_e2ds\_A.fits$ files). These files correspond to 1D extracted spectra for each echelle order that are not corrected for the blaze function and not re-sampled to a constant step in wavelength (in contrast to $*\_s1D\_A.fits$ files, which is the reason to use $*\_e2ds\_A.fits$ files). From $*\_e2ds\_A.fits$ files the algorithm loads the barycentric julian date BJD, the radial velocity of the observer in the Solar-system barycenter $BERV$, the air-mass, the seeing, the read-out noise, and the signal-to-noise ratio of the orders corresponding to an average wavelength of 4050Å, 5560Å, and 6120Å (orders 10, 50 and 60 in the case of HARPS).

[1] The algorithm is written in *python* programming language
[2] In Aymara (native south-American language) Naira means "the one with the big eyes"

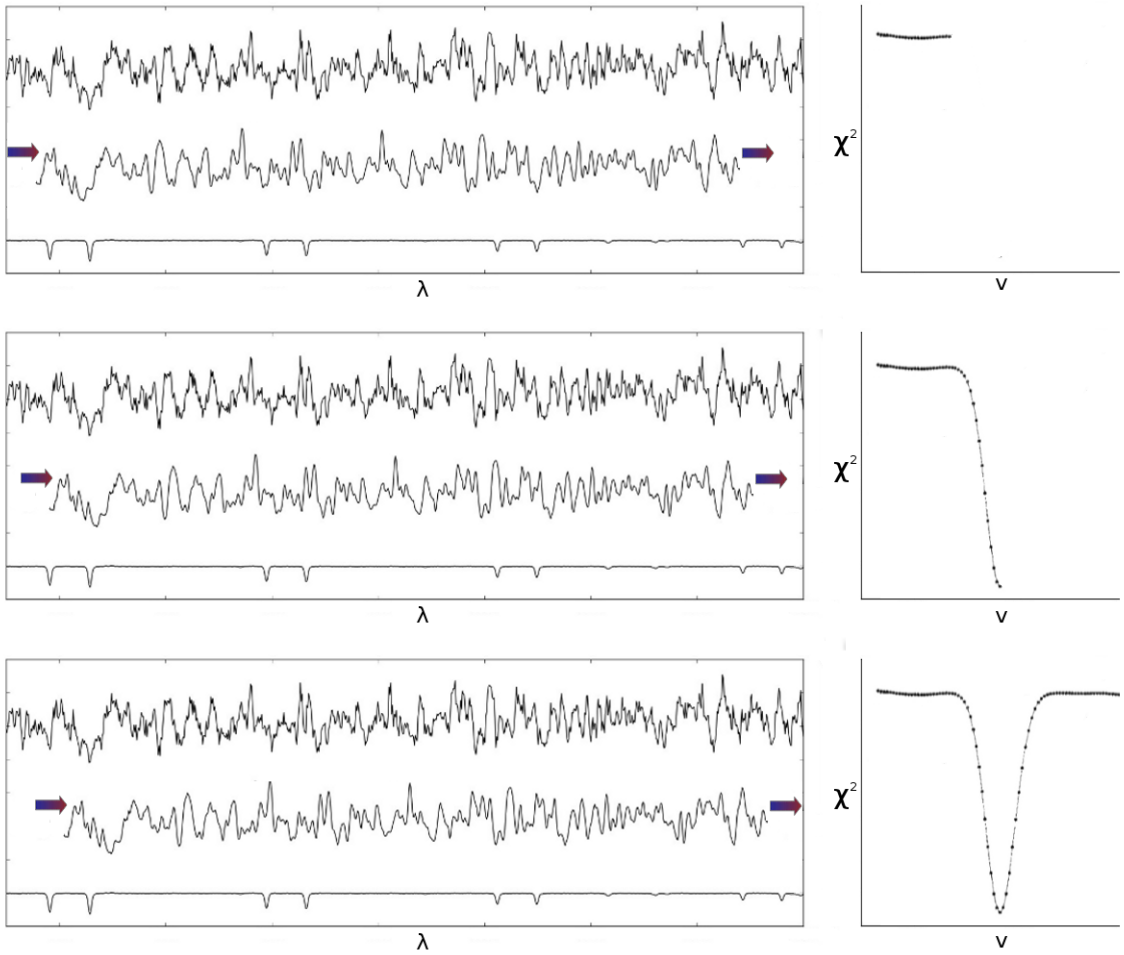

Figure 4.2: Sketch showing the χ^2-minimisation process (χ^2, right panels) using a stellar template (middle spectrum in left panels, which is shifted at different velocities from top to bottom). An observed spectrum (the top one) and the telluric template (the bottom one) are represented in left panels. The telluric template is used to discard telluric zones.

- The files $*\_wave\_A.fits$ containing the correspondence from pixel to wavelength. Such file is specified in $*\_e2ds\_A.fits$ headers. Alternatively, the algorithm can also generate the wavelength-pixel correspondence using the following entries specified in $*\_e2ds\_A.fits$ headers: number of orders, degree of the polynomial fit LL, degree of the polynomial fit X, the length of data axis 1, and length of data axis 2; however, this will make the process slower.

- The instrument pipeline (on HARPS, HARPS-N, SOPHIE) derives radial velocities from the cross-correlation function and are saved to $*\_ccf\_A.fits$ files; these radial velocities are used a as a first guess in our procedure (see below). NAIRA reads radial velocities from $*\_ccf\_A.fits$ files or tabulated in a *.rdb* file.

- The instrument pipeline generates $*\_blaze\_A.fits$ files containing the blaze function estimated for each night, which is specified in $*\_e2ds\_A.fits$ headers. NAIRA reads the $*\_blaze\_A.fits$ files.

– Optionally, the contrast, the full-width at half-maximum and the bisector span of the cross-correlation function are loaded from $*\_bis\_*\_A.fits$ files. Later, these parameters are saved together with the radial velocities from NAIRA.

4.1.2 Building the stellar template

The *main* algorithm builds the template in four steps. Generally speaking, the first two steps implements a first estimation of the stellar template and the telluric template, while the third and fourth steps optimise both the stellar and telluric templates by masking-out the zones contaminated with telluric – that is, the process iterates once.

The canonical Doppler factor $\beta = 1 + v_r/c$ (where c is the speed of light) is used to align spectra to a common reference frame. Stellar ($RV_\star$) and observer ($BERV$) radial velocities are combined to shift spectra in either the rest frame or the stellar frame. Therefore, the following Doppler factors

$$\beta_{rest} = \frac{c + BERV}{c + RV_\star} \tag{4.1}$$

$$\beta_{star} = \frac{c + RV_\star}{c + BERV} \tag{4.2}$$

are used to shift to the rest frame – Eq. (4.1) – or the stellar frame – Eq. (4.2).

For each i^{th} spectrum with its respective $RV_{\star,i}$ and $BERV_i$, and for each j^{th} order, we suppose a set of values in the form $X^{i,j} = \{X^1, ..., X^k, ..., X^n\}^{i,j}$, namely, X is a $\#spectra \times \#orders \times \#pixels$ cubic matrix. The superscript k refers to the k^{th} pixel. Henceforth j and k are omitted, although all the pixels and orders of a given i^{th} spectrum are considered in equations. X represents the counts N in stellar spectra (background corrected), or the blaze function B, or the wavelength-pixel correspondence W. In the case of HARPS data, for example, $j \in [1, 72]$ and $k \in [1, n = 4096]$.

First step: deriving the stellar-template

The procedure to obtain a first estimation of the stellar-template is, for each spectrum and order, as follows

1. Normalise by the corresponding blaze function and scale to unity

$$N^i_{NBl} = \frac{N^i}{B^i} \cdot \frac{med(B^i)}{med(N^i)} \tag{4.3}$$

   where N^i_{NBl} is the blaze-normalised and scaled spectrum, $med(N^i)$ and $med(B^i)$ represent the median along the k-axis of 2D-spectra and the blaze function respectively.

2. Spectra are Doppler shifted to the rest frame according to the RV and BERV of the i^{th} observation using Eq. (4.1): $W^i_{rest} = W^i \cdot \beta^i_{rest}$

   A reference wavelength (W_{ref}) is selected among the whole set of W^i_{rest}, which will be the wavelength-pixel correspondence for the template. For convenience, I chose the one corresponding to the bluer-shifted spectrum.

3. Since a given shift does not correspond to an integer number of pixels along the spectra, an interpolation is necessary. (N^i_{resamp}) is re-sampled by computing a cubic spline to [W^i_{rest}, N^i_{NBl}], which

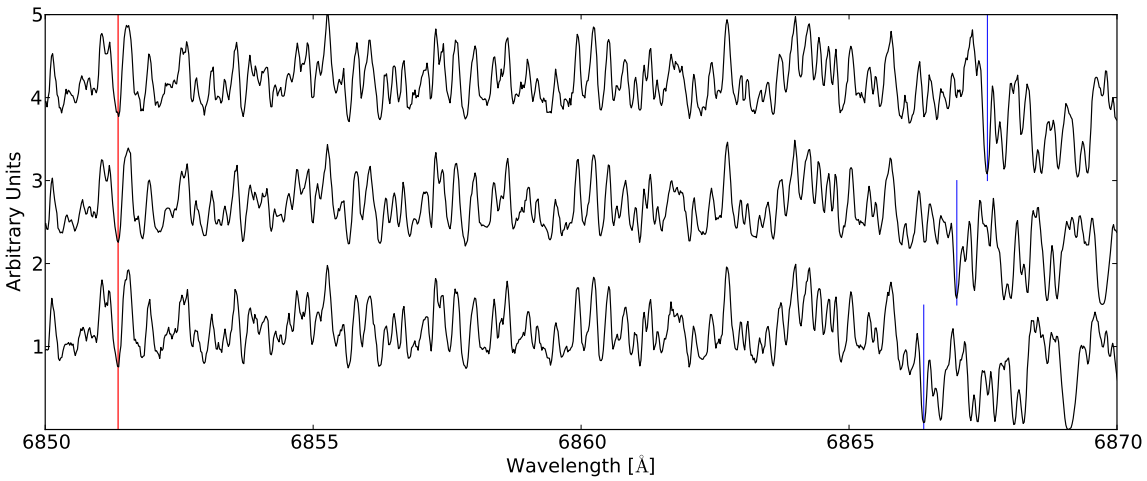

Figure 4.3: Three spectra of Gl 436 acquired in different epochs and shifted to the rest frame. From top to bottom $BERV = -26.7, 0.2, 25.2$ $[km\,s^{-1}]$. Red vertical line indicates a stellar feature and blue vertical lines indicate the shifted position of a telluric feature.

is evaluated in W_{ref}.

4. A first stellar-template $T_{\star,1} = \{T_1, ..., T_k, ..., T_n\}_{\star,1}$ is obtained by computing the median of N^i_{resamp} along the i-axis, which corresponds to the vertical axis in figure 4.3. At this stage the stellar lines are aligned while the telluric lines are shifted by the opposite of the barycentric velocity of each epoch (see Fig. 4.3). In this configuration and assuming that the number of spectra is sufficient, the benefit of the median is that it filter-out telluric. An example of the result is shown in top panel of figure 4.4.

5. The standard deviation of N^i_{resamp} is computed along the i-axis. The bottom panel in figure 4.4 shows an example where it is observed that the standard deviation is larger in a range ± 30 $[km\,s^{-1}]$ affected by telluric, as expected.

6. As spectra are Doppler shifted, the spline extrapolate certain regions of the edges that we do not use. Therefore, the number of elements that are extrapolated are retrieved, which are later used to trim the edges.

Second step: deriving the telluric-template

The stellar-template $T^j_{\star,1}$, which consists in a median stellar-spectrum for the j^{th} order and its wavelength W^j_{ref}, is now used to derive a template telluric-spectrum. For this

1. W^j_{ref} is shifted to the star frame at the date of the i^{th} observation using Eq. (4.2): $W^j_{star,ref} = W^j_{ref} \cdot \beta^i_{star}$

2. The stellar template is re-sampled, because it has a higher signal-to-noise (S/N) ratio compared to observed spectra. A cubic spline to $[W^j_{star,ref},\ T^j_{\star,1}]$ is used to re-sample the stellar-template and we evaluate it in W^i, resulting in $T^i_{\star,1,s}$.

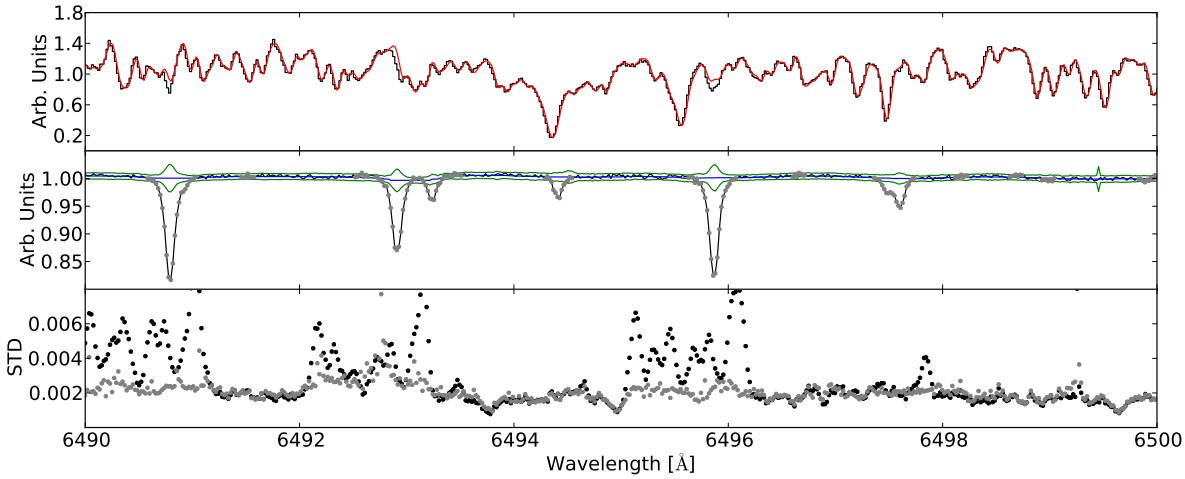

Figure 4.4: *Top:* The stellar-template obtained from the first iteration is represented by the red curve and the black step-curve depicts an observed spectrum. The telluric spectrum is embedded in the residuals coming from the ratio between the black and red curves. *Middle:* The telluric-template derived in the first iteration (black curve). The blue curve is the estimated continuum while the two green curves are $\pm 3\sigma$, where σ is computed from the telluric spectra set. Grey points represent an estimation of zones affected by telluric, which are used to built a binary telluric-template. *Bottom:* Black and grey points are the standard deviation of re-sampled spectrum in the first step ($N^{i,j}_{resamp}$) and the third step ($N^{i,j}_{resamp^*,clean}$) along the i-axis. This example comes from Gl 436, where 127 spectra were used.

3. We multiply by the normalised blaze function and we scale to the each observed spectrum

$$T^i_{\star,1,s,Bl} = T^i_{\star,1,s} \cdot B^i \cdot \frac{med(N^i)}{med(B^i)} \tag{4.4}$$

4. The ratio between spectra and the stellar-template is obtained

$$T^i_{\oplus,1} = \frac{N^i}{T^i_{\star,1,s,Bl}}$$

   In this situation telluric lines were aligned, and therefore, the telluric spectrum of each epoch come out over residuals (see top panel in figure 4.4).

5. A telluric-template is obtained ($T_{\oplus,1}$) calculating the median of $T^i_{\oplus,1}$ along the i-axis.

6. The standard deviation of $T^i_{\oplus,1}$ along the i-axis is computed, resulting in $T_{\oplus,Std}$

7. We mask telluric zones and we built a binary (0,1) telluric template. For this, a median filter to $T_{\oplus,1}$ along the k-axis is applied to recognise the continuum C, where the median filter window size (50 elements) is wide enough to avoid the narrow telluric features. A $k - element$ is classified as affected by telluric if it meets any of the following relationships

$$T_{\oplus,1} < C - 3 \cdot T_{\oplus,Std}$$
$$T_{\oplus,1} > C + 3 \cdot T_{\oplus,Std}$$

   Some elements close to each side of a telluric region do not satisfy the above relationships, but are

still part of telluric features (the part of the wings that meet the continuum). In general, we note that three elements to each side of the telluric zones corresponds to the wings of a telluric feature; these three elements are added to the telluric mask. An example is shown in middle panel figure 4.4.

Third step: optimising the stellar-template

Having a binary telluric-template, the first step is repeated but now we masked-out those zones affected by telluric (X_{clean}). Namely

1. The spectra are blaze-normalised. Those pixels affected by tellurics are discarded in both the stellar and the blaze spectra of the i^{th} observation (N^i_{clean}, B^i_{clean}); then, we normalise

$$N^i_{NBl^*} = \frac{N^i}{B^i} \cdot \frac{med(B^i_{clean})}{med(N^i_{clean})} \tag{4.5}$$

   where $N^i_{NBl^*}$ is the blaze-normalised and improved-scaled 2D-spectrum, while $med(N^i_{clean})$ and $med(B^i_{clean})$ represent the median along the k-axis of N^i_{clean} and B^i_{clean} respectively.

2. Spectra are shifted to the rest frame using Eq. (4.1): $W^i_{rest} = W^i \cdot \beta^i_{rest}$

3. A cubic spline to $[W^i_{rest},\ N^i_{NBl^*}]$ is obtained and it is evaluated in W_{ref}, this produces re-sampled spectra ($N^i_{resamp^*}$) where stellar lines are aligned.

4. Considering $RV_\star$ and $BERV$, telluric zones are removed $N^i_{resamp^*,clean}$ (not set to zero) by shifting the telluric binary mask.

5. The final stellar-template ($T_\star = \{T_1, ..., T_k, ..., T_n\}_\star$) is obtained by computing the median of $N^i_{resamp^*,clean}$ along the i-axis. As the normalisation was improved, specially for those orders affected by telluric features, the median stellar-template is improved as well. However, certain zones may always be affected by telluric (if the zone is crowded with telluric separated by less than 60 $km\,s^{-1}$) and, if that is the case, the template is set to zero. This situation can also occur if all the data are acquired having very close BERVs.

6. The standard deviation of $N^i_{resamp^*,clean}$ is computed along the i-axis. Now, specially in those zones affected by telluric, the standard deviation is more representative of the photonic uncertainty. In the example shown in the bottom panel of figure 4.4 we notice that in zones affected by telluric the standard deviation decreases.

Fourth step: optimising the telluric-template

This step is equivalent to the second iteration dedicated to derive a telluric-template. But we use now spectra where pixels affected by telluric are discarded (for a better scale to each i^{th} spectrum). To clarify the procedure, we repeat here the different steps

1. W_{ref} is shifted to the star frame using Eq. (4.2): $W_{star,ref} = W_{ref} \cdot \beta^i_{star}$

2. A cubic spline to $[W_{star,ref},\ T_\star]$ is computed and evaluated in W^i, resulting in $T^i_{\star,s}$.

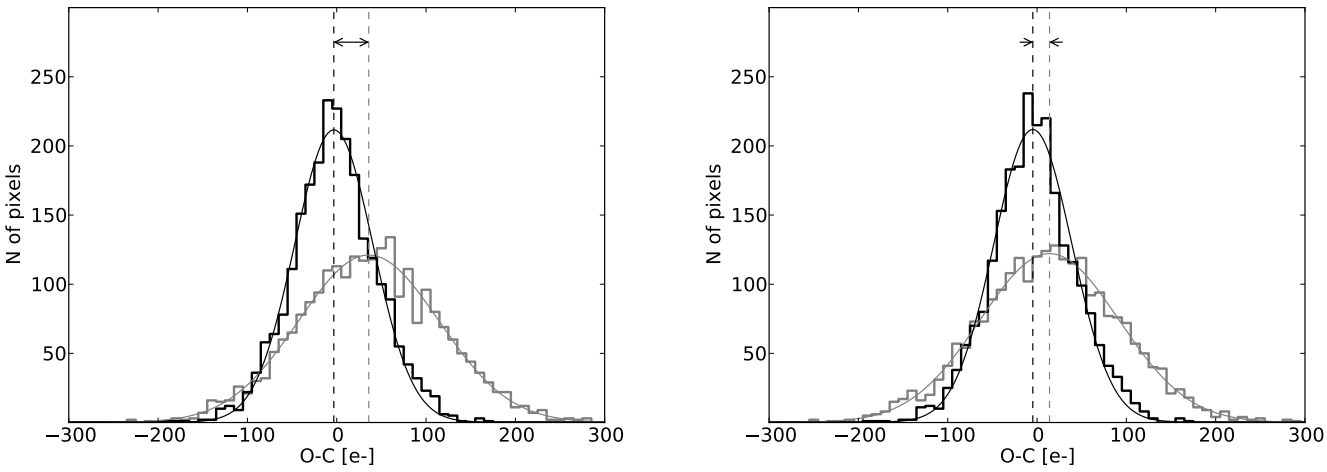

Figure 4.5: Histogram of the residuals – and its Gaussian fits – for the order 66 of two spectra of Gl 436 acquired with air-masses of 1.78 (black curve) and 2.24 (grey curve). The stellar-template was scaled to each observed spectrum using Eq. (4.4) (left panel) and Eq. (4.6) (right panel). Printed arrows depicts the difference between the peaks of the black and grey distributions; such difference is 39.1 $[e^-]$ in the left panel, while when we improve the scale factor (right panel) this difference is 18.7 $[e^-]$. In the right panel black and grey distributions have σ=77.9 and 43.9.

3. We multiply by the blaze function and we discard telluric zones $(N^i_{clean}, B^i_{clean})$, then we scale it to the 2D-spectrum of each epoch

$$T^i_{\star,s,Bl} = T^i_{\star,s} \cdot B^i \cdot \frac{med(N^i_{clean})}{med(B^i_{clean})} \tag{4.6}$$

4. Now telluric lines are aligned and the residuals between spectra and the re-sampled stellar-template are derived

$$T^i_{\oplus} = \frac{N^i}{T_{\star,s,Bl}}$$

which gives the telluric spectrum of each epoch.

5. The final telluric-template $(T_{\oplus})$ is obtained calculating the median of $T^i_{\oplus}$ along the i-axis. In comparison to the telluric-template obtained from the second step, now the contrast between telluric features and the continuum is slightly larger.

6. The standard deviation of $T^i_{\oplus}$ is obtained along the i-axis.

7. For each j-order, the reference wavelength, the stellar- and telluric-template, its uncertainties, and the number of elements to discarded in the edges (trim) are saved in a file.

Is it worth to iterate? The bottom panel of figure 4.4 shows that the stellar-template obtained after the third iteration presents a smaller standard deviation in zones affected by telluric, and hence, the stellar-template is more representative of pure stellar lines.

When matching the stellar template to an observed spectrum, it is important to have a correct scaling between both spectra; for that, we rely on the blaze function and a scaling factor. To show the reliability of this procedure, I analysed the result from equations (4.4) and (4.6), differing by the fact that the

telluric zones were removed in Eq. (4.6). For the analysis, I used the order 66 (6472Å to 6545Å, which has telluric features) from two spectra of Gl 436 acquired in very different conditions. These spectra were acquired with an air-mass of 1.78 ($S/N = 77.2$) and 2.24 ($S/N = 47.4$), and therefore, a variation in the strength of telluric is expected; such variation affects the quantity $med(N^{i,j})$ in the scaling factor. Each panel in figure 4.5 shows the distribution of the residuals (subtraction of the scaled stellar-template to the spectrum) for the two spectra. Figure 4.5 shows that the difference between the peaks of distribution is significantly lower (from 39.1 to 18.7 $[e^-]$) when Eq. (4.6) is used (right panel) instead of not iterating – Eq. (4.4) – (left panel), resulting in an improvement in the derivation of the stellar- and telluric-template when iterating. Furthermore, the S/N computed by the HARPS *DRS-3.5* in the centre of this order (66) for these spectra ($S/N = 77.2,\ 47.4$) are in excellent agreement with the standard deviation of residuals (78.8, 47.4) when the stellar-template is scaled using Eq. (4.6), namely, the dispersion of residuals is very consistent with pure photon noise (Poisson statistics). This fact argues in favour that another iteration will not improve the template.

4.1.3 Calculating radial velocities: χ^2-minimisation

The *main* algorithm derives radial velocities (RVs) by a χ^2-minimisation or goodness-of-fit test. The minimisation is resolved numerically as we look for the minimum χ^2 from a set of guess-RVs – or Doppler factors β –, another approach could be analytic where an expression of χ^2 is obtained and its derivative equals zero (e.g. Anglada-Escudé and Butler, 2012). Our philosophy is to compute a *pure* (without any weight different from 0 or 1) χ^2 using spectral regions containing Doppler information and to avoid manipulating the observed spectrum at all, i.e., the spectrum to which we want to extract the RV is not normalised and the template is scaled to it. The blaze function is used when scaling.

The extraction of the RV of the i^{th}-spectrum is done in two iterations, where the main difference between them is that telluric regions, regions without Doppler information and outliers pixels we reject in the second iteration.

Common to both iterations

1. The stellar- and telluric-templates are loaded.

2. I have a set of radial velocities $RV = \{RV_1, ..., RV_s, ..., RV_m\}$ where the minimum (RV_1) and the maximum (RV_m) are given manually or are automatically set according to $< RV_{CCF} > \pm 13\ [km\,s^{-1}]$; the step in RV depends on the iteration (see below). The set of radial velocities is equivalent to a set of Doppler factors in the star frame $\beta^i = \{\beta_1, ..., \beta_s, ..., \beta_m\}^i$ given for the i^{th} spectrum by
$$\beta_s^i = \frac{c + RV_s}{c + BERV_i} \tag{4.7}$$

3. The j^{th}-order is analysed if it satisfies $med(N^i) \geq 20\ [e^-]$. Under $S/N \approx 4$, in the case of HARPS, the background subtraction is not fully reliable.

4. The reference wavelength of the stellar-template is shifted with the guess-RV in the stellar frame using Eq. (4.7): $W_{star,ref,s} = W_{ref} \cdot \beta_s^i$

5. A cubic spline to $[W_{star,ref,s},\ T_\star]$ is computed and then evaluated in the pixel-wavelength correspondence of the observed spectrum W^i, resulting in a shifted and re-sampled stellar-template (T_s^i)

6. I multiply T_s^i by the blaze function B^i and we scale to the observed spectrum N^i, where the scaling factor (C^{Scl}) depends on the iteration (see below); this results in

$$T^i_{s,Bl,Scl} = T^i_s \cdot B^i \cdot C^{Scl} \tag{4.8}$$

$$C^{Scl} = \frac{med(N^i)}{med(T^i_s \cdot B^i)}$$

7. The regions where the stellar-template has been set to zero are discarded (see 4.1.2). In a conservative way, 20 pixels to each side of those regions are also rejected.

8. As the stellar-template has been shifted according to β^i_s, some regions in the edges are extrapolated. The number of elements that are extrapolated are saved.

9. The final rejected zones are the combination of all the problematic regions from 6 in 4.1.2, and 7, 8 from this part. Hereafter we assume that observed spectrum and template are free of these zones.

10. The $\chi^{2_i}_s$ associated to the Doppler factor β^i_s is computed as

$$\begin{aligned} \chi^{2_i}_s &= \frac{1}{df} \cdot \sum \left(\frac{N^i - T^i_{s,Bl,Scl}}{\sigma_i} \right)^2 \\ \sigma_i &= \sqrt{T^i_{s,Bl,Scl} + \sigma^{2_i}_{ro}} \end{aligned} \tag{4.9}$$

where N^i, $T^i_{s,Bl,Scl}$ and σ_i are the observed flux, the template flux and the photon-error, respectively, σ^i_{ro} is the CCD read-out-noise; $df = n_o \cdot n - 2$ is the degrees-of-freedom; the reason for a double sum (over wavelength elements and orders) is because the χ^2 is computed considering the whole spectral domain of the spectrograph (from 380 to 630 in the case of HARPS) at once, with the exception of rejected zones (e.g. telluric or pixel outliers, hence in the case of HARPS, $n < 4096$ and $n_o < 72$, as for M dwarfs the bluer orders have little flux) that depend on the iteration (see below). In practice, the residuals scaled by photon-errors are stored for each j^{th}-order, then the squared sum is performed, and finally, we normalise by the degrees-of-freedom. The set $RV = \{RV_1, ..., RV_s, ..., RV_m\}$ results in a set of $\chi^{2_i} = \{\chi^2_1, ..., \chi^2_s, ..., \chi^2_m\}^i$ describing a χ^2-profile.

11. There is the possibility to plot the process for each RV_s step. With it, we visualise the decrease of the squared residuals scaled by photon-errors as RV_s approach to the true stellar RV.

First step: estimating RV

In this step the main goal is to derive a first RV estimation by template-matching, which will be used in a second step to identify the regions to be rejected (telluric regions, zones without Doppler information and outliers pixels). These regions are identified by an analysis (see second step below) once the stellar-template is shifted, in the star frame, according to this first RV. Although one losses the possibility to plot this part of the process – useful to visualise which regions will be rejected in the second step –, it is possible to skip this step and load the RVs from the traditional CCF or from a table containing RVs. One may want to iterate by loading the table containing RVs resulting from the algorithm, but – by testing

with Gl 436 – I found that it effectively converges after the second step (first iteration). The tasks being carried out in this part are

1. The RV step is fixed to be equal to the plate scale (ps) [3] of the instrument, which is in velocity, the mean size of a pixel ($ps = 0.82\ [km\,s^{-1}\,pix^{-1}]$ in the case of HARPS).

2. The scaling factor is computed – item 6, Eq (4.8). As I showed in figure 4.5, there is a difference when computing this scaling factor whether or not rejecting telluric regions. Therefore in the second step, when telluric regions and outliers pixels are rejected, the scaling will improve the match between the observed spectrum and the stellar-template.

3. I compute χ^{2i}_s as described in the item 10 from *Common to both iterations*. The resulting χ^2-profile is fitted by a Voigtian and Gaussian functions and the centroid of the Gaussian fit is retained as the first estimation of the RV (RV_1).

As an example of the first step, figure 4.6 shows a snapshot – as shown by the algorithm – of the process. There we see how the normalised residuals are affected by telluric regions and a mediocre scaling. Indeed, the figure clearly shows the regions strongly affected by telluric (e.g. $\lambda \approx$630, 690 nm); we also note that the order centred on 690 nm has a systematic offset. Effects from telluric and bad scaling are visible in the difference between the residuals distribution and its Gaussian fit ($N - G_{fit}$ in Fig 4.6): telluric are responsible of a *"noise"* for $(O-C)/\sigma < -3$ (for $(O-C)/\sigma > 3$ the pattern is flatter) and the offset due to bad scales orders produce structure in the normalised residuals for $2 < (O-C)/\sigma < 4$ (this structure comes from a skewness in the distribution of residuals).

Second step: optimising RV

This step shifts the stellar-template to RV_1 in the star frame – using Eq. (4.7) – and, since spectral lines containing Doppler information are related to its derivative (Bouchy et al., 2001), the first derivative of the stellar- and telluric-templates is analysed to reject zones with telluric or without Doppler information. The idea is to analyse a region only if the Doppler information of the stellar-template is several times greater than the Doppler information in the telluric-template (this factor is estimated below). In this step, the residuals from the observed spectrum and the shifted stellar-template are also analysed (to perform a 5σ-clipping). The algorithm derive the classical active tracer S- and $H\alpha$-index and, as an experimental part, the second derivative of the stellar-template is also computed to score the wings and cores of spectral lines; the idea is to detect a change in the lines concavity, and then, the RV are computed separately for the concave upward and downward parts of spectral lines. With this in mind, the tasks performed in this step are

1. The RV step is fixed to be $ps/10\ [km\,s^{-1}]$ if the RV-guess is $ps \cdot c/R$ (or ps, depending on the user's choice) around RV_1; that is, near the χ^2 minimum. R is the instrument resolution. When the RV-guess is outside the above range (far from the minimum) the RV guess is fixed to be $ps/2\ [km\,s^{-1}]$.

[3] $ps = \frac{c}{N_{pix}} \left(\frac{1}{N_{ord}} \sum_{i=1}^{N_{ord}} \frac{\Delta\lambda_i}{<\lambda_i>} \right)$
with N_{pix}, N_{ord} : CCD number of pixels, orders; $\Delta\lambda_i$, $<\lambda_i>$: coverage, average wavelength of the i^{th}-order.

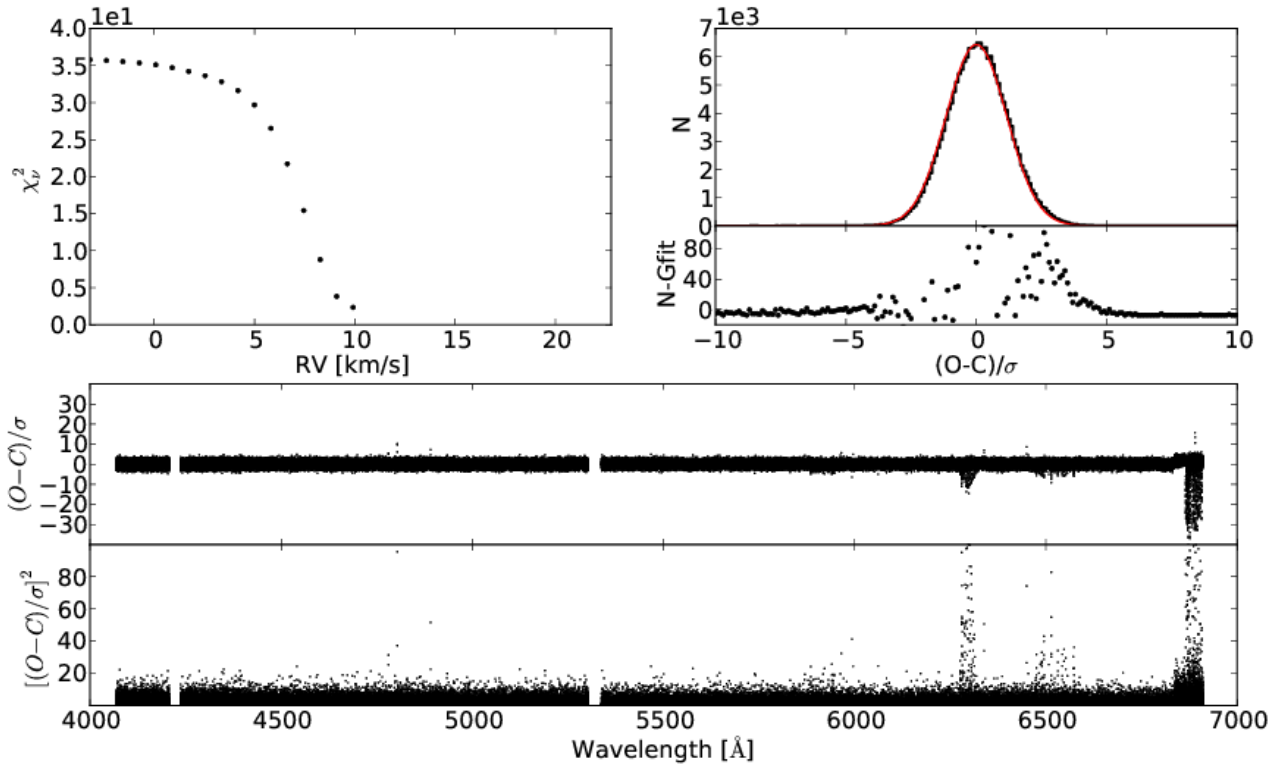

Figure 4.6: Example (Gl 436) of the χ^2-minimisation from the first step in 4.1.3, where the snapshot corresponds to a RV_s near the χ^2-minimum. The upper left panel shows the χ^2-profile; the upper right panel shows the distribution of the residuals (black) and a Gaussian fit to it (red), just below is the difference between the residuals and the Gaussian fit; middle panel shows the residuals normalised by the uncertainties and bottom panel shows the squared normalised residuals.

2. The telluric-template is multiplied by the blaze function and we scale to the observed spectrum

$$T^i_{\oplus,Bl,Scl} = T_\oplus \cdot B^i \cdot \frac{med(N^i)}{med(T^j_\oplus \cdot B^i)}$$

3. I compute $\partial T^i_{\oplus,Bl,Scl}/\partial\lambda$, the derivative of $T^i_{\oplus,Bl,Scl}$. The derivative of the k^{th}-element (k being the pixel number) is approximated to the slope of a first order polynomial fitted to seven elements centred on the k^{th}-element.

4. The stellar-template is shifted to RV_1 in the star frame, we multiply by the blaze function and by the telluric-template, then we scale to the observed spectrum – 6, Eq (4.8). This operation results in $T^i_{RV_1,Bl,Scl,\oplus}$

5. Analogously to the item 3, $\partial T^i_{RV_1,Bl,Scl}/\partial\lambda$, the derivative of $T^i_{RV_1,Bl,Scl}$ is obtained.

6. The ratio ($R_{\partial X/\partial\lambda}$) between the derivatives of the stellar- and telluric-templates is computed. The

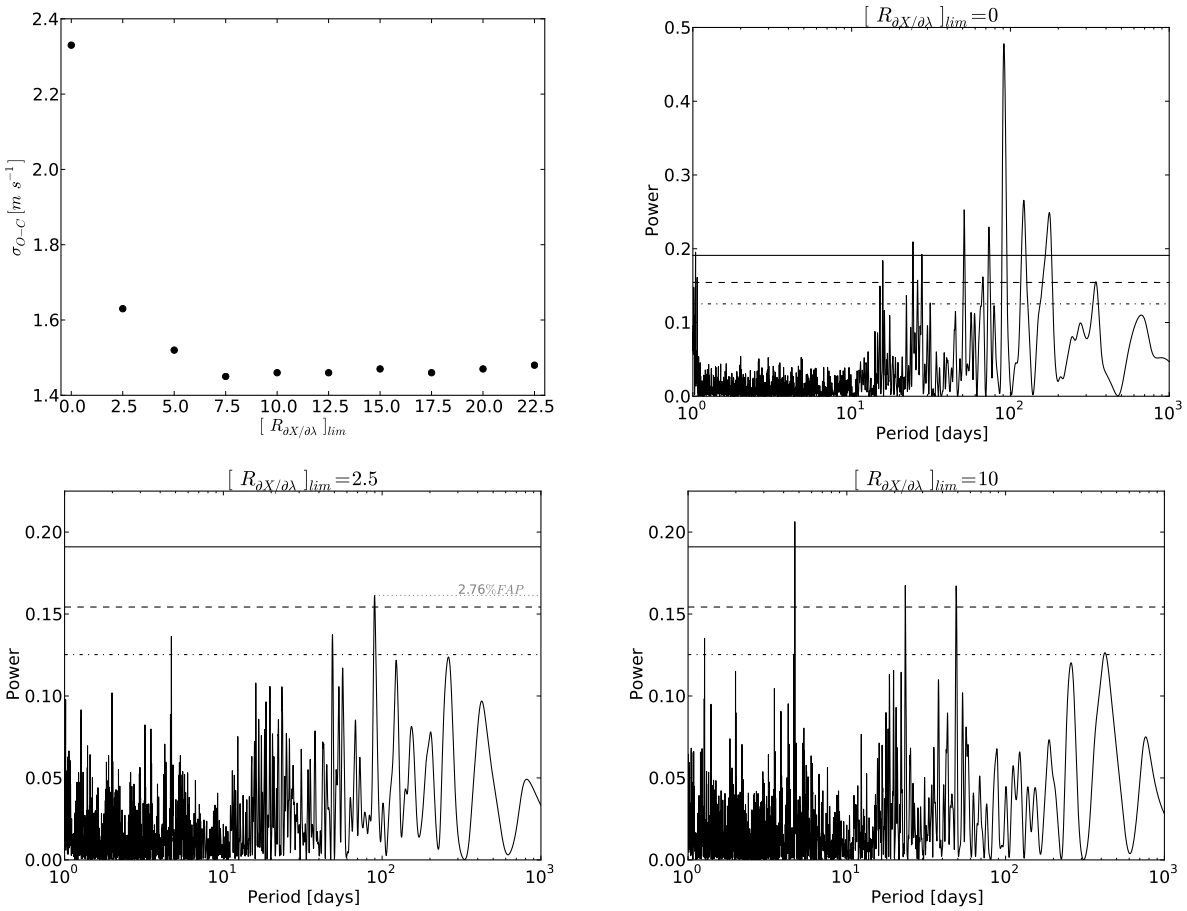

Figure 4.7: *Top left panel* shows the dispersion of the RVs residuals (σ_{O-C}) – when subtracting the signal from Gl 436b – as a function of different $R_{\partial X/\partial\lambda}$ limits (see Eq. 4.10); σ_{O-C} remains constant for $[R_{\partial X/\partial\lambda}]_{lim} \geq 7.5$. Normalised periodograms for the RVs residuals are shown in *top right and bottom panels* for different $[R_{\partial X/\partial\lambda}]_{lim}$. Peaks at 90, 120 and 180 days in *top right panel* come from telluric effects; these peaks decrease drastically in *bottom left panel* and completely disappear in *bottom right panel*, demonstrating that the procedure is efficient in removing telluric. In the latter panel the dominant peak comes from stellar activity (see Sect. 4.1.5 below).

regions to be rejected (interpreted as telluric or with poor – or lack –Doppler information) satisfy

$$R^i_{\partial X/\partial\lambda} = \frac{|\partial T^i_{RV_1,Bl,Scl}/\partial\lambda|}{|\partial T^i_{\oplus,Bl,Scl}/\partial\lambda|} < 10 \tag{4.10}$$

These regions are combined with previous rejected regions (9 in 4.1.3). The choice $R^i_{\partial X/\partial\lambda} < 10$ comes from a test performed for Gl 436, where I gave several limits for the slope ratio (from 0 to 22.5 with a step of 2.5) and analyse the dispersion of the residuals when subtracting the signal from Gl 436b (Fig 4.7). In such analysis, I also performed periodograms normalised so that the power=1 stands for a perfect fit of a sine wave to RVs and power=0 means no improvement over a constant model (Zechmeister and Kürster, 2009).

7. We iterate over the scaling factor – Eq (4.8) – after rejecting in the observed and template spectra the region identified during the precedent step (item 6).

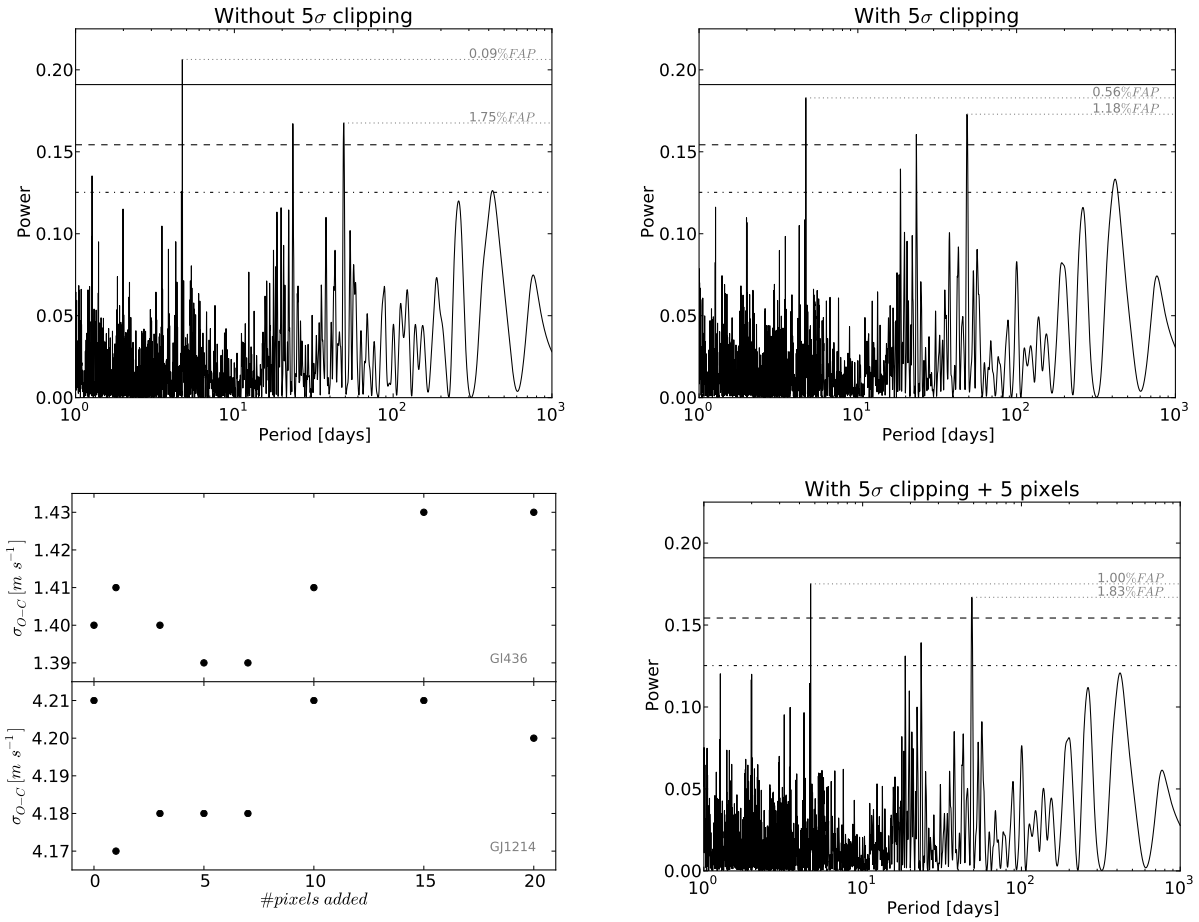

Figure 4.8: *Top panels:* Normalised periodogram for (Gl 436) RVs residuals with and without 5σ-clipping. Two peaks are associated to Gl 436 surface inhomogeneities at 4.7 and 48 days (see Sect. 4.1.5). We note a significant decrease in the 4.7 d peak when performing a 5σ-clipping. *Bottom panels:* The *left panel* shows, for the cases of Gl 436 and GJ 1214, the dispersion of RVs residuals as a function of how many pixels are added to either side of those satisfying $(O-C)^i_{norm} > 5$; the *right panel* is the periodogram of Gl 436 RVs residuals when 5 pixels are added to either side of 5σ-clipped zones, in that case the power of both peaks at 4.7 and 48 days are the lowest.

8. I determine if a σ-clipping procedure is needed on the observed spectrum to remove cosmic rays or, in general, any pixel that does not follow the Poisson distribution. For that, the normalised residuals are computed

$$(O-C)^i_{norm} = \frac{N^i - T^i_{RV_1,Bl,Scl}}{\sqrt{T^i_{RV_1,Bl,Scl} + \sigma^{2_i}_{ro}}} \tag{4.11}$$

and the choice is a 5σ-clipping, i.e., I remove zones satisfying $(O-C)^i_{norm} > 5$. When removing the signal from Gl 436b, the dispersion in the RVs residuals (σ_{O-C}) decreases from 1.46 to 1.40 $m\,s^{-1}$; moreover, the responsible of such a difference is the stellar activity (Fig. 4.8), as variations (from the stellar-template) in the shape of spectral lines do not follow a Poisson distribution.

I empirically explored how pixels adjacent to those satisfying $(O-C)^i_{norm} > 5$ may affect the χ^2-minimisation. For that, I performed a test (on Gl 436 and GJ 1214) adding a different amount of pixels (1, 3, 5, 7, 10, 15, 20) to either side of pixels satisfying $(O-C)^i_{norm} > 5$ and then, I

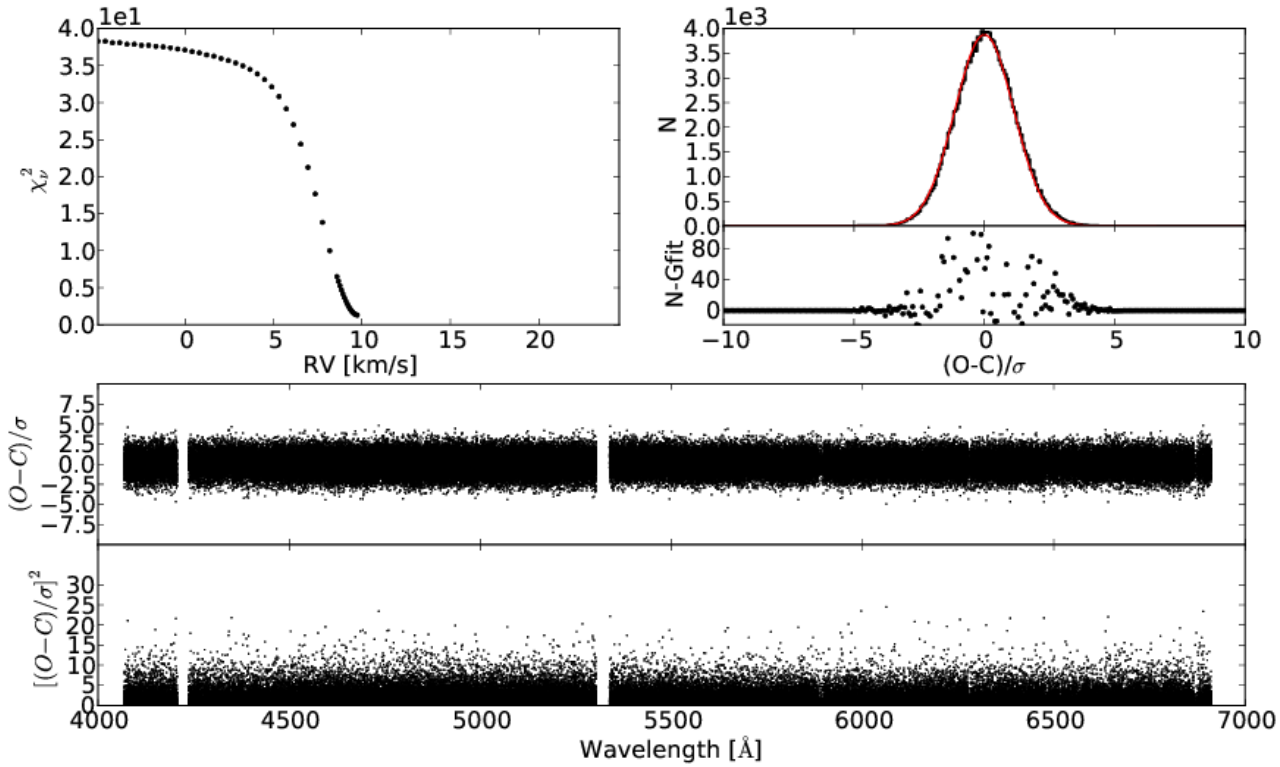

Figure 4.9: Example (Gl 436) of the χ^2-minimisation from the second step in 4.1.3, where the snapshot corresponds to a RV_s near the χ^2-minimum. Description panels are the same as in figure 4.6.

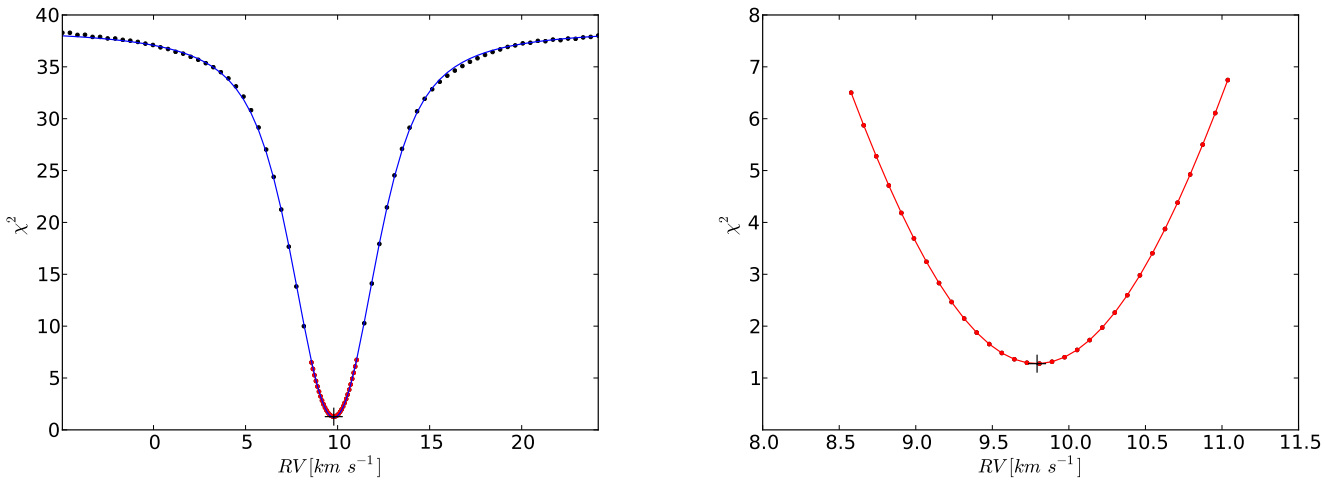

Figure 4.10: These panels show the full χ^2-profile and its Voigtian- (blue) and Gaussian fit (red) – second step; the black cross at the bottom represents the inferred RV (centroid of the Gaussian fit). Black points in left panel represent RVs which step is $ps/2$ while red points have a RV-step of $ps/10$ (the Gaussian is fitted only to these points; right panel shows a zoom to the bottom part of the χ^2-profile).

analysed the dispersion and periodogram of RVs residuals. Although the variation in σ_{O-C} does not allow a significant conclusion (bottom left panel in Fig. 4.8), I conservatively add 5 pixels to

either side of 5σ-clipped zones; in addition, with this choice the effect of Gl 436 activity in RVs slightly decrease (Fig. 4.8 bottom right panel).

9. A last iteration is done over the scaling factor – Eq. (4.8) – after rejection of region with the σ-clipping procedure. We end up with *clean* k^{th}-elements to compute the $\chi^{2_i}_s$ – Eq. (4.9).

10. A Voigtian to the $\chi^{2_i} = \{\chi^2_1, ..., \chi^2_s, ..., \chi^2_m\}^i$ profile and a Gaussian where the RV_s step is $ps/10$ (the bottom of the $\chi 2$ profile, see 1) are fitted. The centroid of both functions is stored, where I use the centroid of the Gaussian fit as the final RV (Fig. 4.10).

11. The error of the final RV is computed following Bouchy et al. (2001). Considering a noise free reference spectrum A_0 ($A_{rms,0} = 0$) and a Doppler shifted spectrum A at the same intensity ($A = A_0$), the Doppler shift and its dispersion of the i^{th}-pixel is given by

$$\frac{\delta v(i)}{c} = \frac{A(i) - A_0(i)}{\lambda(i)[\partial A_0(i)/\partial\lambda(i)]}$$
$$\frac{\delta v_{rms}(i)}{c} = \frac{[A(i) - A_0(i)]_{rms}}{\lambda(i)[\partial A_0(i)/\partial\lambda(i)]} \tag{4.12}$$

where Eq. (4.12) defines the optimum weight of the i^{th}-pixel as $W(i) = [\delta v_{rms}(i)/c]^{-2}$ and photon-noise is assumed $A_{rms}(i) = \sqrt{A(i) + \sigma^2_{ro}}$. Hence, from Eq. (4.12) we have

$$W(i) = \frac{\lambda(i)^2[\partial A_0(i)/\partial\lambda(i)]^2}{A_0(i) + \sigma^2_{ro}} \tag{4.13}$$

Equation (4.13) is computed with $A_0 = T^j_{RV_1,Bl,Scl}$, $\lambda = W^{i,j}$, while the derivative is computed as described in 3 (now the linear fit is performed over 3 pixels). With this, the RV error is calculated as

$$\delta v_{rms} = \frac{c}{\sqrt{\sum W(i)}} \tag{4.14}$$

12. Stellar activity tracers: the S- and $H\alpha$-index are derived from the observed spectrum without the blaze function. To compute the S-index, I used the same pass bands as Vaughan et al. (1978), namely, two triangular pass-band with FWHM=1.09Å centred in the Ca II H&K lines, and two 20Å-wide pass-bands centred in 3901Å and 4001Å. On the other hand, the $H\alpha$-index is computed using a 31 $km\,s^{-1}$-wide pass-band centred in 6562.808Å, and two pass-bands limited by 6545.495-6556.245Å and 6575.934-6584.684Å (Kürster et al., 2003; Bonfils et al., 2007). Experimentally, I derive RVs when only using the concave upward and downward parts of spectral lines; for that, the second derivative is computed analogously to the item 3; next, regions where $\partial^2 T^j_{RV_1,Bl,Scl}/\partial\lambda^2$ is greater or lower than zero are stored. This results in a set of $\chi^{2_i}_{up}$ and $\chi^{2_i}_{down}$, to which I fit a Gaussian (see item 10), and then, the difference between the RVs obtained from each χ^2-profile is calculated, resulting in $RV_{\chi^2-bis} = RV_{up} - RV_{down}$. Figure 4.11 shows an example of this result for the moderate active Gl 674 (e.g. Bonfils et al., 2007) and for the very active Gl 388 (e.g. Morin et al., 2008). I demonstrated in Fig. 4.11 that we obtain a correlation between RV and bisector, in the case of active stars more accurate than the obtained from the classical CCF.

Figure 4.9 shows a snapshot of the *"Second step: optimising RV"*. When comparing to the *"First step: estimating RV"* (Fig 4.6) we note that the iteration over the scaling factor has corrected the offset

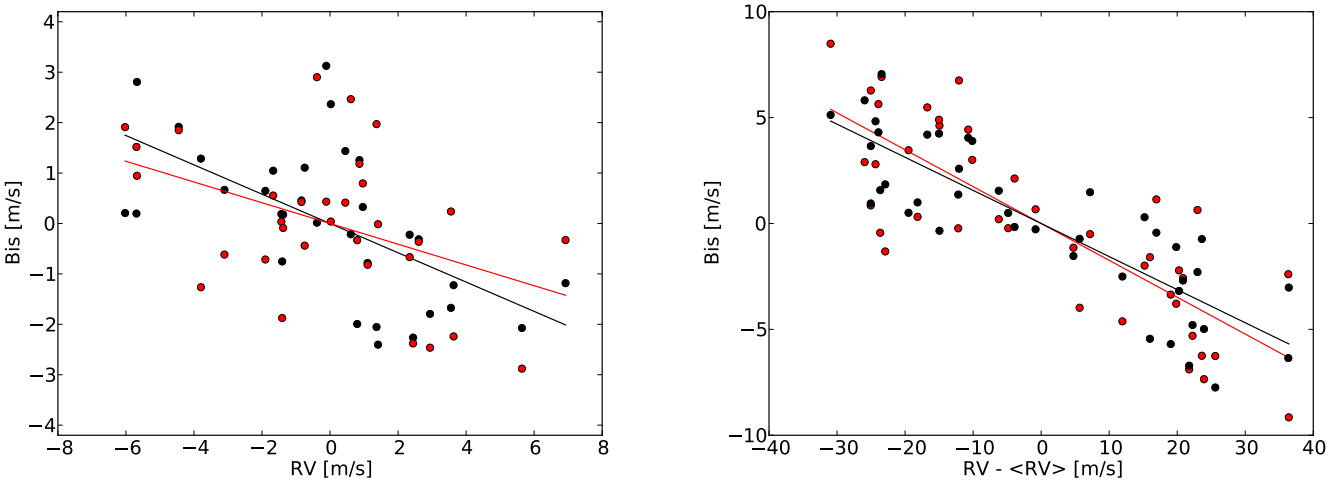

Figure 4.11: This example shows the comparison between the bisector-span derived by the CCF (red) and the experimental RV_{χ^2-bis} (black) from NAIRA. Left panel corresponds to data from Gl 674 ($P_{rot} \approx 35\ d$), a star with a planetary companion – which signal was removed – and an active region; the *RMS* of the linear fits are 1.27 (CCF) and 1.18 (NAIRA). In the right panel I used data from the very active star Gl 388 (AD Leo, $P_{rot} \approx 2.24\ d$), in this case the *RMS* of the linear fits are 2.54 (CCF) and 1.94 (NAIRA).

seen in the order centred in 690 *nm* (as bad regions are removed), and that telluric zones were removed. These improvements are also reflected in the difference between the distribution of normalised residuals and its Gaussian fit ($N - G_{fit}$ in Fig 4.9): the *"noise"* for $(O-C)/\sigma < -3$ and the structure for $2 < (O-C)/\sigma < 4$ disappears.

4.1.4 Fraction of rejected wavelength region

As described above, NAIRA rejects: extrapolated zones at the edges due to Doppler shifting, regions with telluric or without Doppler information, and 5σ-clipped pixels plus five elements on each side. Table 4.1 summarises the percentage of rejected zones when extracting RVs from Gl 436 and GJ 1214 spectra, where the total comes from the combination of each rejection criteria. From the table we note that the dominant criteria is the rejection of zones with telluric or/and poor Doppler information (Eq. 4.10, item 6 in the subsection *"Second step: optimising RV"*). As we will see in section 4.2.1 (and in Artigau et al., 2014), with Etienne Artigau we determine that about 4% of the spectral domain from 4030Å to 6830 Å is dominated by telluric lines (that would have introduce a bias in RV). Hence about 27% and 11% of Gl 436 and GJ 1214 spectra is rejected because poor Doppler information (it would have introduced noise in RV). This large difference can be explained by the fact that GJ 1214 spectra have a much more lower S/N than those of Gl 436, which makes difficult to determine regions with poor Doppler information (Eq. 4.10), and in addition, faint to moderate telluric may be lost in the noise. This does not prevent improved results for GJ 1214 when comparing RV from CCF and NAIRA, as I show in section 4.1.5. In the future, this point should be investigated in detail.

Table 4.1: Percentage of rejected pixels in Gl 436 and GJ 1214 RVs extraction.

% rejected	Gl 436	GJ 1214
Total	33.4	17.9
Edges trim	2.7	2.1
Telluric+No Doppler Info.	30.8	15.4
5σ clipping	2.2	1.4

The big picture of the algorithm is shown in figure. 4.12; this flowchart of NAIRA represents the major tasks performed to compute precise RVs. In the following, I will test the results and performances of the algorithm.

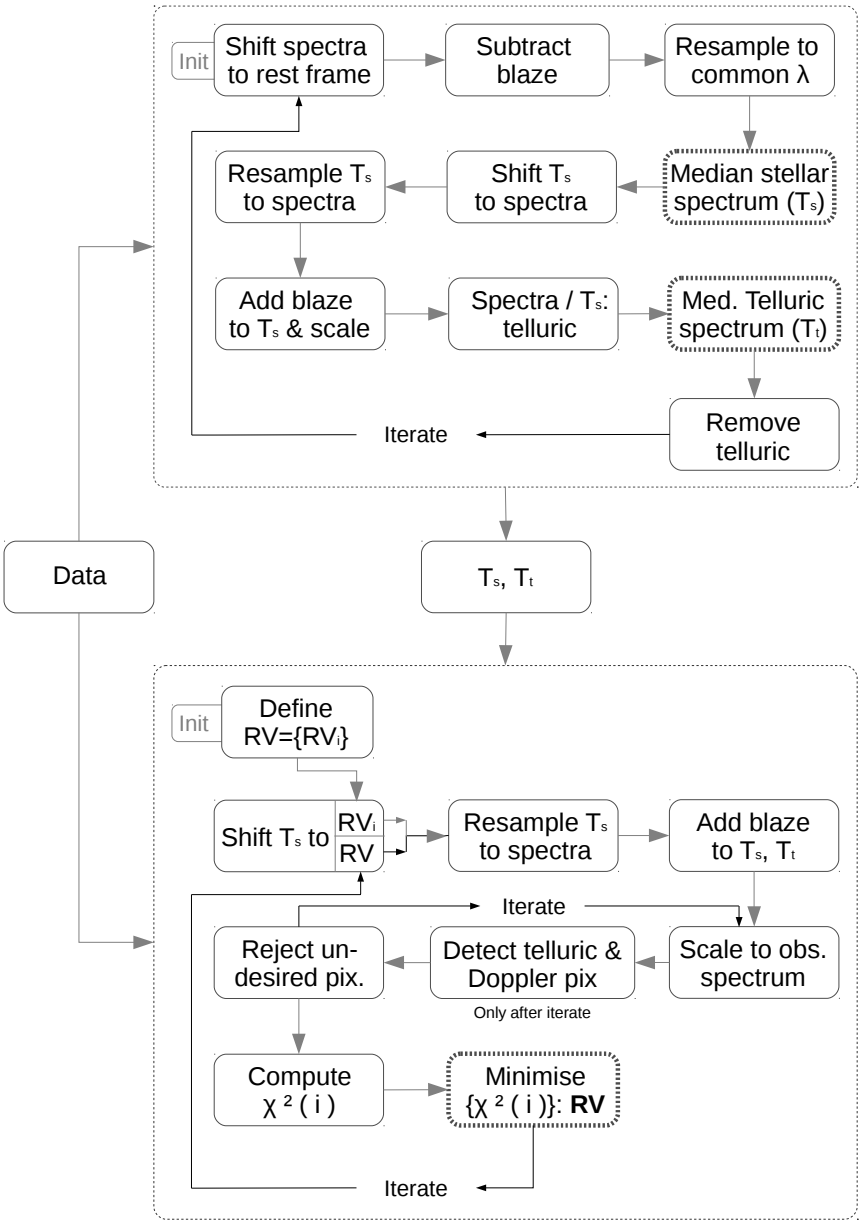

Figure 4.12: Flowchart of the algorithm. The top panel is firstly performed, and then, the bottom one. The *Init* label represents the starting point and dashed rectangles highlight final results.

4.1.5 Performances

Now I turn to the performances achieved by NAIRA. Once data for a given target is stored in a dedicated folder and the target *id* is entered to the algorithm, NAIRA can be initialised without any user intervention. However, some options can be tuned by the user, such choice are:

- Only implement the template, only extract RVs, or perform both. This is useful if the user want to test the RVs extraction using the stellar-template of a different star (experimental).
- In the construction of the template, neglect the spectrum to which the RV will be extracted; this option imply to construct a template for each spectrum. It is useful when the amount of spectra or the S/N are low, avoiding noise auto-correlation.
- Doppler analysis with or without telluric regions. Useful from a pedagogical point of view or to perform tests, because one notices how telluric affect a set of RVs.
- Load the telluric-template from a file specified by the user. If the amount of spectra of a given target or the change in *BERV* are low, or the target is faint, the telluric-template will be not well inferred. It is possible to use a better telluric spectrum.
- The number of threads to be used by the algorithm. This option exploits CPUs that have several cores able to run multi-threads. Useful for impatient.

In the performance test we analyse RV data from Gl 436 and GJ 1214. I choose these two stars because they are in two brightness regimes (and therefore in two $< S/N >$ regimes). Both stars have known planets, ensuring to check that NAIRA is able to retrieve planetary signals. For both stars we dispose of very numerous HARPS exposures. I make use of YORBIT (Damien Ségransan), an heuristic algorithm exploring the orbital parameter space by genetic algorithms and search for Keplerian solutions by non-linear minimisation.

Gl 436

This bright ($V = 10.59$) M dwarf harbour one planet, GJ 436b is a warm-Neptune detected by RVs and transit (Butler et al., 2004; Gillon et al., 2007) and is specially interesting due to its moderate eccentricity in a close-in orbit (where tidal circularisation is expected; e.g. Beust et al., 2012); in addition, Stevenson et al. (2012) claimed two Earth-mass planets detected in transit, however, these two transiting-planets are not detectable by RV (for a complete analysis see Lanotte et al., 2014). I used 127 measures acquired between 2006 January 25 and 2010 April 6 (time span 1531.8 d), where 44 measures recorded in a single night corresponding to a transit event are discarded in this test. I used Gl 436 parallax and proper motion from van Leeuwen (2007) – $\pi = 98.61 \pm 2.33\,[mas]$, $\mu_\alpha,\ \mu_\delta = 896.07,\ -813.54\ [mas\,yr^{-1}]$ – to compute its secular acceleration ($0.34135\ [m\,s^{-1}\,yr^{-1}]$). The secular acceleration was subtracted from RVs computed using the CCF and NAIRA, and then, I ran YORBIT without any prior in the orbital parameters and setting a stellar mass of $0.556 M_\odot$ (Lanotte et al., 2014). Table 4.2 lists the orbital parameters derived from both set of RVs (CCF and NAIRA), where our new RVs show a **18%** improvement (from 1.70 to 1.39 $m\,s^{-1}$ dispersion) in the dispersion of the residuals σ_e (the root-main-square weighted by the errors, which is computed by YORBIT) and an overall improvement in the precision of the orbital parameters – σ_e changes from 1.70 (CCF) to 1.39 (NAIRA) $[m\,s^{-1}]$. However, in both cases the dispersion of the residuals σ_e are about $40\,cm\,s^{-1}$ over the average Doppler uncertainty $\langle\sigma_i\rangle$ – computed by YORBIT. This

dispersion excess could be due to an unseen companion or RV jitter introduced by magnetic activity, although Gl 436 rotation period ($P_{rot} = 48\ d$, Demory et al., 2007) suggests that it is magnetically quiet; additionally, any correlation evidence arose between activity indices and RVs residues. More interesting is that RVs residuals shows periodicity around 4.7 d detected with a 99.0% confidence and a second peak at 48.7 d with a detection slightly above 2σ (see Fig 4.13). While the later peak is consistent with the stellar rotation, the peak at 4.7 d is very close to the signal identified by Ribas et al. (2008) at $P = 5.2\ d$ and reported as a $5M_\oplus$ planet which may be responsible of Gl 436b eccentricity. However, Alonso et al. (2008) found that a planet with this mass should produce detectable dynamic effects on Gl 436b, which is not the case. For a model with two-Keplerian YORBIT converged to the solution previously found for Gl 436b ($P = 2.64\ d$) and for the second signal only forcing solutions near the periodogram peak (4.7 d; $P_2 \in [2, 10]$) allowed the convergence; even so, the solution for the second signal was unreliable after visual inspection. To investigate what is the cause of the 4.7 days period, I split the data in three groups corresponding to the epochs 2007 (22 measures), 2008 (47 measures) and 2009 (42 measures), and I performed periodograms for the RV residuals, the S- and $H\alpha$-index. Figure 4.14 shows that the signal at 4.7 d disappears in 2009, favouring a scenario where the signal is not from a companion. From the same figure we note that periodograms for RVs residuals and the S-index from 2008 presents power excess at 4.7 d, and therefore, the nature of such signal comes certainly from inhomogeneities on the stellar surface.

Table 4.2: One-Keplerian fit for Gl 436 using RVs from CCF and NAIRA.

	CCF	NAIRA
P [d]	2.643860 ± 0.000046	2.643893 ± 0.000037
K_1 $[ms^{-1}]$	17.424 ± 0.222	17.465 ± 0.182
e	0.154 ± 0.013	$0.160 + -0.010$
T_0 [JD-2400000]	54576.063 ± 0.035	54586.639 ± 0.028
ω [deg]	-39.8 ± 5.0	-40.1 ± 3.9
$m\,sin(i)$ $[M_\oplus]$	25.17	25.21
a [AU]	0.0308	0.0308
N_{meas}	127	127
Span $[d]$	1531.8	1531.8
$\langle\sigma_i\rangle$ $[ms^{-1}]$	1.23	1.04
σ_e $[ms^{-1}]$	1.70	1.39
RMS $[ms^{-1}]$	1.87	1.45
χ^2_ν	1.92	1.83

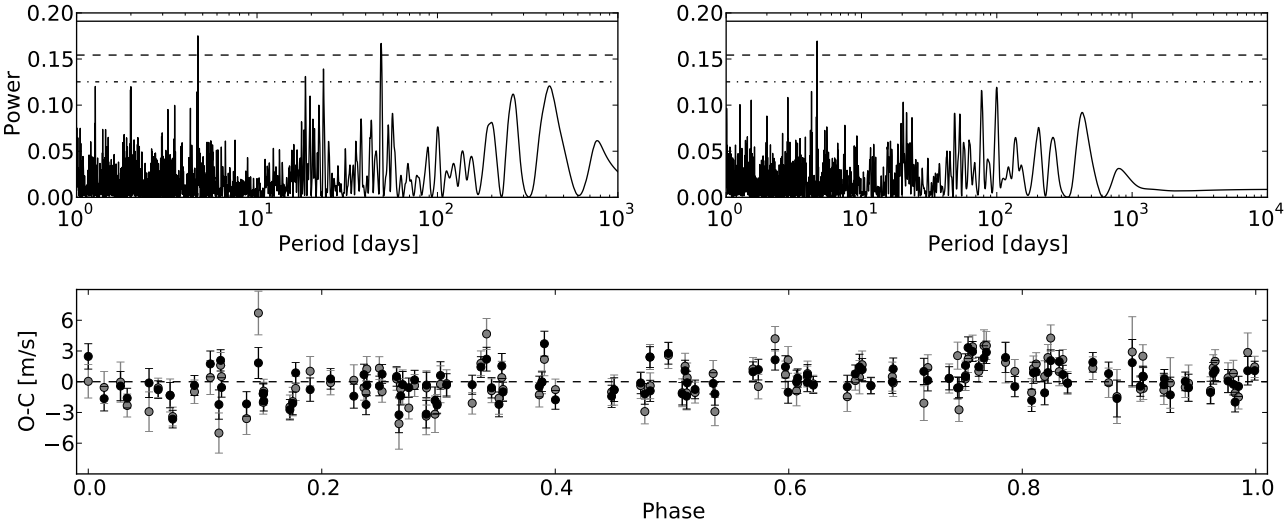

Figure 4.13: *Top panels:* Periodograms of the residuals when subtracting the Gl 436b signal from the RVs derived with NAIRA *(top left)* and with the CCF *(top right)*. Both periodograms show power excess – $p = 0.174$ (*left panel*), 0.169 (*right panel*) – at about 4.7 *d*. Horizontal lines represent 3σ (0.3%FAP, *solid line*), 2σ (4.6%FAP, *dashed line*), 1σ (31.7%FAP, *dotted line*) confidence limits. *Bottom panel* shows the residuals phased with a period of 4.7 *d*, where black points depict RVs from NAIRA ($\sigma_e = 1.43\,m\,s^{-1}$) and grey points represent RVs from the CCF ($\sigma_e = 1.70\,m\,s^{-1}$).

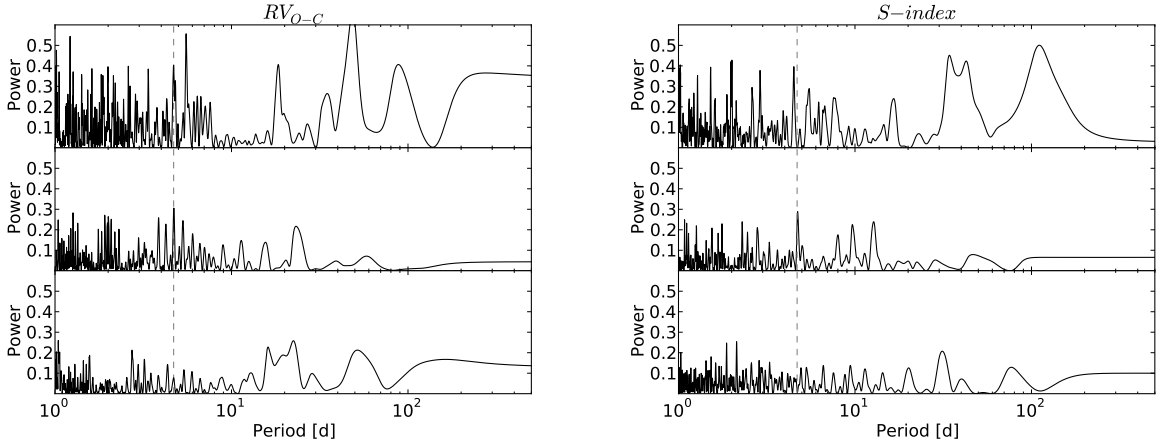

Figure 4.14: Periodograms for the RVs after subtract the Gl 436b signal (*left panel*) and the S-index (*right panel*). The first, second and third rows correspond to epochs 2007, 2008 and 2009, respectively; vertical dashed lines depict the 4.7 *d* period. We note the variability of the 4.7 *d* peak in the periodograms of the RVs residuals and the S-index from 2008 show power excess at 4.7 *d*. In the RVs periodogram from 2007 it is visible the peak (48 *d*) associated to the stellar rotation.

GJ 1214

This faint (V=14.67) M dwarf is orbited by a super-Earth caught in transit (P=1.58 d) and then followed by RVs (Charbonneau et al., 2009), and is nowadays one of the most studied super-Earth. A set of 96 spectra were acquired with HARPS between 2009 July 11 and 2012 September 25. For this test I retain only spectrum with RV_{CCF} error under 7 $m\,s^{-1}$, corresponding to 74 spectra (time span 1201.7 d). Due to the faintness of GJ 1214, the telluric spectrum may not be well derived, and therefore, I used the telluric-template obtained through Gl 436 observations. From the parallax ($\pi = 98.61 \pm 2.33\,[mas]$, Anglada-Escudé et al., 2013) and proper motion ($\mu_\alpha,\ \mu_\delta = 585, -752\ [mas\,yr^{-1}]$, Lépine and Shara, 2005) a secular acceleration of 0.30359 $[m\,s^{-1}\,yr^{-1}]$ is obtained, which was subtracted from RVs extracted by CCF and NAIRA. Both set of RVs were analysed with YORBIT without any prior on the orbital parameters ($M_\star$=0.15$M_\odot$, Charbonneau et al., 2009). Table 4.3 summarises the one-Keplerian model fitted to RVs, where a **23%** improvement in the Keplerian model is obtained using NAIRA: the dispersion on the residuals changes from σ_e=5.43 to 4.18 $[m\,s^{-1}]$ (σ_e=4.47 $[m\,s^{-1}]$ using the telluric-template derived with GJ 1214 spectra). The residuals and periodogram are showed in figure 4.15, and the periodogram from NAIRA analysis show less numerous peaks.

GJ 1214 was independently analysed by Anglada-Escudé et al. (2013) using 21 RVs extracted with HARPS-TERRA (Anglada-Escudé and Butler, 2012), they analysed RVs combined with transit data through a Bayesian Monte Carlo Markov chain method. They found an orbital solution with a considerable lower semi-amplitude and $RMS = 3.40\ m\,s^{-1}$ (table 4.3). Here I extracted RVs with NAIRA considering the same 21 measurements as Anglada-Escudé et al. (2013). It was imperative to use the telluric-template derived from a larger set of spectra, this because the 21 measurements only span 12 d and therefore the very low change in BERV will prevent to correctly extract the telluric spectrum. As above, I used the telluric-template derived with Gl 436 observations. After subtracting the secular acceleration, YORBIT converged to a solution whose $RMS = 3.28\ m\,s^{-1}$ is slightly improved ($\sim 3.5\%$) from the value obtained with RVs(HARPS-TERRA)+transit by Anglada-Escudé et al. (2013) (table 4.3 summarises each solution). However, considerable discrepancies arise in the RV semi-amplitude, I obtain from this 21 epochs $K = 14.97 \pm 1.15\ [ms^{-1}]$ which is in agreement (at $\sim 2\sigma$) with the RV semi-amplitude $K = 12.588 \pm 0.711\ [ms^{-1}]$ I obtain with the complete set. Anglada-Escudé et al. find $K = 10.68 \pm 1.60\ [ms^{-1}]$ which is marginally coherent with the value I derive. This difference in K is attributed to the stellar noise with an estimated RV jitter of 2.7-2.9 $m\,s^{-1}$ (Charbonneau et al., 2009; Anglada-Escudé et al., 2013). We can note that for this case NAIRA obtain better accuracy than HARPS-TERRA. In all the cases, the residual dispersion σ_e is over ($\sim 1\ m\,s^{-1}$) the average Doppler uncertainty $\langle\sigma_i\rangle$. Gillon et al. (2014) ruled-out any additional planet as small as Mars with a 98% confidence; on the other hand, the quietness of GJ 1214 is supported by its low rotation rate, the S-index periodogram shows a 0.16%FAP peak at 86 d (in agreement with the 83 d photometric estimation of Charbonneau et al., 2009); as I quoted above, the plausible explanation is that the $\sim 1\ m\,s^{-1}$ dispersion excess is due to stellar jitter.

Table 4.3: One-Keplerian fit for GJ 1214 using 74 or 21 RVs from CCF, HARPS-TERRA and NAIRA.

	CCF	NAIRA	HARPS-TERRA	NAIRA
	N_{meas}=74, Span=1201.7 d		N_{meas}=21, Span=12 d	
P [d]	1.580357 ± 0.000075	1.580388 ± 0.000056	1.580400 ± 0.000014	1.574 ± 0.011
K_1 $[ms^{-1}]$	12.810 ± 0.912	12.588 ± 0.711	10.68 ± 1.60	14.97 ± 1.15
e	0.074 ± 0.072	0.044 ± 0.061	0.11	0.21 ± 0.09
T_0 [JD-2400000]	55330.70 ± 0.27	55330.92 ± 0.32		
ω [deg]	-113.3 ± 60.6	-60.8 ± 73.0		
$m\,sin(i)$ $[M_\oplus]$	6.57	6.47		
a [AU]	0.0141	0.0141		
$\langle\sigma_i\rangle$ $[ms^{-1}]$	4.55	3.41	1.81+2.90	4.36
σ_e $[ms^{-1}]$	5.43	4.18		3.11
RMS $[ms^{-1}]$	5.51	4.20	3.40	3.28
χ^2_ν	1.49	1.54		0.69

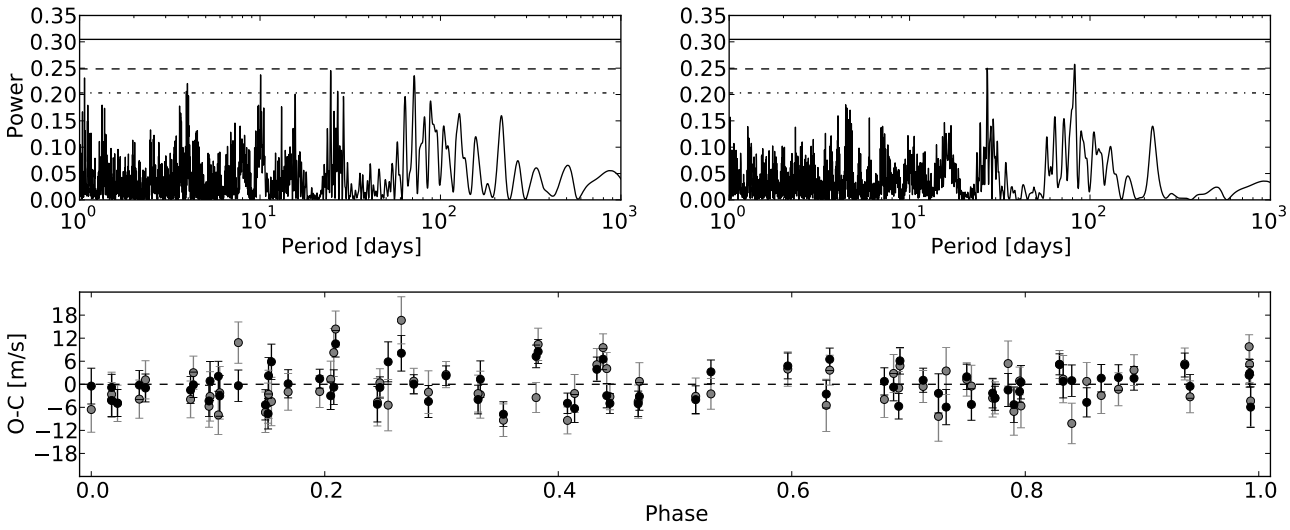

Figure 4.15: *Top panels:* Periodograms of the residuals for RVs extracted with NAIRA *(top left)* and with the CCF *(top right)*. No relevant peak appears, horizontal lines are as in Fig 4.13. *Bottom panel* shows the residuals phased with GJ 1214b period, where black points depict RVs from NAIRA ($\sigma_e = 4.18\,m\,s^{-1}$) and grey points represent RVs from the CCF ($\sigma_e = 5.43\,m\,s^{-1}$).

4.2 Applications

The template matching technique has several applications, for example: derivation of stellar rotation (e.g. Howarth et al., 1997), characterisation of exoplanets atmosphere (e.g. Snellen et al., 2010), stellar binary-system analysis (e.g. Zucker and Mazeh, 2006) and, of course, exoplanets detection/orbit characterisation (e.g. Anglada-Escudé and Butler, 2012). In this section I refer to the studies that, to date, have made use of NAIRA. One of them is about an analysis of the treatment of telluric features when deriving accurate radial velocities, the other is a complete analysis of the RVs of the M dwarfs GJ 3293, GJ 3341 and GJ 3543, which concludes with the discovery of new planets.

4.2.1 Telluric correction

Data acquired from the ground have the imprints of Earth's atmosphere and, as RVs are measured in the Solar-system barycenter frame, these telluric lines are Doppler shifted according to the $BERV$; thus, under the presence of such lines the stellar-template will correlate with them an introduce a spurious signal in the RV set. Therefore, some treatment to telluric features need to be done when deriving stellar RV from spectra. In the optical domain the strongest presence of telluric are around 630, 650 and 690 nm (about 4% of the HARPS wavelength coverage). When the presence is low the treatment may be as simple as removing the zones with telluric. In the optical case, a small but not negligible spectral domain is lost. On the other hand the HARPS pipeline procedure always uses the same spectral domain when performing the CCF, and is more conservative as it rejects $\pm 30\ km\,s^{-1}$ around $> 5\%$-deep telluric features: the rejected zones remains constant over through the year.

In the following SPIE paper we analysed the impact of telluric on accurate RVs; instead of removing telluric zones (as is done with NAIRA), a telluric correction is proposed from a statistical procedure which is useful when making predictive models: the principal-component-analysis (PCA). As its name says, PCA finds the principal components in data variability (e.g. Shlens, 2014). Telluric lines varies in strength due to the change in air-mass and/or species abundance, therefore, the PCA fits in this context. Although the procedure has been tested with HARPS data, which operates in the optical, this work was done in the context of $SPIRou$[4] (Delfosse et al., 2013), and it is relevant for any other nIR spectrograph (e.g. CARMENES, Quirrenbach et al., 2012), because in the nIR the situation is different from the optical as many more bands are seriously affected by telluric (mostly water). Here we show the results from this study, as they are encouraging for both tests carried out with τCet (G8V) and Gl 436 (M3.5V). Indeed, the gain in spectral coverage when telluric zones are corrected is reflected in a gain in RVs accuracy (a lower dispersion in the RV_{O-C}), showing that the telluric correction from PCA works.

For this study Etienne Artigau did the telluric correction by PCA while I made the whole RV analysis using NAIRA. In this paper I tested the effects of masking telluric lines and I show that the conservative approach that rejects $\pm 30\ km\,s^{-1}$ is unnecessary, as any systematic arises when using a different spectral domain across the data set. Not rejecting $\pm 30\ km\,s^{-1}$ takes special relevance in the nIR, because without any telluric correction (i.e. only removing telluric zones) the lost of spectral domain (3-15% for J-, H- and K-bands) does not prevent to achieve the 1 $m\,s^{-1}$ precision.

[4] SPIRou is a near-infrared spectropolarimeter and a high-precision velocimeter optimised for both the detection of Earth-like planets orbiting in the habitable zone of M dwarfs, and the study of forming Sun-like stars and their planets.

Telluric-line subtraction in high-accuracy velocimetry: a PCA-based approach

Étienne Artigau[a], Nicola Astudillo-Defru[b], Xavier Delfosse[b], François Bouchy[c], Xavier Bonfils[c], Christophe Lovis[d], Francesco Pepe[d], Claire Moutou[e], Jean-François Donati[f], René Doyon[a] and Lison Malo[e]

[a]Département de physique and Observatoire du Mont-Mégantic, Université de Montréal, Montréal H3C 3J7, Canada;
[b]Institut de Planéologie et d'Astrophysique de Grenoble, UMR 5274 CNRS, Université Joseph Fourier, BP 53, 38041 Grenoble Cedex 9, France;
[c]Aix Marseille Université, CNRS, LAM (Laboratoire d'Astrophysique de Marseille) UMR 7326, 13388 Marseille, France;
[d]Observatoire Astronomique de l'Université de Genève, 51 Ch. des Maillettes, 1290 Sauverny, Versoix, Switzerland; ;
[e]CFHT Corporation, 65-1238 Mamalahoa Hwy Kamuela, Hawaii 96743, USA;
[f]IRAP-UMR 5277, CNR and Université de Toulouse, 14 Av. E. Belin, F-31400 Toulouse, France

ABSTRACT

Optical velocimetry has led to the detection of more than 500 planets to date and there is a strong effort to push m/s velocimetry to the near-infrared to access cooler and lighter stars. The presence of numerous telluric absorption lines in the nIR brings an important challenge. As the star's barycentric velocity varies through the year, the telluric absorption lines effectively varies in velocity relative to the star's spectrum by the same amount leading to important systematic RV offsets. We present a novel Principal component analysis-based approach for telluric line subtraction and demonstrated its effectiveness with archival HARPS data for GJ436 and τ Ceti, over parts of the R-band that contain strong telluric absorption lines. The main results are: 1) a better RV accuracy with excluding only a few percentage of the domain, 2) better use of the entire spectrum to measure RV and 3) a higher telescope time efficency by using A0V telluric standard from telescope archive.

Keywords: Infrared, velocimetry, data processing, planet

1. INTRODUCTION

The presence of strong telluric absorption lines in the near infrared represents a challenge for m/s velocimetry as it adds a spectral component to all spectra that can be offset by as much as 30 km/s relative to the stellar lines. While the optical domain presents relatively large wavelength intervals free of telluric features (say above a few %), most of the near-infrared domain is affected. Proper handling of telluric absorption would therefore lead to a significant increase in the domain containing Doppler information. The present work has been performed in the context of the development of the SPIRou spectropolarimeter,[1,2] but is relevant for stable, high-resolution ($\lambda/\delta\lambda$ >20 000), near-infrared spectrograph such as CARMENES,[3] GIANO[4] or IRD.[5]

Further author information: (Send correspondence to E.A., artigau@astro.umontreal.ca, Telephone: 1 514-343-6111, ext. 3190

2. PCA APPROACH TO TELLURIC ABSORPTION

We propose a novel approach to telluric line absorption. This approach is based on a simple physical assumption; the observed telluric absorption spectrum is the sum (in absorbance) of a finite (H_2O, O_2, CO_2, N_2O, CH_4) number of chemical species that vary in relative strength. The absorbance spectrum is therefore a linear combination of individual absorbances with weight varying as a function of air mass and weather conditions (most notably from water). Note that single chemical species could contribute more than one independent absorbance spectrum as the specie is distributed vertically through the atmosphere (e.g. steam at 10°C and at high altitude may contribute slightly different spectra with relative weights that are not necessarily correlated). So, if one can build a library of these individual absorbances, then a given science observation can be calibrated using a linear combination of these absorbances.

In practice, this strategy would be implemented by regularly observing telluric standards, ideally rapidly rotating hot stars (A and earlier), at a large variety of air masses and water column. This could be done during poor-seeing nights, a handful of times per night. From these observations, a large library of absorption spectra is built and a principal component analysis (PCA *) is performed to identify independently varying absorbers. The PCA is done by expressing all observed absorption spectra in the library in absorbance. The multiplicative nature of absorption becomes a sum of various absorbances, which lends itself to least-square fitting. For every science spectra we build a least-square fit model with 1) an absorption-free spectra of a similar-type science target and 2) a linear combination of absorbance. This problem is very well constrained linearly as we will have ∼100 000 resolution elements in the spectrum for only a few (< 10) degrees of freedom. Whether this fit is performed piece-wise (e.g., one order at a time) or simultaneously through the entire wavelength domain remains to be seen. Note that very strong (i.e. >20%) absorption features should not be masked at this point as they provide the best constraints on the relative weight of the PCA components in this fit. They can be rejected at a later time in the analysis, for example at the time of the RV measurement;

The advantages of this technique are important; one does not necessarily need simultaneous calibration as long as a large set of observations at similar air mass and water column are present in the input library, leading to an increase in observing efficiency. As the science data itself is used to derive the absorbance to be subtracted, so the calibration is perfectly simultaneous by nature. Furthermore, there is no need to explicitly add RV shifts in the absorption spectra, as the PCA library will, over time, include absorptions at velocities representative of what is expected for a given observation. The drifts in velocity will appear as PCA components. If only one species was present, the first PCA component would be that absorber's signature, while the second component would be the spectral derivative of flux as a function of wavelength. If the absorption has a non-zero velocity in a given observation, we will see changes in the amplitude of that second component. One could explicitly include an additional component when performing the absorption modeling by adding $df/d\lambda$. This has not been implemented yet but would require minimal effort, should the need arise.

One could wonder why such a technique has not been used in the past? The technique can only be used if the telluric spectra are properly resolved. Blends of numerous lines of differing strengths do not scale as the log of absorbance. Furthermore, the wavelength coverage is large enough so that the PCA reconstruction is well constrained. In practice, one needs a number of lines much larger than the number of independent degrees of freedom. In the optical, where most high-resolution spectrograph operate, the interest is modest as most of the domain is relatively free of strong telluric lines. A few authors (Snellen et al.,[6] Birkby et al.[7]) have used a conceptually similar method, where they de-correlate telluric absorption from airmass. Here no telluric absorption model is used, and absorption depth is assumed to scale linearly with airmass, which may not be necessarily the case of chemical species, such as water, that have scale heights that differ significantly from that of the bulk of the atmosphere. This method has been applied in K and L band over limited domains. There has also been efforts to directly model telluric absorption in astronomical datasets, notably by the ESO team developping the *Molecit*[8] toolkit†. Purely empiric methods such as the one proposed here and modelling from line lists are certainly not mutually exclusive, although hybrid methods have not yet been documented. One could, for example, imagine an initial removal of telluric absorption by modelling complemented by a PCA-based approach to the removal of residuals to that subtraction.

* http://en.wikipedia.org/wiki/Principal_component_analysis

†http://www.eso.org/sci/software/pipelines/skytools/molecfit

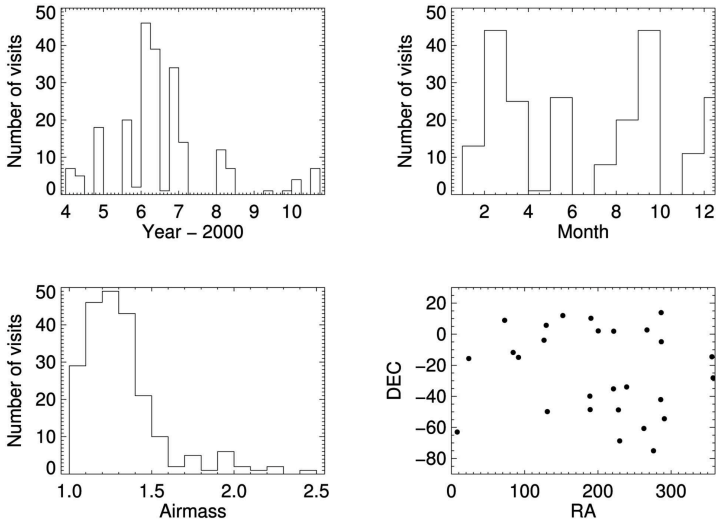

Figure 1. Sky distribution of hot stars used to derive the telluric absorption models (low right). Air mass (lower left), monthly (upper right) and time (upper left) distribution of hot star observations.

3. NUMERICAL IMPLEMENTATION WITH HARPS DATASETS

In order to verify the interest of a PCA-based subtraction of telluric line, we use two datasets obtained with HARPS on τ Ceti (G8V) and GJ436 (M3.5V) having respectively 1526 and 169 observations. τ Ceti observations were averaged in 73 epochs to average-out stellar pulsations on timescales of < 15 min. GJ436 is known to host a super-Earth, which radial velocity signal is clearly detected by the observations presented here. We also retrieved hot star spectra from the HARPS spectral library. A sample of 218 observations of 30 telluric standards with 3 to 23 visits per star were retrieved. The sky distribution of stars, airmass distribution, time distribution and yearly distribution of visits are shown in Figure 1. Observations of the two RV stars and hot stars were not concomitant. The HARPS domain ($378 - 691$ nm) covers telluric absorption features, especially around 630 nm that are comparable in depth with the near-infrared domain. Figure 2 illustrates the domain of interest ($628 - 634$ nm or orders 63 to 67 in HARPS) for estimating the accuracy of the proposed technique in subtracting telluric absorption. As shown in Figure 3, absorption over this wavelength interval is comparable to the absorption seen in near-infrared bandpasses.

The spectra for all hot stars in the library were corrected for blaze function. Low-frequency slopes in the SED were corrected by fitting a low-order polynomial to the absorption-free domain and all orders were normalized to one. A PCA extraction was performed on all hot star spectra and PCA components were saved in decreasing order of importance. For the analysis here, we considered only the 5 first components. This choice was justified by the fact that components beyond the 5^{th} component visually show no line-like feature and that for orders where strong (i.e. 5%) absorption is present, the 5 first components accounted for 95% of the total variance, suggesting that no significant power is left in the remaining components.

For each spectrum, we then perform a least-square fit of the estimate of the star's spectrum (initially assumed to be 1 for all wavelength bins) and the first 5 PCA absorption components. This was performed on all observations, which provide a first estimate of the total absorption. This absorption is then subtracted for all observations, corrected spectra are then registered to a common barycentric velocity and median combined to produce a high S/N, cleaned, reference stellar spectrum. This spectrum, shifted to a given observation's barycentric velocity, is then used in the least-square fit of the PCA components for that observation. After this second iteration, a more accurate estimate of the telluric-free absorption spectrum could be derived and used in again to measure absorption more accurately. In practice, only two iterations were sufficient to obtain satisfactory a convergence at the level of the observational noise.

Figure 4 and Figure 5 respectively show the reconstructed telluric absorption for τ Ceti and GJ436 for

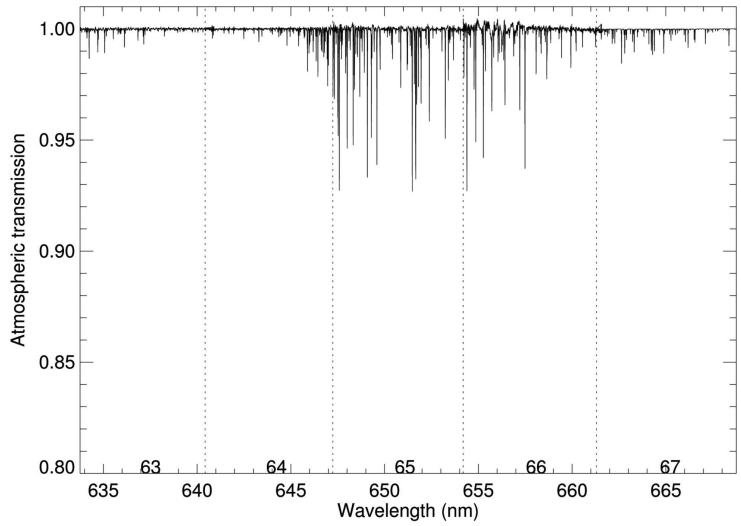

Figure 2. Typical absorption spectrum for orders 63 through 67; numerous lines with a 1-8% depth are present over this domain. This spectrum is derived from hot star observations.

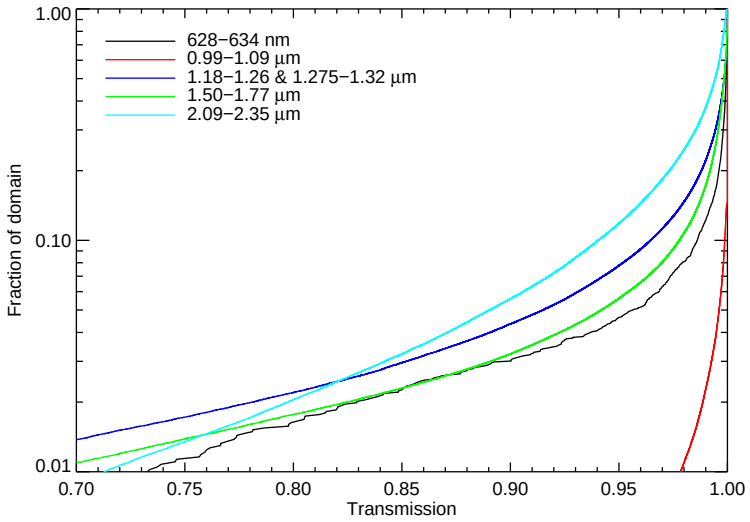

Figure 3. Cumulative distribution of transmission within the bandpass shown in Figure 2 and the four main near-IR windows. The $628-634$ nm, $1.50-1.77\mu$m (H) and $2.09-2.35\mu$m (K) windows all have $\sim$2% of their domains with transmission below 0.75. The $0.99-1.09\mu$m (Y) domain has a transmission below 98% for only 1% of the domain. Overall, the $628-634$ nm has a telluric line content representative of what is seen in the nIR beyond 1.09μm. The near-infrared absorption statistics is typical for the Mauna Kea ($\sim$ 1.6 mm water column) and correspond to the statistics expected for SPIRou. The $628-634$ nm data is for the HARPS dataset (La Silla) described here. Absorption for near-infrared bandpasses are taken from the TAPAS[9] atmosphere absorption models.

sample science integration. The corrected spectra for a single observation are shown compared to the median spectra for the entire dataset shifted at the same barycentric velocity. Residuals between the fitted and observed spectra are shown. No obvious differences between regions affected by absorption and the rest of the domain is seen. Table 1 compiles the RMS of residuals for various levels of absorption. Figure 6 illustrates the same dataset and compares it with the additional RMS from the increase in the relative Poisson noise from decreased flux in areas affected by telluric absorption. Overall, the increase in RMS due to telluric subtraction is larger than can be accounted from only from increased Poisson noise due to the lower flux. The increase is also dependent upon the S/N of the observations; observations of τ Ceti show much lower RMS levels than GJ436, presumably from the poorer fit of telluric absorption, but this would need to be confirmed as GJ436 spectrum is dominated by molecular bands compared to atomic lines in τ Ceti. The spectrum of τ Ceti, dominated by atomic lines, may lend itself to better constraints on absorption.

Table 1. Residual level (expressed in fractional RMS) between the cleaned spectra and reference spectrum as a function of telluric depth. For example, the residuals in the domain where there is $< 1\%$ absorption show a RMS of 1.15% of the median flux level. RMS increases with telluric absorption. The contribution from subtraction has been estimated by quadratically subtracting the RMS without ($< 1\%$) absorption from RMS observed at higher absorptions. For the τ Ceti, the additional RMS is at the level of 0.1%, and $\sim 1\%$ for GJ436. Low ($1 - 5\%$) absorption regions have been divided in two categories; being either adjacent to deeper absorption or from isolated lines. For the GJ436 dataset, residuals are more than 2 times smaller with isolated shallow lines.

Absorption level	GJ436 (628-634 nm)		τ Ceti (628-634 nm)	
	σ	$(\sigma^2 - \sigma_0^2)^{1/2}$	σ	$(\sigma^2 - \sigma_0^2)^{1/2}$
$< 1\%$	1.15%	0.00%	0.24%	0.00%
$1 - 5\%$	1.19%	0.63%	0.26%	0.10%
$1 - 5\%$ not adjacent to deeper absorption	1.31%	0.29%	0.25%	0.09%
$5 - 10\%$	1.26%	0.52%	0.26%	0.09%
$10 - 15\%$	1.44%	0.86%	0.27%	0.12%
$15 - 20\%$	1.60%	1.11%	0.27%	0.12%
$20 - 30\%$	1.83%	1.43%	0.28%	0.14%

Table 2. Same as Table 1, but for orders 62 through 68 ($634 - 667$ nm)

Absorption level	GJ436		τ Ceti	
	σ	$(\sigma^2 - \sigma_0^2)^{1/2}$	σ	$(\sigma^2 - \sigma_0^2)^{1/2}$
$< 1\%$	0.97%	0.00%	0.23%	0.00%
$1 - 5\%$	1.03%	0.33%	0.28%	0.15%
$1 - 5\%$ not adjacent to deeper absorption	1.04%	0.36%	0.29%	0.17%
$5 - 10\%$	1.06%	0.43%	0.32%	0.22%

Overall, a PCA-based analysis shows that one can subtract telluric features to better than a factor of 10 using non-contemporaneous telluric absorption measurements. This technique is likely to be key for near-IR velocimeters in order to maximize the useful RV domain. The technique is of general interest for ground-based optical and near-infrared observations and is by no means limited to RV measurement. It could open-up significant parts of the near infrared to spectroscopic observation, such as the wavelength interval between H and K under low water vapor conditions. Another important avenue to explore in the near future is the use of synthetic spectra (e.g. the TAPAS library[‡]) to derive PCA components. Assessing the interrest and the limitations of using modeled spectra of the atmosphere to subtract absorption is the logical next step in this work.

[‡]http://www.pole-ether.fr/tapas/

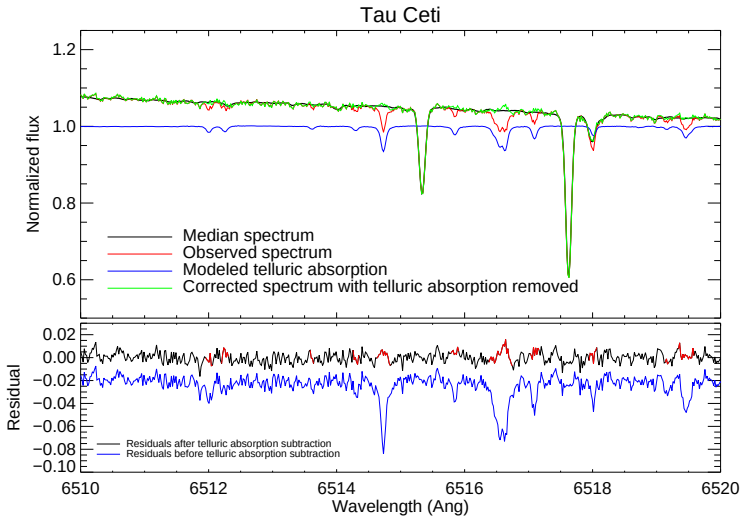

Figure 4. Observed spectrum of τ Ceti over a wavelength domain affected by telluric absorption. This region is part of order 65 (see Figure 2).

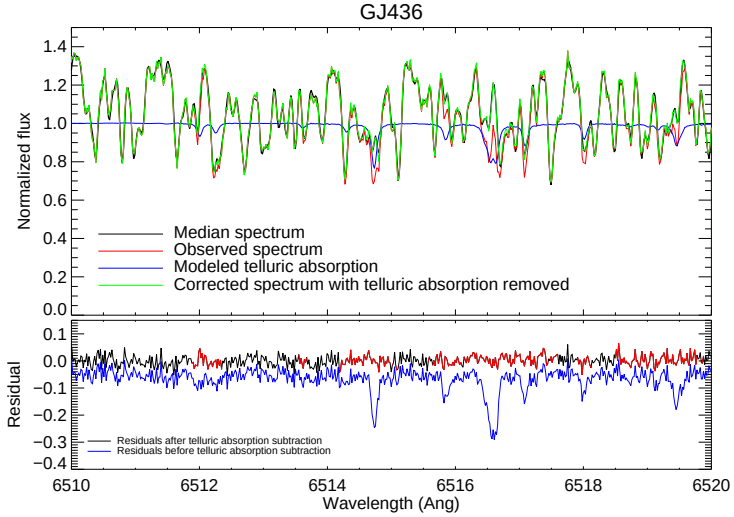

Figure 5. Same as Figure 4, but for GJ436. The spectrum is dominated by molecular bands instead of atomic lines.

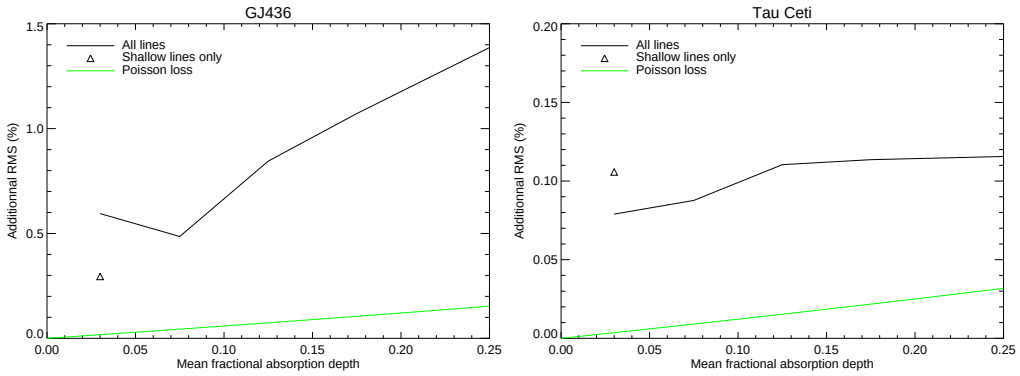

Figure 6. Additional RMS from PCA subtraction as a function of absorption depth for GJ436 (left) and τ Ceti (right). In both cases, deeper absorption features lead to an increase in the residual RMS. For comparison, green lines show the relative increase in the Poisson noise from the loss in signal due to absorption. For τ Ceti, the increase in RMS due to telluric-line subtraction is about 0.1% (right), while it is at the 1% level from GJ436 (left). The shallow lines only represents the contribution of residuals for absorption between 1 and 5% that is not adjacent to a deeper absorption (i.e. center of a shallow line in comparison of the wings of a deeper line).

4. TELLURIC LINE SUBTRACTION AND RV ACCURACY

The PCA telluric absorption subtraction has been performed on GJ436 and τ Ceti HARPS datasets. This allows one to verify that the method does not induce spurious RV signal and, hopefully, slightly improve the HARPS RV measurements that may suffer from low-level absorption unaccounted for by its current pipeline. Overall, there is always a gain in RV accuracy from the use of PCA subtraction (see Table 3). It is important to note that GJ436 has significant RV jitter that is not accounted for by photon noise and instrumental effects alone. This could be due to additional planets in its system and/or stellar activity.

The τ Ceti dataset has an σ_{o-c} of 1.07 ± 0.09 m/s with the original spectrum and 0.93 ± 0.08 m/s with PCA subtracted spectrum, clearly demonstrating that the technique described here does not degrade RV accuracy, but that it also brings an improvement that could be due to the correction of absorption lines that were not rejected by the HARPS pipeline[§]. This results is confirmed by the fact that the measurement performed only on orders 63 through 67 (See Figure 2) without excluding the many 1-8%-deep lines gives a 10.3 m/s RMS with the original spectra (implying that telluric lines completely dominate the RV RMS error budget) and a 1.58 m/s RMS with the PCA method. The fact that we obtain an RV accuracy of ~ 1.6 m/s over a wavelength domain with a large number of telluric lines and < 1 m/s over the entire HARPS domain shows that the PCA method can be successfully applied to obtain m/s RV precision and that no show-stopper is present to would prevent us from applying this method to the nIR. Furthermore, as quantified in Table 4, there is a significant gain in spectral domain from telluric line subtraction. Over orders $63 - 67$, ~ 18 % of the domain is lost to tellurics before subtraction, and this value falls to ~ 5 % after subtraction.

5. THE BENEFIT OF VARIABLE TELLURIC ABSORPTION MASK

The PCA subtraction of telluric lines as described here provides a mean of efficiently subtracting telluric lines. It is not known yet to which depth lines can be accurately subtracted and still allow for m/s velocimetry. We demonstrate that lines as deep as ∼10% are manageable, but what about deeper lines? The HARPS dataset does not allow one answer this question and, at a certain level depth of absorption, one will need to mask telluric lines and exclude the affected domain from the analysis.

OWhen few lines are present, one can exclude domain within ± 30 km/s of strong absorption lines so that the excluded domain remains constant through the year as the line-of-sight barycentric velocity changes. This increases by a factor ~ 10 the domain lost to absorption (telluric lines are a few km/s wide but this requires

[§]http://www.eso.org/sci/facilities/lasilla/instruments/harps/doc/DRS.pdf

Table 3. σ_{o-c} for GJ436 and τ Ceti RV data with and without telluric line subtraction. In all cases, the PCA telluric line subtraction improves the RV measurements. Measurements performed on orders 63-67 sample parts of the R band with significant telluric absorption.

	GJ436	τ Ceti	Rejected domain due to tellurics
Original spectrum, excluding strong telluric absorption not well removed in RV measurement	1.43 m/s	1.07 m/s	4%
PCA subtracted spectrum, excluding telluric absorption in RV measurement	1.39 m/s	0.93 m/s	1.1%
Original spectrum, orders $63-67$, excluding telluric absorption in RV measurement	2.30 m/s	3.6 m/s	17.7%
PCA subtracted spectrum, Orders $63-67$, excluding strong telluric absorption in RV measurement	2.21 m/s	1.77 m/s	4.9%
PCA subtracted spectrum, orders $63-67$, including regions where strong telluric absorption has been subtracted	2.64 m/s	1.58 m/s	

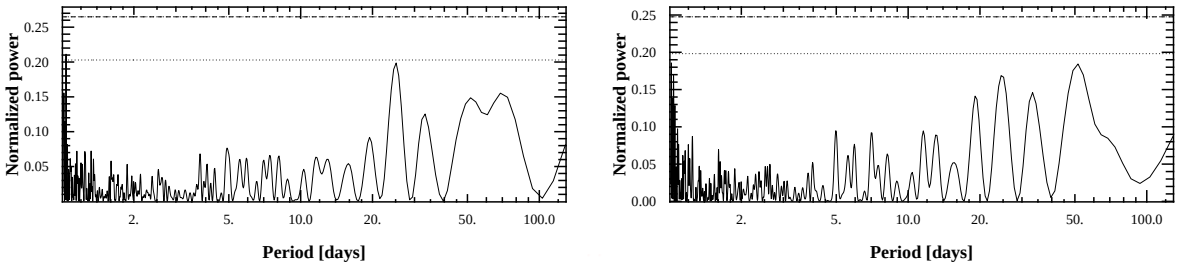

Figure 7. τ Ceti periodogram with (left) and without (right) PCA cleaning of telluric absorption. No spurious periodogram peak is added from the PCA subtraction. Strong telluric residuals should leave a periodogram peak at 1 year and its harmonics, but the observations spawn a baseline too short to show this peak.

excluding ~ 60 km/s windows), but ensures a measurement over the same spectroscopic features through the year (see Table 4). Absorption depths were determined from the ATRAN atmosphere model and a 1.5 mm (i.e. Mauna Kea median) water column. Without a rejection of a ± 30 km/s interval, the loss in RV signal is moderate (3-15%) for the J, H and K bands, even with relatively stringent rejection criteria (<5%). This loss increases rapidly (∼20 to ∼60%) when rejecting ± 30 km/s around telluric lines.

By using a mask that only removes telluric lines of a given epoch, one can significantly increase the usable domain. In the optical, the overall gain is minimal, but in the nIR, this could lead to a significant increase in the RV signal. We also show (Figure 8) that there is little changed in the domain lost to telluric absorption with the water column, suggesting that RV observations can be performed on most (> 95 %) of the nights.

Table 4. Loss in domain from telluric absorption with and without rejection of a ± 30 km/s interval surrounding absorption lines.

Absorption level	Domain lost		
	1.18-1.26 & 1.275-1.32μm	1.50-1.77μm	2.09-2.35μm
$< 5\%$	10.7%	9.2%	22.9%
$< 20\%$	2.8%	3.3%	6.8%
$< 5\%$, ± 30 km/s	40.9%	37.0%	57.0%
$< 20\%$, ± 30 km/s	14.3%	16.5%	25.6%

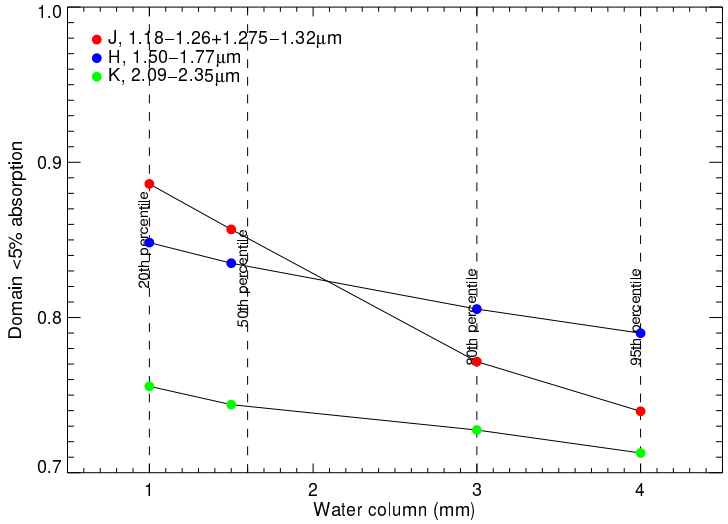

Figure 8. Fraction of the wavelength domain lost as a function of water . In practice, the difference between the 20$^{\text{th}}$ and 95$^{\text{th}}$ percentile for the Mauna Kea is relatively modest. This is due to the presence of saturated lines that vary little with water column.

5.1 Radial velocity measurements with 10% and 20% masked domain

We performed an analysis of the GJ436 and τ Ceti HARPS RV data to determine whether having a fixed mask on telluric lines that is not tracking the barycentric velocity of the star would induce significant systematic effects. We defined a mask consisting of 8 km/s-wide gaps randomly distributed across the HARPS domain and with a fractional coverage of 10% (roughly what is expected in H and K) and 20% (more than any nIR photometric bandpass). The radial velocity was extracted from the dataset with and without masking. From photon-counting statistics alone, one would expect a 5% et 10% decrease in the RV accuracy. Figure 9 shows the RV measurements (black, all wavelength domain, red, excluding 10%, green, excluding 20%) phased to GJ436's planet orbital period (2.643 days). The rejection of 10% of the wavelength domain to simulate the presence of numerous absorption lines only increases the RV RMS by 0.38 m/s (see Table 5). Figure 10 shows RV differences as a function of time, day of year and barycentric velocity. No obvious correlation exists between RV measurement and either barycentric velocity or day of year.

A similar analysis has been performed on τ Ceti's data and the impact of masking 10% and 20% of the domain is minimal (< 10 cm/s) and within the uncertainties on the RMS. This strongly suggests that removing 10% of the domain introduces no systematic bias and that there is no reason to take the conservative approach to reject a ± 30 km/s on either side of telluric lines.

In order to establish the level of systematic residuals from masking, we binned velocity differences as a function of barycentric velocity (8 km/s-bins, see red symbols in Figure 9). The $\chi 2$ ($\chi 2 = 4.6$ for 7 degrees of freedom, p=0.29) for these measurements is consistent with no systematic correlated with the barycentric velocity. Statistically, upper limits can be set on any signal correlated with barycentric velocity from numerical simulations. We set a 1-σ and 2-σ upper limits of 0.13 and 0.24 m/s on any correlated signal between barycentric velocity and difference in RV. The usage of a mask that varies with time significantly improves the RV budget and is not mutually exclusive with the PCA rejection. It would be desirable to both subtract telluric lines and use a rejection mask, the depth of which needs to be determined with actual data.

REFERENCES

[1] Artigau, É. & Donati, J.-F., and Delfosse, X., "Planet Detection, Magnetic Field of Protostars and Brown Dwarfs Meteorology with SPIRou," in [*16th Cambridge Workshop on Cool Stars, Stellar Systems, and the Sun*], Johns-Krull, C., Browning, M. K., and West, A. A., eds., *Astronomical Society of the Pacific Conference Series*, **448**, 771 (2011).

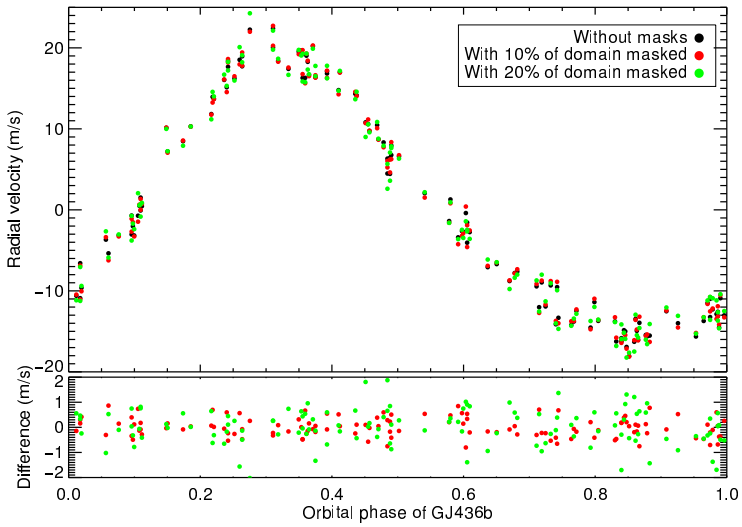

Figure 9. Radial velocity measured with the entire HARPS spectrum (black) and with 10% of the domain excluded with 8 km/s-wide windows (red) and with 20% of the domain excluded (green). The RV measurements closely match; differences between the two measurements have an RMS of 0.37/0.75 (red/green) m/s and show now specific structure as a function of phase.

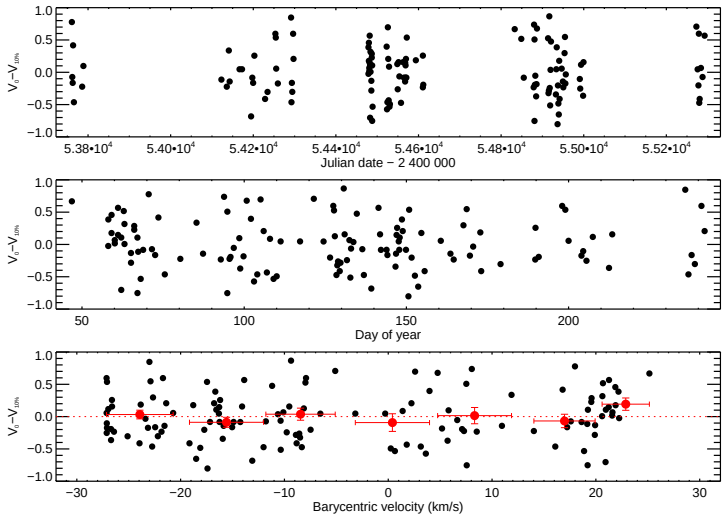

Figure 10. RV difference between velocities measured with and without 10% mask for GJ436. Panels respectively show the differences as a function of date, day of year and barycentric velocity. No systematic trend can be seen with respect to date of barycentric velocity, suggesting that no systematic effect at the tens of cm/s is present and that the RMS is dominated by the increase in photon noise. In the lower panel, red symbols show the mean velocity difference per 8 km/s bin; error bars correspond to the standard error for each of these means.

Table 5. Dispersion in (O-C) RV measurements with the full HARPS coverage (σ_0), the rejection of 10% of the domain to simulate numerous telluric lines ($\sigma_{10\%}$) and the difference between the two RV measurements (σ_{diff}).

	GJ436	τ Ceti
σ_0 (RV measurements)	1.39 m/s	0.93 m/s
$\sigma_{10\%}$ (RV measurements excluding 10% of domain)	1.46 m/s	0.86 m/s
$\sigma_{20\%}$ (RV measurements excluding 20% of domain)	1.60 m/s	0.94 m/s
σ_{diff} (no masking vs 10% masking)	0.38 m/s	0.16 m/s
σ_{diff} (no masking vs 20% masking)	0.75 m/s	0.20 m/s

[2] Delfosse, X., Donati, J.-F., Kouach, D. et al, "World-leading science with SPIRou - The nIR spectropolarimeter / high-precision velocimeter for CFHT," in [*SF2A-2013: Proceedings of the Annual meeting of the French Society of Astronomy and Astrophysics*], Cambresy, L., Martins, F., Nuss, E., and Palacios, A., eds., 497–508 (2013).

[3] Quirrenbach, A., Amado, P. J., Mandel, H. et al, "CARMENES: Calar Alto high-resolution search for M dwarfs with exo-earths with a near-infrared Echelle spectrograph," *Proc. SPIE* **7735** (2010).

[4] Oliva, E., Origlia, L., Maiolino, R. et al, "The GIANO spectrometer: towards its first light at the TNG," *Proc. SPIE* **8446** (2012).

[5] Tamura, M., Suto, H., Nishikawa, J. et al, "Infrared Doppler instrument for the Subaru Telescope (IRD)," *Proc. SPIE* **8446** (2012).

[6] Snellen, I. A. G., de Kok, R. J. & de Mooij, E. J. W., and Albrecht, S., "The orbital motion, absolute mass and high-altitude winds of exoplanet HD209458b," *Nature* **465**, 1049–1051 (2010).

[7] Birkby, J. L., de Kok, R. J., Brogi, M., de Mooij, E. J. W., Schwarz, H. & Albrecht, S., and Snellen, I. A. G., "Detection of water absorption in the day side atmosphere of HD 189733 b using ground-based high-resolution spectroscopy at 3.2 μm," *MNRAS* **436**, L35–L39 (2013).

[8] Kausch, W., Noll, S., Smette, A. et al, "Molecfit: A Package for Telluric Absorption Correction," *ArXiv e-prints* (2014).

[9] Bertaux, J. L., Lallement, R., Ferron, S. & Boonne, C., and Bodichon, R., "TAPAS, a web-based service of atmospheric transmission computation for astronomy," *A&A* **564**, A46 (2014).

4.2.2 A complete analysis of the radial velocities of GJ 3293, GJ 3341 and GJ 3543

M dwarfs are the focus of intense surveys to search for exoplanets (e.g. Bonfils et al., 2013), for which the CCF is the main technique used to extract RVs. Now, NAIRA has started to analyse data acquired under the HARPS M dwarf program (PI: X. Bonfils), and it will soon be used to analyse data under the M dwarf SOPHIE program (PI: X. Delfosse) and some RVs follow up – with HARPS-N and SOPHIE – of $K2$ M dwarfs (PI: A. Santerne).

After analysing with NAIRA the HARPS spectra of 12 M dwarfs, selected to have significant *RMS* excess from classical CCF analysis over the 300 M dwarfs from our HARPS large program, I selected several systems showing a clear periodic signal. Among them GJ 3293, GJ 3341, and GJ 3543 are the topic of the paper presented in this section. The complete HARPS M dwarfs large program sample will be soon analysed with NAIRA.

I present in this section our paper of the RVs analysis for GJ 3293, GJ 3341 and GJ 3543, whose RVs were extracted with NAIRA from HARPS data. The RVs analysis was carried out with YORBIT and a periodogram analysis (Zechmeister and Kürster, 2009), and in parallel, the S and $H\alpha$ activity indices are computed. Three new planets are announced, plus one candidate to be confirmed/rejected with more data: two Neptune-mass planets ($P = 30.60,\ 123.98\ d$) plus one super-Earth candidate orbiting GJ 3293 ($P = 48.14\ d$, if this candidate is confirmed, its orbit falls inside the habitable zone of GJ 3293), and one super-Earth around GJ 3341 ($P = 14.0\ d$). In the case of GJ 3543, the RV variations are more consistent with stellar activity.

When comparing CCF and NAIRA RVs for GJ 3293 and GJ 3341, the Keplerian solution is improved when using NAIRA. Indeed, the analysis of GJ 3293 for CCF RVs rapidly converges to the two strongest signals corresponding to the Neptune-mass planets, however, the fainter signal remains without significance (but visible) in the CCF RVs periodogram. Fitting three Keplerian solutions to the CCF RVs give a dispersion in the residuals $\sigma_e = 2.92 m\,s^{-1}$, which is improved by NAIRA RVs with $\sigma_e = 2.41 m\,s^{-1}$. The case of GJ 3341 is easier to analyse, the dispersion of the CCF RVs residuals is $\sigma_e = 3.40 m\,s^{-1}$, while NAIRA RVs obtain $\sigma_e = 2.86 m\,s^{-1}$. By using NAIRA, besides the tests performed for Gl 436 and GJ 1214, a gain in RV accuracy is also obtained here – GJ 3293 and GJ 3341 solutions are improved by about 17%. Table 4.4 summarises the data analysis using the classical CCF and NAIRA.

Table 4.4: Comparison between RVs derived from CCF and NAIRA for GJ 3293, GJ 3341 and GJ 3543.

	CCF	NAIRA
GJ 3293, N_{meas}=127 (Span=1531.8 d)		
P_b [d]	30.61 ± 0.02	30.60 ± 0.02
$K_{1,\,b}$ $[ms^{-1}]$	9.2 ± 0.5	8.9 ± 0.4
e_b	0.16 ± 0.04	0.09 ± 0.04
$T_{0,\,b}$ [JD-2400000]	55644.4 ± 1.4	55640.3 ± 1.9
ω_b [deg]	-29.7 ± 16.9	-77.7 ± 24.2
$m\,sin(i)_b$ $[M_\oplus]$	25.0	23.9
a_b [AU]	0.1434	0.1434
P_c [d]	48.14 ± 0.16	48.14 ± 0.12
$K_{1,\,c}$ $[ms^{-1}]$	2.2 ± 0.5	2.7 ± 0.4
e_c	0.16 ± 0.19	0.16 ± 0.13
$T_{0,\,c}$ [JD-2400000]	55648.2 ± 8.2	55643.3 ± 6.0
ω_c [deg]	50.3 ± 65.4	17.3 ± 46.3
$m\,sin(i)_c$ $[M_\oplus]$	7.0	7.9
a_c [AU]	0.1940	0.1939
P_d [d]	123.47 ± 0.40	123.98 ± 0.38
$K_{1,\,d}$ $[ms^{-1}]$	5.8 ± 0.5	5.5 ± 0.4
e_d	0.39 ± 0.07	0.37 ± 0.06
$T_{0,\,d}$ [JD-2400000]	55688.2 ± 3.9	55684.9 ± 3.7
ω_d [deg]	-20.1 ± 14.8	-38.0 ± 14.1
$m\,sin(i)_d$ $[M_\oplus]$	23.5	22.2
a_d [AU]	0.3634	0.3644
$\langle\sigma_i\rangle$ $[ms^{-1}]$	2.42	1.76
σ_e $[ms^{-1}]$	2.92	2.41
χ^2_ν	1.56	2.07
GJ 3341, N_{meas}=135 (Span=1455.9 d)		
P_b [d]	14.203 ± 0.006	14.207 ± 0.007
$K_{1,\,b}$ $[ms^{-1}]$	3.64 ± 0.51	3.04 ± 0.41
e_b	0.35 ± 0.11	0.31 ± 0.11
$T_{0,\,b}$ [JD-2400000]	55608.1 ± 0.7	55622.7 ± 0.8
ω_b [deg]	35.6 ± 21.3	42.32 ± 4.3
$m\,sin(i)_b$ $[M_\oplus]$	7.8	6.6
a_b [AU]	0.089	0.089
$\langle\sigma_i\rangle$ $[ms^{-1}]$	2.59	1.89
σ_e $[ms^{-1}]$	3.40	2.86
χ^2_ν	1.71	2.28
GJ 3543, N_{meas}=80 (Span=1918.8 d)		
$\langle\sigma_i\rangle$ $[ms^{-1}]$	1.57	1.21
σ_e $[ms^{-1}]$	3.30	3.02
χ^2_ν	4.24	6.02

Astronomy & Astrophysics manuscript no. GJ3293˙GJ3341˙GJ3543˙vF
January 7, 2015

The HARPS search for southern extra-solar planets⋆,⋆⋆,⋆⋆⋆

XXXVI. Planetary systems and stellar activity of the M dwarfs GJ 3293, GJ 3341, and GJ 3543

N. Astudillo-Defru[1,2], X. Bonfils[1,2], X. Delfosse[1,2], D. Ségransan[3], T. Forveille[1,2], F. Bouchy[3,4], M. Gillon[5], C. Lovis[3], M. Mayor[3], V. Neves[6], F. Pepe[3], C. Perrier[1,2], D. Queloz[3,7], P. Rojo[8], N. C. Santos[9,10], S. Udry[3]

[1] Univ. Grenoble Alpes, IPAG, F-38000 Grenoble, France
[2] CNRS, IPAG, F-38000 Grenoble, France
[3] Observatoire de Genève, Université de Genève, 51 ch. des Maillettes, 1290 Sauverny, Switzerland
[4] Laboratoire d'Astrophysique de Marseille, UMR 6110 CNRS, Université de Provence, 38 rue Frédéric Joliot-Curie, 13388 Marseille Cedex 13, France
[5] Institut d'Astrophysique et de Géophysique, Université de Liège, Allée du 6 Août 17, Bat. B5C, 4000 Liège, Belgium
[6] Departamento de Física, Universidade Federal do Rio Grande do Norte, 59072-970 Natal, RN, Brazil
[7] Cavendish Laboratory, J J Thomson Avenue, Cambridge, CB3 0HE, UK
[8] Departamento de Astronomía, Universidad de Chile, Camino El Observatorio 1515, Las Condes, Santiago, Chile
[9] Centro de Astrofśica, Universidade do Porto, Rua das Estrelas, 4150-762 Porto, Portugal
[10] Departamento de Física e Astronomia, Faculdade de Ciências, Universidade do Porto, Portugal

ABSTRACT

Context. Planetary companions of a fixed mass induce reflex motions with a larger amplitude around lower-mass stars, which adds to making M dwarfs excellent targets for extra-solar planet searches. The most recent velocimeters with a stability of ∼1m/s can detect very low-mass planets out to the habitable zone of these stars. Low-mass small planets are abundant around M dwarfs, and most of the known potentially habitable planets orbit one of these cool stars.
Aims. Our M-dwarf radial velocity monitoring with HARPS on the ESO 3.6m telescope at La Silla observatory makes a major contribution to this sample.
Methods. We present here dense radial velocity (RV) time series for three M dwarfs observed over ∼ five years: GJ 3293 ($0.42M_{\odot}$), GJ 3341 ($0.47M_{\odot}$), and GJ 3543 ($0.45M_{\odot}$). We extracted these RVs through minimum χ^2 -matching of each spectrum against a stack of all observed spectra for the same star that has a high S/N ratio. We then compared potential orbital signals against several stellar activity indicators to distinguish the Keplerian variations induced by planets from the spurious signals that result from rotational modulation of stellar surface inhomogeneities and from activity cycles.
Results. Two Neptune-mass planets - $msin(i) = 1.4 \pm 0.1$ and $1.3 \pm 0.1 M_{nept}$ - orbit GJ 3293 with periods $P = 30.60 \pm 0.02$ d and $P = 123.98 \pm 0.38$ d, possibly together with a super-Earth - $msin(i) \sim 7.9 \pm 1.4 M_{\oplus}$ - with period $P = 48.14 \pm 0.12$ *d*. A super-Earth - $msin(i) \sim 6.1 M_{\oplus}$ - orbits GJ 3341 with $P = 14.207 \pm 0.007$ *d*. The RV variations of GJ 3543, on the other hand, reflect its stellar activity rather than planetary signals.

Key words. stars: individual: GJ 3293, GJ 3341, GJ 3543 – stars: planetary systems – stars: late-type – technique: radial velocities

1. Introduction

A planet of a given mass induces a stronger reflex motion on a less massive host star. Around the low-mass M dwarfs, present-day observing facilities can consequently detect planets that are only a few times more massive than Earth (Fressin et al. 2013; Mayor et al. 2009). These very low-mass stars dominate Galactic populations by approximately 3 to 1 (e.g., van Dokkum & Conroy 2010), and most of them host planets: Bonfils et al. (2013a) estimated that $0.88^{+0.55}_{-0.19}$ planets orbit each early- to mid-M dwarf with a period shorter than 100 days, while Dressing & Charbonneau (2013) found that each star with effective temperatures below $4000K$ is orbited by $0.90^{+0.04}_{-0.03}$ planets with radii between 0.5 and $4R_{\oplus}$ and an orbital period shorter than 50 days. Their high Galactic abundance combined with their abundant planets make M dwarfs excellent targets for planet searches. These stars consequently are the focus of several ongoing surveys – with both radial velocity (RV) (e.g., HARPS Bonfils et al. 2013a) and transit techniques Nutzman & Charbonneau (e.g. MEarth 2008). Several instruments are being developed to specifically target these stars, such as SPIRou, Delfosse et al. (2013b), CARMENES, Quirrenbach et al. (2012), NGTS, Wheatley et al. (2013), and Exoplanets in Transit and their Atmosphere (ExTrA, Bonfils et al. in prep.), mostly in the near-infrared spectral range where M dwarfs are brighter and where a given photon noise can thus be achieved within a much shorter integration time.

⋆ Based on observations made with the HARPS instrument on the ESO 3.6 m telescope under the program IDs 072.C-0488, 082.C-0718 and 183.C-0437 at Cerro La Silla (Chile).
⋆⋆ Tables A.1, A.2, and A.3 are available in electronic form at http://www.aanda.org
⋆⋆⋆ Radial velocity data (tables A.1, A.2, and A.3) are only available in electronic form at the CDS via anonymous ftp to cdsarc.u-strasbg.fr (130.79.128.5) or via http://cdsweb.u-strasbg.fr/cgi-bin/qcat?J/A+A/

Much interest is currently focused on discovering broadly Earth-like planets that orbit within the habitable zone (HZ) of their host star. The HZ zone, by definition, is the range of host star distances for which the incident stellar flux allows water on a planetary surface to remain in the liquid phase, and after accounting for greenhouse effects, it corresponds to a surface equilibrium temperature of between 175K and 270K (Selsis et al. 2007). That zone is much closer in for a low-luminosity M dwarf than for a brighter solar-type star: the orbital period for a HZ planet ranges from a week to a few months across the M dwarf spectral class, compared to one year for the Sun-Earth system. This relaxes the $\sim$10 cm/s precision required to detect an Earth-equivalent orbiting a Sun-equivalent to $\sim$ 1 m/s for the same planet orbiting in the habitable zone of an M dwarf. Characterizing that planet during transit, if any occurs, is furthermore facilitated considerably by the much higher planet-to-stellar surface ratio. The equilibrium surface temperature of a planet secondarily depends on the nature of its atmosphere, making planetary mass an important parameter as well. Bodies with $M < 0.5M_{\oplus}$ are expected to retain atmospheres that are too shallow for any water to be liquid, while planets with $M > 10M_{\oplus}$ are expected to accrete a very thick atmosphere mainly dominated by hydrogen and helium (Selsis et al. 2007). These considerations together make GJ 667Cc (Delfosse et al. 2013a; Bonfils et al. 2013a), GJ 163 (Bonfils et al. 2013b), and *Kepler*-186f (Quintana et al. 2014) some of the best current candidates for potentially habitable planets.

Stellar activity affects habitability (e.g., Vidotto et al. 2013), but more immediately, it can induce false-positives in planet detection. M dwarfs remain active for longer than more massive stars because they do not dissipate their angular momentum as fast as their more massive brethren, and stellar activity correlates strongly with rotation period (Noyes et al. 1984). Additionally, lower mass stars are more active for a fixed rotation period (Kiraga & Stepien 2007). Activity, in turn, affects measured stellar velocities through a number of mechanisms: stellar spots deform spectral lines according to their position on the stellar surface, the up-flowing and down-flowing regions of convective cells introduce blue- and red-shifted components to the line shapes, and stellar oscillations also introduce a RV jitter. Stellar activity diagnostics are therefore essential to filter out spurious radial velocity signals that can otherwise be confused with planets (Bonfils et al. 2007).

Cross-correlation with either an analog or a numerical mask is widely used to extract radial velocities from spectra (Baranne et al. 1996). This technique concentrates the information of all the lines in the mask into an average line with a very high signal-to-noise ratio (S/N). It therefore enables characterizing the line profile in great detail. In addition to the usually minor effect of telluric absorption lines, any variation of the full-width at half-maximum (FWHM), contrast, or bisector-span of the cross-correlation functions that correlate with the radial velocity variations denotes that they originate in stellar phenomena such as spots, visible granulation density, or oscillations (Queloz et al. 2001; Boisse et al. 2011; Dumusque et al. 2011). Plages or filaments on the stellar surface can additionally be detected through emission in the Ca II H&K, and Hα lines, for example (Gomes da Silva et al. 2011).

Here we present analyses of GJ 3293 and GJ 3341 for which our HARPS measurements indicate the presence of planets, and for GJ 3543, for which we conclude that stellar activity more likely explains the RV variations. Section 2 briefly describes the observations and reduction process, Sect. 3 discusses the properties of each star in some detail, while Sects. 4, 5, and 6 describe the RVs analysis and orbital solutions and examines stellar activity. Finally, we conclude in Sect. 7.

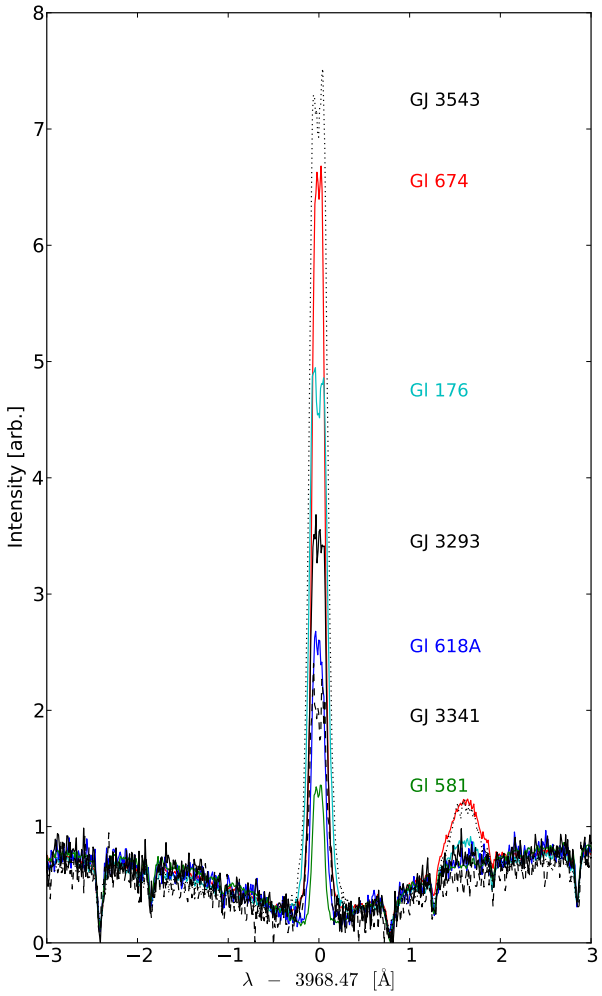

Fig. 1. Median spectra centered on the Ca II H line for reference stars, sorted by increasing rotation period: Gl 674 (red line, M3, P_{rot} = 35 d), Gl 176 (cyan line, M2.5, P_{rot} = 39 d), Gl 618A (blue line, M3, P_{rot} = 57 d), and Gl 581 (green line, M2.5, P_{rot} = 130 d). Median spectra for the targets of this paper, with no *a priori* known rotation period: GJ 3543 (black dotted line, M1.5), GJ 3293 (black full line, M2.5), and GJ 3341 (black dashed line, M2.5).

2. Spectra and Doppler analysis from HARPS

The High Accuracy Radial velocity Planets Searcher (HARPS) is a fiber-fed, cross-dispersed echelle spectrograph installed on the 3.6m telescope at La Silla observatory in Chile. The instrument diffracts the light over two CCDs, where 72 orders cover the 380 to 630 nm spectral range with a resolving power of 115,000 (Mayor et al. 2003). HARPS stands out by its long-term stability, ensured by a vacuum enclosure and a temperature-stabilized environment. To achieve sub-m/s precision, the spectrograph produces spectra for light injected through two fibers. One receives light from the target star, the other can be simulta-

neously (or not) illuminated with a calibration reference to correct instrumental drifts during the observations.

The HARPS pipeline (Lovis & Pepe 2007) automatically reduces the data using nightly calibrations and measures the radial velocity by cross-correlation with a binary mask (Pepe et al. 2002) that depends on the spectral type. The numerical mask for M dwarfs consists of almost 10,000 holes, placed on spectral lines selected for their large amount of Doppler information. The whole procedure is complete shortly after the end of each exposure.

The visual band spectra of the coolest stars contain very many overlapping molecular features with essentially no continua. Under these circumstances, a binary mask makes suboptimal use of the available Doppler information. In this study, we therefore recomputed RVs from the order-by-order spectra extracted by the HARPS pipeline. For each target, we used the RVs measured by the HARPS pipeline for the individual spectra together with the corresponding barycentric correction to align all spectra to the frame of the solar system barycenter. This aligns the stellar lines, while the telluric features are shifted by minus the barycentric velocity of each epoch. We then computed the median of these spectra to produce a high S/N template spectrum for each target. At that stage, we produced a template of the telluric absorption spectrum by computing the median of the residuals (aligned in the laboratory reference frame) of subtracting the high S/N template from the individual spectra. We then used this telluric spectrum to produce an improved stellar template by constructing it again without the now known telluric lines. This process can be iterated in principle, but we found that it effectively converges after the first iteration. Finally, we measured new radial velocities by minimizing the χ^2 of the residuals between the observed spectra and shifted versions of the stellar template, with all spectral elements contaminated by telluric lines masked out (e.g., Howarth et al. 1997; Zucker & Mazeh 2006, Astudillo et al. in prep.). Astudillo et al. (in prep.) will provide a detailed description of the algorithm implementation and will characterize its performance.

Our observation strategy is described in detail in Bonfils et al. (2013a) and is only summarized for convenience here. We chose to observe without illuminating the reference fiber because we only targeted a $\sim 1\ ms^{-1}$ precision; this choice provides clean observations of the Ca II H&K lines for later stellar activity analysis, which is particularly important for M dwarfs. We hence made use of wavelength calibrations acquired before the beginning of the night. The exposure time was 900s for all frames. This is adequate for a $0.80\ ms^{-1}$ precision for visual magnitudes between 7 and 10, but the velocities of the fainter stars we discuss here have significantly higher photon noise errors.

3. Stellar properties of GJ 3293, GJ 3341, and GJ 3543

GJ 3293 (LHS 1672), GJ 3341 (LHS 1748), and GJ 3543 (L 749-34) are high proper motion early-M dwarfs (M2.5, M2.5, and M1.5, respectively). We used the BC_K bolometric correction of Leggett et al. (2001) and the photometric distance of Gliese & Jahreiß (1991) to compute their luminosity. We also estimated the effective temperature (T_{eff}), stellar radius, and luminosity from the $V-K$ color and metallicity relationship of Boyajian et al. (2012); the two luminosities agree well for the three targets. We derived the stellar metallicities - and T_{eff}, for comparison - from our spectra using the methods of Neves et al. (2014); the two determinations of T_{eff} agree to better than their error bars for all three stars, and we only quote the Boyajian et al. (2012) value. The masses were computed using the Delfosse et al. (2000) K-band mass versus absolute magnitude relation. We calculated the UVW space motions with the (Johnson & Soderblom 1987) orientation convention, and assigned kinematic populations following Leggett (1992). We used the proper motion and distance to compute the secular radial acceleration dv/dt (Kürster et al. 2003), from which we corrected the radial velocities. Following Selsis et al. (2007), we adopted recent Venus and early Mars criteria for the inner (HZ_{In}) and outer (HZ_{Out}) edges of the habitable zone. Table 1 summarizes the properties of the three targets.

	GJ 3293	GJ 3341	GJ 3543
Spectral Type	M2.5	M2.5	M1.5
α (J2000)	$04^h28^m35.6^s$	$05^h15^m46.7^s$	$09^h16^m20.7^s$
δ (J2000)	$-25°10'16''$	$-31°17'46''$	$-18°37'33''$
V[(1)]	11.962	12.080	10.739
J[(2)]	8.362 ± 0.024	8.592 ± 0.020	7.351 ± 0.021
H[(2)]	7.749 ± 0.038	7.990 ± 0.049	6.759 ± 0.047
K[(2)]	7.486 ± 0.033	7.733 ± 0.023	6.492 ± 0.024
π $[mas]$[(3,4,3)]	55 ± 9	43.18 ± 1.40	80 ± 15
M_V	10.66 ± 0.31	10.26 ± 0.07	10.25 ± 0.34
M_K	6.19 ± 0.31	5.91 ± 0.07	6.01 ± 0.34
BC_K	2.71 ± 0.08	2.68 ± 0.06	2.68 ± 0.06
L [L_{Sun}][(6)]	0.022	0.029	0.026
M [$M_\odot$][(5)]	0.42	0.47	0.45
R [$R_\odot$][(7)]	0.404 ± 0.027	0.439 ± 0.027	0.432 ± 0.027
T_{eff} [K][(7)]	3466 ± 49	3526 ± 49	3524 ± 49
Fe/H[(8)]	0.02 ± 0.09	−0.09 ± 0.09	−0.13 ± 0.09
μ_α $[mas/yr]$[(9)]	−87 ± 5	504 ± 5	−314.6 ± 3.4
μ_δ $[mas/yr]$[(9)]	−475 ± 5	243 ± 5	148.0 ± 3.3
dv_r/dt $[m/s/yr]$[(10)]	0.097 ± 0.018	0.167 ± 0.008	0.035 ± 0.007
HZ_{In} $[AU]$[(11)]	0.112	0.129	0.124
HZ_{Out} $[AU]$[(11)]	0.305	0.350	0.335

Table 1. Stellar properties of the three targets. The parameter superscripts indicate the references: (1) Zacharias et al. (2012); (2) Cutri et al. (2003); (3) Gliese & Jahreiß (1991); (4) Riedel et al. (2010); from (5) Delfosse et al. (2000), (6) Leggett et al. (2001), (7) Boyajian et al. (2012) and (8) Neves et al. (2014) relationships; (9) Salim & Gould (2003); (10) Kürster et al. (2003); (11) Selsis et al. (2007).

GJ 3293 is located in the Eridanus constellation and is 18.2 ± 2.6 pc (Gliese & Jahreiß 1991) away from the Sun. Its Galactic velocity parameters, $U = -27.3 \pm 17.1\ kms^{-1}$, $V = -25.9 \pm 6.6\ kms^{-1}$, and $W = -22.2 \pm 23.1\ kms^{-1}$, leave its kinematic population uncertain in part because of the large uncertainty on its photometric distance; GJ 3293 could belong either to the young or the young-old disk population. Its metallicity ([Fe/H]=0.02) is close to solar and suggests that it is part of the young disk, but is consistent with either option.

GJ 3341 is located in the Columba constellation at a distance of 23.2 ± 0.7 pc (Riedel et al. 2010). Its proper motion, distance, and systemic velocity ($\gamma = 47.803 \pm 0.003$) result in $U = 52.5 \pm 0.6\ kms^{-1}$, $V = -52.0 \pm 0.8\ kms^{-1}$, and $W = 24.4 \pm 3.2\ kms^{-1}$. This formally makes GJ 3341 a young-old disk member.

GJ 3543 is located in the Hydra constellation and at 12.5 ± 2.0 pc from the Sun (Gliese & Jahreiß 1991). Its space motion components $U = 23.8 \pm 11.3\ kms^{-1}$, $V = -9.0 \pm 2.0\ kms^{-1}$, and $W = -2.7 \pm 1.7\ kms^{-1}$ place GJ 3543 in the young-disk box, while its metallicity ([Fe/H]=-0.13) is somewhat low for the Galactic young disk.

4. Radial velocities of GJ 3293

The 145 RV measurements of GJ 3293 span 1514 d. Their σ_e = $7.69\,ms^{-1}$ dispersion is much higher than the average Doppler uncertainty $\langle\sigma_i\rangle$ = $1.76\,ms^{-1}$, which represents the weighted arithmetic mean of the estimated photon noise (Bouchy et al. 2001) and instrumental errors. Both an F-test with $F = \sigma_e^2/\langle\sigma_i\rangle^2$ and a χ^2 test for a constant model given $\langle\sigma_i\rangle$ returned negligible probabilities ($< 10^{-9}$) that the photon noise combined with wavelength calibration and guiding uncertainties explains the measured dispersion.

We thus searched for periodicity with floating-mean periodograms, with a periodogram-normalization choice where 1 stands for a perfect fit of a sine wave to the data, and 0 points to no improvement over a constant model (Zechmeister & Kürster 2009). In addition to the commonly used 1% false-alarm probability (FAP) confidence level, we plot values covering 68.3%, 95.4%, and 99.7% of the periodogram power distributions, equivalent to 1σ (31.7% FAP), 2σ (4.6% FAP), and 3σ confidences (0.3% FAP).

Figure 2 shows the periodogram of the GJ 3293 time series and reveals a clear power excess around P = 30.6 d, with p_{max} = 0.51. Additional peaks above the 0.3% FAP (p = 0.17) appear at 121.6, 33.3, 48.2, 27.1, 919.5, and 500.9 d, with powers of 0.30, 0.22, 0.21, 0.20, 0.19, and 0.19, respectively. To further evaluate the confidence on the P = 30.6 d signal given our measurement errors and sampling, we generated 1,000 synthetic datasets by rearranging the radial velocities and holding the dates fixed. None of the periodograms generated for these bootstrapped datasets had maximum power above 0.3. The FAP on the 30.6 d signal, with 0.51 power, is therefore well below 1/1,000. The prescription of Horne & Baliunas (1986) for the periodogram interpretation gives $FAP(30.6d) = 2.8\times10^{-19}$, and the 30.6 d peak is well above any of the considered confidence levels.

We used *yorbit* (Ségransan et al. in prep) to adjust Keplerian orbits with an MCMC algorithm. Without any prior on the orbit, this converged on a solution with period $P = 30.565 \pm 0.024\,d$, eccentricity $e = 0.158 \pm 0.082$, and semi-amplitude $K_1 = 8.87 \pm 0.83\,ms^{-1}$. This solution reduces the rms dispersion of the residuals to $\sigma_e = 5.34\,ms^{-1}$ and the reduced χ^2 to $\chi^2_\nu = 9.28 \pm 0.37$. Given an M=0.42M$_\odot$ stellar mass (with 10% uncertainty), the minimum mass for the planet is $m\,sin(i) = 1.4\pm0.1 M_{nept}$. Table 2 summarizes the orbital and derived parameters. The ratio of the eccentricity (e) to its uncertainty (σ_e) is $e/\sigma_e < 2.49$, and therefore is below the usual thresholds for significant eccentricity[1] (Lucy 2013). We adopted the eccentricity that *yorbit* converged on when analyzing the residuals for additional signals, but its low value makes that choice unimportant.

Many of the peaks in the top panel of Fig. 2 have no counterpart in the periodogram of the subtraction residuals of the 30.6 d signal (Fig. 3) and therefore represent no more than aliases of that signal. A peak around 123.4 d dominates this periodogram of the residuals, with p_{max} = 0.64. A bootstrap test with one thousand (1,000) iterations produced no signal above 0.3, and the FAP of the dominant peak is therefore well under 10^{-3}. The prescription of Horne & Baliunas (1986) evaluates the FAP to 3.3×10^{-29} for the 123.4 d peak. Other peaks above a 0.3% FAP (p = 0.17) occur at periods 92.1, 48.2, 218.8, 186.5, 517.2, 55.0, and 41.2 d, and with powers of 0.39, 0.33, 0.27, 0.24, 0.24, 0.22, and 0.19. None of them is sufficiently strong that confusing the 123.4 d signal for one of its aliases would be a problem. We used *yorbit* to model the RVs with two Keplerian signals, again with no prior on the orbital parameters. The parameters of the first Keplerian are essentially unchanged from the one-Keplerian fit, and the second has a period $P = 123.76 \pm 0.30\,d$, eccentricity $e = 0.331 \pm 0.057$, and semi-amplitude $K_1 = 6.430 \pm 0.423\,ms^{-1}$, which correspond to a minimum planetary mass of $m\,sin(i) = 1.5 \pm 0.1 M_{nept}$. Table 3 summarizes the parameters of the two Keplerians. The dispersion and the reduced χ^2 decrease to $\sigma_e = 2.86\,ms^{-1}$ and $\chi^2_\nu = 2.76 \pm 0.20$. An F-test of this new σ_e^2 against the average internal errors $\langle\sigma_i\rangle^2$ and a χ^2 against a constant model return $P(F) = 5.7 \times 10^{-9}$ and $P(\chi^2) < 10^{-9}$, which means that significant dispersion remains above the internal errors.

A single peak dominates the periodogram of the subtraction residuals of the two Keplerians (Fig. 4), implying that the other strong peaks in Figs. 2 and 3 are aliases of the 30.6 and 123.8 d signals. This peak at 48 d has power p_{max} = 0.18, which corresponds to a 0.15% FAP (p = 0.15 corresponds to a 1% FAP and p = 0.17 to a 3σ confidence level). An uncon-

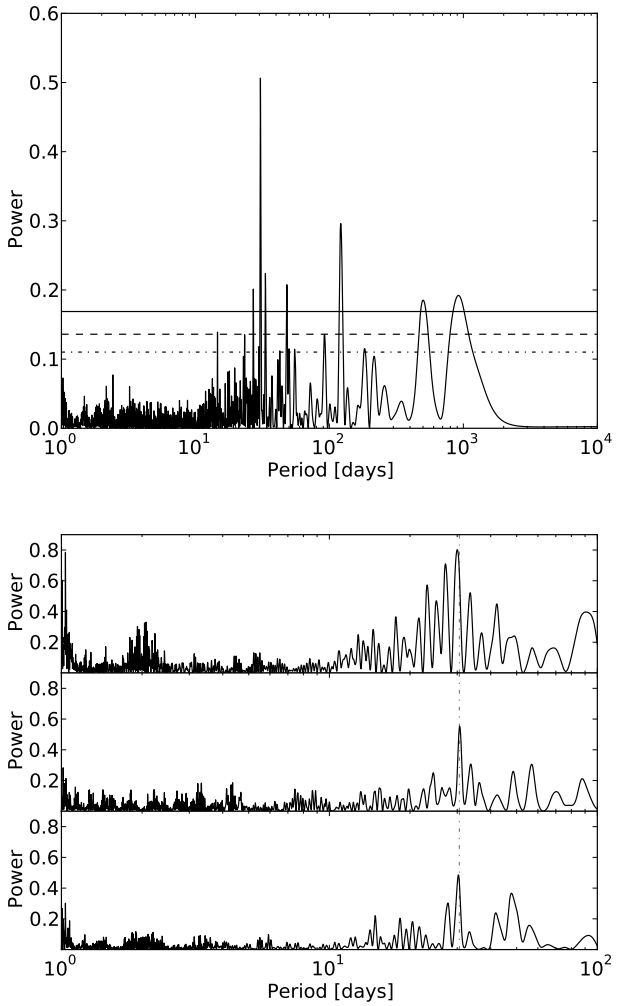

Fig. 2. *Top panel:* Periodogram of the GJ 3293 RVs. The solid line, dashed line, and dashed dotted line represent the 0.3%, 4.6%, and 31.7% FAP levels, corresponding to 3σ, 2σ, and 1σ confidence, respectively. *Bottom panel:* Periodograms for epochs 2008-2009 (34 measurements, first row), 2010-2011 (52 measurements, second row), and 2012-2013 (59 measurements, third row); the stability of the 30 d signal (dash-dotted vertical) is clear.

[1] ε_{95}/μ = 3.34 for the eccentricity upper limit, where $\mu = \sigma_e$ and $\alpha(\%) = 5$ for the detection threshold - using the nomenclature of Lucy (2013).

Table 2. One-Keplerian fit for GJ 3293

	GJ 3293b
P [d]	30.57 ± 0.02
T_0 [JD-2400000]	55661.6 ± 2.3
ω [deg]	169.4 ± 26.7
e	0.16 ± 0.08
K_1 [ms^{-1}]	8.9 ± 0.8
$m\ sin(i)$ [M_{nept}]	1.4 ± 0.1
a [AU]	0.1433
N_{meas}	145
Span [d]	1514
$\langle\sigma_i\rangle$ [ms^{-1}]	1.76
σ_e [ms^{-1}]	5.34
χ^2_ν	9.28

Table 3. Fit for two-Keplerian orbits for GJ 3293

	GJ 3293b	GJ 3293c
P [d]	30.60 ± 0.01	123.75 ± 0.30
T_0 [JD-2400000]	55638.7 ± 2.6	55687.8 ± 3.8
ω [deg]	−103.0 ± 31.3	−21.4 ± 14.2
e	0.07 ± 0.04	0.33 ± 0.06
K_1 [ms^{-1}]	9.6 ± 0.4	6.4 ± 0.4
$m\ sin(i)$ [M_{nept}]	1.5 ± 0.1	1.5 ± 0.1
a [AU]	0.1434	0.3640
N_{meas}	145	
Span [d]	1514	
$\langle\sigma_i\rangle$ [ms^{-1}]	1.76	
σ_e [ms^{-1}]	2.86	
χ^2_ν	2.76	

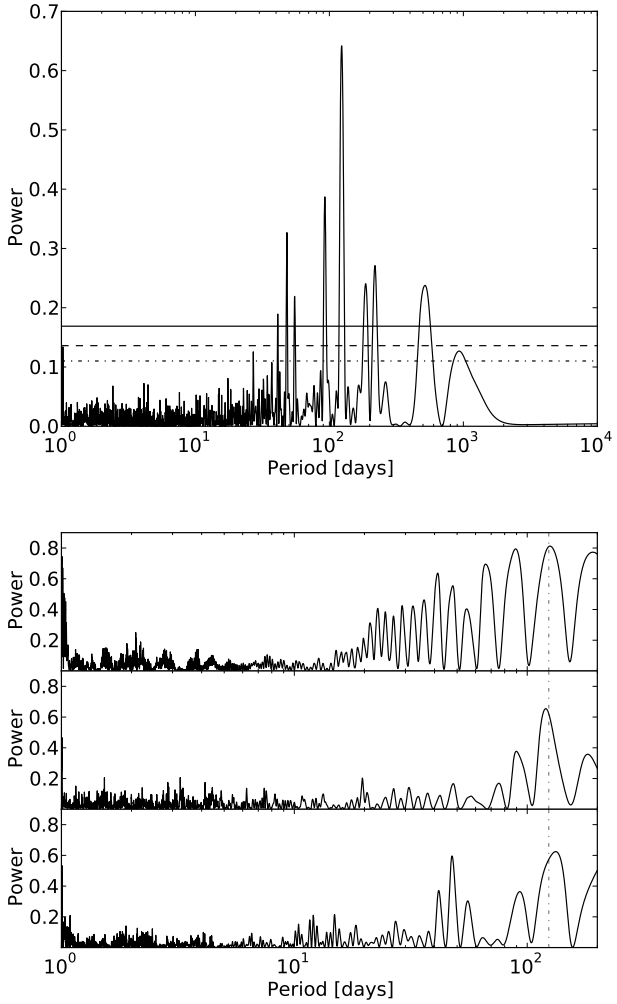

Fig. 3. *Top panel:* Periodogram of the residuals from subtracting the first Keplerian (P=30.6 d). The horizontal lines have the same meaning as in Fig. 2. *Bottom panel:* We split for subsets of the observational epochs, defined in the caption of Fig. 2, and performed their peridogram; in spite of the poor sampling of some of the subsets for a 123 d period, all show a peak around this period.

strained search for a three-Keplerian solution with *yorbit* converged on the two Keplerians described above plus a highly eccentric ($e = 0.925 \pm 0.022$) Keplerian with a period of 439 d period. The third orbit crosses the other two, making the solution almost certainly unstable on very short time scales, and therefore unphysical. Spurious highly eccentric orbits are favored when noise becomes significant and/or sampling is poor, with the highest velocity excursions typically found at the most poorly sampled phases of the orbit. The periodogram of the residuals of that unphysical solution still has a 48 d peak, but with much reduced power ($p = 0.10$, 0.63 FAP, middle panel of Fig. 4). This indicates that our sampling couples signals at periods of 48 and 439 d, but incompletely. We therefore constrained the period of the third Keplerian to the [2, 100] d range to avoid convergence on the spurious longer period eccentric solution. This converged on a Keplerian with $P = 48.072 \pm 0.120\,d$, $e = 0.190 \pm 0.134$, and $K_1 = 2.515 \pm 0.393\,ms^{-1}$, which corresponds to a minimum mass of $m\ sin(i) = 7.9 \pm 1.4 M_\oplus$, plus the two Keplerians with periods of 30.6 and 123.4 d. Following Lucy (2013), $e_b/\mu < 2.49$ and the eccentricity therefore remains below the detection threshold. Figure 5 shows the Keplerian solution. The dispersion is $\sigma_e = 2.45\,ms^{-1}$ and the reduced χ^2 is $\chi^2_\nu = 2.11 \pm 0.18$. An F-test of this σ_e^2 against $\langle\sigma_i\rangle^2$ yields a $P(F) = 4.3 \times 10^{-5}$ probability that this would occur by chance. The RVs therefore vary by significantly more than expected from their known measurement errors. Possible explanations include additional companions, stellar activity, or a non-Gaussian or underestimated noise. The periodogram of the residuals of the three-Keplerian solution (bottom panel of Fig. 4 has no peak above a 12% FAP (11.8% at 13.3 d and 11.7% at 669.6 d). Our final solution (Table 4) additionally includes a quadratic drift, which improves the residuals by a formally significant amount and suggests a possible component at a wider separation.

4.1. Stellar activity

We computed periodograms for the FWHM, bisector span, and contrast of the CCF, as well as for the S and Hα indices, to investigate whether some of the periodicities can be attributed to stellar activity. We also searched for correlations between these activity indicators and the radial velocities and their residuals after subtracting subsets of the Keplerian orbits.

The periodograms of the bisector span, FWHM, contrast, and S-index show no dominant peaks, while that for Hα shows one peak at over 3σ confidence at 41 d (Fig 6 top); since the strength of the Ca II emission in GJ 3293 is intermediate between those for Gl 176 ($P = 39\ d$) and Gl 618A ($P = 57\ d$) - Fig. 1, this peak may reflect the stellar rotation period. We see no correlation between any of the activity indicators and either the

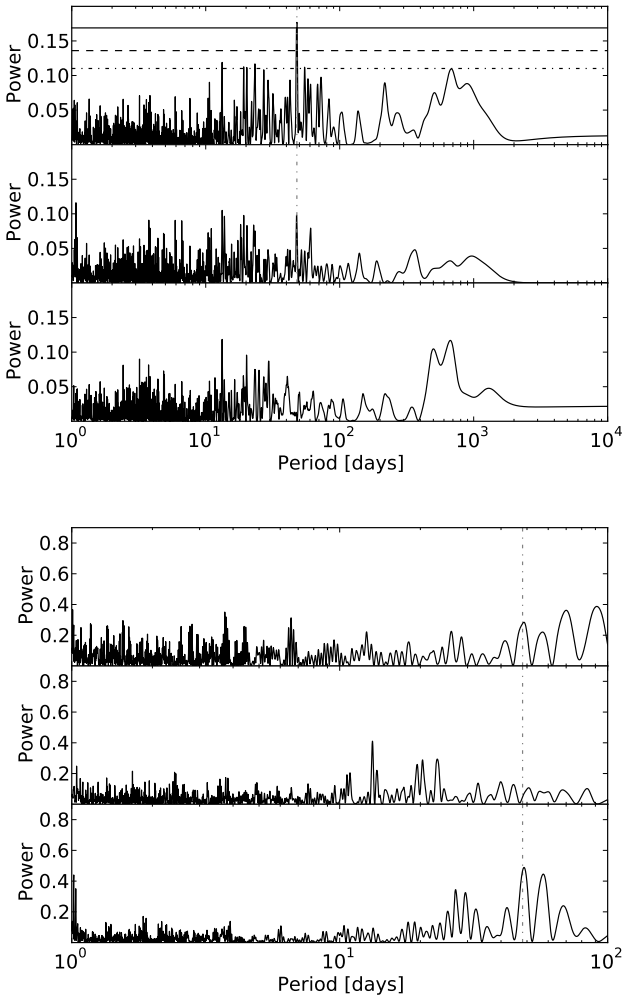

Fig. 4. *Top panel. First row:* Periodogram of the subtraction residuals of two Keplerians with periods of 30.6 and 123.6 d, dominated by a 48 d peak. The horizontal lines represent FAP levels, as described in the captions of Fig. 2. *Second row*: Periodogram of the residuals after subtracting three Keplerians with periods of 30.6, 123.6, and 439 d. The vertical dash-dotted line marks a P = 48 d period. *Third row*: Periodogram of the residuals after subtracting Keplerians with periods of 30.6, 123.6, and 48 d. *Bottom panel*. Periodogram of the residuals after subtracting the 30.6 and 123.6 d signals for each subset of epochs described in the captions of Fig. 2. The 48 d signal is not seen for the 2010-2011 observational epochs, which have a poor sensitivity to that period range because their sampling incidentally concentrates around just two phases.

radial velocities or the residuals from subtracting the Keplerian orbits (Fig. 6, bottom, for $H\alpha$).

To evaluate the stability of the 30.6, 48.1 and 123.8 d signals over time, we split the RVs into three groups of epochs: 2008-2009 (34 measurements), 2010-2011 (52 measurements), and 2012-2013 (59 measurements). We computed periodograms of the RVs and of their residuals after successively subtracting the stronger Keplerians. These seasonal periodograms consistently show strong evidence for the 30.6 and 123.8 d signals. The weaker 48.1 d signal is detected in the 2008-2009 and 2012-2013 periodograms, but not in the 2010-2011 epochs (bottom panels of Figs. 2, 3 and 4). After investigating, we realized that the 2010-2011 measurements are strongly clustered at just two phases for a 48.1 d period and therefore highly insensitive to

Table 4. Fit for three-Keplerian orbits plus a quadratic drift for GJ 3293

	GJ 3293b	GJ 3293(c)	GJ 3293d
P [d]	30.60 ± 0.02	48.14 ± 0.12	123.98 ± 0.38
T_0 [JD-2400000]	55640.3 ± 1.9	55643.3 ± 6.0	55684.9 ± 3.7
ω [deg]	−77.7 ± 24.2	17.3 ± 46.3	−38.0 ± 14.1
e	0.09 ± 0.04	0.16 ± 0.13	0.37 ± 0.06
K_1 $[ms^{-1}]$	8.9 ± 0.4	2.7 ± 0.4	5.5 ± 0.4
$m\,sin(i)$ $[M_{nept}]$	1.4 ± 0.1	0.5 ± 0.1	1.3 ± 0.1
a [AU]	0.1434	0.1939	0.3644
γ $[kms^{-1}]$	13.297 ± 0.018		
$\dot{\gamma}$ $[ms^{-1}yr^{-1}]$	−0.103 ± 0.002		
$\ddot{\gamma}$ $[ms^{-1}yr^{-2}]$	0.325 + −0.001		
N_{meas}	145		
Span [d]	1514		
$\langle\sigma_i\rangle$ $[ms^{-1}]$	1.76		
σ_e $[ms^{-1}]$	2.41		
χ^2_ν	2.07		

that signal. There is consequently strong evidence for the stability and planetary nature of the 30.6 and 123.8 d signal, but somewhat weaker evidence for the 48.1 d signal. The unfortunate phasing of the 2010-2011 measurements and the weaker signal do not allow strong limits against a possibly time-varying amplitude. While the period of that signal is moderately close to the 41 d possible stellar rotation and its true nature thus remains somewhat uncertain, the lack of any significant correlation between radial velocity and the stellar activity indicators suggest that it is planetary.

5. Radial velocities of GJ 3341

We obtained 135 RV measurements of GJ 3341, spanning 1456 d. Their dispersion is $\sigma_e = 3.51 ms^{-1}$, while the combined photon noise and instrumental errors average to $\langle\sigma_i\rangle = 1.89 ms^{-1}$. An F-test and a χ^2 comparison against a constant model yield probabilities $P(F)$ and $P(\chi^2) < 10^{-9}$ that the RV dispersion is explained by the RVs uncertainties. The periodogram (Fig. 7) shows a peak at 14.21 d with power of p=0.31. 1,000 iterations of bootstrap randomization produced no random data set with a power above 0.24, and the FAP for this peak is therefore well below 10^{-3}. The Horne & Baliunas (1986) recipe results in an FAP of 2.73×10^{-8}.

A Keplerian fit with *yorbit* converges on an orbit with period $P = 14.207 \pm 0.007\,d$, eccentricity $e = 0.31 \pm 0.11$, and semi-amplitude $K_1 = 3.036 \pm 0.408$. Given the stellar mass of $M = 0.47 M_\odot$, the corresponding minimum planetary mass is $6.6 \pm 0.1 M_\oplus$. Table 5 summarizes the solution parameters. This solution (Fig. 8) has a reduced χ^2 of $\chi^2 = 2.28 \pm 0.19$ and a $\sigma_e = 2.86 ms^{-1}$ dispersion of the residuals. An F-test and a χ^2 test for a constant model resulted in probabilities $P(F) = 1.18 \times 10^{-6}$ and $P(\chi^2) < 10^{-9}$ that this dispersion is explained by photon noise combined with instrumental errors. The periodogram of the residuals shows a p=0.18 peak at 41 d, above the p=0.16 level for a 1% FAP and grazing the 3σ confidence level. We were unable to reliably fit a Keplerian to these residuals, and stellar activity is therefore a more likely explanation for this additional RV variability.

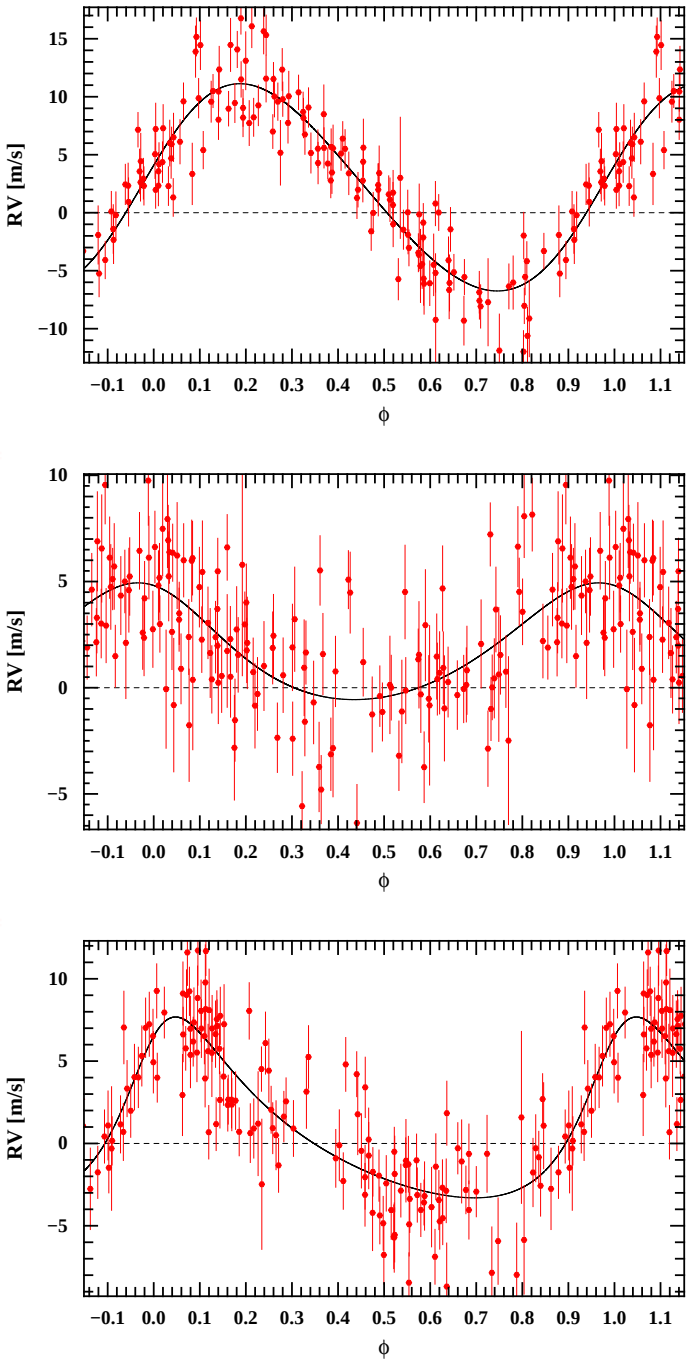

Fig. 5. Radial velocities phased for each signal. P=30.59 d top panel, P=48.07 d middle panel, and P=123.79 d bottom panel.

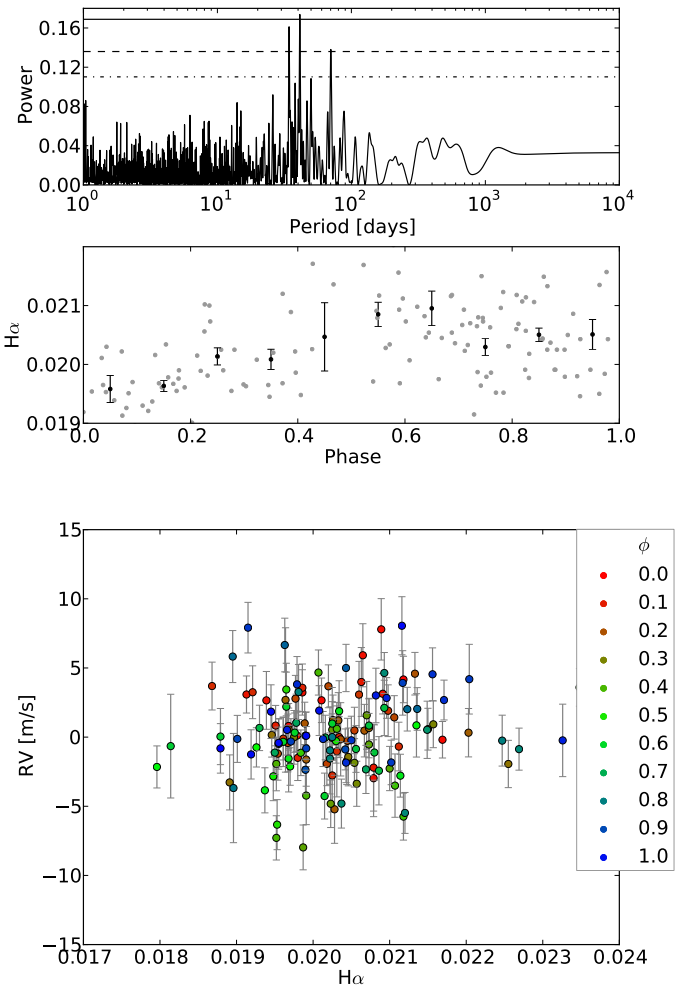

Fig. 6. *Top:* Periodogram of the Hα emission index of GJ 3293, with a peak above the 3σ confidence level at 41 d and two peaks the above 2σ confidence level at 34 and 70 d. *Middle:* the Hα index phased to P=41 d (gray dots); the black dots are binned by 0.1 in phase. *Bottom:* RVs corrected for the 30.6 and 123.8 d signals against the *Hα*-index; the colors represent the phase of the 48 d signal from Table 4 (as represented in the middle panel of Fig. 5).

5.1. Stellar activity

The periodogram of the *Hα* (Fig. 9) and *S* indices, contrast, bisector-span, and FWHM of the CCF show no evidence of stellar activity which could explain the RVs variations, and nor do plots of the RV as a function of these parameters. Subtracting a long-term trend visible in *Hα* index, however, increases the power in a pre-existing 46 d peak of its periodogram (Fig. 9) to 0.24, above the 3σ confidence level. Phasing the Hα index with this period produces relatively smooth and approximately sinusoidal variations, compatible with the signature of stellar rotation. This period is somewhat shorter than expected from the relatively weak Ca II emission of GJ 3341, which is intermediate in strength between those of Gl 618A (P=57 d) and Gl 581 (P=130 d) (Fig. 1), but probably within the dispersion of the period-activity relation. The period closely matches that found in the RV residuals, reinforcing activity as an explanation for them.

To evaluate the stability of the 14 d signal, we split the RVs into four seasons (BJD-2400000=54800-55000, 55400-55600, 55800-56050, 56150-56300; 25, 32, 43, 32 measurements per epoch) and computed periodograms for each. The 14 d is consistently present in every periodogram.

6. Radial velocities of GJ 3543

We obtained 80 RV measurements of GJ 3543 spanning 1919 d, with a dispersion $\sigma_e = 3.02\,ms^{-1}$ compared to an average photon noise combined with instrumental error of $\langle\sigma_i\rangle = 1.21 ms^{-1}$. An F-test and a χ^2 test for a constant model find a $P < 10^{-9}$ probability that these known measurement errors explain the dispersion. The periodogram (Fig. 10) of the GJ 3543 RVs exhibits

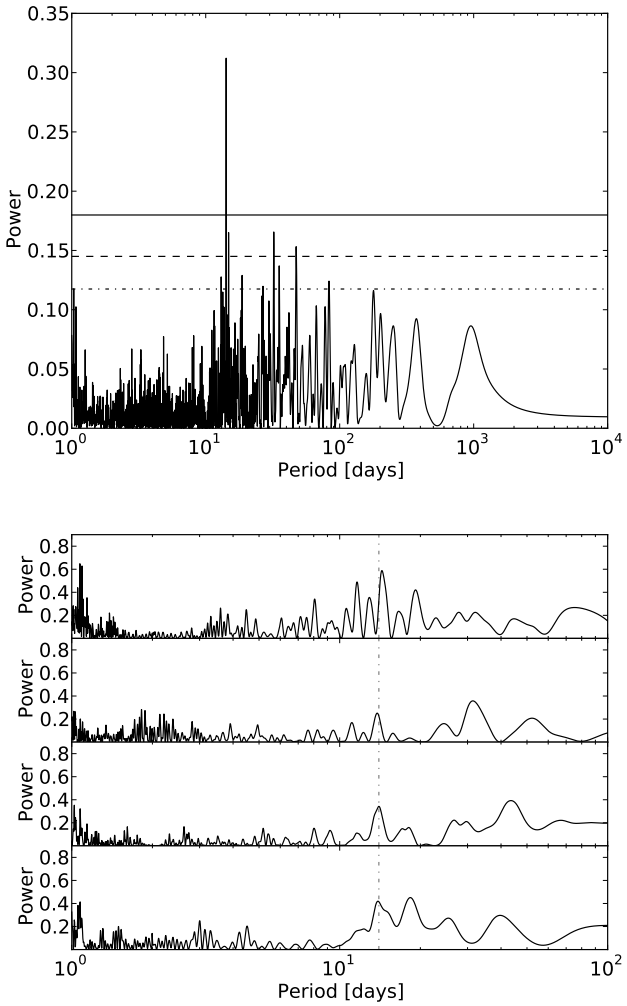

Fig. 7. *Top panel:* Periodogram of the GJ 3341 radial velocities, with a peak above the 3σ confidence limit at 14 d (continuous black line). *Bottom panel*: Periodograms for four subsets of epochs (BJD-2400000=54800-55000, 55400-55600, 55800-56050, 56150-56300); the 14 d (vertical dash-dotted line) peak is always present.

two strong peaks with powers of 0.37 and 0.34 at 1.1 and 9.2 d. Both peaks are well above the p=0.29 for power at 0.3% FAP confidence level.

Our first *yorbit* one-Keplerian fit to the RVs converged on an orbit with period $P = 1.11913 \pm 0.00006$, eccentricity $e = 0.13 \pm 0.16$, and semi-amplitude $K_1 = 2.70 \pm 0.38$ ($2.6 \pm 0.4 M_\oplus$). This solution decreases the dispersion to $\sigma_e = 2.32\, ms^{-1}$ and the reduced χ^2 of the residuals to $\chi^2 = 3.80 \pm 0.32$. The 9.2 d signal disappears in the periodogram of the residuals, demonstrating that the 1.1 and 9.2 d peaks are aliases of each other. If we introduce a prior that mildly favors a longer period, the fit instead converges on an orbit with period $P = 9.161 \pm 0.004$, eccentricity $e = 0.20 \pm 0.15$, and semi-amplitude $K_1 = 2.73 \pm 0.44$ ($5.1 \pm 0.9 M_\oplus$), and the 1.1 d signal disappears in the periodogram of the residuals. Their dispersion is $\sigma_e = 2.42\, ms^{-1}$, and the reduced χ^2 is $\chi^2 = 4.14 \pm 0.33$. In either case the strongest peak in the periodogram of the residuals occurs at 23 d and has a power p=0.25, which corresponds to a ~2.5% FAP. The daily sampling of the observations and the periodogram analysis both suggest that the 1.1 and 9.2 d signals are aliases of one other ($1/1.119 + 1/9.161 = 1/1.003$). The residuals of the two fits do not differ enough to ascertain which represents the true signal, and Fig. 11 therefore plots both solutions.

Table 5. One-Keplerian fit for GJ 3341

	GJ 3341b
P [d]	14.207 ± 0.007
T_0 [JD-2400000]	55622.7 ± 0.8
ω [deg]	42.32 ± 4.3
e	0.31 ± 0.11
K_1 $[ms^{-1}]$	3.04 ± 0.41
$m\, sin(i)$ $[M_\oplus]$	6.6 ± 0.1
a [AU]	0.089
γ $[kms^{-1}]$	47.803 ± 0.003
N_{meas}	135
Span [d]	1455.9
$\langle\sigma_i\rangle$ $[ms^{-1}]$	1.89
σ_e $[ms^{-1}]$	2.86
χ^2_ν	2.28

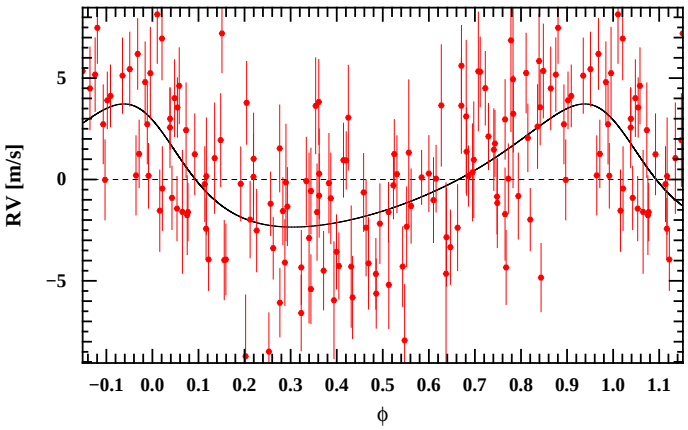

Fig. 8. GJ 3341 radial velocities phased for a 14.2 d period.

Table 6. Fit for one-Keplerian of GJ 3543

	GJ 3543(b)	GJ 3543(b)
P [d]	1.11913 ± 0.00006	9.161 ± 0.004
T_0 [JD-2400000]	55739.52 ± 0.18	55745.6 ± 1.0
ω [deg]	-100 ± 60	39.7 ± 43.3
e	0.13 ± 0.16	0.20 ± 0.15
K_1 $[ms^{-1}]$	2.70 ± 0.38	2.73 ± 0.44
$m\, sin(i)$ $[M_\oplus]$	2.6 ± 0.4	5.1 ± 0.9
a [AU]	0 .0162	0.0657
γ $[kms^{-1}]$	15.0927 ± 0.0004	15.0932 ± 0.0005
N_{meas}	80	80
Span [d]	1918.8	1918.8
$\langle\sigma_i\rangle$ $[ms^{-1}]$	1.21	1.21
σ_e $[ms^{-1}]$	2.32	2.42
χ^2_ν	3.80	4.14

6.1. Stellar activity

The power in the strongest peak in the periodogram of the S-index, (Fig. 12, second row), at 22 d, is p=0.193 and just below the p=0.198 needed for the 1σ confidence level. The strongest

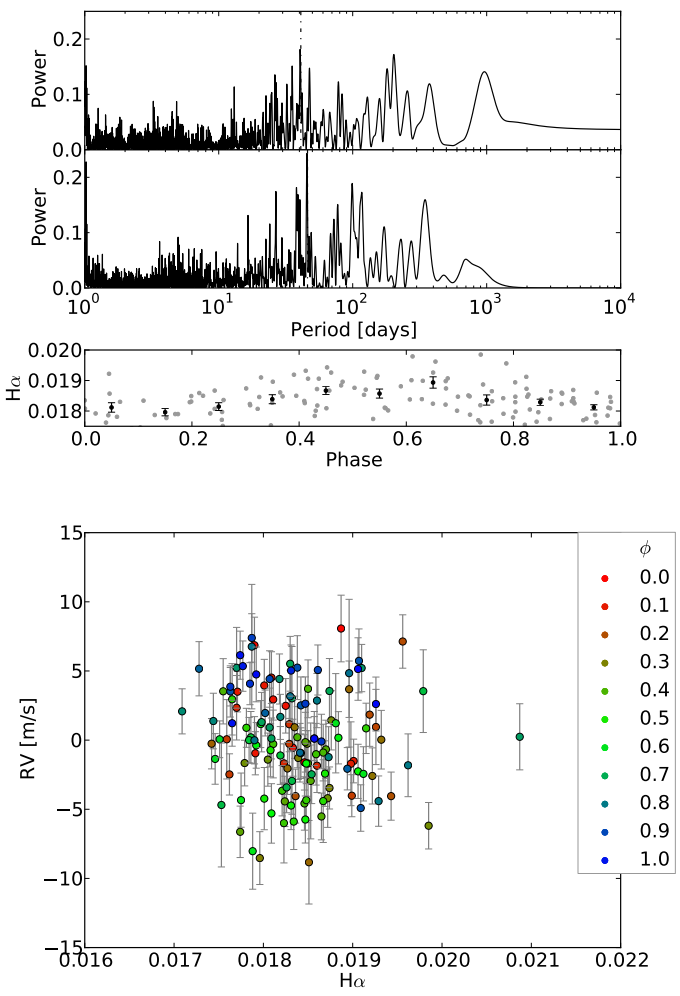

Fig. 9. *Top:* Periodogram of the Hα emission index for GJ 3341, with a peak above the 3σ confidence level (continuous line) at 46 d. *Middle:* The Hα emission index phased to 46 d, which may represent the rotation period. *Bottom:* RV against *Hα* index, with colors representing the phase for the 14 d signal as in Fig. 8, T_0 from Table 5.

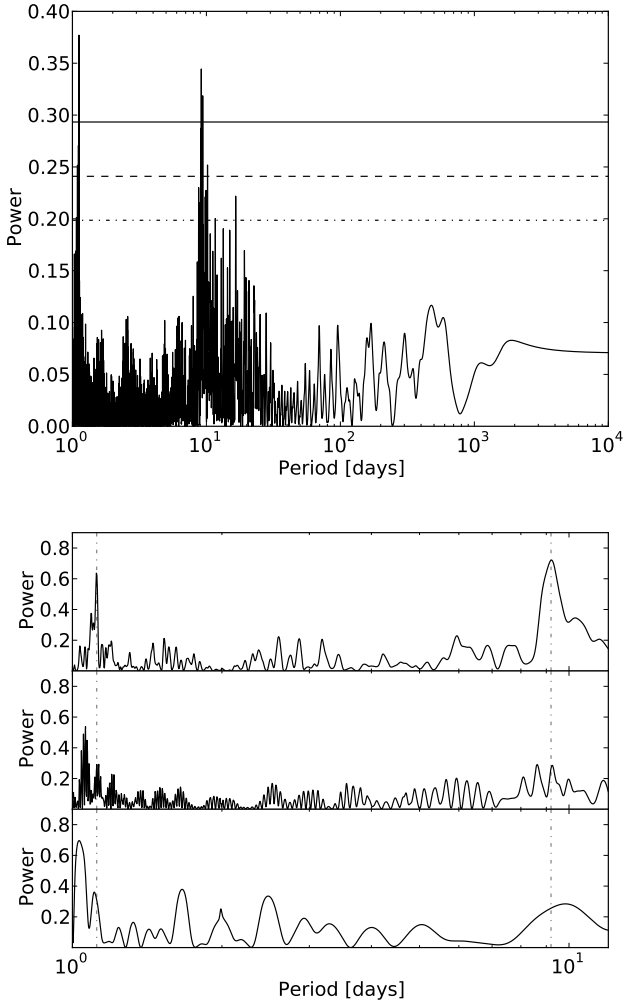

Fig. 10. *Top panel:* Periodogram of the radial velocities of GJ 3543. The horizontal lines represent the same false-alarm levels as in Fig. 2. The two peaks at 1.1 and 9.2 d have an FAP lower than 0.3% . *Bottom panel:* Periodograms for three independent subsets of observation epochs (BJD-2400000=55500-55750, first row; 55850-56050, second row; 56340-56380, third row). The 1.1 and 9.2 d peaks (marked by vertical dash-dotted lines) are both unstable over time.

peak in the periodogram of the Hα index (Fig. 12, third row), at 19 d, is above the 1σ confidence level but still has a 14% FAP. Either period would be consistent with the strength of the Ca II emission line (Fig. 1), which suggest a stellar rotation period shorter than 35 d. While both activity signals have low significance, the P=9.2 d radial velocity period is close the the first harmonic of either 19 or 22 d, and the tentative 23 d peak in the periodogram of the RV residuals (Fig. 12, first row) is also close to both. We evaluated the stability of the 1.1 or 9.2 d signal by computing periodograms for three disjoint seasons, BJD-2400000=55500-55750, 55850-56050, and 56340-56380, which contain 25, 30, and 14 measurements. The two aliased signals are only present in the first season and are absent from the second and third seasons (Fig. 10, bottom panel). The seasonal datasets have too few measurements for a similar exercise for the tentative 23 d peak in the periodogram of the residuals. Our best guess is that stellar activity is responsible for the RVs variation, although we see no correlation between the variations of the RV and of the *S* or *Hα* indices. More data are needed to ascertain the source of the RV dispersion.

The radial velocity signal at half the stellar rotation period found here for GJ 3543 has an analog in the recent reanalysis by Robertson et al. (2014) of the Forveille et al. (2011) GJ 581 data. This analogy provides an opportunity to summarize here the views of our team on the physical reality of the up to six planets that have been claimed to to orbit GJ 581, with heated controversies on the statistical significance of the weaker signals.

Our group announced the discoveries of 'b' in 2005, followed by 'c' and 'd' in 2007 and then 'e' in 2009 (Bonfils et al. 2005; Udry et al. 2007; Mayor et al. 2009), after considering both planetary and activity models in the interpretation of the observed periodic signals. The estimated rotational period of GJ 581 was much longer than the putative orbital periods of b, c and e, which consequently were immediately accepted as planets. The interpretation of the 'd' signal was less straightforward because it occurred at a plausible rotational period for GJ 581. We discarded that explanation at the time, on the grounds that the Doppler variations, if caused by a spot on the rotating star, would have come together with larger photometric variations than ob-

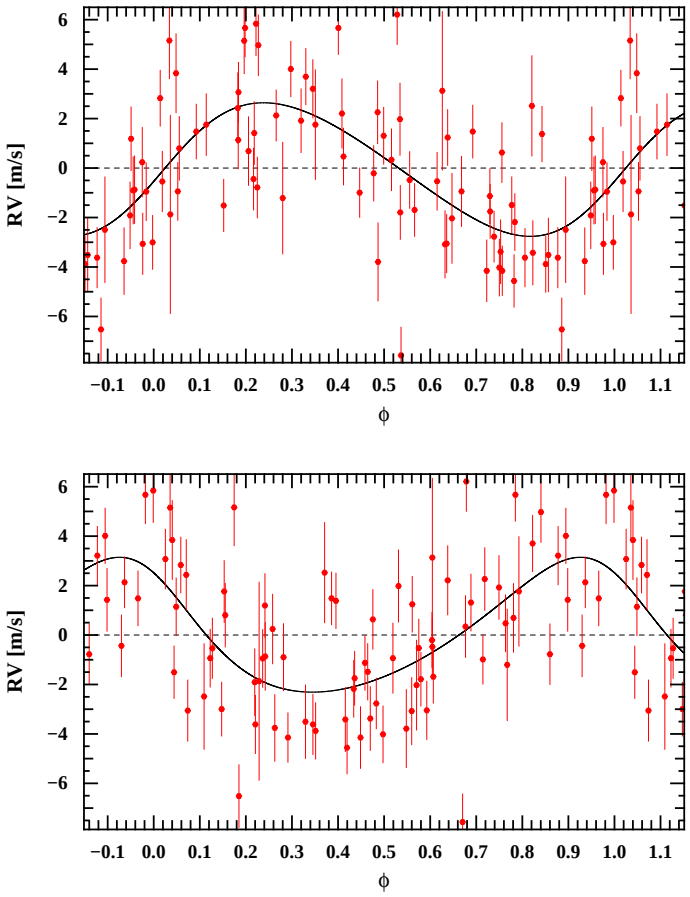

Fig. 11. Radials velocities for GJ 3543 RVs phased to the 1.1 d (top) and 9.2 d (bottom) period.

served (e.g., Bonfils et al. 2007). This made the planet the most likely interpretation, at that time.

Vogt et al. (2010) then combined the 2004 to 2008 HARPS data with new HIRES data, with most of the statistical weight on the HARPS side, to announce two additional planets in the system, f and g. We were monitoring GJ 581 very intensively, and we quickly reacted to the announcement of Vogt et al. (2010) by showing that our new HARPS data were incompatible with these additional two planets (Forveille et al. 2011). In that manuscript we relied on the measurement of Vogt et al. of a 90-day rotational period for GJ 581 to conclude that GJ 581d was a bona fide planet, since its period was comfortably away from any harmonic of the presumed rotational period.

Strong doubts, on different grounds, on the reality of GJ 581 f and g were also expressed by others (Tuomi 2011; Gregory 2011; Baluev 2013). Baluev et al. additionally questioned whether GJ 581 d exists, finding that accounting for the correlated noise in the radial velocity measurements of GJ 581 decreased the significance of 'd' to ∼1.5 σ. Robertson et al. more recently identified the astrophysical source of that correlated noise, showing that GJ 581 obeys a more complex RV-activity relation than previously thought. Instead of star spots, they invoked convection inhibition within active regions that locally changes the balance of ascending vs. descending material. Such active regions move as the star rotates and induce apparent Doppler shifts, but do not necessarily induce brightness variations. Robertson et al. additionally found the true rotation period of GJ 581 to be 130 days, quite different from that announced by

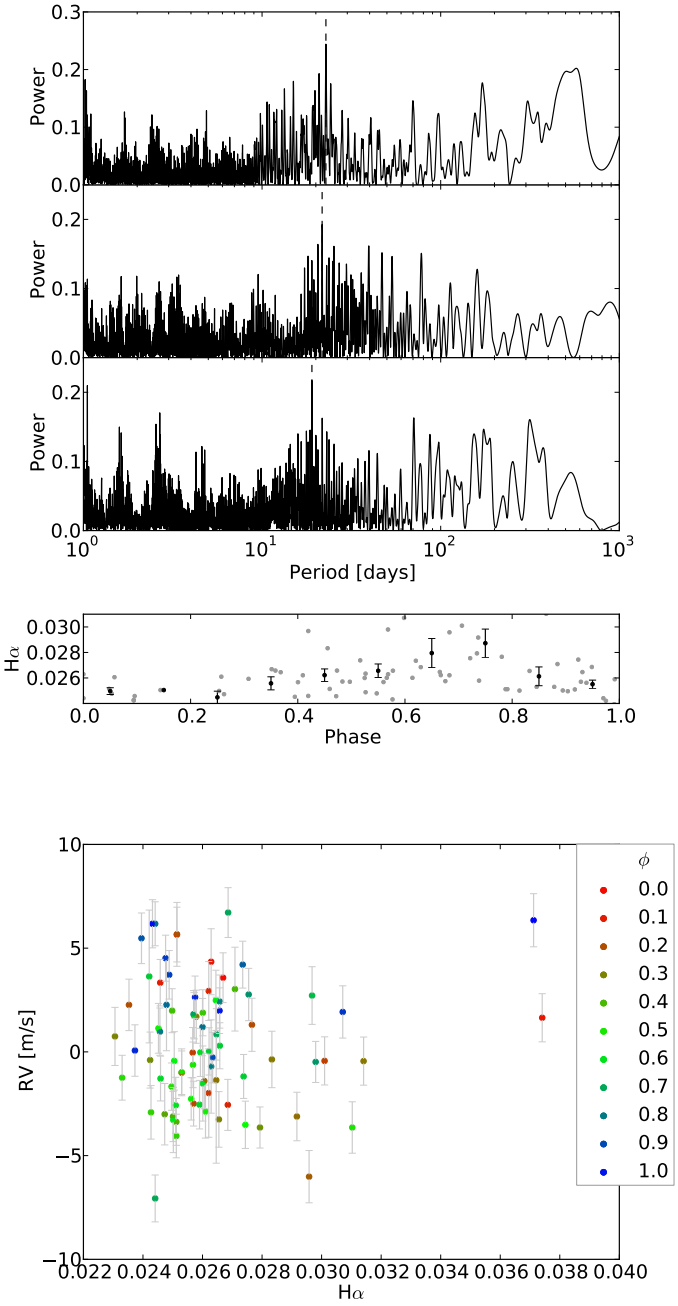

Fig. 12. *Top panel: First row*: Periodogram of the residuals of the GJ 3543 radial velocities after subtracting the 1.1 d Keplerian orbit. The power excess at P=23 *d* has a 2.5% FAP. *Second row*: Periodogram of the S-index of GJ 3543. The significance of the 22 d peak is just under 1σ. *Third row*: Periodogram of the Hα index of GJ 3543. The false-alarm probability of the 19 d peak is 14%. *Middle panel*: The Hα index phased to the 19 d period. *Bottom panel:* RVs against the *H*α-index, the colors represents phase for the 9.2 d period, as represented in Fig. 11 (bottom), T_0 from Table 6.

Vogt et al. and twice the period of 'd'. These findings together mean that the 65-day radial velocity signal is most probably due to two longitudinally opposed active regions, and show that extra caution is warranted when RV periodicities are found near a harmonic of the rotation period. This occurs here for GJ 3543, and might also be the case for the GJ 667C system (Delfosse et al.

2013a; Anglada-Escudé et al. 2013; Feroz & Hobson 2014), although its rotation period remains slightly uncertain.

7. Summary and conclusions

We analyzed observations of three early-M dwarfs with the HARPS spectrograph mounted on the 3.6m telescope at La Silla observatory (ESO). We identified a planetary system orbiting GJ 3293, composed of two Neptunes with periods near the 4:1 resonance (30.6 ± 0.02 and 123.98 ± 0.38 d), and more tentatively a super-Earth with an orbital period of 48.14 ± 0.12 d. Although the RV variations appear to be uncorrelated with any stellar activity indicator, the orbital period of the least massive planet candidate remains moderately close to the plausible stellar rotation period. This signal is present and stable for the 2008-2009 and 2012-2013 subsets of the data, while the 2010-2011 subset has inadequate sampling to probe a 48 d period. More data are needed to fully confirm this planet candidate. With a 0.194 AU semi-major axis it orbits in the habitable zone of GJ 3293, and with a minimum mass of $7.9 \pm 1.4 M_{\oplus}$ it could be rocky. The hierarchical structure of the system warrants a dynamical analysis.

GJ 3341 is orbited by a super-Earth ($msin(i) \sim 6.6 M_{\oplus}$) that is placed by its period of 14.207 ± 0.007 d in the inner habitable zone of its host star.

The periodogram of the radial velocities of GJ 3543 is dominated by two mutually aliased peaks at 1.1 and 9.2 d, but they are only present in a subset of the epochs. The periodograms of the stellar activity indices suggest a stellar rotation period of about 20 d, or approximately twice the 9.2 d period, which further reinforces the assumption that stellar activity is responsible for the unstable radial velocity signal - see Boisse et al. (2011).

GJ 3293 and GJ 3341 have approximately solar metallicity, consistently with the observation that the frequency of super-Earth and Neptune planets seems to be uncorrelated with stellar metallicity (Mayor et al. 2011; Sousa et al. 2011; Neves et al. 2013). As the sample of well-characterized planetary systems increases and stellar properties are more accurately known, we will refine the statistical relations between the presence of planets and the stellar properties of their hosts, which will help constrain planet formation and evolution models.

Acknowledgements. N. A. acknowledges support from CONICYT Becas-Chile 72120460. This publication makes use of data products from the Two Micron All Sky Survey, which is a joint project of the University of Massachusetts and the Infrared Processing and Analysis Center/California Institute of Technology, funded by the National Aeronautics and Space Administration and the National Science Foundation. X. B., X. D., and T. F. acknowledge the support of the French Agence Nationale de la Recherche (ANR), under the program ANR-12-BS05-0012 Exo-atmos. X.B. acknowledges funding from the European Research Council under the ERC Grant Agreement n. 337591-ExTrA. NCS acknowledges the support from the European Research Council/European Community under the FP7 through Starting Grant agreement number 239953. NCS further acknowledges the support from Fundação para a Ciência e a Tecnologia (FCT, Portugal) through FEDER funds in program COMPETE, as well as through national funds, in the form of grants reference RECI/FIS-AST/0176/2012 (FCOMP-01-0124-FEDER-027493), and RECI/FIS-AST/0163/2012 (FCOMP-01-0124-FEDER-027492), and through the Investigador FCT contract reference IF/00169/2012 and POPH/FSE (EC) by FEDER funding through the program "Programa Operacional de Factores de Competitividade - COMPETE.

References

Anglada-Escudé, G., Tuomi, M., Gerlach, E., et al. 2013, A&A, 556, A126
Baluev, R. V. 2013, MNRAS, 429, 2052
Baranne, A., Queloz, D., Mayor, M., et al. 1996, A&AS, 119, 373
Boisse, I., Bouchy, F., Hébrard, G., et al. 2011, A&A, 528, A4
Bonfils, X., Delfosse, X., Udry, S., et al. 2013a, A&A, 549, A109
Bonfils, X., Forveille, T., Delfosse, X., et al. 2005, A&A, 443, L15
Bonfils, X., Lo Curto, G., Correia, A. C. M., et al. 2013b, A&A, 556, A110
Bonfils, X., Mayor, M., Delfosse, X., et al. 2007, A&A, 474, 293
Bouchy, F., Pepe, F., & Queloz, D. 2001, A&A, 374, 733
Boyajian, T. S., von Braun, K., van Belle, G., et al. 2012, ApJ, 757, 112
Cutri, R. M., Skrutskie, M. F., van Dyk, S., et al. 2003, VizieR Online Data Catalog, 2246, 0
Delfosse, X., Bonfils, X., Forveille, T., et al. 2013a, A&A, 553, A8
Delfosse, X., Donati, J.-F., Kouach, D., et al. 2013b, in SF2A-2013: Proceedings of the Annual meeting of the French Society of Astronomy and Astrophysics, ed. L. Cambresy, F. Martins, E. Nuss, & A. Palacios, 497–508
Delfosse, X., Forveille, T., Ségransan, D., et al. 2000, A&A, 364, 217
Dressing, C. D. & Charbonneau, D. 2013, ApJ, 767, 95
Dumusque, X., Santos, N. C., Udry, S., Lovis, C., & Bonfils, X. 2011, A&A, 527, A82
Feroz, F. & Hobson, M. P. 2014, MNRAS, 437, 3540
Forveille, T., Bonfils, X., Delfosse, X., et al. 2011, ArXiv e-print:1109.2505
Fressin, F., Torres, G., Charbonneau, D., et al. 2013, ApJ, 766, 81
Gliese, W. & Jahreiß, H. 1991, Preliminary Version of the Third Catalogue of Nearby Stars, Tech. rep.
Gomes da Silva, J., Santos, N. C., Bonfils, X., et al. 2011, A&A, 534, A30
Gregory, P. C. 2011, MNRAS, 415, 2523
Horne, J. H. & Baliunas, S. L. 1986, ApJ, 302, 757
Howarth, I. D., Siebert, K. W., Hussain, G. A. J., & Prinja, R. K. 1997, MNRAS, 284, 265
Johnson, D. R. H. & Soderblom, D. R. 1987, AJ, 93, 864
Kiraga, M. & Stepien, K. 2007, Acta Astron., 57, 149
Kürster, M., Endl, M., Rouesnel, F., et al. 2003, A&A, 403, 1077
Leggett, S. K. 1992, ApJS, 82, 351
Leggett, S. K., Allard, F., Geballe, T. R., Hauschildt, P. H., & Schweitzer, A. 2001, ApJ, 548, 908
Lovis, C. & Pepe, F. 2007, A&A, 468, 1115
Lucy, L. B. 2013, A&A, 551, A47
Mayor, M., Bonfils, X., Forveille, T., et al. 2009, A&A, 507, 487
Mayor, M., Marmier, M., Lovis, C., et al. 2011, ArXiv e-print:1109.2497
Mayor, M., Pepe, F., Queloz, D., et al. 2003, The Messenger, 114, 20
Neves, V., Bonfils, X., Santos, N. C., et al. 2013, A&A, 551, A36
Neves, V., Bonfils, X., Santos, N. C., et al. 2014, A&A, 568, A121
Noyes, R. W., Hartmann, L. W., Baliunas, S. L., Duncan, D. K., & Vaughan, A. H. 1984, ApJ, 279, 763
Nutzman, P. & Charbonneau, D. 2008, PASP, 120, 317
Pepe, F., Mayor, M., Galland, F., et al. 2002, A&A, 388, 632
Queloz, D., Henry, G. W., Sivan, J. P., et al. 2001, A&A, 379, 279
Quintana, E. V., Barclay, T., Raymond, S. N., et al. 2014, Science, 344, 277
Quirrenbach, A., Amado, P. J., Seifert, W., et al. 2012, in Society of Photo-Optical Instrumentation Engineers (SPIE) Conference Series, Vol. 8446, Society of Photo-Optical Instrumentation Engineers (SPIE) Conference Series
Riedel, A. R., Subasavage, J. P., Finch, C. T., et al. 2010, AJ, 140, 897
Robertson, P., Mahadevan, S., Endl, M., & Roy, A. 2014, Science, 345, 440
Salim, S. & Gould, A. 2003, ApJ, 582, 1011
Selsis, F., Kasting, J. F., Levrard, B., et al. 2007, A&A, 476, 1373
Sousa, S. G., Santos, N. C., Israelian, G., Mayor, M., & Udry, S. 2011, A&A, 533, A141
Tuomi, M. 2011, A&A, 528, L5
Udry, S., Bonfils, X., Delfosse, X., et al. 2007, A&A, 469, L43
van Dokkum, P. G. & Conroy, C. 2010, Nature, 468, 940
Vidotto, A. A., Jardine, M., Morin, J., et al. 2013, A&A, 557, A67
Vogt, S. S., Butler, R. P., Rivera, E. J., et al. 2010, ApJ, 723, 954
Wheatley, P. J., Pollacco, D. L., Queloz, D., et al. 2013, in European Physical Journal Web of Conferences, Vol. 47, European Physical Journal Web of Conferences, 13002
Zacharias, N., Finch, C. T., Girard, T. M., et al. 2012, VizieR Online Data Catalog, 1322, 0
Zechmeister, M. & Kürster, M. 2009, A&A, 496, 577
Zucker, S. & Mazeh, T. 2006, MNRAS, 371, 1513

Appendix A: RVs

The RVs are in the barycentric frame and are corrected for secular acceleration. The RVs were extracted through χ^2 matching to a template with a high signal-to-noise ratio. The errors combine the estimated photon noise with the an estimate of the residual instrumental error ($0.60 ms^{-1}$). We also tabulate the FWHM and bisector span (BIS) of the cross-correlation function, as well as the activity indices of $H\alpha$ and Ca II from *Mount Wilson* S.

Table A.1. GJ 3293 RVs, their uncertainty and activity indicators.

BJD - 2400000	RV $[kms^{-1}]$	σ_{RV} $[kms^{-1}]$	FWHM $[kms^{-1}]$	Contrast	BIS $[kms^{-1}]$	S-index	$H\alpha$
54805.68424	13.28536	0.00375	3.60254	25.79888	-0.01715	1.42156	0.01814
54825.64027	13.30846	0.00132	3.60782	25.14589	-0.00589	1.46394	0.02169
54826.63445	13.31021	0.00146	3.60512	25.07722	-0.00330	1.33697	0.02091
54827.64845	13.30529	0.00148	3.60866	24.69961	-0.01048	1.16751	0.02034
54828.66060	13.30270	0.00176	3.59488	24.71040	-0.00372	1.42195	0.02112
54829.76990	13.30312	0.00187	3.59572	25.10511	-0.01030	1.17184	0.02098
54830.66322	13.29993	0.00168	3.60334	24.87551	-0.01416	1.20943	0.02054
54831.65871	13.29726	0.00163	3.61586	24.87951	-0.01441	1.19192	0.02045
54832.67287	13.29552	0.00265	3.60512	25.07722	-0.01191	1.28864	0.02036
54833.66016	13.29525	0.00201	3.59258	24.73141	-0.00866	1.16719	0.02033
54834.71626	13.29312	0.00151	3.60281	25.05025	-0.00988	1.28836	0.02150
54848.62098	13.30394	0.00142	3.60453	24.78696	-0.01505	1.04256	0.01926
54850.61453	13.30143	0.00163	3.60655	24.93891	-0.01737	1.00371	0.01937
54852.63392	13.30466	0.00142	3.59689	25.03757	-0.00639	0.99302	0.01976
54854.62660	13.30131	0.00169	3.58326	24.82394	-0.01598	1.16644	0.02056
54879.59166	13.30268	0.00168	3.59159	25.00795	-0.00765	1.27681	0.01977
54881.62441	13.29896	0.00193	3.62406	24.69537	-0.01938	1.28265	0.01991
54883.52494	13.29997	0.00160	3.60304	24.86785	-0.01956	1.11932	0.01946
54885.56408	13.29871	0.00169	3.61087	24.90341	-0.01129	1.31220	0.02157
55045.92231	13.28938	0.00261	3.59152	24.95034	-0.00510	0.81714	0.02025
55047.91349	13.28374	0.00247	3.59427	24.86074	-0.00797	1.37098	0.02086
55049.92289	13.28389	0.00158	3.60506	24.76291	-0.01402	1.17482	0.01950
55052.90367	13.28542	0.00152	3.59590	24.69413	-0.00863	1.18646	0.02269
55121.83805	13.29732	0.00190	3.61108	25.01686	-0.02151	1.21001	0.02067
55126.73175	13.29736	0.00163	3.60254	25.79888	-0.01083	1.42142	0.02057
55129.71232	13.29868	0.00148	3.62406	24.69537	-0.00903	1.27998	0.02025
55132.80321	13.29327	0.00165	3.60603	24.90897	-0.00752	1.21409	0.01984
55135.70052	13.28911	0.00159	3.59773	24.87190	-0.00699	1.18975	0.02030
55137.70695	13.28387	0.00136	3.60094	24.84526	-0.00258	1.18268	0.01970
55139.73873	13.28154	0.00241	3.58700	25.11331	-0.01970	1.11593	0.01968
55141.71517	13.28093	0.00179	3.60334	24.87551	-0.01763	1.04440	0.01961
55143.68335	13.28173	0.00193	3.60264	24.91751	-0.01376	1.32279	0.02073
55168.59826	13.28915	0.00157	3.59427	24.86074	-0.01506	1.23032	0.02106
55169.62393	13.29108	0.00154	3.59996	25.14133	-0.00173	1.29228	0.02133
55230.60800	13.29104	0.00190	3.61222	25.09914	-0.00660	1.31543	0.01965
55403.92062	13.29672	0.00278	3.58700	25.11331	-0.00791	1.59816	0.02079
55411.88037	13.29203	0.00522	3.59664	24.89766	0.010910	1.23556	0.01964
55428.88535	13.30621	0.00220	3.59963	24.74944	-0.01358	1.44940	0.02034
55437.86529	13.30170	0.00148	3.60730	25.03872	-0.01640	1.28391	0.02120
55444.82380	13.29678	0.00165	3.61464	25.10732	-0.01627	1.19867	0.01971
55450.88896	13.29711	0.00168	3.58700	25.11331	-0.00821	1.28313	0.02118
55453.89333	13.29977	0.00172	3.59617	24.94721	-0.00742	1.14084	0.01986
55454.82171	13.30149	0.00173	3.60655	24.93891	-0.00572	1.17555	0.01868
55455.84630	13.30279	0.00240	3.60733	24.96234	0.003990	1.44517	0.02060
55456.83313	13.29964	0.00158	3.60334	24.87551	-0.00749	1.16269	0.02018
55457.86351	13.30165	0.00171	3.61401	24.96484	-0.01388	1.14233	0.02044
55493.82107	13.30899	0.00183	3.60161	24.82933	-0.00736	1.01267	0.01915
55494.76977	13.30460	0.00201	3.60531	24.80336	-0.01000	0.90454	0.01979
55495.88051	13.30289	0.00147	3.60443	25.03226	-0.01423	1.15078	0.02096
55497.75076	13.29815	0.00172	3.59634	24.89247	-0.01173	1.45566	0.01991
55500.80695	13.29347	0.00177	3.59427	24.86074	-0.00835	1.08966	0.01979
55501.75111	13.29021	0.00164	3.60512	25.07722	-0.00234	1.20944	0.01980
55505.64461	13.28387	0.00192	3.61087	24.90341	-0.00057	1.05933	0.01954
55514.68731	13.28270	0.00160	3.62495	25.00670	-0.00980	1.29677	0.02100
55521.72610	13.29585	0.00176	3.59152	24.95034	-0.01461	0.99529	0.01948
55523.71392	13.29791	0.00152	3.59773	24.87190	-0.01286	1.07141	0.01796
55547.63328	13.29735	0.00161	3.60982	25.12058	-0.00594	1.25905	0.02011
55548.59915	13.29992	0.00209	3.60418	24.92648	-0.00740	1.10584	0.01939
55549.69948	13.30091	0.00146	3.59773	24.87190	-0.00374	1.26415	0.01951
55576.59973	13.29605	0.00200	3.60971	24.95140	-0.01486	1.36858	0.02080
55579.69290	13.30053	0.00174	3.60157	24.88640	-0.00178	1.26789	0.02069
55586.57901	13.31199	0.00171	3.60418	24.92648	-0.00736	1.41550	0.02043
55612.54944	13.30369	0.00163	3.60987	24.95725	-0.00820	0.95858	0.02007
55615.50571	13.30480	0.00136	3.59152	24.95034	-0.01308	1.34022	0.02348
55621.49969	13.29348	0.00155	3.61108	25.00144	-0.00568	1.04788	0.02114
55817.89452	13.29597	0.00200	3.60593	24.70919	-0.00960	1.31675	0.02093

Table A.1. continued.

BJD - 2400000	RV $[kms^{-1}]$	σ_{RV} $[kms^{-1}]$	FWHM $[kms^{-1}]$	Contrast	BIS $[kms^{-1}]$	S-index	$H\alpha$
55822.87888	13.30537	0.00148	3.59427	24.86074	-0.01346	1.08820	0.02093
55825.89910	13.30804	0.00158	3.60626	24.86616	-0.01014	1.28318	0.02123
55828.89202	13.30764	0.00148	3.61087	24.90341	-0.01200	1.21319	0.02042
55829.85421	13.30775	0.00158	3.61053	24.63378	-0.01634	1.03953	0.01991
55830.87234	13.30798	0.00174	3.61108	25.01686	-0.00494	1.05729	0.02050
55831.83366	13.30569	0.00145	3.59617	24.94721	-0.01498	1.16617	0.02043
55834.83622	13.30246	0.00178	3.60731	24.76752	-0.01487	0.90912	0.01919
55835.76068	13.30133	0.00179	3.60731	24.76752	-0.00685	1.04509	0.01879
55837.83127	13.30134	0.00134	3.61401	24.96484	-0.00813	0.99007	0.01913
55839.82111	13.29755	0.00191	3.61053	24.63378	-0.00665	1.24796	0.01921
55840.87205	13.29215	0.00154	3.60593	24.70919	-0.01234	1.15323	0.01961
55841.75022	13.29021	0.00209	3.60443	25.03226	-0.00016	1.12326	0.01967
55843.85888	13.28824	0.00153	3.63220	24.65556	-0.00897	1.15736	0.01989
55870.76889	13.28400	0.00177	3.60512	25.07722	-0.00916	1.18192	0.02037
55887.68502	13.29405	0.00264	3.60475	24.90774	-0.01196	1.31407	0.02025
55890.67297	13.30346	0.00155	3.61108	25.00144	-0.00800	1.32079	0.02020
55893.65958	13.30051	0.00181	3.60987	24.95725	-0.00797	1.33008	0.02026
55924.64545	13.30390	0.00173	3.59588	24.67017	-0.00658	1.23348	0.01990
55925.65007	13.30571	0.00170	3.59588	24.67017	-0.01338	1.05004	0.01901
55926.63066	13.30337	0.00161	3.60593	24.70919	-0.00782	1.34434	0.02102
55927.63859	13.30422	0.00199	3.59468	24.91635	-0.02377	1.13228	0.02013
55928.68246	13.30283	0.00183	3.60414	24.99914	-0.01468	1.02394	0.01955
55929.61470	13.30281	0.00182	3.59996	25.14133	-0.00695	1.06086	0.01966
55930.63306	13.30300	0.00180	3.60094	24.84526	-0.01513	1.32293	0.02008
55931.61582	13.30170	0.00194	3.60673	24.81264	-0.01145	0.95326	0.01945
55932.61626	13.29942	0.00163	3.60836	25.01811	-0.01263	1.26315	0.01968
55933.63090	13.30062	0.00164	3.60987	24.95725	-0.01078	1.28021	0.01986
55940.55035	13.28895	0.00246	3.60512	25.07722	-0.01183	1.54123	0.02028
55941.64214	13.29572	0.00152	3.60512	25.07722	-0.01156	1.34513	0.01968
55942.69832	13.29324	0.00199	3.59387	24.89050	-0.00825	0.78451	0.01891
55943.63946	13.29661	0.00209	3.59159	25.00795	-0.01181	1.39953	0.02046
55944.63016	13.29985	0.00194	3.60512	25.07722	-0.00650	1.27652	0.01975
55945.64138	13.29997	0.00175	3.60836	25.01811	-0.00485	1.12134	0.02054
55946.63701	13.29891	0.00172	3.61087	24.90341	-0.00512	1.19637	0.02023
55947.62134	13.29747	0.00162	3.60847	24.79972	-0.01226	1.11409	0.01987
55949.61627	13.30076	0.00160	3.60593	24.70919	-0.00916	1.27358	0.01952
55950.62808	13.30303	0.00170	3.59427	24.86074	0.002250	1.40957	0.02118
55997.53126	13.27822	0.00210	3.59661	24.78567	-0.01016	1.19986	0.01991
56001.48895	13.27508	0.00181	3.59152	24.95034	-0.01171	1.11461	0.01953
56008.50764	13.28963	0.00166	3.60475	24.90774	-0.01240	0.91820	0.02015
56010.51342	13.29753	0.00169	3.60687	24.94252	-0.01324	1.23211	0.01990
56022.50593	13.29470	0.00233	3.60414	24.99914	-0.01226	1.26817	0.02117
56025.48481	13.28588	0.00262	3.61057	24.94123	-0.00658	1.71769	0.02326
56030.48582	13.27992	0.00314	3.62180	24.78081	-0.00097	1.08995	0.02079
56032.47450	13.28219	0.00329	3.61087	24.90341	-0.00691	0.94920	0.02031
56158.86499	13.29079	0.00207	3.61087	24.90341	-0.00884	1.01209	0.02149
56160.88634	13.29507	0.00184	3.60945	24.54870	-0.01014	1.32960	0.02247
56171.84600	13.30300	0.00173	3.61245	24.91672	-0.01102	1.04735	0.01955
56208.85566	13.29100	0.00315	3.60161	24.82933	-0.02114	1.55485	0.02022
56209.86400	13.28648	0.00395	3.60161	24.82933	0.005810	1.43810	0.01896
56210.84941	13.29442	0.00188	3.61586	24.87951	-0.00965	1.14180	0.01895
56221.86931	13.30292	0.00222	3.60731	24.76752	-0.02148	1.17186	0.02089
56229.75711	13.30168	0.00175	3.60945	24.54870	-0.00017	1.20497	0.02203
56230.70914	13.30124	0.00215	3.60945	24.54870	-0.01921	1.27728	0.02073
56231.78090	13.29747	0.00171	3.60414	24.99914	-0.01103	1.22611	0.02255
56235.66439	13.29494	0.00245	3.60094	24.84526	-0.01364	1.24985	0.02070
56236.65314	13.29105	0.00225	3.60161	24.82933	-0.00832	1.19125	0.02073
56237.64360	13.28785	0.00194	3.60687	24.94252	-0.00697	0.99914	0.01952
56238.61253	13.28867	0.00191	3.61290	24.88298	-0.00562	1.03800	0.02031
56239.66651	13.28278	0.00229	3.59152	24.95034	-0.01184	1.39054	0.02107
56245.61339	13.28206	0.00229	3.60094	24.84526	-0.01789	1.08137	0.02135
56248.64851	13.28634	0.00250	3.59152	24.95034	-0.01662	1.04436	0.01965
56249.67253	13.28603	0.00203	3.61977	24.86813	-0.00928	1.04205	0.01879
56251.69011	13.29099	0.00164	3.61977	24.86813	-0.01375	0.97448	0.01930
56252.65403	13.29243	0.00161	3.59427	24.86074	-0.01224	0.90649	0.02016
56253.65586	13.29557	0.00207	3.61057	24.94123	-0.01020	1.04962	0.01978

Table A.1. continued.

BJD - 2400000	RV $[kms^{-1}]$	σ_{RV} $[kms^{-1}]$	FWHM $[kms^{-1}]$	Contrast	BIS $[kms^{-1}]$	S-index	$H\alpha$
56256.68998	13.30221	0.00199	3.61028	25.10494	-0.01632	0.91982	0.01981
56257.72995	13.29963	0.00168	3.59427	24.86074	-0.00962	1.14657	0.02025
56259.64344	13.30642	0.00194	3.59427	24.86074	-0.01992	1.25647	0.01963
56263.63688	13.30049	0.00252	3.61977	24.86813	-0.01724	1.26143	0.02204
56264.78151	13.29736	0.00144	3.61057	24.94123	-0.01889	1.41208	0.02171
56283.56533	13.29611	0.00203	3.60761	24.95206	-0.02231	1.07310	0.02025
56304.65270	13.29140	0.00186	3.61977	24.86813	-0.00839	1.22813	0.02022
56307.60791	13.29589	0.00154	3.60660	24.80012	-0.01032	1.22408	0.02136
56312.60633	13.30676	0.00191	3.60660	24.80012	-0.01124	1.24584	0.02156
56314.60875	13.30923	0.00197	3.60660	24.80012	-0.01178	1.19865	0.02082
56316.64222	13.31724	0.00210	3.60687	24.94252	-0.01251	0.84569	0.02116
56318.64452	13.31640	0.00228	3.59152	24.95034	0.001300	1.25696	0.02065
56319.65567	13.31447	0.00249	3.59152	24.95034	-0.01262	1.13835	0.02063

Table A.2. GJ 3341 RVs, its uncertainty and activity indicators.

BJD - 2400000	RV $[kms^{-1}]$	σ_{RV} $[kms^{-1}]$	FWHM $[kms^{-1}]$	Contrast	BIS $[kms^{-1}]$	S-index	$H\alpha$
54807.69849	47.79778	0.00448	3.59435	25.43663	-0.00157	0.26432	0.01753
54825.66746	47.80633	0.00139	3.59007	24.79779	-0.01287	0.98919	0.01763
54826.64838	47.80369	0.00166	3.59320	24.70898	-0.01375	0.94571	0.01765
54827.66095	47.80152	0.00156	3.58260	24.76051	-0.01041	0.98700	0.01791
54828.67307	47.80220	0.00184	3.60239	24.53064	-0.00977	0.95732	0.01829
54829.78186	47.80221	0.00182	3.59904	24.80998	-0.00928	1.06308	0.01742
54830.65130	47.79394	0.00191	3.60239	24.53064	-0.01033	0.80047	0.01796
54831.64673	47.79584	0.00186	3.60781	24.79868	-0.00639	0.86513	0.01774
54832.65658	47.79647	0.00288	3.61297	24.63142	-0.01826	0.95837	0.01823
54833.64792	47.80005	0.00237	3.58617	24.68657	0.004100	0.98841	0.01869
54834.77493	47.79813	0.00196	3.58447	24.62698	-0.00381	0.89096	0.01775
54849.56753	47.80253	0.00133	3.60043	24.95740	-0.01658	0.76761	0.01751
54851.62802	47.80455	0.00163	3.59861	24.84315	-0.00214	0.86549	0.01709
54881.63742	47.80599	0.00185	3.60168	24.77744	-0.01260	0.88508	0.01763
54882.59568	47.80655	0.00152	3.57915	24.67109	-0.00921	0.87898	0.01785
54885.54247	47.79999	0.00149	3.59581	24.69552	-0.01145	0.72763	0.01762
54932.48536	47.80336	0.00141	3.59952	24.69259	-0.00620	0.98036	0.01781
54934.48545	47.80111	0.00183	3.57877	24.88057	-0.00601	0.93246	0.01746
54937.48457	47.80246	0.00171	3.59007	24.79779	-0.01399	0.71549	0.01790
54940.49248	47.80722	0.00198	3.59435	25.43663	-0.01607	0.75937	0.01792
54941.48780	47.80597	0.00146	3.59595	24.58150	-0.01188	0.78320	0.01771
54949.46243	47.80247	0.00164	3.60630	24.90630	-0.00476	0.89015	0.01784
54950.46139	47.80259	0.00148	3.60283	24.58144	-0.01222	0.83795	0.01809
54954.46978	47.80861	0.00174	3.58580	24.60535	-0.01058	0.52661	0.01774
54955.46854	47.80541	0.00149	3.58382	24.68647	0.002070	0.93699	0.01811
55220.56224	47.80338	0.00285	3.61297	24.63142	-0.01453	0.81790	0.01807
55225.54498	47.80642	0.00189	3.57878	24.65019	-0.01519	0.78821	0.01801
55229.69119	47.79952	0.00419	3.59055	24.71588	-0.01973	1.01882	0.01853
55423.91008	47.81054	0.00241	3.60986	24.65434	-0.00866	0.73691	0.01887
55425.90482	47.80960	0.00193	3.59595	24.58150	-0.01869	0.97592	0.01956
55427.92239	47.80106	0.00192	3.60196	24.58954	-0.01762	1.00509	0.01805
55428.90390	47.80268	0.00221	3.60507	24.73606	-0.02268	0.72720	0.01838
55434.88752	47.80564	0.00188	3.60725	24.58705	-0.00987	0.89913	0.01830
55437.84917	47.80258	0.00159	3.58580	24.60535	-0.01455	0.79242	0.01857
55444.85801	47.79774	0.00174	3.58447	24.62698	-0.00217	0.79058	0.01831
55480.81601	47.80086	0.00200	3.59904	24.80998	-0.00349	0.35148	0.01846
55483.80314	47.79988	0.00203	3.59435	25.43663	-0.00897	0.86845	0.01922
55486.76213	47.79658	0.00202	3.61114	24.58479	-0.02042	0.86073	0.01834
55492.87155	47.80689	0.00204	3.60507	24.73606	-0.01635	0.23161	0.01807
55495.89290	47.80079	0.00141	3.57375	25.51735	-0.00911	0.45954	0.01823
55497.80927	47.80042	0.00188	3.59822	24.88792	-0.00811	0.62883	0.01827
55499.87347	47.80078	0.00237	3.60630	24.90630	-0.01653	0.57420	0.01850
55501.81020	47.80021	0.00196	3.58758	24.75806	-0.01099	0.39399	0.01906
55505.70282	47.79806	0.00182	3.61193	24.76277	-0.01927	0.33693	0.01929
55506.78000	47.79756	0.00168	3.59007	24.79779	-0.01096	0.64716	0.01909
55509.76158	47.80096	0.00158	3.58447	24.62698	-0.00909	0.77938	0.01901
55510.73594	47.79845	0.00152	3.58758	24.75806	-0.01222	0.64301	0.01899
55512.72825	47.79901	0.00152	3.61448	24.53406	-0.00851	0.69542	0.01874
55513.74985	47.80232	0.00216	3.60000	24.56756	-0.00294	0.71029	0.01847
55514.75421	47.79813	0.00163	3.61448	24.53406	-0.01779	0.72800	0.01848
55518.69233	47.80377	0.00215	3.60202	24.58428	-0.00779	0.85978	0.01798
55519.63904	47.80124	0.00220	3.58447	24.62698	-0.00783	0.77323	0.01873
55521.74963	47.80237	0.00197	3.60000	24.56756	-0.00606	0.67096	0.01865
55522.70507	47.80259	0.00195	3.60158	24.22742	-0.01546	0.74732	0.01857
55523.75227	47.80495	0.00197	3.58240	24.93187	-0.00250	0.80502	0.01825
55539.63328	47.79842	0.00195	3.59768	24.61102	-0.01136	0.57500	0.01836
55542.69632	47.79789	0.00193	3.59055	24.71588	-0.01205	0.73343	0.01846
55544.69892	47.80078	0.00146	3.61297	24.63142	-0.00999	0.64341	0.01848
55546.60740	47.79905	0.00183	3.58382	24.68647	-0.01044	0.83876	0.01826
55547.68313	47.80689	0.00181	3.61073	24.59018	-0.01538	0.71074	0.01818
55817.91683	47.80415	0.00163	3.58758	24.75806	-0.01648	0.69149	0.01819
55871.72296	47.80264	0.00189	3.56078	24.55298	-0.00979	0.76060	0.01884
55875.75986	47.80443	0.00166	3.60406	24.82217	-0.01232	0.78623	0.01802
55887.80195	47.80000	0.00212	3.59476	24.55047	-0.00840	0.83975	0.01854
55889.67389	47.80156	0.00212	3.59822	24.88792	-0.02224	0.85840	0.01841
55891.67563	47.80750	0.00185	3.61297	24.63142	-0.01742	0.53778	0.01831

Table A.2. continued.

BJD - 2400000	RV $[kms^{-1}]$	σ_{RV} $[kms^{-1}]$	FWHM $[kms^{-1}]$	Contrast	BIS $[kms^{-1}]$	S-index	$H\alpha$
55893.67046	47.80062	0.00194	3.58916	24.51550	-0.01489	0.63131	0.01860
55895.71856	47.80340	0.00225	3.56078	24.55298	-0.00774	0.95793	0.01835
55924.65743	47.80118	0.00156	3.62850	24.25183	-0.01020	0.60524	0.01839
55925.60322	47.79804	0.00182	3.59435	25.43663	-0.01511	1.38852	0.01824
55926.68814	47.79881	0.00182	3.59476	24.55047	-0.00395	0.63496	0.01821
55927.67658	47.79824	0.00225	3.59061	24.89397	-0.01865	0.93117	0.01801
55928.78900	47.79444	0.00275	3.62850	24.25183	-0.01484	0.38422	0.01788
55929.67904	47.80136	0.00209	3.59492	24.50066	-0.01258	0.69748	0.01819
55930.68755	47.80549	0.00375	3.59861	24.84315	-0.01588	0.89780	0.01832
55931.63830	47.80153	0.00183	3.59435	25.43663	-0.00241	0.73302	0.01842
55932.66330	47.80040	0.00153	3.59597	24.72643	-0.01358	0.67666	0.01894
55933.70230	47.80510	0.00194	3.59435	25.43663	-0.01285	0.69418	0.01847
55940.66160	47.80219	0.00245	3.60240	24.72910	0.001540	0.65311	0.01811
55941.73303	47.80174	0.00192	3.60202	24.58428	-0.00592	0.53807	0.01808
55942.65135	47.80209	0.00165	3.58580	24.60535	-0.00790	0.83814	0.01792
55943.74352	47.80267	0.00187	3.60196	24.58954	-0.01134	0.89701	0.01786
55944.74860	47.80799	0.00198	3.57878	24.65019	-0.00388	0.88405	0.01830
55945.74749	47.80385	0.00201	3.59861	24.84315	-0.01403	1.17721	0.01744
55946.74356	47.80763	0.00196	3.61448	24.53406	-0.00446	0.48098	0.01728
55947.72814	47.80986	0.00175	3.60507	24.73606	-0.01318	0.47686	0.01787
55948.72736	47.80782	0.00182	3.59435	25.43663	-0.01832	0.67393	0.01777
55949.72113	47.80933	0.00203	3.60071	24.82345	-0.02080	0.70198	0.01790
55950.73282	47.80362	0.00199	3.59822	24.88792	-0.01702	0.89344	0.01829
55997.54782	47.80145	0.00223	3.59899	24.73087	-0.01361	0.77080	0.01859
55999.50620	47.80363	0.00170	3.60071	24.82345	-0.01048	0.99767	0.01797
56001.57468	47.80602	0.00235	3.59061	24.89397	-0.01014	1.01487	0.01874
56004.48819	47.80754	0.00181	3.58120	24.91090	-0.01921	0.81673	0.01861
56006.56154	47.80192	0.00206	3.60283	24.58144	-0.01552	0.85736	0.01833
56008.52020	47.79842	0.00174	3.60406	24.82217	-0.00322	0.95240	0.01943
56013.54468	47.79717	0.00215	3.59818	24.55765	-0.00810	0.98921	0.01809
56021.50098	47.80481	0.00233	3.60196	24.58954	-0.00390	0.78758	0.01770
56024.48555	47.80081	0.00165	3.58729	24.69291	-0.01661	0.49211	0.01779
56025.49723	47.80600	0.00236	3.59492	24.50066	-0.02052	1.52699	0.01755
56026.50327	47.80542	0.00258	3.57878	24.65019	-0.00644	0.65928	0.01765
56029.52945	47.79952	0.00241	3.58729	24.69291	-0.01481	0.43675	0.01832
56030.51172	47.80770	0.00292	3.58758	24.75806	0.009850	0.35110	0.01770
56031.51835	47.80923	0.00450	3.59858	24.52790	-0.05071	0.37144	0.01787
56180.85874	47.80221	0.00287	3.60353	24.35406	-0.01243	0.91964	0.01849
56181.87228	47.80618	0.00209	3.60071	24.82345	-0.01439	1.07214	0.01850
56182.87143	47.79806	0.00299	3.58335	24.87303	-0.00710	0.36638	0.01867
56186.84912	47.80768	0.00171	3.59858	24.52790	-0.01119	1.00343	0.01910
56187.86191	47.80731	0.00534	3.59861	24.84315	0.001580	1.51751	0.01896
56190.88488	47.80761	0.00226	3.59858	24.52790	0.002050	0.85908	0.01906
56192.86732	47.80342	0.00272	3.59595	24.58150	-0.00316	0.88605	0.01926
56193.85343	47.80615	0.00204	3.59822	24.88792	-0.01101	1.09271	0.01896
56194.87392	47.80390	0.00214	3.59061	24.89397	-0.00833	0.69008	0.01876
56195.83731	47.80180	0.00211	3.58335	24.87303	-0.00925	0.79571	0.01870
56196.84078	47.80332	0.00182	3.60071	24.82345	-0.00746	0.93673	0.01915
56198.85435	47.80369	0.00359	3.61448	24.53406	-0.01265	0.03357	0.01881
56199.85744	47.80601	0.00299	3.60353	24.35406	-0.01251	0.48219	0.01979
56200.82093	47.80271	0.00239	3.61448	24.53406	-0.02950	0.95819	0.02087
56201.82289	47.80065	0.00227	3.57375	25.51735	-0.00588	1.16869	0.01962
56202.87283	47.80820	0.00231	3.59299	24.63871	-0.01651	0.92122	0.01907
56235.67528	47.80431	0.00229	3.61565	24.52854	-0.01613	0.67675	0.01919
56236.68649	47.80250	0.00212	3.60071	24.82345	-0.01686	1.06575	0.01932
56237.65447	47.79827	0.00211	3.61565	24.52854	-0.00715	0.80598	0.01872
56238.71167	47.80157	0.00205	3.59299	24.63871	-0.01038	0.84328	0.01867
56245.62430	47.80771	0.00231	3.59858	24.52790	-0.01033	1.22042	0.01838
56247.61995	47.80508	0.00195	3.59858	24.52790	-0.01245	0.41762	0.01926
56248.70192	47.80076	0.00303	3.61222	24.92663	-0.01091	0.72502	0.01898
56250.65160	47.79364	0.00302	3.58479	24.64203	-0.00648	0.69128	0.01851
56251.70851	47.79628	0.00168	3.60071	24.82345	-0.01358	0.98762	0.01985
56252.66497	47.79695	0.00169	3.59861	24.84315	-0.00728	0.91803	0.01865
56254.67894	47.79673	0.00170	3.60071	24.82345	-0.01269	0.90922	0.01847
56255.61817	47.80003	0.00196	3.59861	24.84315	-0.01083	0.85057	0.01912
56258.65243	47.80533	0.00196	3.61222	24.92663	-0.01172	0.99596	0.01860

Table A.2. continued.

BJD - 2400000	RV $[kms^{-1}]$	σ_{RV} $[kms^{-1}]$	FWHM $[kms^{-1}]$	Contrast	BIS $[kms^{-1}]$	S-index	$H\alpha$
56259.65469	47.80498	0.00206	3.59858	24.52790	-0.01031	0.71719	0.01842
56262.81151	47.80699	0.00187	3.61222	24.92663	-0.00262	0.97329	0.01809
56263.64804	47.80253	0.00287	3.59861	24.84315	0.001800	0.60908	0.01759

Table A.3. GJ 3543 RVs, its uncertainty and activity indicators.

BJD - 2400000	RV $[kms^{-1}]$	σ_{RV} $[kms^{-1}]$	FWHM $[kms^{-1}]$	Contrast	BIS $[kms^{-1}]$	S-index	$H\alpha$
54455.81748	15.09084	0.00134	3.72672	20.74941	-0.00725	2.42133	0.02606
54825.82158	15.09106	0.00106	3.72954	20.77381	-0.01019	2.56120	0.02738
54826.80721	15.09176	0.00099	3.72600	20.51434	-0.01092	2.81219	0.02980
54827.79556	15.09645	0.00113	3.72417	20.60870	-0.01565	2.50082	0.02735
54828.84278	15.09488	0.00102	3.72244	20.63083	-0.00892	2.44846	0.02575
54829.86968	15.09389	0.00116	3.72703	20.57069	-0.01032	3.22177	0.03741
54830.84558	15.09355	0.00128	3.72672	20.74941	-0.00975	2.52963	0.02766
54831.83059	15.08899	0.00134	3.74139	20.73712	-0.01837	2.36949	0.02655
54832.82130	15.09527	0.00202	3.72834	20.68230	-0.01583	2.49733	0.02709
54833.84856	15.08998	0.00102	3.72406	20.60702	-0.01285	2.34166	0.02562
54834.85241	15.08970	0.00117	3.72600	20.51434	-0.01553	2.34512	0.02590
55585.79129	15.09399	0.00112	3.73041	20.77120	-0.00931	2.31790	0.02572
55589.80228	15.09859	0.00128	3.72267	20.56052	-0.01017	3.38598	0.03712
55593.78829	15.09057	0.00114	3.72497	20.54240	-0.01024	2.32222	0.02496
55622.60745	15.09096	0.00108	3.71482	20.57990	-0.01538	2.38990	0.02459
55628.66836	15.09394	0.00128	3.72876	20.54426	-0.01323	2.43931	0.02579
55629.67559	15.08887	0.00113	3.72244	20.63083	-0.00841	2.38816	0.02512
55630.71219	15.09126	0.00113	3.72556	20.54603	-0.00792	2.26502	0.02530
55632.67210	15.09896	0.00120	3.73159	20.72365	-0.01588	2.48187	0.02686
55633.64839	15.09842	0.00106	3.72956	20.71123	-0.01093	2.22836	0.02441
55634.65201	15.09676	0.00111	3.73331	20.43016	-0.01097	2.21318	0.02476
55638.63504	15.08924	0.00148	3.72343	20.56211	-0.00809	2.33684	0.02473
55639.61274	15.09100	0.00108	3.72834	20.68230	-0.00523	2.07769	0.02330
55642.61391	15.09322	0.00114	3.72020	20.23990	-0.00761	2.28483	0.02457
55643.65849	15.09596	0.00117	3.72889	20.73374	-0.01364	2.40455	0.02488
55644.61310	15.09842	0.00116	3.72672	20.74941	-0.01466	2.29391	0.02432
55648.62383	15.08819	0.00105	3.73091	20.59071	-0.01140	2.31546	0.02512
55652.47921	15.09772	0.00122	3.73159	20.72365	-0.01962	2.10686	0.02395
55654.47899	15.09558	0.00112	3.73555	20.57637	-0.00779	2.20247	0.02458
55657.47653	15.09423	0.00106	3.73033	20.64375	-0.01483	2.19046	0.02498
55659.47423	15.09254	0.00111	3.72149	20.50567	-0.01244	2.39384	0.02658
55663.47053	15.09659	0.00159	3.73030	20.62977	-0.01156	2.30264	0.02629
55672.58915	15.09790	0.00132	3.72621	20.59418	-0.00882	2.40820	0.02514
55676.56936	15.08937	0.00128	3.72149	20.50567	-0.01097	2.46696	0.02610
55677.53431	15.09222	0.00116	3.72684	20.52647	-0.01197	2.42020	0.02593
55711.48912	15.09185	0.00135	3.72591	20.59257	-0.00970	2.20280	0.02424
55871.80485	15.09344	0.00138	3.72668	20.74823	-0.01336	2.40549	0.02600
55874.81344	15.09026	0.00213	3.72822	20.66578	-0.01024	1.82523	0.02621
55875.83369	15.08913	0.00117	3.72700	20.55149	-0.01043	2.49935	0.02917
55878.83418	15.08896	0.00157	3.73700	20.74596	-0.00988	1.98883	0.02502
55880.84096	15.09154	0.00225	3.73700	20.74596	-0.00593	1.89586	0.02629
55887.84060	15.09473	0.00145	3.72962	20.59683	-0.00095	2.11055	0.02645
55888.81874	15.09496	0.00139	3.72538	20.63755	-0.02545	2.28485	0.02968
55889.83853	15.09467	0.00128	3.72729	20.55800	-0.01148	2.24282	0.02658
55890.85136	15.09197	0.00122	3.72556	20.54603	-0.01304	2.23126	0.02634
55891.82222	15.09423	0.00110	3.72834	20.68230	-0.00681	2.22775	0.02657
55892.81128	15.08969	0.00123	3.73033	20.64375	-0.01456	2.19169	0.02685
55893.82921	15.08623	0.00126	3.72497	20.54240	-0.00686	2.63181	0.02958
55894.80379	15.08860	0.00099	3.71482	20.57990	-0.01143	2.44420	0.02793
55996.71895	15.08933	0.00129	3.72834	20.68230	-0.01343	2.20589	0.02427
55997.66483	15.09181	0.00141	3.72429	20.76135	-0.01131	2.00610	0.02505
56002.71704	15.09518	0.00142	3.72385	20.47525	-0.00842	2.51458	0.02621
56003.66997	15.09791	0.00154	3.72703	20.57069	-0.01109	2.11422	0.02514
56005.69427	15.09413	0.00111	3.72385	20.47525	-0.00943	2.22501	0.02601
56007.61106	15.09227	0.00114	3.72834	20.68230	-0.01083	2.16732	0.02622
56008.65231	15.09501	0.00126	3.72406	20.60702	-0.01046	2.43808	0.02755
56010.58917	15.09231	0.00124	3.71482	20.57990	-0.01457	2.09934	0.02373
56011.63581	15.09124	0.00105	3.72834	20.68230	-0.00894	2.21262	0.02530
56012.58228	15.08975	0.00108	3.72668	20.74823	-0.00738	2.13713	0.02570
56020.62473	15.09582	0.00120	3.72889	20.73374	-0.01451	2.35845	0.02669
56021.55890	15.09221	0.00121	3.72874	20.80548	-0.01195	2.20731	0.02567
56022.61059	15.09188	0.00136	3.72429	20.76135	-0.01761	2.29623	0.02833
56024.59278	15.09162	0.00110	3.72729	20.55800	-0.00916	2.19298	0.02568
56025.61982	15.09072	0.00181	3.72729	20.55800	-0.01316	2.05005	0.02601
56026.59209	15.09309	0.00124	3.72874	20.55294	-0.01012	2.54414	0.02647
56031.65055	15.09088	0.00400	3.71807	20.53797	-0.00700	0.88335	0.02646

Table A.3. continued.

BJD - 2400000	RV $[kms^{-1}]$	σ_{RV} $[kms^{-1}]$	FWHM $[kms^{-1}]$	Contrast	BIS $[kms^{-1}]$	S-index	$H\alpha$
56354.75925	15.08873	0.00114	3.72874	20.80548	-0.01113	2.28217	0.02744
56355.73982	15.09588	0.00320	3.72516	20.45809	-0.01596	0.79015	0.02421
56360.76207	15.09451	0.00124	3.73555	20.57637	-0.00976	2.18953	0.02353
56361.72566	15.09299	0.00140	3.71807	20.53797	-0.01023	1.86769	0.02306
56363.71853	15.09338	0.00120	3.72889	20.73374	-0.00886	2.04838	0.02452
56365.66954	15.09406	0.00114	3.72889	20.73374	-0.01144	2.21021	0.02570
56366.62280	15.09451	0.00221	3.72149	20.50567	-0.02034	2.23726	0.02479
56367.59345	15.09417	0.00126	3.71482	20.57990	-0.01291	3.05196	0.03071
56369.64591	15.09181	0.00116	3.72874	20.55294	-0.00923	2.62690	0.03010
56370.68844	15.09180	0.00116	3.72149	20.50567	-0.00527	3.07099	0.03141
56371.68821	15.08913	0.00121	3.72149	20.50567	-0.01343	2.26730	0.02501
56372.63459	15.08860	0.00124	3.75693	20.44840	-0.01294	2.76210	0.03103
56373.65240	15.08967	0.00135	3.72874	20.80548	-0.01542	2.24918	0.02510
56374.66466	15.08518	0.00113	3.72149	20.50567	-0.00944	2.12089	0.02441

References

Alonso, R., Barbieri, M., Rabus, M., Deeg, H. J., Belmonte, J. A., Almenara, J. M., 2008. Limits to the planet candidate GJ 436c. A&A 487, L5–L8, 0804.3030.

Anglada-Escudé, G., Butler, R. P., 2012. The HARPS-TERRA Project. I. Description of the Algorithms, Performance, and New Measurements on a Few Remarkable Stars Observed by HARPS. ApJS 200, 15, 1202.2570.

Anglada-Escudé, G., Rojas-Ayala, B., Boss, A. P., Weinberger, A. J., Lloyd, J. P., 2013. GJ 1214 reviewed. Trigonometric parallax, stellar parameters, new orbital solution, and bulk properties for the super-Earth GJ 1214b. A&A 551, A48, 1210.8087.

Artigau, É., Astudillo-Defru, N., Delfosse, X., Bouchy, F., Bonfils, X., Lovis, C., Pepe, F., Moutou, C., Donati, J.-F., Doyon, R., Malo, L., 2014. Telluric-line subtraction in high-accuracy velocimetry: a PCA-based approach. In: Society of Photo-Optical Instrumentation Engineers (SPIE) Conference Series. Vol. 9149 of Society of Photo-Optical Instrumentation Engineers (SPIE) Conference Series. p. 5.

Beust, H., Bonfils, X., Montagnier, G., Delfosse, X., Forveille, T., 2012. Dynamical evolution of the Gliese 436 planetary system. Kozai migration as a potential source for Gliese 436b's eccentricity. A&A 545, A88, 1208.0237.

Bonfils, X., Delfosse, X., Udry, S., Forveille, T., Mayor, M., Perrier, C., Bouchy, F., Gillon, M., Lovis, C., Pepe, F., Queloz, D., Santos, N. C., Ségransan, D., Bertaux, J.-L., 2013. The HARPS search for southern extra-solar planets. XXXI. The M-dwarf sample. A&A 549, A109, 1111.5019.

Bonfils, X., Mayor, M., Delfosse, X., Forveille, T., Gillon, M., Perrier, C., Udry, S., Bouchy, F., Lovis, C., Pepe, F., Queloz, D., Santos, N. C., Bertaux, J.-L., 2007. The HARPS search for southern extra-solar planets. X. A m sin i = 11 $M\_\oplus$ planet around the nearby spotted M dwarf ¡ASTROBJ¿GJ 674¡/ASTROBJ¿. A&A 474, 293–299, 0704.0270.

Bouchy, F., Pepe, F., Queloz, D., 2001. Fundamental photon noise limit to radial velocity measurements. A&A 374, 733–739.

Butler, R. P., Vogt, S. S., Marcy, G. W., Fischer, D. A., Wright, J. T., Henry, G. W., Laughlin, G., Lissauer, J. J., 2004. A Neptune-Mass Planet Orbiting the Nearby M Dwarf GJ 436. ApJ 617, 580–588, astro-ph/0408587.

Charbonneau, D., Berta, Z. K., Irwin, J., Burke, C. J., Nutzman, P., Buchhave, L. A., Lovis, C., Bonfils, X., Latham, D. W., Udry, S., Murray-Clay, R. A., Holman, M. J., Falco, E. E., Winn, J. N., Queloz, D., Pepe, F., Mayor, M., Delfosse, X., Forveille, T., 2009. A super-Earth transiting a nearby low-mass star. Nature 462, 891–894, 0912.3229.

Chelli, A., 2000. Optimizing Doppler estimates for extrasolar planet detection. I. A specific algorithm for shifted spectra. A&A 358, L59–L62.

Delfosse, X., Donati, J.-F., Kouach, D., Hébrard, G., Doyon, R., Artigau, E., Bouchy, F., Boisse, I., Brun, A. S., Hennebelle, P., Widemann, T., Bouvier, J., Bonfils, X., Morin, J., Moutou, C., Pepe, F., Udry, S., do Nascimento, J.-D., Alencar, S. H. P., Castilho, B. V., Martioli, E., Wang, S. Y., Figueira, P., Santos, N. C., 2013. World-leading science with SPIRou - The nIR spectropolarimeter / high-precision velocimeter for CFHT. In: Cambresy, L., Martins, F., Nuss, E., Palacios, A. (Eds.), SF2A-2013: Proceedings of the Annual meeting of the French Society of Astronomy and Astrophysics. pp. 497–508.

Demory, B.-O., Gillon, M., Barman, T., Bonfils, X., Mayor, M., Mazeh, T., Queloz, D., Udry, S., Bouchy, F., Delfosse, X., Forveille, T., Mallmann, F., Pepe, F., Perrier, C., 2007. Characterization of the hot Neptune GJ 436 b with Spitzer and ground-based observations. A&A 475, 1125–1129, 0707.3809.

Galland, F., Lagrange, A.-M., Udry, S., Chelli, A., Pepe, F., Queloz, D., Beuzit, J.-L., Mayor, M., 2005. Extrasolar planets and brown dwarfs around A-F type stars. I. Performances of radial velocity measurements, first analyses of variations. A&A 443, 337–345, astro-ph/0509111.

Gillon, M., Demory, B.-O., Madhusudhan, N., Deming, D., Seager, S., Zsom, A., Knutson, H. A., Lanotte, A. A., Bonfils, X., Désert, J.-M., Delrez, L., Jehin, E., Fraine, J. D., Magain, P., Triaud, A. H. M. J., 2014. Search for a habitable terrestrial planet transiting the nearby red dwarf GJ 1214. A&A 563, A21, 1307.6722.

Gillon, M., Pont, F., Demory, B.-O., Mallmann, F., Mayor, M., Mazeh, T., Queloz, D., Shporer, A., Udry, S., Vuissoz, C., 2007. Detection of transits of the nearby hot Neptune GJ 436 b. A&A 472, L13–L16, 0705.2219.

Howarth, I. D., Siebert, K. W., Hussain, G. A. J., Prinja, R. K., 1997. Cross-correlation characteristics of OB stars from IUE spectroscopy. MNRAS 284, 265–285.

Kürster, M., Endl, M., Rouesnel, F., Els, S., Kaufer, A., Brillant, S., Hatzes, A. P., Saar, S. H., Cochran, W. D., 2003. The low-level radial velocity variability in Barnard's star (= GJ 699). Secular acceleration, indications for convective redshift, and planet mass limits. A&A 403, 1077–1087, astro-ph/0303528.

Lanotte, A. A., Gillon, M., Demory, B.-O., Fortney, J. J., Astudillo, N., Bonfils, X., Magain, P., Delfosse, X., Forveille, T., Lovis, C., Mayor, M., Neves, V., Pepe, F., Queloz, D., Santos, N., Udry, S., 2014. A global analysis of Spitzer and new HARPS data confirms the loneliness and metal-richness of GJ 436 b. A&A 572, A73, 1409.4038.

Lépine, S., Shara, M. M., 2005. A Catalog of Northern Stars with Annual Proper Motions Larger than 0.15" (LSPM-NORTH Catalog). AJ 129, 1483–1522, astro-ph/0412070.

Mann, A. W., Gaidos, E., Ansdell, M., 2013. Spectro-thermometry of M Dwarfs and Their Candidate Planets: Too Hot, Too Cool, or Just Right? ApJ 779, 188, 1311.0003.

Morin, J., Donati, J.-F., Petit, P., Delfosse, X., Forveille, T., Albert, L., Aurière, M., Cabanac, R., Dintrans, B., Fares, R., Gastine, T., Jardine, M. M., Lignières, F., Paletou, F., Ramirez Velez, J. C., Théado, S., 2008. Large-scale magnetic topologies of mid M dwarfs. MNRAS 390, 567–581, 0808.1423.

Quirrenbach, A., Amado, P. J., Seifert, W., Sánchez Carrasco, M. A., Mandel, H., Caballero, J. A., Mundt, R., Ribas, I., Reiners, A., Abril, M., Aceituno, J., Alonso-Floriano, J., Ammler-von Eiff, M., Anglada-Escude, G., Antona Jiménez, R., Anwand-Heerwart, H., Barrado y Navascués, D., Becerril, S., Bejar, V., Benitez, D., Cardenas, C., Claret, A., Colome, J., Cortés-Contreras, M., Czesla, S., del Burgo, C., Doellinger, M., Dorda, R., Dreizler, S., Feiz, C., Fernandez, M., Galadi, D., Garrido, R., González Hernández, J., Guardia, J., Guenther, E., de Guindos, E., Gutiérrez-Soto, J., Hagen, H. J., Hatzes, A., Hauschildt, P., Helmling, J., Henning, T., Herrero, E., Huber, A., Huber, K., Jeffers, S., Joergens, V., de Juan, E., Kehr, M., Klutsch, A., Kürster, M., Lalitha, S., Laun, W., Lemke, U., Lenzen, R., Lizon, J.-L., López del Fresno, M., López-Morales, M., López-Santiago, J., Mall, U., Martin, E., Martín-Ruiz, S., Mirabet, E., Montes, D., Morales, J. C., Morales Muñoz, R., Moya, A., Naranjo, V., Oreiro, R., Pérez Medialdea, D., Pluto, M., Rabaza, O., Ramon, A., Rebolo, R., Reffert, S., Rhode, P., Rix, H.-W., Rodler, F., Rodríguez, E., Rodríguez López, C., Rodríguez Pérez, E., Rodriguez Trinidad, A., Rohloff, R.-R., Sánchez-Blanco, E., Sanz-Forcada, J., Schäfer, S., Schiller, J., Schmidt, C., Schmitt, J., Solano, E., Stahl, O., Storz, C., Stürmer, J., Suarez, J. C., Thiele, U., Ulbrich, R., Vidal-Dasilva, M., Wagner, K., Winkler, J., Xu, W., Zapatero Osorio, M. R., Zechmeister, M., 2012. CARMENES. I: instrument and survey overview. In: Society of Photo-Optical Instrumentation Engineers (SPIE) Conference Series. Vol. 8446 of Society of Photo-Optical Instrumentation Engineers (SPIE) Conference Series.

Ribas, I., Font-Ribera, A., Beaulieu, J.-P., 2008. A ˜5 $M_{\oplus}$; Super-Earth Orbiting GJ 436? The Power of Near-Grazing Transits. ApJ 677, L59–L62, 0801.3230.

Shlens, J., 2014. A Tutorial on Principal Component Analysis. ArXiv e-prints 1404.1100.

Snellen, I. A. G., de Kok, R. J., de Mooij, E. J. W., Albrecht, S., 2010. The orbital motion, absolute mass and high-altitude winds of exoplanet HD209458b. Nature 465, 1049–1051, 1006.4364.

Stevenson, K. B., Harrington, J., Lust, N. B., Lewis, N. K., Montagnier, G., Moses, J. I., Visscher, C., Blecic, J., Hardy, R. A., Cubillos, P., Campo, C. J., 2012. Two nearby Sub-Earth-sized Exoplanet Candidates in the GJ 436 System. ApJ 755, 9, 1207.4245.

van Leeuwen, F., 2007. Validation of the new Hipparcos reduction. A&A 474, 653–664, 0708.1752.

Vaughan, A. H., Preston, G. W., Wilson, O. C., 1978. Flux measurements of CA II H and K emission. PASP 90, 267–274.

Zechmeister, M., Kürster, M., 2009. The generalised Lomb-Scargle periodogram. A new formalism for the floating-mean and Keplerian periodograms. A&A 496, 577–584, 0901.2573.

Zucker, S., Mazeh, T., 2006. TIRAVEL - Template-Independent RAdial VELocity measurement. MNRAS 371, 1513–1518, astro-ph/0607293.

Chapter 5

Conclusions and future prospects

Summary and conclusions

During my thesis I analysed the stellar activity of M dwarfs through the Ca II H&K lines. The R'_{HK}-index is an activity tracer that scales the emission on the Ca II H&K lines to the bolometric luminosity (bolometric calibration, C_{cf}) and subtracts the photospheric component of such emission (photospheric calibration, R_{phot}). The R'_{HK}-index is therefore a true measurement of the stellar activity and it allows to compare the activity levels for stars of different spectral types. I calibrated for the first time the R'_{HK}-index for M dwarfs (up to M6) by providing relationships for both the bolometric and photospheric calibration as a function three colour-indices (B-V, V-K and I-K).

I provide reliable R'_{HK} values for the *HARPS* M dwarf sample (403 stars). I analysed the R'_{HK}–P_{rot} dependence for 31 M dwarfs having well determined rotation periods. From this analysis I obtained for the first time the R'_{HK} vs. P_{rot} relationship for M dwarfs. The dependence between R'_{HK} and P_{rot} shows the differentiation of two activity regimes (saturated and unsaturated) occurring at about $P_{rot} = 10$ days, in agreement with previous evidences of the saturated and unsaturated activity regimes (e.g. obtained from the L_X/L_{bol} vs. rotation analysis; Pizzolato et al. 2003, Kiraga and Stepien 2007). From the unsaturated regime in the R'_{HK} vs. P_{rot} relationship, we observed that the magnetic activity in fully convective stars (M< 0.35M$_\odot$) is dependent on the rotation period, as expected. By using this relationship it is now possible to infer rotation periods from R'_{HK} values of M dwarfs. This is particularly essential in the search for extrasolar planets orbiting low-mass stars, because it allows to determine if radial velocity periodic variations could be due to stellar activity (rejecting false-positives).

We show a dependence between the R'_{HK} and the mass of M dwarfs. When plotting R'_{HK} vs. mass a lower envelope shows that the basal magnetic activity increases with mass for stars ranging 0.35-0.6M$_\odot$; outside these limits the lower envelope remains at constant basal R'_{HK}. The activity-mass dependence has been noticed by other authors (e.g. Kiraga and Stepien 2007, Mittag et al. 2013). However, the origin of the dependence of activity with masses of cool-stars is still unclear and further work is needed to better understand it. We also showed that M dwarfs presenting larger R'_{HK} variations are the most active, which is also the case for GK dwarfs (Lovis et al. 2011).

The second block of my thesis was dedicated to optimise the extraction of radial velocities from high-resolution spectra of M dwarfs. I developed an algorithm (NAIRA) to extract radial velocities from a χ^2-minimisation approach by using a true stellar-template. The stellar-template consists in a high signal-to-noise spectrum of the star itself obtained from the median of the whole data set. A telluric-template is derived and used to reject zones with telluric and/or with poor Doppler information. This methodology shows significant improvements in the accurateness of radial velocities (by obtaining lower RV dispersion) when compared to the classical cross-correlation function, or even when comparing to the HARPS-TERRA software (a comparison with other stars should be performed). NAIRA also derives a velocity bisector

span (RV_{χ^2-bis}) obtained from the difference between the radial velocity computed using only the wings or cores of spectral lines. The RV_{χ^2-bis} has shown slight improvements compared to the bisector span obtained form the CCF.

With the development and the test of NAIRA I demonstrated that RV extraction from a calibrated spectrum could be improved and that RV software can be a limitation in RV accuracy if it is not optimised (even if it is carefully developed as the *HARPS* or *SOPHIE* official pipelines). The detection of some planets is secured with NAIRA while they are outside detection capabilities of classical *CCF* method. NAIRA is now available and will be systematically used to derive RV of M dwarfs from the programs of the Grenoble team.

Prospects

The work performed during a thesis does not end when the thesis is completed. There are questions waiting for answers and work to be refined. Some short-term prospects related to this thesis are,

On stellar activity:

- We want to refine the R'_{HK} vs. P_{rot} relationship by adding new stars with rotation periods obtained from photometric or activity-indices modulation. This would allow to sample several mass bins along the M dwarfs domain, with a sufficient number of stars in each bin to test if the R'_{HK} vs. P_{rot} relationship is really dependent to the mass for these spectral types.
- Obtaining absolute calibration for other activity proxies should be extremely useful for extra-solar planet search programs. In the visible the behaviour of Na I D and Hα as a function of P_{rot} and stellar parameters should be explored with same attention as what we have done for Ca II H&K lines. In particular it is demonstrated that Hα- and S-index does not correlate in all cases, as for a few stars the two signals are uncorrelated and even sometimes anticorrelated. Meunier & Delfosse (2009) show that the correlation varies along the magnetic cycle because filaments dilute the strong correlation in bright active regions. A calibration of such behaviour could be used to obtain a proxy of the phase of stellar magnetic field.
- From my R'_{HK} study we dispose of a large sample of M dwarfs with a well determined activity level. This sample should be used to search for and characterise the best activity index in infrared. This point is crucial for the future *SPIRou* program.
- A R'_{HK} vs. RV_{RMS} analysis need to be done to determine the expected minimal RV *jitter*.

On radial velocity extraction with NAIRA:

- We are working on a paper presenting the discovery of new planets which are undetected by the CCF classical method.
- When using NAIRA, we need to characterise the accuracy gain in function of the number of spectra (depending on their signal-to-noise) available to build the stellar-template.
- The analysis of radial velocities extracted with NAIRA show lower values for the *RMS* but, in some cases, greater χ^2_ν values than those from CCF. This means that we need to determine the source producing underestimated errors.

- In the case of faint stars, using the telluric-template derived from another star than the one being analysed shows improved radial velocities. We need to test if this is also true when using the stellar-template from another star.
- The whole *HARPS* M dwarf sample will be re-analysed by extracting radial velocities with NAIRA. After that, the occurrence of planets orbiting M dwarfs will be updated.
- We need to test if the use of NAIRA improves the extraction of radial velocities in stars of earlier spectral type. The preliminary results I obtained on τCeti (and published in the Artigau et al. 2014 SPIE paper) seems very encouraging about the potential of NAIRA for another spectral type than M dwarfs.
- NAIRA will be declined for *SOPHIE* and will be developed to be used for future *SPIRou* data.

Appendix A

Publications related to this thesis

Refereed papers

Astudillo-Defru, N., Bonfils, X., Delfosse, X., Ségransan, D., Forveille, T., Bouchy, F., Gillon, M., Lovis, C., Mayor, M., Neves, V., Pepe, F., Perrier, C., Queloz, D., Rojo, P., Santos, N. C., Udry, S., 2015. The HARPS search for southern extra-solar planets. XXXVI. Planetary systems and stellar activity of the M dwarfs GJ 3293, GJ 3341, and GJ 3543. A&A 575, A119, 1411.7048.

Bonfils, X., Lo Curto, G., Correia, A. C. M., Laskar, J., Udry, S., Delfosse, X., Forveille, T., **Astudillo- Defru, N.**, Benz, W., Bouchy, F., Gillon, M., Hébrard, G., Lovis, C., Mayor, M., Moutou, C., Naef, D., Neves, V., Pepe, F., Perrier, C., Queloz, D., Santos, N. C., Ségransan, D., 2013. The HARPS search for southern extra-solar planets. XXXIV. A planetary system around the nearby M dwarf GJ 163, with a super-Earth possibly in the habitable zone. A&A 556, A110, 1306.0904.

Borgniet, S., Boisse, I., Lagrange, A.-M., Bouchy, F., Arnold, L., Díaz, R. F., Galland, F., Delorme, P., Hébrard, G., Santerne, A., Ehrenreich, D., Ségransan, D., Bonfils, X., Delfosse, X., Santos, N. C., Forveille, T., Moutou, C., Udry, S., Eggenberger, A., Pepe, F., **Astudillo, N.**, Montagnier, G., 2014. Extrasolar planets and brown dwarfs around A-F type stars. VIII. A giant planet orbiting the young star HD 113337. A&A 561, A65, 1310.1994.

Lanotte, A. A., Gillon, M., Demory, B.-O., Fortney, J. J., **Astudillo, N.**, Bonfils, X., Magain, P., Delfosse, X., Forveille, T., Lovis, C., Mayor, M., Neves, V., Pepe, F., Queloz, D., Santos, N., Udry, S., 2014. A global analysis of Spitzer and new HARPS data confirms the loneliness and metal-richness of GJ 436 b. A&A 572, A73, 1409.4038.

Moutou, C., Hébrard, G., Bouchy, F., Arnold, L., Santos, N. C., **Astudillo-Defru, N.**, Boisse, I., Bonfils, X., Borgniet, S., Delfosse, X., Díaz, R. F., Ehrenreich, D., Forveille, T., Gregorio, J., Labrevoir, O., Lagrange, A.-M., Montagnier, G., Montalto, M., Pepe, F., Sahlmann, J., Santerne, A., Ségransan, D., Udry, S., Vanhuysse, M., 2014. The SOPHIE search for northern extrasolar planets. VI. Three new hot Jupiters in multi-planet extrasolar systems. A&A 563, A22, 1311.5271.

Non refereed papers

Artigau, E., **Astudillo-Defru, N.**, Delfosse, X., Bouchy, F., Bonfils, X., Lovis, C., Pepe, F., Moutou, C., Donati, J.-F., Doyon, R., Malo, L., 2014. Telluric-line subtraction in high-accuracy velocimetry: a PCA-based approach. In: Society of Photo-Optical Instrumentation Engineers (SPIE) Conference Series. Vol. 9149 of Society of Photo-Optical Instrumentation Engineers (SPIE) Conference Series. p. 5.